Use of optical imaging in brain slices from developing rats to evaluate spatio-temporal dynamics of large-scale neuronal coalitions: effects of physiological and pharmacological manipulations

Antoine-Scott P. Badin

Saint Edmund Hall College, Oxford

This dissertation is submitted to the University of Oxford for the degree of Doctor of Philosophy

Department of Physiology, Anatomy and Genetics

University of Oxford

Hilary term 2017

Word count:

49 332

Supervisor:

Prof. Susan A. Greenfield

Co-supervisor:

Dr. Edward Mann

Location:

Department of Pharmacology, University of Oxford

-

Neuro-Bio Ltd., Culham Science Centre

Time frame:

Michaelmas 2012 – Hilary 2017

"Science does not know its debt to imagination"

– Ralph Waldo Emerson

Dédiée à mon grand-père, Dr. Georges Noêl

ACKNOWLEDGEMENTS

There are numerous people to whom I would like to express my gratitude for the contributions they have brought me for this project. I would like to thank my supervisors, Prof. Susan Greenfield and Dr. Ed Mann for the opportunities they have provided me, and their continued support throughout the length of this project. I must also thank Prof. Zoltan Molnar for his guidance, and his lab members for their help in carrying out DAPI staining procedures.

I am also grateful to Dr. Ian Devonshire and Dr. Francesco Fermani for all the practical and methodological help, as well as in providing continued support in data analysis and use of mathematical software.

Finally, I would like to thank my family, and in particular my parents, for all their amazing support, financial and otherwise, as well as for tolerating my lack of visits over the last few years. I could not have completed this project without them.

ABSTRACT

Use of optical imaging in brain slices from developing rats to evaluate spatio-temporal dynamics of large-scale neuronal coalitions: effects of physiological and pharmacological manipulations

By Antoine-Scott Badin, Saint Edmund Hall College, Oxford, for the degree of Doctor of Philosophy

Voltage-sensitive dye imaging (VSDI), is a relatively novel technique which enables the recording and observation of neuronal population activity at the meso-scale of brain organisation. This optical imaging technique is used here in combination with extracellular electrophysiology (field potentials) in order to investigate 'Neuronal Assemblies', i.e. the phenomenon of synchronous and dynamic activation of millions of inter-connected neurons, giving rise to detectable patterns of large-scale population activity. For the experiments presented here, VSDI and field potentials were used to characterise and compare assemblies evoked in 2 cortical and 2 sub-cortical preparations: for the former, the well-studied primary somatosensory cortex (S1BF) was chosen, in addition to the agranular insular cortex (AIC) which has been less extensively studied. For the latter sub-cortical areas, responses were evoked in ventroposteromedial (VPM) thalamic nucleus and basal forebrain (BF). These investigations suggested cortical tissue produced similar response dynamics regardless of location, meaning large neuronal assemblies may be a inherent property of cortical tissue, since these response types were not found in sub-cortical structures. In addition to this, comparisons of evoked assemblies highlighted clear differences between cortical, thalamocortical and sub-cortical activity patterns, with evoked responses appearing geared for their biological functions, and allowed for the selection of 3 preparations of interest, i.e. S1BF LIV, AIC LII/III and thalamocortical stimulations, for characterising more fully the impact of anaesthetics on the parameters of neuronal assemblies. All anaesthetics tested here induced dose-dependent inhibitions of cortical activity, which were significantly more pronounced when assemblies were triggered via thalamocortical (remote) activation and in BF. Comparison of anaesthetic effects seen here with those induced on target proteins (from the literature) highlighted $GABA_A$ and nicotinic acetylcholine (nACh) receptors as key effectors in anaesthetic-induced inhibition by group 1 anaesthetics, while experiments with ketamine highlighted NMDA and nACh receptors in addition to HCN channels. These data describe more fully the manner in which anaesthetics rely on multi-target mechanisms, as well as exemplifying the practicality of combining VSDI with field potentials in the investigation of drug action on neuronal assembly functioning and cerebral function.

CONTENTS

1. Chapter 1: INTRODUCTION
   - 1.1. Hypothesis and aims……..1
   - 1.2. Hierarchal levels of organisation……...3
     - 1.2.1. From macromolecules to coherent, dynamic brain activity……..3
     - 1.2.2. Defining the spatio-temporal parameters of the 'micro-' and 'macro-scales'……..4
     - 1.2.3. Investigating cerebral functioning……6
   - 1.3. Intervening levels of organisation……...15
     - 1.3.1. Emergence of activity from microscopic neuronal events……..16
     - 1.3.2. Bridging the micro- and macro-scales using the intervening meso-scale level of organisation……18
   - 1.4. 'Neuronal assemblies', the functional units of mesoscopic brain functioning……20
     - 1.4.1. Definition of 'neuronal assemblies'……20
     - 1.4.2. Reciprocal impact of assembly dynamics between micro- and macro-scale events…..22
   - 1.5. Brain states as sensitive indices of cerebral functional state……..…27
     - 1.5.1. Event-related, functional cerebral events……27
     - 1.5.2. Linking dysfunctional population dynamics with atypical behavioural function……...31
     - 1.5.3.Clinical relevance of neuronal assemblies…….…..32
   - 1.6. Monitoring neuronal assemblies in vitro…….…35
     - 1.6.1. Brain slice preparation……...35
     - 1.6.2. Visualisation of neuronal assembly dynamics using voltage-sensitive dye imaging….37

2. Chapter 2: Methods
   - 2.1. Introduction……41
     - 2.1.1.Online monitoring of neuronal activity……...41
     - 2.1.2.Electrophysiology as a means of recording dynamic neuronal events……42
     - 2.1.3.Imaging as a means of recording population activity whit high spatio-temporal resolution……44
     - 2.1.4.Using voltage-sensitive dyes for imaging population dynamics……46
     - 2.1.5.Reporting electrical potential fluctuations in brain tissue using di-4-ANEPPS……..49
     - 2.1.6.Sources of noise within VSDI recordings……...56
   - 2.2. Sampling sites within rodent brain……..60
     - 2.2.1.Cortical structures……60
     - 2.2.2.Sub-cortical structures……63

2.3. Methodology and preparation of reagents and experiments……...65
2.3.1. Artificial cerebrospinal fluid (aCSF) solution……65
2.3.2. Drug solution……...68
2.3.3. Rig maintenance……..68
2.4. Harvesting of brain slices……69
2.4.1. Animals……....69
2.4.2. Anaesthesia and Schedule I culling……69
2.4.3. Surgical procedure……...70
2.4.4. Slicing of brain for isolation of specific sub-regions of interest……70
2.5. VSD staining……...72
2.6. Neuroanatomical studies using DAPI……75
2.7. Experimental preparation……75
2.7.1. Rig setup……..75
2.7.2. Stimulating electrode……...76
2.7.3. Electrophysiology……77
2.7.4. VSD imaging……...79
2.7.5. Stimulation protocols……...81
2.8. Analysis and presentation of data……85
2.8.1. Calculation and presentation of LFP data……85
2.8.2. Methods for analysis of 3-dimensional VSDI data……..86
2.8.3. Processing of BrainVision files……...……86
2.8.4. Rasterisation of averaged epoch-data files using a pre-drawn geometry……89
2.8.5. Statistical testing……..97

3. Chapter 3: RESULTS I – CHARACTERISATION AND QUANTIFICATION OF EVOKED NEURONAL ASSEMBLIES IN SELECTED CORTICAL AND SUB-CORTICAL STRUCTURES

3.1. Introduction……....99
3.1.1. Cortical structures……..101
3.1.2. Sub-cortical structures……...113
3.2. Materials and methods……...116
3.2.1. Drugs used for investigating internal assembly dynamics……....116
3.2.2. Radial and tangential geometries for analysis of VSDI data……119
3.3. Results……...121
3.3.1. Somatosensory cortex……121
3.3.2. Agranular insular cortex……137

3.3.3. Basal forebrain……...144
3.3.4. Characterisation of neuronal activity within assemblies……...149
3.4. Discussion……..159
3.4.1. Generating cortical assemblies using direct electrical stimulation……159
3.4.2. Measurement of dynamic assembly parameters……164
3.4.3. Mesoscopic population activity as a sensitive index of brain functioning……169
3.4.4. Complementarity of VSDI and LFP……..185
3.4.5. Conclusions……189

4. Chapter 4: RESULTS II – ANAESTHETIC ACTION ON MESOSCOPIC DYNAMICS OF CORTICAL AND SUB-CORTICAL NEURONAL ASSEMBLIES

4.1. Introduction……...192
4.1.1. A brief history of the discovery of anaesthetic drugs……193
4.1.2. The mode of action of anaesthetic drugs……...197
4.1.3. Trans-membrane ion channels relevant to anaesthesia……..200
4.1.4. Relating impaired assembly dynamics to anaesthesia……...212
4.1.5. Advantages of studying anaesthetic action at the meso-scale……...……213
4.2. Methods……215
4.2.1. Experimental anaesthetic concentrations……...215
4.2.2. Preparation of anaesthetic stock solutions……216
4.2.3. Normalisation of multi-epoch data……217
4.3. Results……...……219
4.3.1. Control experiments……..219
4.3.2. Anaesthetic effect on evoked cortical responses……...223
4.3.3. Effects of anaesthetics on assembly parameters……236
4.3.4. Effects of anaesthetics on LFP and comparison with VSDI……..240
4.3.5. Anaesthetic effect in basal forebrain……243
4.4. Discussion……246
4.4.1. Validation of experimental protocol……..246
4.4.2. Differential effects of anaesthetics in cortical and sub-cortical areas……...249
4.4.3. Interpreting in vitro data with respect to target effectors of anaesthesia……...254
4.4.4. Relevance of in vitro optical imaging and electrophysiological data in the study of anaesthesia.……264
4.4.5. Effect of anaesthesia on mesoscopic cortical computations……..268
4.4.6. Conclusions……....271

5. Chapter 5: GENERAL DISCUSSION

5.1. Investigating assemblies across brain regions using VSDI and electrophysiology……...274

5.2. Effects of anaesthetics on cortical and sub-cortical assemblies……276

5.3. Final comments……..277

6. REFERENCES……..279

"*Des chercheurs qui cherchent, on en trouve. Des chercheurs qui trouvent, on en cherche.*"

– General Charles de Gaule

Chapter 1: INTRODUCTION

1.1 Hypothesis and aims

The study of dynamic neuronal communication ('on-line recordings') has benefitted from novel advancements in the last few decades, in part due to the development of imaging techniques with very high resolution both in space and time which can be used to acquire comprehensive records of activity in real-time. The development of such techniques has indeed helped gather telling insights into a range of micro- and macroscopic processes from intracellular impulse propagation within neurons (Konnerth et al., 1987), dynamics of synaptic interactions (Parsons et al., 1989; Salzberg, 1989), and neuronal population behaviour in a wide range of brain states (Bourgeois et al., 2014; Hazra et al., 2013; Zhang et al., 2010). In particular, optical imaging using voltage-sensitive dyes (VSDI) has proven to be especially efficient in indiscriminately visualising such complex neuronal (population) events with breath-taking spatio-temporal resolution. Since the development of this technique, some 3 decades ago, it has been successfully adapted for use in a growing range of experimental designs (Grinvald and Hildesheim, 2004; Tang et al., 2016). More specifically, VSDI has been utilised in order to gain a greater understanding of synchronous population activity emerging from the interconnection of millions of neurons into organised networks throughout the brain, and how these systems are affected by bioactive compounds. Neuronal networks, and their dynamic cell assemblies, i.e. 'neuronal assemblies', have recently been implicated as the functional units of brain function, to a greater extent than their individual constituting neurons (Miller et al., 2014): it is therefore becoming increasingly important to understand their behaviour better, and their relationship to appropriate executive function. To this end, a combination of comprehensive description of neuronal dynamics at the network level as well as the predictive power of advanced

mathematical modelling approaches are desirable. In the present thesis, the concepts of synchronous neuronal population activity representing the basic functional unit of brain processing are investigated further. In so doing, the use of both physiological and pharmacological manipulations will be used to shed more light on the phenomenon of neuronal assemblies, such as to reach the three over-arching aims of the present thesis:

- To characterise and quantify the mesoscopic activity and decay dynamics of neuronal assemblies evoked in selected cerebral areas (primary somatosensory barrel field cortex, S1BF, and thalamocortical S1BF; Agranular insular cortex, AIC; thalamus, VPM, and basal forebrain; BF), and highlight conspicuous differences in the context of their respective underlying network organisation and/or stimulation paradigm.
- To characterise and quantify the effects of common anaesthetics (ketamine, etomidate and pentobarbital) on the above-measured assembly dynamics: Investigate to what extent anaesthetics act via similar or distinct mechanisms of action and how these effects may relate to clinically-relevant effects.
- Assess the extent to which voltage-sensitive dye imaging (VSDI) and electrophysiology are proficient approaches to studying the effects of both physiological and pharmacological manipulations, and consider the implications of using VSDI as a drug-screening method

In this first chapter, the over-arching topics which are of direct relevance to the study of network dynamics is discussed. In this introductory chapter, the terminology of distinct levels of organisation is defined and put into context, from *micro*- to *macro*-scale. Secondly, the concept of 'neuronal assemblies' is introduced and defined, i.e. how this emergent phenomenon may represent faithful measures of physiological

function. Finally, background information is provided on how assemblies have indeed already been measured as sensitive indices of physiological state and function in the past, both in animals and humans.

1.2 Hierarchal levels of brain organisation

1.2.1 From macromolecules to coherent, dynamic brain activity

In the central nervous system (CNS), and in particular the brain, neurons are arranged into networks of tightly interconnected cells, specialised for reciprocal electro-chemical communication. These complex and dynamic neuronal networks, instead of single neurons, have recently been proposed as the functional units of emergent cortical activity, to a greater extent than their constituting single neurons, thereby representing the building blocks of greater neuronal systems (Miller et al., 2014). Indeed, focusing on the dynamic activity of single cells, yet necessary, is not sufficient for understanding higher-level brain functioning as it offers only a fractured description at best, of the overall processing actions of entire, highly distributed, neural networks (Defelipe, 2011; Hopfield, 1982). Yet, this arrangement of neuronal systems is the fabric of the physical brain and it is the cohesion of all their constituting neuronal types which allow for the emergence of their extraordinarily complex property: large-scale, synchronised population activity (Nicolelis et al., 1995). So far, the study of neuroscience has highlighted key processes taking place at seemingly different levels of organisation: investigations have uncovered functionally-important phenomena at the *micro*-scale, i.e. within and between individual neurons (Karakas et al., 2000); for example the precise and sensitive balance of charges across neuronal cell membranes (the cell's 'resting membrane potential' – 'V_m') which, when altered in specific ways, creates the

electrochemical driving force responsible for a plethora of neuronal events central to appropriate neuronal communication (Magistretti et al., 1999). Similarly, functionally-relevant phenomena have also been shown at higher levels of organisation, i.e. the *macro*-scale, such as for example the phenomenon of synchronised population activity within the brain, which has far-reaching impacts on their constituting neurons, as well as in their larger functionally-relevant and highly developed sensory systems (Engel and Singer, 2001).

1.2.2 Defining the spatio-temporal parameters of the 'micro-', and 'macro-scales'

The key concept delineating the 'levels of organisation' referred to here is the obvious disparity in the spatial and temporal scales at which the range of biophysical processes involved in neuronal communication take place. Since the duration of a single *neuronal* action potential lasts up to a single milliseconds (ms) (Bullock and Horridge, 1965; Holt and Koch, 1999), it follows that the vast majority of protein-mediated mechanisms involved in this process (as suggested above) take place on a microsecond (μs) basis; other relevant examples of micro-scale events include all-important spike generation events (production and propagation of action potentials), the time-constants of which have also been measured in the μs range (10^{-6} – 10^{-4} seconds) (Connors et al., 1982; Sabatini and Regehr, 1999), for example that of current repolarisation inside dendrites following spike generation (Liu and Tsien, 1995; Softky, 1994).

On the other end of the spatio-temporal spectrum, i.e. the macro-scale, events take place at spatio-temporal scales that are orders of magnitude greater, involving vast numbers of neurons over relatively large distances. For example, the communication of sensory stimuli from the peripheral nervous system (PNS) to the CNS travels first

from peripheral nerve endings to the spinal cord and then to the sensory cortices, generating the subjective feeling of this sensation. This entire process requires the synchronised (locally) and serial (at larger spatial scales) activation of hundreds of millions of neurons which can take place in total over distances spanning dozens of centimetre with temporal scales reaching up to 200-400 ms, for evoked events (Sergent et al., 2005; Vogel et al., 1998). As mentioned above therefore, one can appreciate the vast disparity in spatio-temporal scales separating the former example, taking place at the *micro*-scales from that of the latter *macro*-scale phenomena. In the case of the micro- and macroscopic levels described here, both of those levels have been extensively investigated in the literature and, when defined within the spatio-temporal scales specified above, represent the two extremes of the scales at which events and phenomena considered in the study of neuroscience are generally found to take place. Unfortunately, this large difference in spatio-temporal scales is often too vast to establish robust and meaningful links between the multitudes of events taking place within neuronal cell compartments (micro-scale) and the resulting dynamic population events (macro-scale), yet their respective behaviour remains inextricably linked. As a result, in trying to understand such links between micro- and macroscopic neuronal events, there is not only an inherent motive to acquire this level of understanding but also, and foremost, the requirement for the adoption of an over-arching theoretical methodology which would then allow for the latter investigative endeavour.

1.2.3 Investigating cerebral functioning

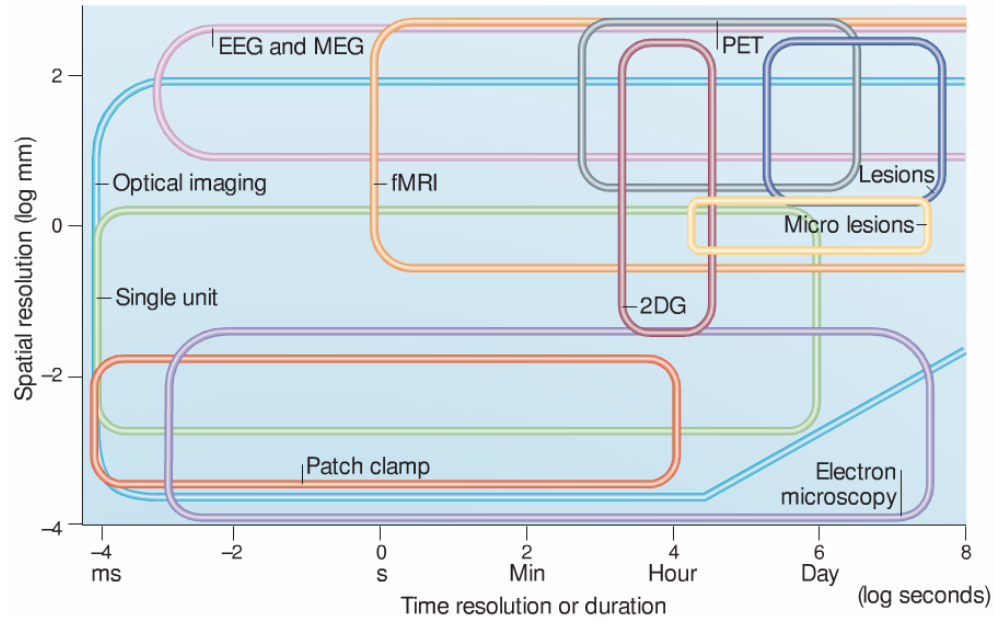

Figure 1: Spatio-temporal resolution plot of neuroscience recording techniques. The spatial and temporal sampling resolution (also known as the 'coverage') of each technique is delineated by the height and width of their respective box, allowing for direct comparison. Note the extent of the light-blue 'Optical imaging' box, of which VSDI is a part, which nearly covers the entire plot, from the bottom-left (micro-scale) to the top-right corner (macro-scale). Yet crucially, this technique allows for monitoring of neural activity with higher spatio-temporal resolution than any other technique (see bottom left corner of 'Optical imaging' box, near origin of axes). Also: note the similar temporal resolution of 'Optical imaging' and 'Single unit' electrophysiological records, yet with optical imaging offering a significantly higher spatial resolution, especially at higher scales. Adapted from (Grinvald and Hildesheim, 2004).

In neuroscience, complex brain events and dynamics can be applied to the study of two interdependent features, which are especially obvious in the cortex: there is **a)** the organisation of the brain – the physical arrangement of cortical cells (i.e. arranged into modular, repeating networks or 'columns' within layered cortical tissue, see below) which provide the medium within which **b)** emergent dynamic cellular signalling of neuronal populations takes place – i.e. the overall information processing of neuronal computations. This is particularly complex due to the wide

diversity of neuronal types (see **Figure 2A**) and the synaptic contacts (see **Figure 2E**) they harbour. There exists however, an extensively-studied model of mammalian brain functioning which groups both of the above principles: the rodent primary somatosensory 'barrel field' cortex (S1BF). It is named as such due to its conspicuous one-to-one topographical arrangement of highly developed whisker-related cortical structures (**a**, termed 'barrels') specialised for sensory processing and integration (**b**, dynamic activity), altogether behaving as a coherent system (Woolsey, 1988).

- *The modular cortical column*

Many investigators have looked to the modular organisation of the brain to try and understand the relationship between its physical construct and the dynamic activity which emerges from these 'canonical circuits' – repeated iteratively within a greater structure, i.e. cortical columns (Douglas and Martin, 1991; Logothetis, 2008). Physiologically and functionally, columnar neuronal organisation was first proposed by Vernon Mountcastle in 1955 in the cat somatosensory cortex (Mountcastle, 1997), and represented an attractive concept of brain organisation which was quickly adopted (Horton and Adams, 2005). Since then, the concept of modular cortical columns has become widely accepted as an iterative form of inter-linked small-world network with distinct processing and memory capabilities (He et al., 2007; Watts and Strogatz, 1998), organised into recursive and complementary units, effectively equating to the intermediate-level neural substrate of information processing (Beul and Hilgetag, 2014), linking single neurons to whole-population activity.

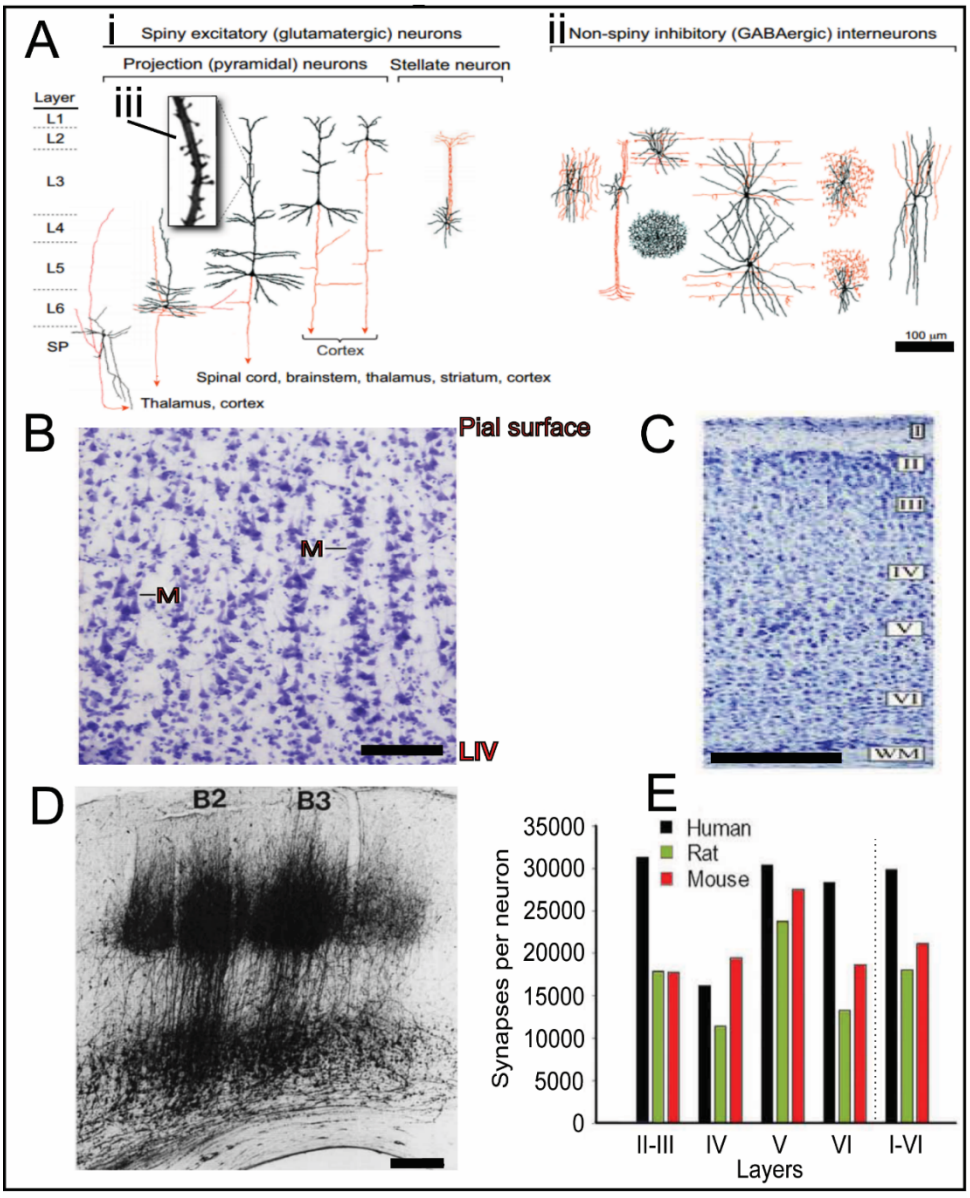

Figure 2: Neuronal types of the neocortex and their network-level organisation. **A**. summary of the types of excitatory glutamatergic (**i**) and inhibitory GABAergic (**ii**) neurons found in cortex. Neurons feature membranous protrusions referred to as 'spines' or 'boutons' (**iii**), located on their dendrites, and which represent the main input for incoming information to the CNS. Scale bar: 100 µm. Orange projections depict the axons of the cells in question, while black projections depict their dendrites. Excitatory cells found in the deep layers (LVI, LV) and sub-plate (SP) generally project to the cortex and sub-cortical structures (i.e. thalamus, striatum, brainstem and spinal cord), whereas those found in the superficial layers (LIV, LIII, LII) are more often found to project their axons within the cortex. Non-spiny interneurons project into their local circuits only, where they also display layer-specific differences in their morphology, neurochemistry and electrophysiological properties, thereby conferring yet more layer differences in local network circuitry; adapted from (Kwan et al., 2012). **B**. High-power photomicrograph of a 100 µm-thick vibratome section of human brain from Brodmann's area 39 (parietal cortex) stained with thionin, showing the presence

of clear groupings of cells into radial micro-columns (labelled 'M') here seen in a sample slice of LII/III cortex. These micro-columns are between 30 and 40 μm in diameter and associate together into bigger clusters ('hypercolumns'). Scale bar: 100 μm. **C**. Low-power photomicrograph of a 100 μm-thick vibratome section of rat area 3b (also parietal cortex) showing approximate layer locations – in this image, the resolution appears too low to distinguish cellular clusters or layer differences. Scale bar: 250 μm; **B** & **C** adapted from (Defelipe, 2011). **D**. Photomicrograph of a rat somatosensory slice oriented along whisker-barrel row B; barrels corresponding to whiskers B2 and B3 are visible in this section, and represent an example of hypercolumns (>300 μm in diameter). Scale bar: 200 μm; adapted from (Chmielowska et al., 1989). **E**. Histogram showing the layer-specific and overall average number of synapses per cortical neuron found in human, rat and mouse brains – note that synapse abundance is not indicative of cerebral complexity or cognitive power, suggesting such an ability is mediated by other features of cerebral/neuronal organisation and functioning; adapted from (DeFelipe et al., 2002).

The cortical column was first described as both a physical and functional arrangement of specific neuronal types into vertical (radial) clusters, formed during structured developmental stages (Rakic, 2009), which would share similar functional properties, such as receptive fields and tuning frequencies (Favorov and Diamond, 1990; Hubel and Wiesel, 1962; Hubel and Wiesel, 1968), yet where the constituting neurons would fire sparsely. Accordingly, it became evident that (hyper)columns, though found ubiquitously in mammalian neocortex, did not simply possess a one-to-one '*generic*' function across all brain areas and/or species. About a decade ago, the different aspects, principles and empirical data relating to the concept of the modular cortical columns were reviewed (Horton and Adams, 2005), where the authors concluded that in the end, the cortical column is a peculiar structure without a function: "… it is unclear what advantage, if any, is conveyed by this form of columnar segregation. […] Unravelling the organisation of the cerebral cortex will require a painstaking description of the circuits, projections and response properties peculiar to cells in each of its various areas".

With regards to columnar signal flow, a firm understanding of the exact functional network dynamics which take place within cortical columns remains largely elusive to this day, in part due to the high complexity of its many simultaneous computations, yet progress is being made; **Figure 3** below shows a schematic diagram of columnar information flow highlighting some of the major stages involved in information processing within cortical columns.

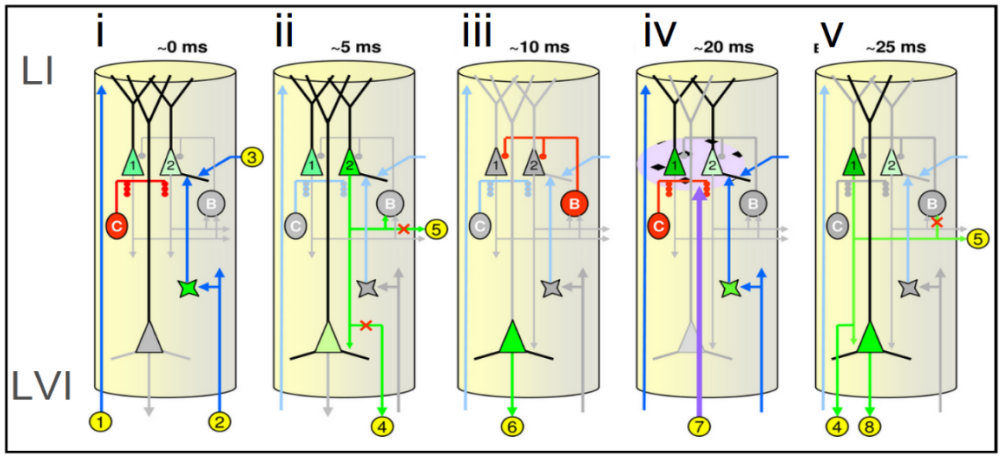

Figure 3: Schematic diagram depicting the main steps involved in information processing within cortical columns. **i**. Convergence and integration of incoming stimuli originating from sub-cortical sources targeting LII/III both via mono- (**1**) and poly-synaptic (**2**) circuits (Rockland and Pandya, 1979), triggering activation of overall columnar networks. **ii**. Resulting intra-columnar signal flow targeting LV/VI (**4**) and subsequent inhibitory network activation (**5**). During the first dozen milliseconds, extra-columnar signal propagation is inhibited (**4** & **5**); possibly via the simultaneous activation of double bouquet cells in (**i**) which possess 'horsetail' axons ideally suited for making contacts with a substantial portion of laterally-oriented (tangential) processes (DeFelipe et al., 2006; Peters and Sethares, 1997), not shown here. **iii**. Activation of LV/VI, following shunting of activity in superficial layers (LI–III) via basket cell activity (red 'B' cell) (Brown and Hestrin, 2009), relaying processed information to sub-cortical structures and other long-range partners (**6**). **iv**. Sub-cortical computations are returned to the column such as to modulate its activity (such as in the form of neuromodulatory influences, **7**, purple area) and triggering further activity/processing in superficial layers (blue arrow) in particular that of pyramidal and chandelier cells (red 'C' cell). **v**. Final output of the cortical column communicates the processed information to sub-cortical structures (**4** & **8**) and laterally to neighbouring columns (**5**) via recurrent activation of local lateral connections (Gilbert and Wiesel, 1989) thereby providing temporal context to the local networks. Adapted from (Rinkus, 2010).

Nowadays, hypercolumnar networks are seen as highly versatile processing units, featuring different combinations of active neurons specific to the nature (orientation, colour, movement) of incoming stimuli which in turn drive an active recruitment process and triggers network activity in a specific way. In addition, the large range of neuronal types mentioned above (**Figure 2**) are arranged into a complex three-dimensional structure (cortex) of layers (horizontally), columns and septa (vertically) (Brumberg et al., 1999), where each combination features specific and sometimes highly heterogeneous network organisations amassing together large numbers of receptive fields (Barth and Poulet, 2012; Lefort et al., 2008; Rinkus, 2010; Watts and Strogatz, 1998); these 'sub-networks' are themselves interconnected with each other into three-dimensional subgroups which are structurally known as columns (via intra- and inter-layer/columnar connections, **Figure 3**): it is their interactivity which gives rise to appropriate cortical integration and processing (Bressler and Kelso, 2001; Mesulam, 1990). **Figure 3** above attempts to provide a summarised description of the mechanisms of excitatory signal flow through cortical columns as seen in rat S1BF, proposed by (Rinkus, 2010) – this graphical representation remains highly speculative however, making abstraction of many important steps and processes (such as intermediate processing stages, recurrent excitation and extrinsic influences among others). Yet, this simplistic reproduction still provides a reliable starting point for attempting to grasp the complex principles by which incoming stimuli are processed in somatosensory cortical columns, and offers a method for gaining a greater understanding of the steps involved in this highly complex process, as well as offering the possibility of falsifying such hypotheses experimentally.

It is therefore clear that cortical columns operate highly complex processing, however they are not found everywhere in cortical tissue: sensory areas are more generally made up of columnar organisation, but many areas of cortex do not show

such organised cytoarchitecture. In particular association areas often lack this columnar organisation, yet population activity can be elicited and maintained in all cortical areas. The focus of this thesis will be on studying the dynamics of this population activity, often spanning large areas of cortex and uniting together hundreds of millions of interconnected neurons, at the *meso-scale* of brain organisation.

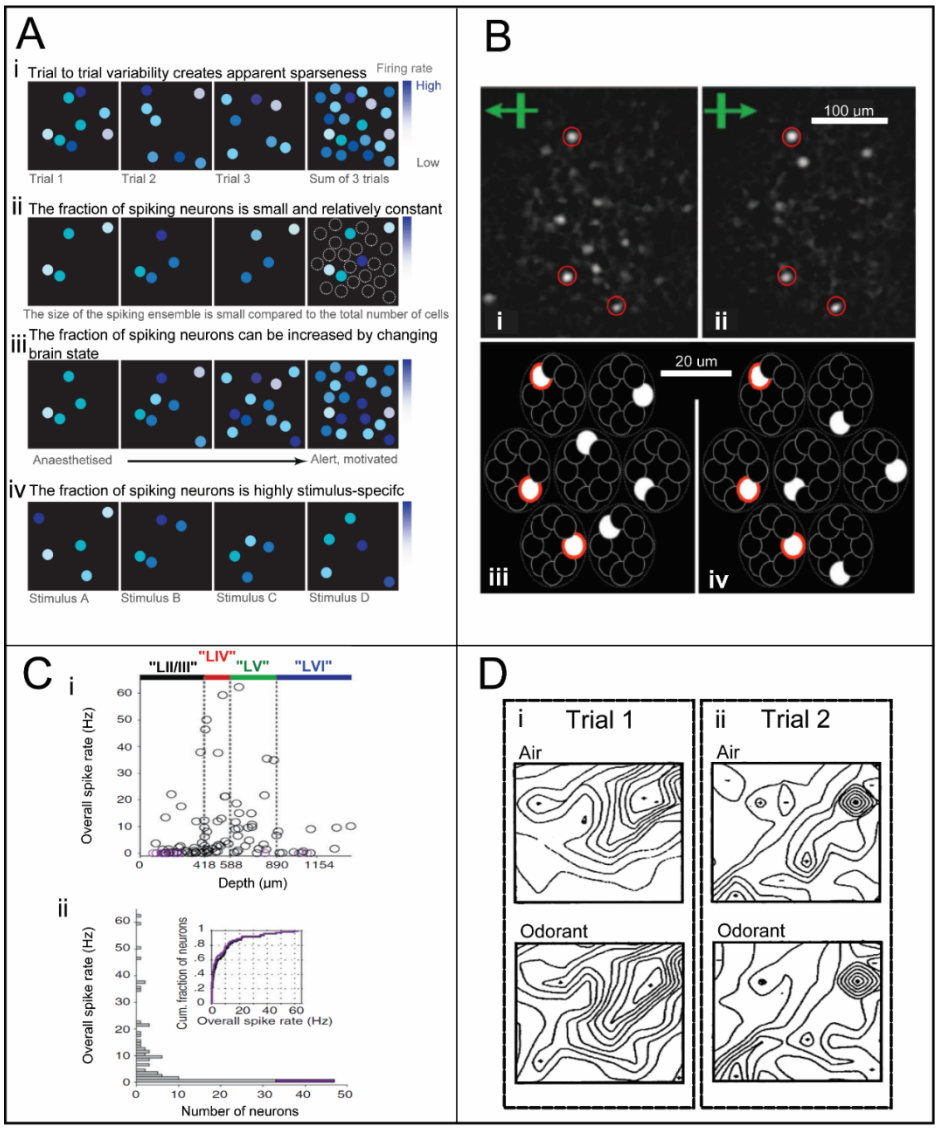

Figure 4: Profile of stimulus-evoked columnar activity in the neocortex. **A**. Models of sparse spike coding: (**i**) separate trials giving rise to variable profiles of active neurons (either due to network or intrinsic cellular properties) gives the impression of sparse spiking, which can be overcome with larger sampling epochs for analysis. (**ii**) A smaller but consistent contingent of highly-responsive neurons fire with more ease than the other cells within the network, becoming increasingly apparent over many trials. (**iii**) The subset of spiking

neurons is sensitive to behavioural state, such as for example anaesthetised versus alert, motivated. (**iv**) Subsets of neurons with highly stimulus-specific activation properties give the impression of sparseness. Adapted from (Barth and Poulet, 2012). **B**. Still frames taken of movie data from (Ohki et al., 2005) showing cortical networks/columns from LII/III of rat visual cortex activating sparsely and simultaneously in response to leftward (**i**) or rightward (**ii**) drifting gratings. Diagram representing the data seen in the two images shown in **i** & **ii** highlighting the sparseness of stimulus-specific mini-column activation throughout the population; red circles highlight the mini-columns which represent homology between codes for different stimuli. Adapted from (Rinkus, 2010). **C**. The vast majority of spikes within a population are fired by a small subset of its neurons: (**i**) firing rate of selected neurons as a function of cortical depth, during an active sensory task in mice – circles denote single cells (purple: 'silent' neurons), laminar boundaries are colour-coded at the top of the graph, a lot of cells show very low (yet non-zero) firing rates. (**ii**) Histogram compiling firing rates of the neurons shown in **i**; purple bar indicates number of silent neurons. Inset: cumulative histogram of data with (purple) and without (black) inclusion of silent neurons. Adapted from (O'Connor et al., 2010). **D**. Contour plots showing response amplitudes in rodent olfactory cortex as a result of control (air) and odorant trials and showing the high amount of variability seen in evoked spatial activity patterns, 2 weeks separate trials 1 and 2 where the same odorant was presented. Adapted from (Freeman, 2000).

- *Meso-scale neuronal, or 'population', events*

Studying the manner in which different levels of organisation relate and influence each other poses particularly difficult tasks, as previously mentioned, since the measures of space and time are unequal and therefore often hard to reconcile on a single, common spatio-temporal metric. As a result, it is often much more complicated to establish causal inference *between* levels of organisation than it is to establish *within* a same level, in particular when the gap separating the two levels under investigation is large. In such a scenario however, the best method to approach the investigation is to conceive, distinguish and characterise intervening levels of organisation, which physicists refer to as *mesoscopic* (Imry, 1997; Ingber, 1992). It is the goal of the present thesis to describe and characterise further this specific mesoscopic, or '*meso-scale*', level of organisation which exists between single neurons and whole-brain systems; as well as to link the micro-dynamics of the

former with the macro-scale events of the latter using specific pharmacological manipulation.

This idea of a mesoscopic level of brain organisation is quite new, relative to those of micro- and macro-scale levels, and thus requires more thorough investigations. In order to do so, however, (**a**) a firm understanding of the relationship between recording technique resolution and their appropriate recording level of organisation is necessary, as well as (**b**) highlighting the need for appropriate mesoscopic on-line monitoring techniques which, in turn, allow for a greater understanding of the intermediate level bridging single neuron activity to macro-scale functional brain activity. Such multidisciplinary research is bringing together investigators specialised in a wide range of branches of study, including philosophy, mathematics, biophysics, computational modelling, pharmacology, cognitive psychology and of course fundamental neuroscience (Chemla and Chavane, 2010; Gray and Singer, 1989; Mirollo and Strogatz, 1990; Sommers and Kopell, 1993; Steriade et al., 2001; Whittington and Traub, 2003) in order to address all aspects of the highly complex phenomenon of emergent population activity. Therefore, in an attempt to gain a greater understanding of fundamental cerebral computations, the current investigative strategy is concentrated on realising two broad goals. The first is of acquiring as much data as possible relating to the specific functional cytoarchitecture of neuronal network and their resulting dynamics (neuroscience, pharmacology and biophysics), such as to define the underlying governing dynamics. The second is to build computational models accurately replicating the complex diversity, physiology and behaviour of cortical columns according to this 'real-world' data which exhibits and defines their precise mode of action; i.e. predicting 'meso-scale' network activity using combinations of mathematical, computational modelling and cognitive psychology approaches (Muller and Destexhe, 2012).

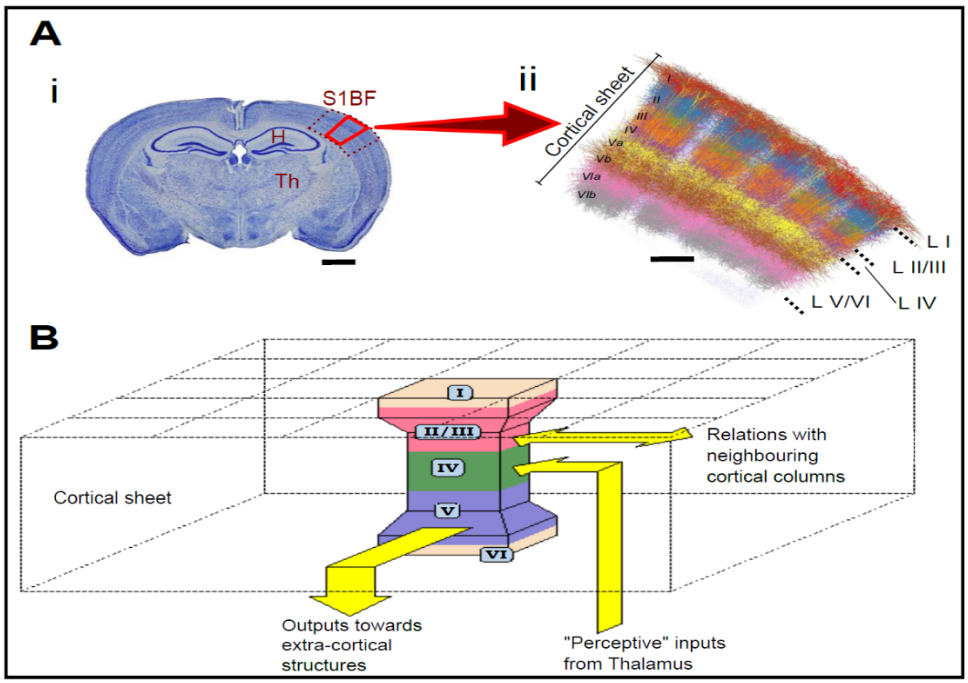

Figure 5: Anatomy of a cortical column, as seen in rat primary somatosensory cortex. **A**. DAPI-stained 400 µm-thick coronal slice cut (**i**; adapted from (Defelipe, 2011)) showing the location of the S1BF, hippocampus (H) and Thalamus (Th). Computational reconstruction of 5 somatosensory cortical columns (**ii**), with colour-coded layer-specific cells and their processes. Scale bars: (i) 1000 µm, (ii) 250 µm. **B**. Schematic representation of the widely accepted mechanism of information flow, integration and processing through a generic cortical columns.

1.3 Intervening levels of organisation: functional relevance of mesoscopic neuronal dynamics

In the present thesis, the intervening mesoscopic level of brain organisation is defined as events taking place on a spatio-temporal scale of millimetres to centimetres (10^{-4}–10^{-2} metres) and milliseconds (10^{-3}–10^{-2} seconds) (Werner, 2007). The mesoscopic resolution is therefore found between that of micro- and macro-scale events, and is a particularly interesting spatio-temporal scale as it indeed seems to represent a credible ‘bridge’ linking intracellular events to whole-brain dynamics (Papo et al., 2014). Spatially, meso-scale resolution thus allows for data acquisition

of signal output from neuronal clusters comprising a relatively small number of cells, while temporally, mesoscopic events take place on a scale commensurate with that of the most physiologically-relevant microscopic event: action potential generation and propagation. When considering dynamic network activity, mesoscopic patterns of activity therefore manifest as large overall depolarisations within volumes of neuronal tissue which can last several hundred milliseconds; resembling activity patterns usually associated with macroscopic events rather than short discrete blips of information seen with action potentials, which dominate at the micro-scale, lasting up to a millisecond (Borst et al., 1995; Gray and McCormick, 1996; Sabatini and Regehr, 1999).

1.3.1 Emergence of mesoscopic activity from microscopic neuronal events

The generation of organised higher-scale neuronal activity is more commonly thought of as arising from bottom-up effects however, i.e. from the micro-scale upwards to finally emerge at the macro-scale. The emergence of meso- and ultimately macroscopic activity arises from depolarised areas, where spiking activity in neurons that depolarise past threshold provoke the release of neurotransmitters into synapses, at the micro-scale, affecting a myriad of ligand-activated receptors. The most widely studied receptors of direct relevance to the principles of cellular signalling discussed here include the ligand-gated ion channels (LGIC) and G-protein coupled receptors (GPCRs): upon ligand binding to their receptor, electronic redistribution takes place within the native conformation of the receptor, stabilising its structure to an open state, allowing ionic currents to flow through the receptor/membrane, down their electrochemical gradients for small periods of time of the order of 1 or 2 milliseconds (Sabatini and Regehr, 1999). In

turn, for positively charged ions, this creates small, localised increases in resting V_m, referred to as excitatory post-synaptic potentials (EPSPs), which represent the hallmark of the mechanism of neuronal depolarisation (Hille, 2001). In the case of GPCRs, the mode of signalling is somewhat different: the binding of the ligand to GPCRs also triggers a conformational change releasing a membrane-bound intracellular G-protein which gets activated upon release, the active G-protein reaches a secondary effector (for example: the catalytic enzyme adenylyl cyclase) and triggers it to produce a secondary messenger (in this case: cAMP) which then diffuses in the cell's cytoplasm to induce far-reaching effects in multiple intracellular processes (Tuteja, 2009). LGICs and GPCRs represent but two of the most important paths employed in synaptic signalling, yet in this thesis, since the focus is on dynamic, sub-second neuronal communication, greater attention is given to LGICs as they are much more specifically involved in fast cellular communication compared to GPCRs. Intracellular signalling cascades can also be initiated via ionic influence, as seen with calcium ions (Ca^{2+}), which act as intracellular messengers within neurons (Berridge, 1998; Bootman et al., 2002), and can even trigger apoptosis when intracellular concentrations reach critical levels. Scaling up from these processes by a few orders of magnitude, mesoscopic networks are ubiquitously made up of very intricate and organised configurations of vastly different neuronal types both excitatory and inhibitory (see **Figure 2A**), interconnected among themselves with specific configurations of feed-forward and feed-back projections and especially in the cortex: dominated by recurrent excitation giving rise to reverberating activity (Douglas and Martin, 2004; Lorente de No, 1992). Furthermore, regarding the highly complex and specific configuration of interconnection between neuronal types, cortical neurons are part of highly distributed circuits, where each neuron receives input from and targets thousands of other neurons (see **Figure 2E**), both in their immediate vicinity as well as from, and to, long-range partners (Abeles, 1991; Miller et al., 2014). Such a configuration of

interconnected cells with specific processing abilities allows for dynamical integration and relay of incoming information and, when collectively occurring in synchrony, provides the prerequisite parameters for the emergence of unified higher-scale activity. Once a neuronal depolarising event (whether intrinsic or from afferent sources) reaches supra-threshold states, it immediately spreads to the rest of the cell and depolarises its synaptic partners, creating an 'epicentre' of activity where the assembly originates from, within a small loci of neuronal tissue (Lopes da Silva, 1991b). In turn, this small collection of active neurons (the epicentre) will deliver high amounts of EPSPs to their monosynaptic partners, driving microscopic neuronal events into the mesoscale, with the generation of waves of depolarisation spreading in different directions by way of cortico-cortical connections (Prechtl et al., 1997).

In summary, investigations focus on dynamic neuronal activity at the meso-scale, where the synchronous activity of millions of interconnected neurons manifests as sub-second propagating waves of activity, spreading across several millimetres of brain tissue. Indeed, this concept of unified depolarising front spreading outwards is not new: it has in fact been observed in nearly every type of investigations focused on mesoscopic cortical processing, both with VSDI and electrophysiology (Adrian and Matthews, 1934; Muller and Destexhe, 2012; Roland et al., 2006; Sato et al., 2012; Takahashi et al., 2011; Watt et al., 2009; Wu et al., 2008; Xu et al., 2007).

1.3.2 Bridging the micro- and macro-scales using the intervening meso-scale level of organisation

Mesoscopic patterns of evoked activity have been extensively described, and have been reported to manifest as fast propagating waves of activity, using both optical imaging techniques (Bourgeois et al., 2014; Metherate and Cruikshank, 1999;

Wester and Contreras, 2012; Wu et al., 1999; Wu et al., 2008) and electrode microarrays (Pisciotta et al., 2010; Schevon et al., 2010; van Kerkoerle et al., 2014). Therefore, driven by microscopic events, neuronal network activity spreads outwards producing a response profile reminiscent of those seen with macroscopic events, hence providing a mechanistic tool which can be used to understand more fully how events at one level of organisation give rise to those seen at higher levels and which can be tested for robust links in bridging both extremes of the spatio-temporal spectrum. Indeed, the study of mesoscopic neuronal population activity patterns has become the focus of renewed investigative interest in recent times: one more reason for this is their increasingly evident relevance to physiological function (Muller and Destexhe, 2012). Seminal studies which initially reported such stereotypical temporal signatures were carried out in the olfactory system of the terrestrial mollusc in the 1990's using extracellular electrophysiology measuring local field potential (LFP) resulting from summation of total rhythmic population EPSPs (Gelperin et al., 1993; Gelperin and Tank, 1990). One recurrent finding however, which gained significant importance and attention as a result of investigating mesoscopic neuronal population activity, was the detection of a wide range of different oscillatory activity patterns almost ubiquitously throughout the cortex, with specificity regarding their location and relationship to brain state (Gray, 1994; Llinas and Ribary, 1993; Murthy and Fetz, 1996). This finding in turn led to the conclusion that oscillatory activity patterns are an intrinsic property of mammalian brains (Gelperin and Tank, 1990). These patterns were subsequently found to be so stereotypical that their deviation from the norm could be used as a sensitive index for the diagnosis of many neurological disorders (Bosboom et al., 2006; Rodriguez et al., 2011; Spencer et al., 2008).

1.4 'Neuronal assemblies', the functional units of mesoscopic brain functioning

1.4.1 Definition of the concept of 'neuronal assemblies'

The generation of activity in the cortical mantle, in the *in vivo* brain, occurs on a millisecond basis, giving rise to highly complex spatio-temporal activity patterns, constantly in a dynamic state of flux. 'Neuronal assemblies' is a term used to describe a concept of synchronised cell assembly which accounts for the spatial segregation of co-active neuronal groups: "a diffuse structure comprising cells in the cortex and diencephalon, capable of acting briefly as a closed-system delivering facilitation to other such systems" (Hebb, 1949; Nicolelis et al., 1997). Such dynamic and synchronous coalitions of cells all activating simultaneously manifest as unified areas of depolarised neuronal tissue (more positive overall V_m) within an area of comparatively low V_m (more negative, hyperpolarised): it is these sub-second changes in electrical potential over space that are measured in EEG records (Buzsaki et al., 2012; Kuhn et al., 2008; Murakami and Okada, 2006). Mesoscopic activity patterns (neuronal assemblies) have already been extensively studied, further highlighting their importance as relevant neural correlates of functional network state, and in so doing, have been given multiple names in the literature over the past two to three decades including 'propagating waves of activity' (Han et al., 2008; Rubino et al., 2006; Wu et al., 2008), 'dynamic/neuronal ensembles' (Carrillo-Reid et al., 2015; Miller et al., 2014; Nicolelis et al., 1995; Pais-Vieira et al., 2013), as well as more generally 'mesoscopic' or 'population' activity (Ringach, 2009), yet all equate to the same concept of Hebbian neuronal cell assemblies (Hebb, 1949), which describe a concept of preferentially-connected cells activating together on a millisecond time-frame, synchronising their activity and triggering plastic processes (Gerstner and Kistler, 2002).

This exact phenomenon of Hebbian cell assemblies has previously been simply referred to as 'neuronal assemblies' in investigations from our lab (Badin et al., 2013; Badin et al., 2017; Badin et al., 2016; Chakraborty et al., 2007; Collins et al., 2007a; Devonshire et al., 2010a; Devonshire et al., 2010b; Greenfield and Collins, 2005; Mann and Paulsen, 2005; Mann et al., 2005a; Mann et al., 2005b) and others (Maldonado and Gerstein, 1996; Nicolelis et al., 1997; Singer et al., 1997; Wu et al., 1999), and will continue to be referred to as such throughout this thesis. The specific definition of neuronal assemblies (or 'assemblies') used here refers to the phenomenon of meso-scale synchronous and sub-second dynamic coalition of millions of neurons manifesting as propagating waves of depolarisation/activity (Muller and Destexhe, 2012; Takahashi et al., 2011). Assemblies are most often physically depicted as hotspots of activity within their centre with exponentially decreasing activity with distance from that centre, as demonstrated in **Figure 6**: it is these highly transient patterns of activity which are picked up by brain-monitoring techniques, and matched to relevant functional activity, implicating assemblies as the mesoscopic neural correlate of functionally-linked cerebral activity (Bryan et al., 2011; Buzsaki and Draguhn, 2004; Singer et al., 1997).

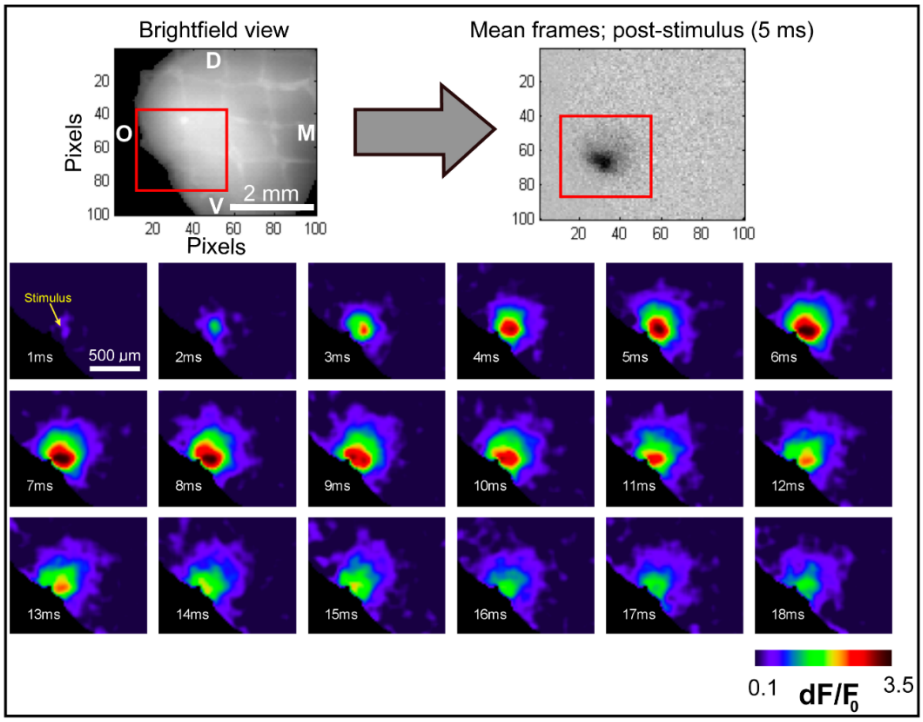

Figure 6: Sequential activation of an assembly evoked with a single 30 Volts electrical pulse to Layer II/III of AIC visualised using voltage-sensitive dye imaging (see later). Top left: bright-field view of a coronal slice from rat brain containing AIC, as seen under the imaging setup, 'D' – dorsal, 'O' – orbital, 'V' – ventral, 'M' – medial. Top left: Raw data images showing the averaged evoked activity signal from the first 5 ms (1 recorded frame per millisecond) after stimulus delivery (0.1 ms in duration). Bottom: sequential activation displaying the area of the slice isolated in the red square in top panels: this figure provides a visual depiction of a) the high spatio-temporal resolution of VSDI, b) the very fast nature of assembly generation (1 – 6 ms) and decay (7 – 150 ms, here truncated at 18 ms), and c) the profile of propagating waves of activity emanating from an epicentre, as seen in cortical tissue. Figure adapted from (Badin et al., 2017).

1.4.2 Reciprocal impact of assembly dynamics between micro- and macro-scale events

Assembly dynamics are directly affected by the nature of activity at other scales. Such inter-linked control of neuronal dynamics between levels of organisation can come from the micro-scale upwards, i.e. '**bottom-up**' control, where the collective V_m, nature and selectivity of individual constituting neurons set the pace and

modality of the resulting mesoscopic activity. In turn, the concept of bottom-up control of higher-scale activity can be easily pictured, as any influence on effectors of microscopic neuronal communication will be translated up. This was shown for example in the thalamocortical system: slower spindle waves (lowering spiking frequency) are induced in thalamocortical neurons when increasing the impact of the inhibitory component in thalamic nuclei (with application of a barbiturate $GABA_AR$ agonist) (Steriade and Deschenes, 1988), i.e. translating into a calmer/reduced population activity at higher scales. Additionally, high-frequency burst-mode activity in thalamocortical neurons has been implicated in the expression of spike-wave seizures (Blumenfeld, 2005), confirming that both inhibitory and excitatory lower-scale processes have significant higher-order manifestations. Similarly, macro-scale events can induce a '**top-down**' control of neuronal populations at the meso-scale, as seen with large-scale neuronal population activity/recruitment resulting from changes in attentional control in response to attention-directing cues (Hopfinger et al., 2000). Another example can be seen in the top-down control of layer-specific activity in somatosensory cortex as a result of activity evoked in the molecular Layer I by long-range afferents (Kuhn et al., 2008). Other notable examples include the bi-directional (simultaneous top-down and bottom-up) control mechanisms mediated by slow-wave patterns reported in cat visual cortex (Bernasconi et al., 2000); such slow wave patterns (<1Hz) can also be recorded in other regions of the brain, including the thalamocortical system and the entorhinal cortex (Achermann and Borbely, 1997; Crunelli and Hughes, 2010; Steriade, 2006), and have been endowed a causal role in the process of sleep-associated new memory consolidation (Marshall et al., 2006). Other examples of bi-directional, cross-level control include neuromodulatory influences on meso-scale/assembly dynamics from long-range diffuse projections (Brown et al., 1979), such as those of neuropeptides (Chan-Palay et al., 1986), as well as of cholinergic and monoaminergic processes (Descarries and Mechawar, 2000; Descarries et al.,

1977; Melander et al., 1986; Pinto et al., 2013) acting widely and tonically on cortical networks via volume transmission (Agnati et al., 2010; Fuxe et al., 2010; Zoli et al., 1999). Another type of top-down control takes place when the activation of a specific area of cortex subsequently (in the range of 10-100 ms) causes a large spread of activity to neighbouring areas (spreading several millimetres from the origin of activation): in this instance, the propagating front of the depolarisation gains ground at the meso-scale, via action potential propagation and synaptic contacts driving the resulting summation of EPSPs at the micro-scale as described above, and in doing so, will 'prime' the average V_m of surrounding neuronal populations affected by the wide-spreading depolarisation front to higher, more depolarised, levels (Azouz and Gray, 1999; Chawla et al., 1999; Grinvald and Hildesheim, 2004; Roland et al., 2006). In turn, this process can facilitate spiking activity in these affected neuronal populations when a second wave of depolarisation then spreads into the same area, or if a specific stimulus is then delivered to the primed area (Silva et al., 1991), within a certain time-window: a mechanism particularly important in the case of brain-state-induced frequencies of oscillatory mesoscopic activity (Bal et al., 1995; Maldonado and Gerstein, 1996; Poulet and Petersen, 2008; Silva et al., 1991). Such processes, i.e. pairing pre-existing heightened sub-threshold V_m with subsequent incoming action potentials, are believed to play a central role in appropriate network functioning as they have already been shown to be implicated in sensory signal amplification and induction of long-term potentiation (Magee and Johnston, 1997; Sharon et al., 2007). One further example of such a phenomenon emerging as a result of mesoscopic mechanisms of top-down control have been reported in rat visual cortex (Xu et al., 2007), where propagating waves evoked in V1 *in vivo* have been shown to 'compress' at the anatomically-defined V1/V2 border, rather than spreading homogenously into V2; particularly interesting was the finding that this wave compression was dependent on $GABA_AR$ signalling and did *not* occur for

spontaneously-activated propagating waves, suggesting the specific mechanism of wave compression is involved in appropriate visual processing.

Propagating waves have been referred to as 'feed-forward', i.e. when the generation of the assembly produces a depolarising wave front that originates from a specific locus and spreads outwards, yet have also even been reported to 'feed-back', i.e. to spread outwards before 'compressing' and then 'bouncing' back, spreading in the direction they came from, see **Figure 7** (Roland et al., 2006; Xu et al., 2007). Yet the most extensively studied example of such modulation remains the activation of rodent somatosensory-evoked responses to whisker deflections (Derdikman et al., 2003): in the rat for example, whisker deflections trigger activity within that whisker's barrel, however this initially localised activity then rapidly spreads, via supra- and infra-granular cortical layers, to neighbouring barrels within just a few milliseconds, both *in vivo* (Derdikman et al., 2003; Devonshire et al., 2010a; Devonshire et al., 2010b) and *in vitro* (Egger et al., 2008; Petersen and Sakmann, 2001; Staiger et al., 2004). In turn this process induces disturbances in the overall V_m of neighbouring barrels, affecting their stimulus sensitivity by pre-disposing their individual neurons to activate more or less easily than would otherwise occur if whisker-related activity had previously remained low. Taken together these findings implicate the mesoscopic phenomenon of neuronal assemblies as 1) indicative of functionally-relevant neuronal events, 2) representing the manifestation of distinct mesoscopic processes in their own right (see **Figure 6** & **7**), and 3) a Rosetta stone-type process, which translates micro-scale effects to the macro-scale and vice versa.

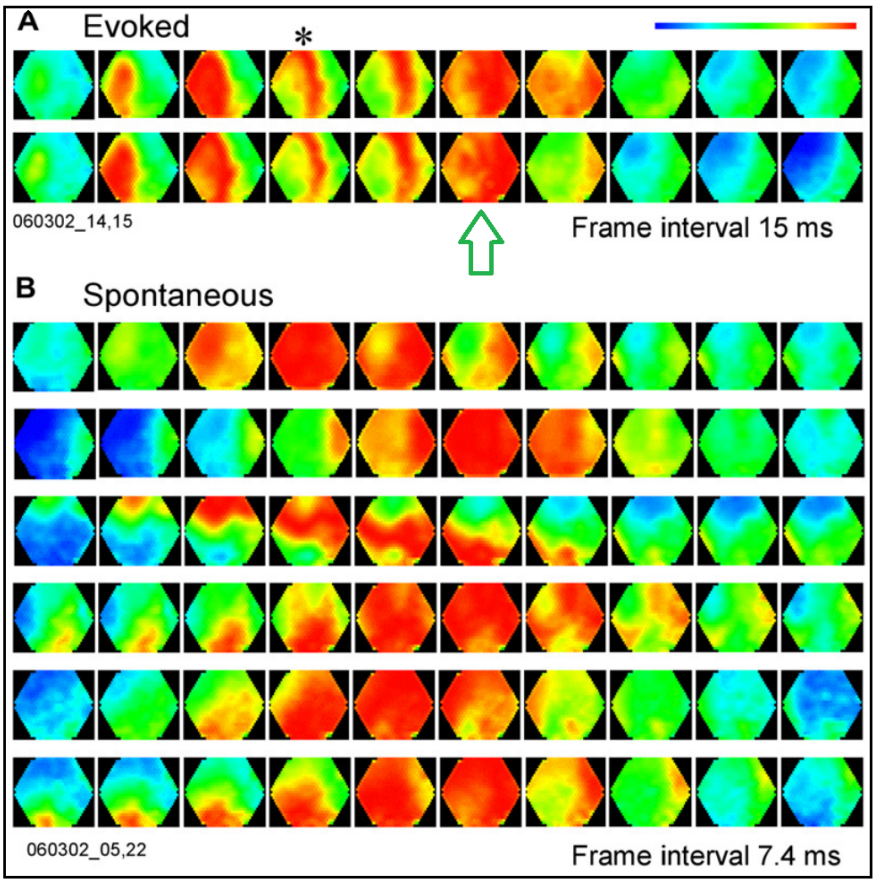

Figure 7: 'Bouncing' propagating waves in visual cortex. **A**. Sequential activation of 2 travelling assemblies evoked by visual stimulation in the primary visual cortex (V1), which compresses upon arrival at the border with secondary visual cortex (V2), as seen in the frame with an asterisk, and then spreads both forward into V2 and backwards into V1 (green arrow). **B**. Sequential activation from 6 spontaneously-generated travelling assemblies originating from different loci within V1 – no compression is seen in any of these cases. Frame interval in **B** (7.4) is half of that shown in **A** (15 ms) for clarity purposes, as spontaneous assemblies propagated faster than those evoked with visual stimuli. Colour scale: amplitude of detected signal was converted to pseudo-colour according to a linear colour scale; red = peak amplitude of signal, blue = hyperpolarisation. Adapted from (Xu et al., 2007).

The general theory therefore, suggests that being able to monitor and study mesoscopic neuronal events could offer even more reliable insights into the normal function of meso-scale neuronal networks, in particular when trying to understand how assemblies may be affected by specific pharmacological manipulations relevant to clinical sciences (such as with anaesthesia). In turn, such findings could help us

gain a greater understanding of how micro-scale effects induced by such agents manifest at the meso-scale level. The concept that coherent cerebral activity, resulting from all levels of organisation, is correlated with sensory perception and functional state is indeed central to this theory: it should therefore be possible to correlate dysfunctional brain processes, pathological or pharmacologically-induced, to respective alterations in 'normal' physiological function (Filion and Tremblay, 1991; Hampel et al., 2004; Homayoun and Moghaddam, 2007). In all cases, importantly, patients' EEG records feature profiles of altered macro-scale dynamics which vary considerably from those usually recorded in healthy controls. If those investigations were conducted at the meso-scale level, a great deal of additional and complementary information about the pathology-associated underlying faulty dynamics could potentially be obtained, and possibly help identify novel therapies in the longer term.

1.5 Brain states as sensitive indices of cerebral functional state

1.5.1 Event-related, functional cerebral events

Importantly, on-line recording techniques have been instrumental in detecting the stereotypical activity oscillations described previously (**Section 1.4**), where large-scale sub-second regional depolarisations (assemblies) emerge over entire areas of brain tissue, which can in some cases even spread over several millimetres, as seen for example in cortical tissue.

One important finding to date, is the finding that dynamic, rhythmic/oscillatory and synchronous population activity, recorded using EEG for instance, are correlated with brain/behavioural state and function (Jones, 2005; Poulet and Petersen, 2008); to the point where they can even be clearly defined into frequency bands (see **Figure**

8). In particular, high amplitude, slow oscillatory activity profiles (between 'up' and 'down' states) at specific frequencies have been associated with 'inactive', or idle, cortical fields (Pfurtscheller et al., 1996). These high-amplitude oscillatory patterns reflect a high level of synchrony and coherence in activity from individual neurons to population dynamics, i.e. large assemblies with slow dynamics occurring across entire areas of cortical tissue (Pfurtscheller et al., 1996; Práwdicz-Neminski, 1925): such 'idling' state dynamics have been found, across species, as an intrinsic feature of mammalian cortical activity (Riedner et al., 2007; Vyazovskiy et al., 2007). When cortical tissue becomes active however, rhythmic oscillatory patterns are inhibited and replaced with high frequency desynchronised activity which characterises the profile of active, cortical processing(Adrian and Matthews, 1934; Alegre et al., 2002).

Examples of associations between behavioural/brain state and stereotypical patterns of brain activity in humans include: alpha (α) waves, or 'Berger rhythms', a characteristic high-amplitude oscillation (of the order of 50-100 μV) of electric potentials with frequencies ranging from 8 to 13 Hertz (Hz), recorded using EEG on the surface of the scalp (Lopes da Silva, 1991b), with subsequent analysis suggesting alpha brain waves most often originate from a location within occipital cortex (Adrian and Matthews, 1934), and associated with behavioural states of resting wakefulness. Another such example are delta (Δ) waves, most often recorded in thalamus and cortex, which are also high-amplitude, slow oscillations (with frequencies ranging from 0.5 to 3 Hz) associated with deep unconsciousness, such as stage 3 non-rapid eye movement (N-REM) sleep (Steriade, 1999).

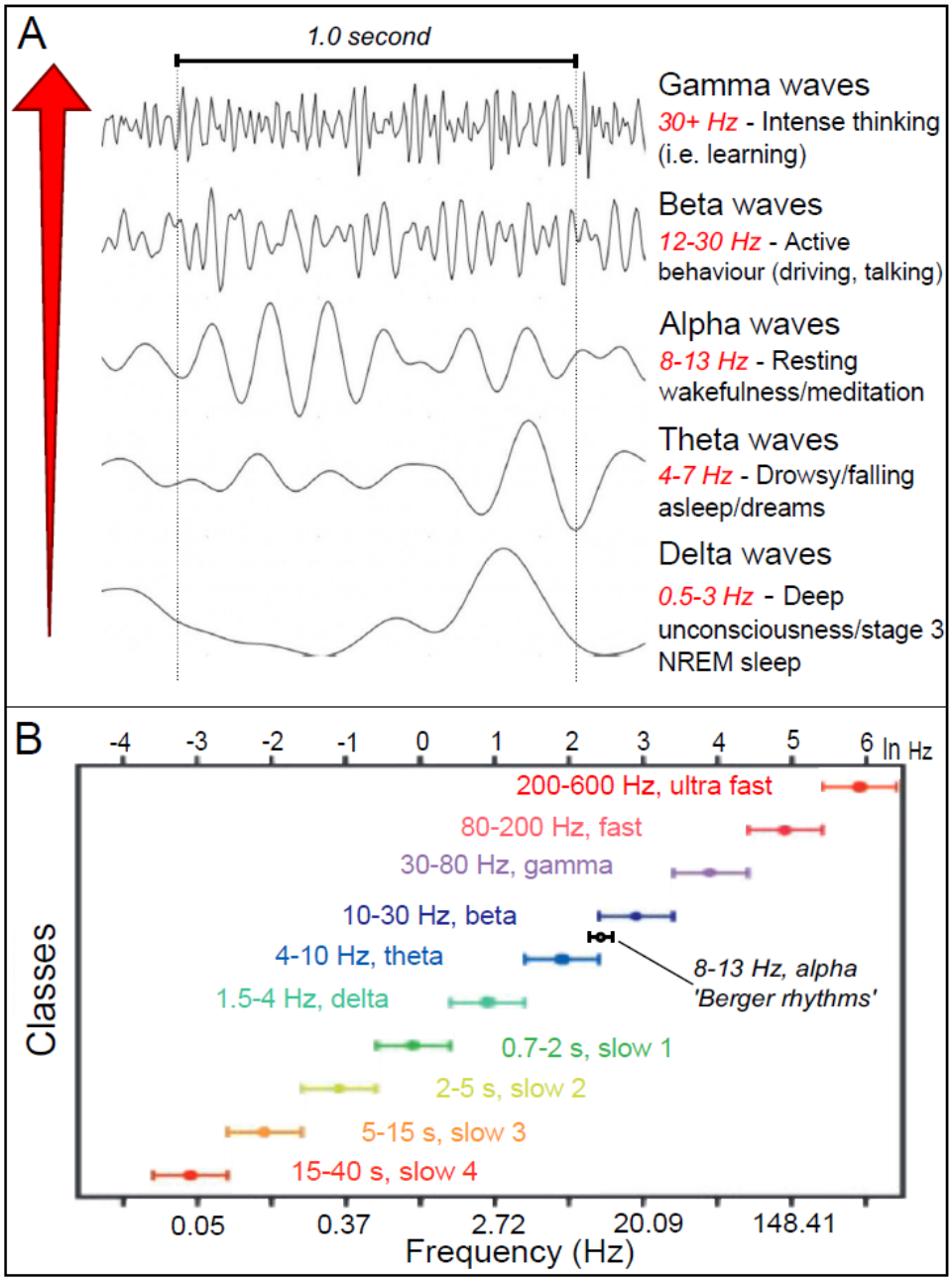

Figure 8: Comparison of some of the most common brain waves recorded at the macro- (**A**) and micro-/meso-scales (**B**). **A**. With increasing cortical processing burden (from bottom to top), brain waves feature notable increases in the frequency of their oscillations (Hz, red arrow, left). **B**. Cortical network activity frequency bands showing matching classes to those recorded using scalp EEG in human brains. Recording techniques: **A**. non-invasive EEG; **B**. cortical multi-unit recordings (Moiseeva and Aleksanian, 1986), intra-/extra-cellular electrophysiology(Penttonen et al., 1999). Adapted from (Penttonen and Buzsaki, 2003).

One of the omnipresent features of brain dynamics, at the mesoscopic level, is the presence of these widespread, rhythmic, patterns of synchronised neuronal activity, i.e. rhythmic transitions between up- and down-states. When looking at the processing and integration functions of specific brain sub-regions, it is now widely accepted, as a result of repeat and predictable observation, that in many cases not only the emergence of oscillatory population activity, but also their specific spatio-temporal parameters (location, spread and frequency) are correlated with brain state and physiological function (Lopes da Silva, 1991a); suggesting further that large-scale population activity (assemblies) could serve as a sensitive index of cerebral functional state. Indeed, seminal investigations into the temporal signatures of recorded cerebral activity in relation to physical events in the environment have led to the discovery of what are now referred to as 'event-related potentials', or 'ERP's (Donchin and Smith, 1970; Goodin, 1990), using EEG. The electrical potential waveform deflections which represent the hallmark of ERPs, arise from the collective and synchronous activity of the underlying individual neurons, purposely activated with a stimulus (Hopfinger and Maxwell, 2005). It is this cooperation between hundreds of thousands of interconnected neurons, forming networks and dynamic cell assemblies closely packed together, which together induce a change in electrical potential over an entire area of tissue compared to its surrounding: providing the start of a mechanistic basis for the microscopic origin of emergent neuronal population activity and their associated ERP temporal signatures. ERPs therefore originate from the cooperation of local neuronal networks, and are propagated and modulated by long-range connections linking distant brain sub-regions together. ERPs only become apparent on EEG records after extensive averaging of multiple repeat trials where the same stimulus is presented; in part due to the effect of intrinsically-generated network activity and alternating brain-states, producing variable responses (Fox et al., 2005), as mentioned earlier.

1.5.2 Linking dysfunctional population dynamics with atypical behavioural function

Electroencephalogram (EEG) recordings, which pick up even minute alterations in overall population V_m from spatially segregated locations across the cortical mantle, taken from schizophrenic patients have shown disruptions of temporal connectivity of overall normal gamma-band oscillations , which are believed to be a crucial mechanism in the binding of distributed neural activity throughout the brain (Engel and Singer, 2001; Tallon-Baudry and Bertrand, 1999). As previously stated, these alterations reflect recurring assembly generation and summation within the underlying cortical tissue. Furthermore, functional magnetic resonance imaging (fMRI) studies have implicated changes in frontal cortices-specific macroscopic dynamics as a hallmark of schizophrenia, such as significant reductions in metabolic activity in frontal cortices and disruptions in columnar dynamic interactions (Andreasen et al., 1997; Greicius, 2008; Li et al., 2008; Tregellas et al., 2007), which have been attributed to pathological changes in monoaminergic signalling in the frontal cortices (Weinberger and Berman, 1988) and may help explain the phenotypic expression of this particular pathology. Similarly, disturbances in normal functional brain lateralisation, detected via analysis of large databases of EEG data, have been reported in patients with autism (Dinstein et al., 2011; Maxim et al., 2005; Stroganova et al., 2007). Dementia sufferers have also been shown to feature noticeable changes in their EEG spectrum compared to healthy controls, which are characterised by an overall reduced complexity and altered synchrony of EEG signals (Jeong, 2004; Maxim et al., 2005; Stam et al., 2007). Some of these changes may also be attributable, at least in part, to an altered mode of monoaminergic signalling throughout the cortex (Ganguly and Guha, 2008), and has even led to the conclusion that the progression of the disease is associated with a lessened dynamic brain responsivity to external stimuli, rather than to a generalised

loss of dimension in the acquisition of sensory stimuli. These findings suggest the symptoms of dementia arise as a result of inappropriate internal processing of environmental cues (i.e. computed within cortical activity), rather than to dysfunctional sensory perception. It goes without saying however, that the nature of the alterations to normal EEG rhythms characterising each of these pathologies obviously manifest in their own distinct ways, yet it is those differences that allow for the detection and diagnosis of such disorders in the clinic. However the main point being asserted here, without the need to go into too much detail regarding the above neuropsychological disorders, is that dynamic population activity recorded using coarse-grain methods is already being used as a sensitive measures of appropriate cerebral function; such distinctions can also be made between different physiological states within normal healthy conditions, i.e. non-pathological behavioural states (for example those characterising sleep, quite wakefulness, or active sensory processing, among others). Taken together, these observations highlight further the reliability of neuronal assemblies in reflecting functionally-relevant brain processing.

1.5.3 Clinical relevance of neuronal assemblies

It has been reported that EEG data features a sensitivity which will register deflections resulting from sizeable and synchronous activation (assembly) of 10 000 – 50 000 neurons or more (Murakami and Okada, 2006), providing the putative minimum requirement for detection on EEG records. Assemblies manifest as a result of a highly successful neuronal recruitment process which affects the resting membrane potential of up to several hundreds of thousands of individual neurons: one study has attempted to estimate the number of neurons present per millimetre cubed (mm^3) of cortical tissue in the visual cortex of macaque monkeys, finding that

as many as 120 000 individual neurons may be present in such a volume (O'Kusky and Colonnier, 1982). Importantly, assemblies have been found to often spread wider than a millimetre in diameter, both laterally along layers and radially across the thickness of the cortex both *in vitro* (Badin et al., 2013; Badin et al., 2016; Petersen and Sakmann, 2001; Yuste et al., 1997) and *in vivo* (Devonshire et al., 2010b; Kuhn et al., 2008; Petersen et al., 2003). It therefore follows that EEG data reflects the dynamic activity of functionally-relevant neuronal assemblies. In accordance with this deduction, is the fact that faulty neural processes in the activation, maintenance and decay dynamics of such assemblies resulting from neuropathological conditions have also been shown to become obvious on EEG records. Imaging techniques such as functional MRI (fMRI) and PET, which record secondary measures of mesoscopic activity such as metabolic activity (for example: O_2 and/or glucose content), also report changes in activity profiles in accordance with those seen in EEG when monitoring faulty cerebral processes.

Therefore, the greater the magnitude of assembly activation, the more readily such fluctuations in activity (electrical potential) over space and time can be detected, yet EEG and imaging techniques can only tell us about a deviation from normal cerebral activity. Despite their extensive use in diagnostic medicine for detection of such anomalies, macro-scale monitoring techniques provide little information as to the specific mechanisms that have been affected, in part due to the coarse-grain nature of such recording techniques (low intrinsic spatial or temporal resolutions, or both) as well as to the complexity of the signals generated. Therefore, by applying the principles of recursive decomposition, as suggested above, the events recorded using EEG and imaging techniques can be described more fully at a lower level of organisation, i.e. the meso-scale of brain organisation, in an attempt to yield a more robust and complete description of the processes which generate and govern assembly dynamics.

Such studies would investigate the apparent link between meso-scale activation patterns and appropriate cerebral function; and thus how alterations at the meso-scale of brain functioning translate into discernible effects in their associated macro-scale manifestations. This phenomenon, of bottom-up alterations of cortical dynamics, therefore leads pathology-induced neuronal network malfunctions to translate into atypical macro-scale activity, thereby highlighting the clear links which exist between the micro- and macro-scales. Furthermore, in the separate case of anaesthesia: profiles of on-going macro-scale activity can be measured with distinct patterns attributed to different levels of anaesthesia (Devonshire et al., 2010b), further inciting the need to study more comprehensively how alterations in macro-scale dynamics would arise from their respectively altered meso-scale level activity. The convergence of the above-described lines of investigation are to some extent also accountable for the renewed interest in investigating the relationship linking meso-scale with macro-scale dynamics to physiological function: most of this research (as listed above) therefore focuses on comparing meso-scale dynamics in normal versus pathological states as well as under a range of pharmacological manipulations. This particular field of on-line monitoring of meso-scale dynamics uses a number of approaches, particularly *in vitro*: including electrophysiology (Baker et al., 1999; Nordhausen et al., 1996) and high-resolution imaging, in particular with voltage-sensitive dye imaging (VSDI) (Chemla and Chavane, 2010; Grinvald and Hildesheim, 2004), as the techniques of choice utilised to record synchronous neuronal population activity.

1.6 Monitoring of neuronal assemblies *in vitro*

1.6.1 Brain slice preparation

Because of the complex dynamics of neuronal network dynamics when recorded *in vivo*, techniques used to record population activity in a calmer, more controlled *in vitro* setting can present some important advantages. *In vitro* preparations may encompass a wide range of different approaches, however in this thesis the focus is on brain slice preparation. This approach consists of isolating small volumes of cerebral tissue within the thickness of a brain slice cut (400 μm-thick, see **Figure 9**), while making sure to keep the neurons and by extension, the networks they form, located within the slice alive and as healthy as possible (Dingledine, 2013). If kept under reasonable temperatures (in the approximate range of 25 to 34°C) in aCSF containing appropriate salt concentrations and oxygenation (see **Chapter 2**, **Section 2.3**), live neurons within slices can be kept alive within their native networks and retaining their overall excitable state, albeit inevitably somewhat affected by the manipulation, for protracted periods of time of up to 6 hours. As such, and via the longer range cortico-cortical connections which link neighbouring cortical columns and their inter-locked networks together, it is possible to activate a wide area of neuronal tissue – see **Figure 6** for assemblies evoked in an AIC slice preparation. **Figure 9** displays a schematic diagram of a slice illustrating the above-mentioned principles of *in vitro* slice preparation. Using this paradigm, cortical networks remain mostly silent, with only minor manifestations of spontaneous activity (Ringach, 2009), thereby providing a calm system to study evoked activity with a high single-to-noise ratio (SNR).

Another advantage of using brain slices is the possibility of imaging structures which would normally be out of the reach of conventional *in vivo* optical imaging: structures found sub-cortically, within orbital (such as AIC, part of the orbitofrontal cortex) or lateral cortical areas are impossible (for the former) or difficult (for the

latter) to image simply due to their location within the skull. It is possible for investigators to image the dorsal surface of the cortical mantle as in this case simply removing the top of the skull offers direct access to the cortical surface over a wide area, however it is much harder to access any other area of cortex not found directly under the dorsal part of the skull. The same is tru for imaging of sub-cortical structures. It is in fact one of the objects of this thesis to compare for the first time, using the same exact experimental setup and protocol, the activity profiles of different cortical and sub-cortical areas (see **Chapter 3**). Furthermore, the isolation of neuronal populations and networks in brain slices allows for quiet recordings with very little non-specific activation (noise) and which therefore yield data with very high intrinsic SNR, allowing for the characterisation and quantification of activation and decay dynamics of mesoscopic neuronal networks/assemblies under baseline and drug conditions.

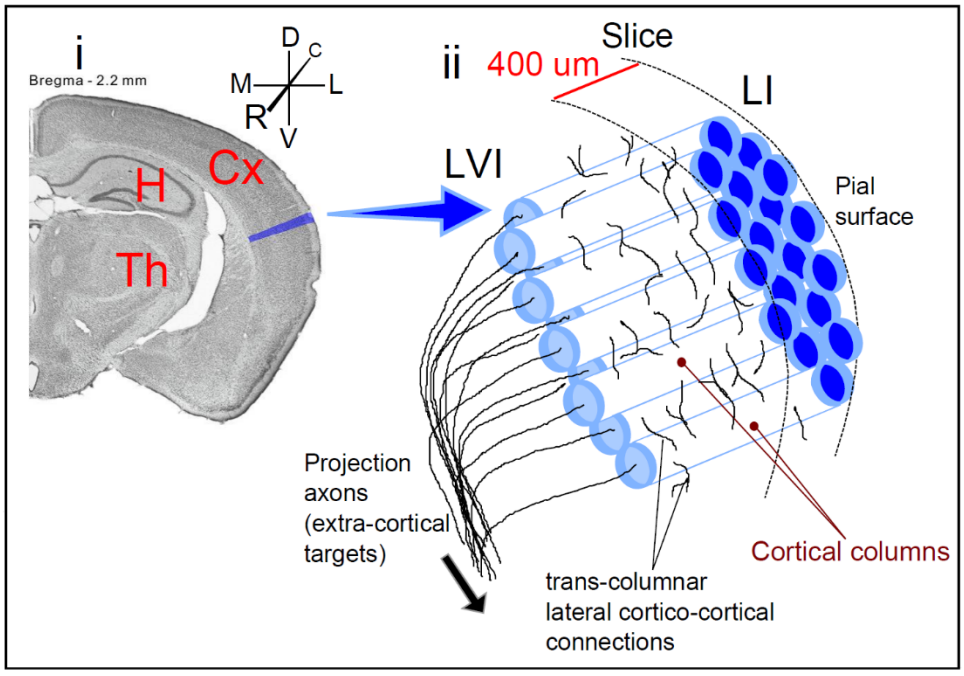

Figure 9: Schematic organisation of cortical columns within slices. Coronal cuts maintain the radial columnar arrangement of cortical networks within the thickness of the slice (400 µm) which is approximately 1 hypercolumn thick (300-600 µm). Application of an extrinsic electrode to the cortical tissue delivers an electric pulse to the column with which it comes into direct contact, with the signal being very quickly transferred to surrounding columns via poly-synaptic network activation (active recruitment of cells and networks).

1.6.2 Visualisation of neuronal assembly dynamics using voltage-sensitive dye imaging

a. Limitations of traditional electrophysiology

For the study of dynamic neuronal communication, investigators have traditionally used techniques that have allowed them to record changes in electrical potentials across neuronal cell membranes specifically, using electrophysiology; i.e. by means of either extra- or intra-cellular electrodes recording changes in the extracellular matrix (Speckmann et al., 1984)or within neurons (Molleman, 2003), respectively. In either case however, using electrodes to 'eavesdrop' on neuronal communication represents, at the very least, an invasive intervention which provides only a limited account of how information is differentially processed in distinct cellular compartments of a single neuron; as is the case between information transfer inside axons and within dendrites (Koch, 1999). One such example in intra-cellular electrophysiology is the inability to record from a neuron's dendritic spines as the electrode is too large for such a small target compartment; dendritic spines however, are arguably one of the most salient neuronal compartment to record from, as they represent the primary site of synaptic input within the brain (Hering and Sheng, 2001; Sorra and Harris, 2000); see **Figure 2Aiii**. At the meso-scale, electrophysiology (extracellular field potentials) provides an indiscriminate description of the activity evoked within neuronal assemblies (Peterka et al., 2011), where the waveforms are very complex and it is therefore very hard to identify salient features of network functioning from the recorded deflections, if considered alone rather than in the context of other comparable field potentials records. Finally, electrophysiology features an intrinsically low spatial resolution as a result of the nature of the recording: electrodes can only report alterations in electrical potential occurring at their very tip, with the extent of their receptive field still the subject of much controversy (Linden et al., 2011). In order to go around this significant

limitation, electrophysiologists developed micro-electrode arrays (MEA), which combine multiple LFP electrodes into a single array, positioned at specific angles and distances from each other to gather data at an appropriate temporal resolution over closely located points within an area of interest. This approach however can increases mechanical damage incurred on neuronal networks, in addition to the recorded data providing information about distinct and discrete loci within the area of interest, rather than a unified vision of a continuous assembly over space and time as is provided by molecular probes such as VSDs (Arieli et al., 1996).

b. Imaging neuronal dynamics using voltage-sensitive dyes

When taking the effect of physical damage into consideration, researchers turned towards optical imaging as a solution to the invasive electrophysiological monitoring of mesoscopic dynamics. Crucial to this endeavour, was the development of ultra-fast imaging techniques using molecular probes, in particular voltage-sensitive dyes (VSDI) – a new recording technique which prompted an entire field of study in the 70's (Ross et al., 1977; Waggoner and Grinvald, 1977; Woolum and Strumwasser, 1978), that was elaborated in the 80's and 90's (Antic et al., 1999; Ebner and Chen, 1995; Grinvald et al., 1982; Gupta et al., 2000; Konnerth et al., 1987), with imaging capacities recently improved further by achieving ever higher overall signal-to-noise ratios (Lippert et al., 2007; Zochowski et al., 2000) and ultimately in the development of revolutionary methods of imaging cortical activity in freely moving animals (Ferezou et al., 2006; Greenberg et al., 2008). VSD molecules are electrochromic molecules which possess both charged and lipophilic properties, which grant them the ability to impede in cell membranes and transduce electrical signal into fluorescence (Scanziani and Hausser, 2009; Tominaga et al.,

2000) – see **Chapter 2**, **Section 2.1.4**. Another specific property of VSDs is their sensitivity to small voltage changes, albeit with low signal-to-noise ratios, in response to which these molecular probes produce sizeable alterations within their fluorescence profile: in turn, this property of VSDs means that resulting data is dominated by sub-threshold changes (Berger et al., 2007; Denk et al., 1990; Yuste et al., 1997). Because assemblies represent a very efficient way for neuronal networks to impose a top-down mechanism of population V_m control in their constituting cells (see **Section 1.4**), it is often advantageous to record both supra- as well as sub-threshold effects. In turn, and to the contrary of data acquired using MEAs, data acquired using VSDI provides continuous information about traveling depolarising wave-fronts (i.e. spreading assemblies); this is one of the greatest advantages of VSDI as it endows this approach with the capacity to provide a comprehensive account of mesoscopic neuronal activation patterns (assembly dynamics) over continuous space and time with respective resolutions which fit the mesoscopic level of organisation of micrometres and milliseconds, respectively.

In conclusion, any kind of evoked neuronal activity at the micro-scale, if large enough, will drive a highly efficient process of neuronal recruitment (Wong et al., 2016), i.e. generation of assemblies, which can be readily detected using on-line recording techniques (an example of which are ERPs): these activity patterns have been reliably used to differentiate active from idle cortical fields, to identify distinct activity signatures relating to specific brain states, as well as in the diagnosis of neurological disorders by comparison with healthy controls, highlighting their relevance as markers of physiological function and appropriate processing state, respectively. The reliability of this phenomenon therefore implicates neuronal assemblies, or mesoscopic brain activity, as the salient feature of brain operations which can therefore serve as an all-important measure of cerebral integrative and processing capabilities.

Chapter 2: METHODS

2.1 Introduction

2.1.1 On-line monitoring of neuronal activity

In the late 1700's, Jan Swammerdam was one of the first investigators to record dynamic cellular communication directly, with the use of primitive electrophysiological techniques in frog limbs (Cobb, 2002). It was found that neurons, specialised in cellular communication, had the ability of transducing information in the form of electrical blips (APs) into chemical messengers (neurotransmitters), and back from chemical messengers to AP. In particular, much attention has been given to cellular mechanisms of membrane de/repolarisation, as it is the central process at the heart of cellular communication, and with the careful arrangement of neurons into networks, allows for the emergence of coherent population activity. It is the recording of this particular type of dynamic, cellular communication which soon became the focus of scientific investigations using a range of approaches from electrophysiological to imaging techniques operating at a range of spatio-temporal scales (see **Chapter 1**, **Figure 1**).

2.1.2 Electrophysiology as a means of recording dynamic neuronal events

The concept of recording neuronal communication in real time and possibly decipher the language of neurons has always been the focus of much fascination and effort from electrophysiologists, however it very quickly became evident that deciphering this language with respect to behavioural function would be a much more difficult task than originally hoped. Electrophysiological signals are recorded, amplified and filtered in order to isolate the low frequencies (<500 Hz) which provide a reading of the local field potential (LFP), while when high-pass filtered (>500 Hz), the signal provides a reading of the local network spiking activity, either from single neurons (termed 'single units' or 'SU' LFP) or from multiple spiking neurons (termed 'multi-unit activity' or 'MUA' LFP) (Burns et al., 2010; Buzsaki et al., 2012). For the scope of this thesis, single-electrode extracellular electrophysiology (low-pass filtered LFP) provided a starting point from which to record population activity, as it would indiscriminately record sizeable electrical changes emanating from all neuronal types around the electrode tip (Mitzdorf, 1985) – however the reach of the receptive field of such a method of acquisition remains unclear to this day (Kowalski et al., 1996a; Kowalski et al., 1996b; Linden et al., 2011; Schmitzer-Torbert et al., 2005). The controversy surrounding the physical reach of the receptive field of single-electrode LFP recordings stems from the summation of all neuronal and/or cellular sources of alterations in voltage signal, and include: synaptic activity, fast action potentials, slow calcium spikes, intrinsic membrane currents, higher-order interactions such as neuron-glia interactions as well as voltage changes resulting from ephaptic effects (Buzsaki et al., 2012). LFP therefore reports the average voltage changes from all neuronal types and compartments (listed above) present around the electrode tip involved in

synaptic communication (Nunez, 2006). Furthermore, whereas high-pass filtered LFP signals provide information about *output spiking activity* of a local network, low-pass filtered LFP provides a more reliable measure of the *input activation* (Linden et al., 2011): i.e. synaptic and dendritic spine activity, which can be driven either by the activity of local recurrent neuronal networks or from afferents of more distant brain regions (Lorente de No, 1947), or both. Furthermore, it has been found that an extracellular field potential generated by a synaptic current is highly dependent on the morphology of the cell (i.e. which type of neuron) in which this EPSP occurred, as well as dependent on the spatial position and orientation of the recording electrode (Linden et al., 2010). More specifically, several studies have implicated pyramidal dendritic synapses in particular, as being the major contributors in the generation of LFP as a result of their reported cellular 'open-field' arrangement (Johnston and Wu, 1995; Mitzdorf, 1985; Rall, 1962). This 'open-field' arrangement refers to a specific type of cellular morphology, and more specifically to the layout of cellular compartments, whereby the soma and axon face and extend in one direction while the dendritic tree extends in another; this arrangement is particularly relevant for pyramidal cells and, upon synchronous activation of the dendrites, creates a strong dipole moment between the locus of stimulation and the soma, which is readily detectable using LFP. Taking all the above into consideration, in addition to the further publication of more recent studies (Berens et al., 2008), it can be concluded that LFP recordings (such as employed here) provide data which relates to the overall input electrical potential generated from small areas/volumes of neuronal tissue. Furthermore, depending on the types of neurons present and the extent and nature of network inter-wiring, data providing information regarding the size of the area from which this signal originates may show high levels of variability (Linden et al., 2011). Reports have estimated this area to be of the order of a few hundred micrometres

(Katzner et al., 2009; Xing et al., 2009) to a few millimetres (Kreiman et al., 2006) in diameter: LFP data therefore provides information originating from a small volume of neuronal tissue surrounding the electrode tip, and represents the propensity of a network to integrate and process information, with an emphasis on synchronously-driven dendritic input (Mitzdorf, 1985).

2.1.3 Imaging as a means of recording population activity with high spatio-temporal resolution

However, in an attempt to record two-dimensional activity over a wide region of interest, a capacity that is not easily achievable using electrophysiological techniques, investigators soon turned to the use of imaging. This approach became increasingly attractive in part as a result of the laborious and often problematic process of mapping the anatomical organisation of sensory cortical fields using electrophysiological techniques alone; for example, as was done for cat visual cortex in the late 1970's (Palmer et al., 1978; Tusa et al., 1978; Tusa et al., 1979). The mammalian cortex is organised into iterative constructs of networks defined according to like-properties of their neuronal receptive fields (i.e. cortical columns), yet for example in visual cortex particularly, this columnar and macro-columnar organisation is renowned for its extraordinarily complex scatter arrangement: it consists of neuronal clusters grouped together on the basis of specific receptive field properties, such as for example orientation and position, organised in typical 'pinwheel' macro-columnar arrangement (Chen et al., 2012; Gray and Singer, 1989). The very large number of repeat electrode penetrations which would therefore be required in such a system to produce an accurate description or map of such cortical fields, in addition to the collateral damage such procedures would

inflict to the tissue under consideration, strengthened the necessity for better, more adequate, monitoring techniques (Scanziani and Hausser, 2009).

Many optical techniques have been developed, however high temporal and spatial resolution is currently achieved particularly well by techniques which image signals given off by molecular probes sensitive to changes in membrane electrical potential (Cohen and Lesher, 1986; Cohen and Salzberg, 1978), such as voltage-sensitive dyes (VSDs). The most obvious draw-back of such a method is that, contrary to traditional electrophysiology which records the 'actual' language of the brain in terms of voltage deflections, voltage-sensitive probes report these same membrane potential fluctuations in terms of a secondary measure: either fluorescence or absorption (Bashford, 1981). This was at first controversial, as doubts were initially cast as to the origin of the emitted signal reported by VSD imaging, as well as to the extent of its contamination with sources of non-specific signal: for example, with that emitted from glial cells ubiquitously present within neuronal tissue, which were shown to exhibit a much slower time-course than that evoked by neuronal activity (Grinvald and Hildesheim, 2004). Over the last two decades however, it has become clear beyond reasonable doubt, mostly via the analysis of data in combination with electrophysiological techniques, that VSDI indeed provides records which accurately reflected true changes in neuronal dynamics (Chemla and Witharana, 2016; Spors and Grinvald, 2002; Tsytsarev et al., 2012).

2.1.4 Using voltage-sensitive dyes for imaging population dynamics

Seminal experiments using such molecular probes were carried out in squid giant axon (Ross et al., 1977; Salzberg et al., 1973; Tasaki and Warashina, 1976; Tasaki et al., 1968) and showed that in reality, fluorescence and/or absorption readings of intracellular VSD imaging produced deflections that share the same activity profile as those recorded using traditional intracellular electrophysiology (Cohen and Salzberg, 1978; Ross et al., 1977), see **Figure 3A**. These initial experiments employed photomultiplier tubes for; these were then replaced with photo diodes, focused on individual neurons, for imaging of absorption changes of extrinsic molecular probes correlated with neuronal activity (Grinvald et al., 1977; Salzberg et al., 1977). A few years later, the same group successfully imaged the combined activity of local neuronal populations using large arrays of photo diodes, also in invertebrate ganglia (Grinvald et al., 1981). The following year, this same technique was extended further to image population activity evoked in mammalian brain slices, in this case: rat hippocampal population activity (Grinvald et al., 1982). Taken together, these initial studies demonstrated the ever-growing advantages of using VSDI as a powerful tool in acquiring novel insights into the mechanisms of neuronal dynamics *in vitro*, whether at the single-cell or population level, and its application soon followed *in vivo* (Grinvald and Hildesheim, 2004; Scanziani and Hausser, 2009).

When considering this type of imaging however, it is useful to try and understand how the recorded signal (fluorescence) is generated and where it originates from. VSDs are potentiometric dye molecules which are used as molecular probes: as such, they report minute alterations in one, elusive, parameter (in this case 'electrical potential') as changes in another, readily recordable measure ('fluorescence' in terms of percent change from baseline) with respect to a predictable relationship

(Loew, 1996), which in the best of cases is linear (see **Figure 3Aii** below). To this day, hundreds of dye molecules have been probed (Ebner and Chen, 1995; Grinvald et al., 1982), each having their own specific physical and biochemical properties which in turn affect their efficacy, stability, solubility, fluorescence and/or absorption spectra (among other crucial parameters). Only about a dozen of all potential dyes tested were found to be useful as molecular probes of neural activity. One VSD in particular has consistently show suitable features for the purpose of imaging neuronal activity in a range of different preparations: di-4-ANEPPS (Grandy et al., 2012; Preuss and Stein, 2013; Tominaga et al., 2000), or 4-(2-(6-(Dibutylamino)-2-naphthalenyl)ethenyl)-1-(3-sulfopropyl)pyridinium hydroxide inner salt. Di-4-ANEPPS is even described as being one of the most sensitive probes featuring some of the most reliable responses seen among a range of dyes compared in one study (Fluhler et al., 1985).

- *Di-4-ANEPPS as a versatile voltage-sensitive molecular probe*

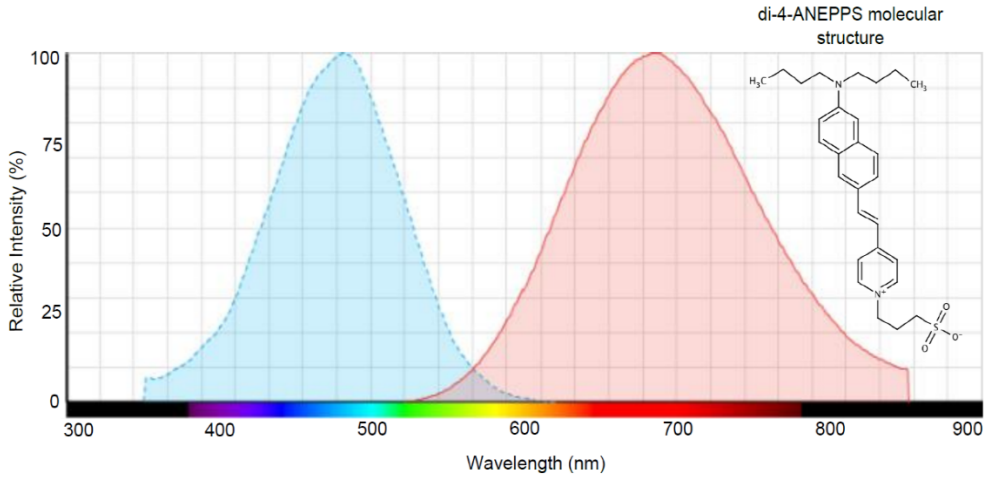

Figure 1: Fluorescence parameters of voltage-sensitive molecular probe di-4-ANEPPS. Graph displays the wavelengths of excitation (blue curve) and emission spectra (red curve) specific to di-4-ANEPPS – chemical structure of di-4-ANEPPS shown as an inset on the right hand side of the graph: note the double-bonded carbon backbone construct granting

this molecule with both a rigid structure and a delocalised electron system. Absorption spectra and molecular structure of di-4-ANEPPS (inset) both taken from Thermo Fisher Scientific website (https://www.thermofisher.com/order/catalog/product/D1199).

As can be seen in **Figure 1**, the molecular structure of di-4-ANEPPS consists of a charged domain, featuring both a sulphite group (SO_3^{2-}) and a quaternary amine (N^+) group, followed by a long hydrophobic unsaturated carbon-ring chain (**Figure 1** inset). This long hydrophobic carbon chain anchors the molecule within the hydrophobic domain of the phospholipid bilayer in an energetically-favourable manner, while the presence of double bonds grants the molecule with a high level of physical rigidity, as well as an extensive system of delocalised electrons between the respective p-orbitals of the conjugated carbons. As a result of the arrangement of the hydrophilic 'head' of di-4-ANEPPS and its long hydrophobic tail, anchoring in cell membranes in the manner of a fishing float (**Figure 2A**), molecules remain at all times stably arranged between phospholipids (Fluhler et al., 1985), parallel to the vector of the electric field generated by cross-membrane electrical potentials (Cohen and Lesher, 1986). The combination of the precise structure of the molecule, electron cloud configuration and hydrophobic-to-hydrophilic atomic arrangement of di-4-ANEPPS is what makes it such a successful probe, reporting changes in membrane potential with a time-constant far lower than a single millisecond (Tsytsarev et al., 2014).

2.1.5 Reporting electrical potential fluctuations in brain tissue using di-4-ANEPPS, and complementary with electrophysiological techniques

First of all, it is important to consider that application of the dye occurs via simple diffusion, which is a slow process. Additionally, both the penetration of the excitation illumination as well as that of the emission in highly light-scattering media, such as brain tissue, altogether restricts the acquisition of data to the first 100 micrometres of tissue only (Hill and Greenfield, 2014). This would nonetheless include sufficiently extensive networks of interconnected of mini-columns from which activity can be recorded. It remains still unclear how *exactly* VSDs report changes in electrical potential: a few mechanisms have been proposed however, as described in **Figure 2C** below, and include the electrical repulsion of negatively-charged groups of VSD molecule out of cell membranes (**Figure 2Ci**), a change in molecular orientation (**Figure 2Cii**), and/or even a re-arrangement of the molecular structure of the VSD itself (**Figure 2Ciii**) (Tsytsarev et al., 2014). In each case, the change in location, orientation or shape (respectively) leads to shifts in their emission or absorption spectra. Whatever the precise mechanism, it is crucial to bear in mind that application of VSDs to neuronal cell membranes can also incur unwanted effects if not carried out with great care.

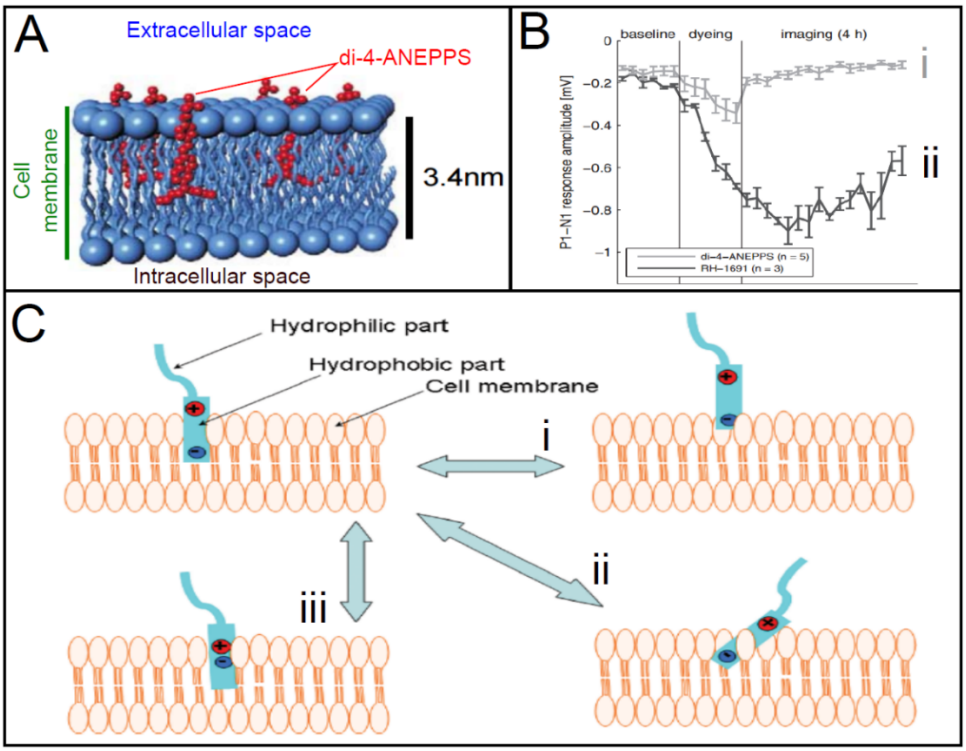

Figure 2: Di-4-ANEPPS features weak and reversible effects within the cell membrane. Di-4-ANEPPS molecules embed in cell membranes by means of their long hydrophobic carbon chains, adopting an orientation akin to that of phospholipids (**A**), and while this may affect membrane homeostasis, di-4-ANEPPS does so to a much lesser extent than other VSDs (**B**), such as RH-1691 (**Bi**); here shown to dramatically increase cortical LFP amplitude *in vivo*. The possible mechanisms responsible for the change in emitted photon wavelength are proposed in panel **C**: intracellular depolarisation (becoming more positive) may cause VSD molecules to be pushed out of the cell membrane (**i**), shift orientation (**ii**), or undergo internal atomic re-arrangement (**iii**), or some combination of two or more of these proposed mechanisms. Panel **A** was adapted from (Knopfel et al., 2006), Panel **B** was adapted from (Grandy et al., 2012) and Panel **C** was adapted from (Tsytsarev et al., 2014).

- *Side effects of application of di-4-ANEPPS in live tissue*

The intense illumination that is required to obtain a satisfactory signal with high signal-to-noise ratio has previously been shown to generate reactive oxygen species (ROS) from the interaction of light, oxygen and electrochromic dye molecules (Grinvald et al., 1988): this side effect of current VSDI techniques therefore induce some damage to cells and tissues, an effect described as photo-toxicity. In addition to the possibility of photo-toxic damage, there are also sources of light-independent

pharmacological side effects induced by addition of di-4-ANEPPS to live tissue preparations: the first is a non-specific effect resulting from the aggregation of exogenous lipophilic molecules within cell membranes. This is because cell membranes consist of sensitive environments which regulate the interaction of a cell with its surrounding extracellular space. When high VSD concentrations are added to the extracellular media, dye molecules aggregate in the lipophilic environments of cell membranes and to some extent disrupt their normal homeostasis (Grinvald et al., 1988). The second source of light-independent pharmacological side effects is specific to di-4-ANEPPS's molecular structure, as well as that of a few other VSDs, and involves a slight potentiation of $GABA_A$ receptor currents (Mennerick et al., 2010). This effect has been shown to cause a heightened response from the inhibitory component of live neuronal networks and may induce some reductions in overall recorded signal, however the overall impact of this effect remains unclear (Mennerick et al., 2010). The above-mentioned limitations of using VSDs, and di-4-ANEPPS in particular, must be taken into account when planning experiments and interpreting the results, however in general these effects have been found to induce only small changes to evoked responses and that therefore successful experiments can be undertaken (Loew, 1996; Tominaga et al., 2000). Importantly however, and especially with di-4-ANEPPS, these detrimental effects are largely outweighed by the advantages this dye offers over others, such as 'blue' dyes, for example RH-1691 and RH-1692 (Shoham et al., 1999), which require much greater staining periods, tend to wash out of neuronal tissue much faster than di-4-ANEPPS, induce a significantly more potent modulation of evoked responses and produce more phototoxic side-effects (Grandy et al., 2012), as shown in **Figure 2B**.

- *Interpretation of VSDI data from mesoscopic population activity*

Imaging intracellular neuronal dynamics shows an impressive level of conformity with intracellular electrophysiological records of membrane potential fluctuations (Ferezou et al., 2006; Petersen et al., 2003; Salzberg et al., 1973). However when comparing fluorescence readings with *population* responses (LFP), such as was done in the primary visual cortex of behaving monkeys (Chen et al., 2012), VSDI and LFP data show some discrepancies. Nevertheless, VSD imaging signals provide a very good linear measure of intracellular V_m, this is also true for average V_m of neuronal populations yet with VSDI records showing larger receptive fields than those of single neurons (see **Figure 3B**); the differences seen between LFP and VSDI tuning curves are comparable to the discrepancies seen between receptive field sizes of supra- and sub-threshold responses in individual V1 neurons (Chen et al., 2012). It is important at this stage however to stress the fact that though VSDI signals are largely correlated with membrane potential (V_m), neither of those two measures are linearly correlated with AP spiking activity, which itself has previously been shown to share a non-linear relationship with V_m using electrophysiology (Anderson et al., 2000; Priebe et al., 2004).

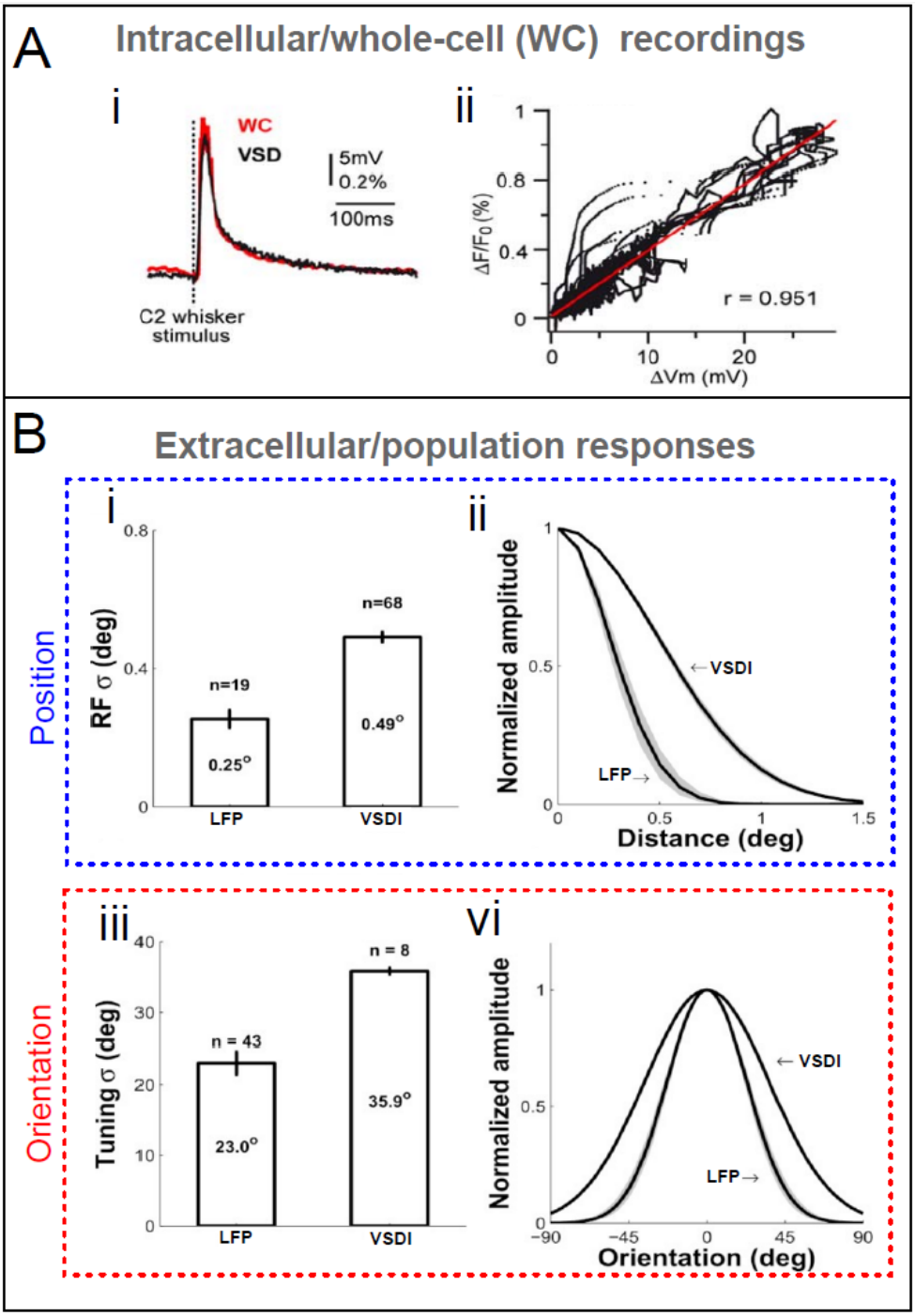

Figure 3: Fluorescence VSDI signal is linearly correlated with intracellular V_m. Fluorescence signal recorded within single neurons (**A**) is impressively well correlated with intracellular V_m (**i**), and exhibits a linear relationship (**ii**). At the population level (**B**), VSDI signals show a greater receptive field and higher sensitivity than LFP recordings, as seen *in vivo* in visual cortex both in position tuning (**i**, **ii**) and orientation preference (**iii**, **iv**). Panel **A** was adapted from (Ferezou et al., 2006), while panel **B** was adapted from (Chen et al., 2012).

- *Limitations of imaging of molecular probes and further developments*

In addition to the use of voltage-sensitive dyes, several other methods have been used with the aim of imaging neuronal dynamics, such as calcium-sensitive and pH-sensitive indicators. With respect to calcium-sensitive dye imaging (CaSDI), specific molecular probes are used, which alter their fluorescence properties in the presence of increasing concentrations of calcium ions (Ca^{2+}); however, the imaging data produced from such recordings is tethered to the time constants of cellular calcium dynamics. These feature protracted time courses relative to voltage-sensitive dyes, which instead follow the fast temporal profiles of trans-membrane voltage changes (Tominaga et al., 2000). As a result, the maximum frequency of oscillations which can be readily detected using CaSDI seldom exceeds 10 Hz (Takahashi et al., 2007), also meaning the dynamics recorded using CaSDI are often uncorrelated from transmembrane voltage fluctuations. Despite these limitations, the larger signals recorded with CaSDI compared to VSDI, make this technique at least as popular for monitoring electrical changes resulting from neuronal activity, and in particular action potential firing (Gobel and Helmchen, 2007). In all cases, inherent to the application of molecular probes for imaging of population activity: this prevents the identification of specific cell types within the network (such as GABAergic, cholinergic or even glutamatergic neurons), while simultaneously not being able to isolate the activity of specific functional pathways. Additionally, the high lipid solubility of molecular probes means they stain all membranes indiscriminately; this includes those of non-neuronal elements, such as astrocytes, oligodendrocytes, microglia and blood vessels, among others. These cells are also electrically active, yet may feature dynamics on time scales which are vastly different from those of neurons. In turn these effects may introduce non-specific background signal leading to i) an overall reduced signal-to-noise ratio, and ii) the

contamination of the signal of interest with non-specific optical fluctuations (Konnerth et al., 1987). The final limitation associated with extracellularly-applied VSDs or CaSDs regards their relative toxicity, meaning experiments can only take place over relatively short periods of time of up to a few hours at most, and thus cannot be used for protracted experiments attempting to elucidate processes linking neuronal activity with behaviour.

In the last 20 years, investigators have turned to the use of genetically-encoded voltage/calcium indicators, i.e. GEVIs and GECIs respectively (Knopfel, 2012; Knopfel et al., 2006; Siegel and Isacoff, 1997). This approach, of creating genetically-encoded reporters of neuronal activity provides a number of advantages, including the ability of specifying the cell type(s) which in which these indicators are expressed, the non-toxic nature of such dyes meaning they can indeed be used for experiments with protracted time courses (necessary for relating behaviour to dynamic activity), in addition to the less invasive nature of experiments using such indicators (as there is no need for removal of the dura matter). GEVIs provide a useful tool in imaging the *synaptic input* entering a neuronal circuit, whereas data acquired using GECIs has been shown to report the resulting *spiking output* of neuronal networks (Antic et al., 2016). In turn, the input to a neuronal network (i.e. using GEVIs) provides an indication of its signal integration and processing dynamics (Poirazi et al., 2003), while monitoring network output using GECIs provides more focused indications as to the outcome of those computations (Antic et al., 2016).

2.1.6 Sources of noise within VSDI recordings

Noise, i.e. random disturbances of recorded signals, can be introduced into VSDI recordings at multiple stages and in a range of forms, each of which must be at least considered when conducting optical imaging experiments using voltage-sensitive dyes: the first is that which is induced by movement, or vibrations. Such a noise component may be introduced either from the tissue sample under investigation (as could be the case with tumultuous bath solution perfusion): whether by the bath solution surface, at its interface with air and located in the camera light-path, or even by the imaging location itself (as can be the case with vibrating buildings, tables or instruments).

Secondly, noise may be introduced by the light source used to illuminate the slice, as well as from the acquisition of photons by the camera: also known as 'shot noise'. Noise originating from the light source arises as a result of variations in emitted light, which in turn can arise due to alterations in power supply intensity, inadequate optic fibres, variations in resistance of the light filament as well as various thermal effects (Brown, 1993). In the case of the present investigations, the light source used in the imaging setup was equipped with tungsten-halogen lamps, for which the above-mentioned variations (shot noise) are relatively small, to the point where they can be discarded as having a prominent effect. Additionally, since the intent here was to image mesoscopic, network-wide activity, the effects of light scattering on recorded dynamics only induced minimal effects with respect to the overall spatial acquisition of data.

Third and fourthly, noise can appear within the recording as a result of fixed-pattern and/or random noise, both of which are linked to the functioning of the camera (Reibel et al., 2003). Fixed-pattern noise originates from variations in the response properties of individual camera pixels, and as its name suggests, this fixed-pattern

noise is static and can thus be removed. On the other hand, random noise is unpredictable, and can therefore pose a greater problem in terms of final image quality. Random noise arises mostly from the combination of reset noise, photon shot noise, output amplifier noise and dark current noise (Reibel et al., 2003): of all these contributors, only dark current and photon shot noise can be influenced by investigators, the others are intrinsic noise properties of the apparatus used. Dark noise is usually found to induce low levels of variability when using complementary metal-oxide-semiconductor (CMOS) cameras (as used here); photon shot noise on the other hand constitutes the main source of optical noise when carrying out VSDI experiments using CMOS cameras to image fluorescence.

- *Optimising data acquisition for low-noise recordings*

VSDI data intrinsically produces relatively noisy recordings, both as a result of the above-mentioned sources of noise as well as a result of both the very high sensitivity of di-4-ANEPPS and the acquisition system in reporting membrane potential changes (Tominaga et al., 2000). This specific VSD is in fact so sensitive to minute alterations in membrane potential that it affects its signal-to-noise ratio (SNR), recording both large (supra-threshold) and, in majority, small (sub-threshold) potential changes (Berger et al., 2007; Petersen et al., 2003), yet can be increased via repeat-trial averaging (Fehervari et al., 2015). Yet this is not to say that sub-threshold membrane potential changes are a source of noise within VSDI recordings – indeed, they represent real and discriminatory dynamics in neuronal population communication as an integral component of normal neuronal coding (Izhikevich, 2002; Magee and Johnston, 1997; Steinmetz et al., 2000), and this ability is therefore an important advantage of VSDI.

Vibrational noise was reduced with the use of i) a Newport air table (MKS Instruments, https://www.newport.com), ii) a small nylon mesh to keep the slice immobile at the bottom of the well, as well as iii) a microscope glass slip broken into and placed above the bath, at the interface of the bath solution and air. The glass slide was broken in a way to produce shards thin enough to fit over the well without hindering the path of the electrodes, yet large enough to cover the entire field of view of the camera over the slice, creating a smooth imaging medium. This was particularly useful in keeping the surface of the bath static even with the use of an air inlet needle to the bath, which blew Carbogen gas (95% O2 – 5% CO2 gas) over the surface of the well not covered by the glass shard (see **Figure 4C** inset). This helped both in keeping the bath aCSF well oxygenated as well as allowing for a more distributed solution mixing within the well, helping to ensure any addition of chemicals or bioactive ligands to the perfusion aCSF would immediately and thoroughly mix within the bath: in turn this strategy ensured a uniform impact of perfused drugs on the sample tissue.

A narrow excitation light filter ($\lambda = 530 \pm 5$ nm) was used here, as this has been found to reduce the extent of phototoxic damage and vibration noise (Jin et al., 2002), in order to filter green light onto the sample. Additionally, narrow excitation filters require lower illumination intensity compared to wider filters for adequate recording – helping to increase the time-windows during which the sample tissue can be recorded from while keeping photo-toxic effects to a minimum (Tsau et al., 1999). Finally, in order to rid the setup of any electrical noise, a home-made 1.0 x 0.8 x 1.0 m (W x L x H) grounded Faraday cage made from a hexagonal metal-wire mesh with aperture size of maximum 1 cm, was also placed over the air-table and setup (see **Figure 4B**). In order to reduce noise further, instruments were either battery-operated (such as the stimulator box), directly grounded and/or enveloped in grounded aluminium foil (such as the heater control power cord), or simply turned

off during data acquisition (such as the light source inside the rig for visibility during setting up of experiments).

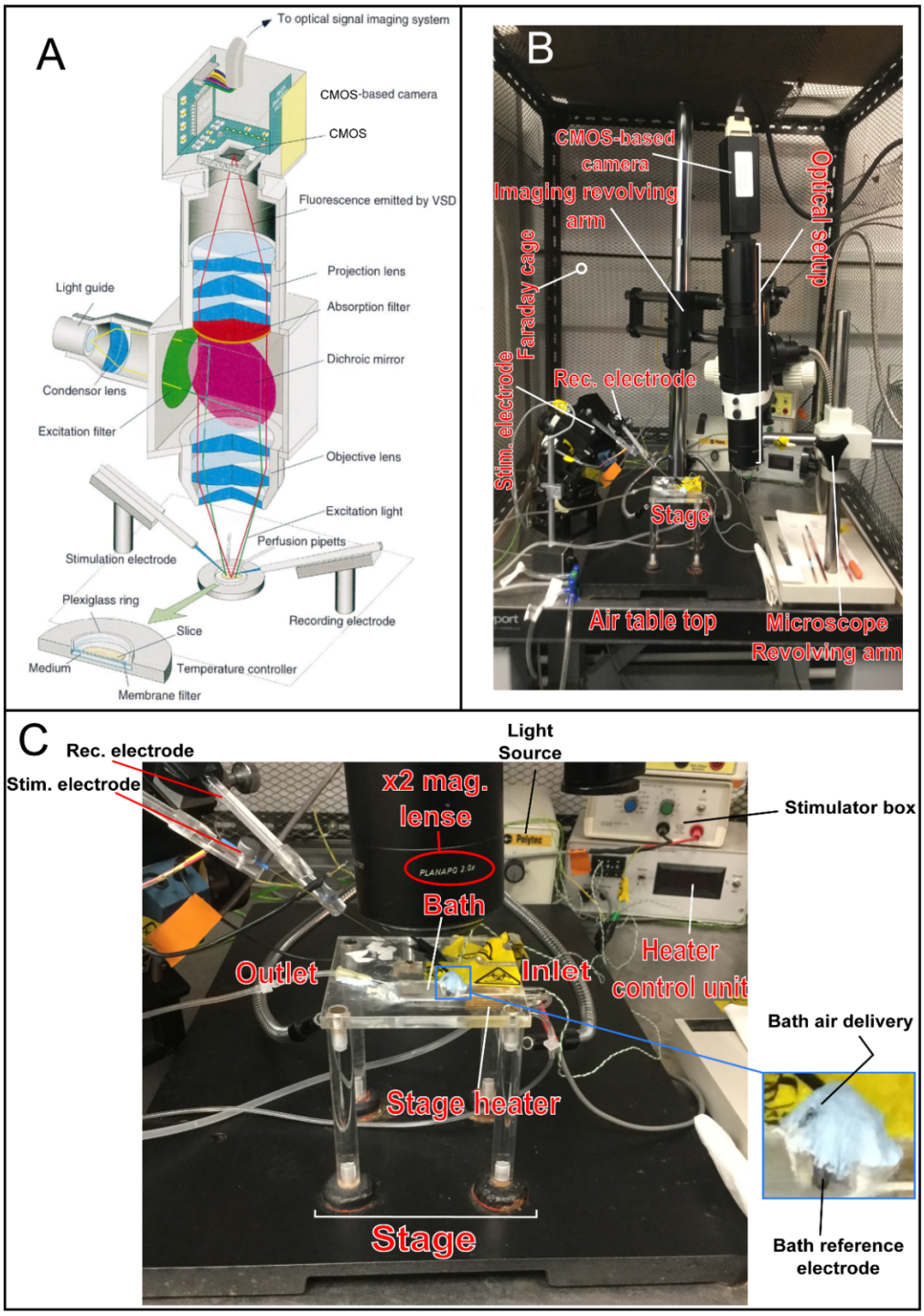

Figure 4: The experimental setup used for all experiments. Schematic diagram of a VSDI setup (**A**) with particular emphasis and detail given to the optics arrangement, whereby light from a halogen lamp is directed into the excitation filter from the light guide, which isolated the appropriate light wavelengths, in this case: 530 ± 5 nm, before they are reflected down

onto the sample by means of a dichroic mirror. The light reflected up from the sample passes a series of lenses, which focus the light, through the dichroic mirror and into the emission filter (> 590 nm), isolating the VSDI signal. These final photons reach the CMOS camera and are recorded for subsequent analysis. The diagram also features the arrangement of the stage, the bath and electrodes, a setup which differs only slightly from the one used here (**B**). A close-up view of the stage (**C**) shows this similar setup, including the essential stimulating and recording electrodes, a simplified bath as well as an additional bath air-delivery inlet (**C** inset). Panel **A** was adapted from (Tominaga et al., 2000).

2.2 Sampling sites within rodent brain

2.2.1 Cortical structures

a. The primary somatosensory cortex (S1BF)

The S1BF is by far the most extensively studied region of neocortex in rodent brain. It has been used as the basis for studying network functionality and columnar organisation, by virtue of the very large area of rodent cortex dedicated to this sensory modality featuring specialised cytoarchitecture forming barrels which process sensory information from mystacial (Woolsey and Van der Loos, 1970), see **Chapter 3**. It has been extensively studied both *in vivo* and *in vitro*, using whisker deflections and direct/thalamic stimulations respectively, as a model system for columnar processing in the cortex. Stimulations were delivered to two different locations within *coronal* S1BF slices: i) within the 'input' granule cell layer (LIV), as this is the main target of thalamocortical afferents to the S1BF, and ii) the supragranular (superficial) layers (LII/III) since these layers represent portions of the S1BF cortical thickness where a large amount of computations take place, before they are relayed onto the infragranular (deep) layers (LV/VI) – the 'output' layers (Mountcastle, 1997). Coronal slices containing S1BF were gathered between -1.60 and -3.14 mm with respect to the position of the bregma (Paxinos and Watson,

1998): basically slices were gathered as soon as the CA3 hippocampal formation became evident (slicing starting in the frontal lobes and continuing in a rostro-caudal direction) – slices were gathered from that point until 3 or 4 cuts (400 μm each) further into the brain, yielding a total of 6 to 8 brain slices with large enough areas of S1BF.

Additionally, and arguably most importantly, separate experiments were conducted where activation of the S1BF was triggered via stimulation of the ventroposterior medial nucleus (VPM), which reciprocally links the thalamus to the S1BF with afferent and efferent connections, see **Chapter 3 Section 3.1.1c**. With a specific slice angle adapted from that of (Agmon and Connors, 1991), see **Figure 5**, and referred to in this thesis as the 'thalamocortical angle slice cut' or 'TC angle' slices, connections inter-linking these two brain sub-regions can be effectively conserved to a high enough degree that stimulation in the VPM can be transmitted to the cortex and produce a neuronal, i.e. more physiological, activation of the cortex. The methods for the preparation in the original publication, which was perfected on smaller mouse brains, states a 55° angle cut, however after much difficulty in acquiring my own functional thalamocortical connections with Wistar rats, the slice angle was adjusted to 50°: this alterations, also reported elsewhere (Land and Kandler, 2002), drastically increased the amount of slices with intact connections gathered per animal.

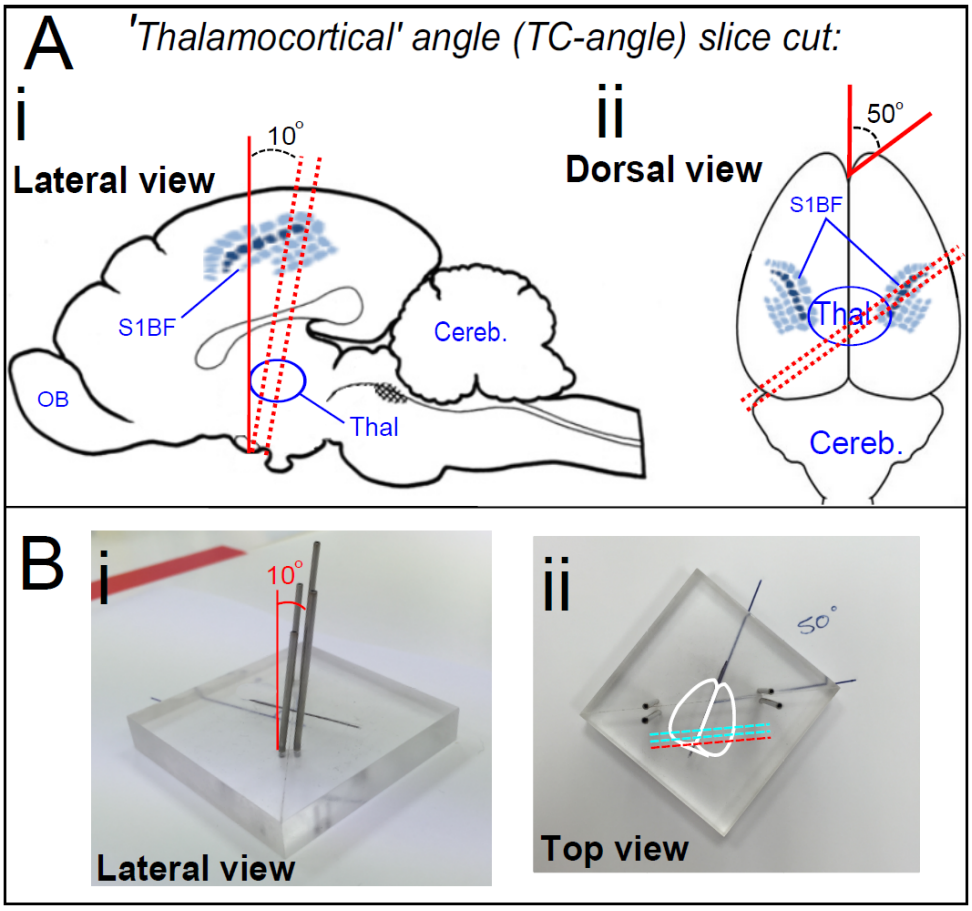

Figure 5: Slicing of thalamocortical angle cut. **A**. Schematic representation of rat brain showing the angles required to isolate functional thalamocortical slices. These were achieved using a small custom-made stage (**B**) to guide the blade and which achieved both the vertical 10° (**i**) and lateral 50° (**ii**) angles in a single cut, performed within seconds following removal of the brain from the skull, in a receptacle filled with ice-cold aCSF. Dotted lines in **A** and **Bii** represent the approximate location of active thalamocortical slices (in all cases, slices were 400 µm-thick).

b. The agranular insular frontal cortex (AIC)

The AIC is a region of neocortex part of the prefrontal cortex which differs significantly from that found in S1BF (from parietal cortex) as it is 'agranular', i.e. lacking a Layer IV, see **Chapter 3 Section 3.1.1a**. In addition to this, the AIC has been found to possess different information processing properties in that it is a region of association cortex (Beul and Hilgetag, 2014), contrary to S1BF which is a primary sensory area. In the experiments presented in the next chapters, direct cortical stimulations were delivered to both superficial and deep layers of AIC, LII/III and V/VI respectively. Slices containing AIC were taken from the frontal

lobes, between +3.70 and +2.20 mm with respect to position of bregma (Paxinos & Watson, 1998). In total, these indications yield up to 4 useable slices (400 μm thick), providing up to 8 slices containing AIC in their ventro-orbital cortical region.

2.2.2 Sub-cortical structures

a. The ventroposterior medial nucleus of the thalamus (VPM)

The VPM is a region of the thalamus which acts as a relay station for incoming information from the mystacial whisker pad, see **Chapter 3**, **Section 3.1.2a**. The major difference here is that the VPM is a sub-cortical structure: this has many implications with regards to the organisation and function of its neuronal networks compared to that of neocortex. The VPM communicates information generated by sensory receptors from the periphery to the sensory cortex: as such, the organisation of local neuronal networks is drastically different from that of cortical networks. For example, lacking inhibitory interneurons, favouring fast transfer of information from afferents originating in the brainstem nuclei to thalamocortical efferents.

b. The basal forebrain (BF)

The basal forebrain is a collection of sub-cortical nuclei co-localised in a small area of brain found ventro-medially, at the approximate coronal border between the frontal lobes and the rest of the brain. As described in **Chapter 3**, **Section 3.1.2b**, the neuronal networks found within this sub-cortical structure feature an organisation and composition which varies wildly from that usually found in cortex. This is because, just like for the VPM, the basal forebrain is a relay station, with a slightly different role however: the VPM relays sensory signals via glutamatergic

transmission to a primary sensory area. The basal forebrain on the other hand is the region from which cholinergic 'fountain'-like projections originate and innervate the entire brain, a neurotransmitter system highly implicated in cognition and attentional control (Avery et al., 2014; Sarter et al., 2001; Voytko, 1996; Whitehouse et al., 1982). It has been the focus of much investigative interest in the last few decades for its implication in the progression of Alzheimer's disease which is characterised by, among multiple different symptoms, a decrease in acetylcholine levels in the brain and correlated loss of cholinergic neurons from the basal forebrain (Whitehouse et al., 1982).

The group of nuclei chosen as the focus of the present investigations in basal forebrain are often considered in the literature as complexes (Brashear et al., 1986): the medial septal nucleus and diagonal band of Broca complex (MS-dBB, see **Figure 6**), which includes the medial septal nucleus (MS), the vertical diagonal band of Broca (VDB) and the horizontal diagonal band of Broca (HDB). Slices containing MS-dBB in the coronal plane were found between +1.00 and 0.00 with respect to the bregma (Paxinos & Watson, 1998). The basal forebrain could be clearly seen in slices to the naked eye as a thin band of white matter bordering the slice on its ventro-septal edge (see **Figure 6i** & **ii**). These indications yielded either 2 or 3 cuts per brain, thereby providing 4 or 6 slices. Of those, slices were inspected for the presence of the greatest amount of white matter in the MS-dBB location: the 2 or 3 slices containing the most white matter, clearly discernible within a region featuring a shape closely resembling the anatomical delineation of the MS-dBB complex as seen in the Rat Brain Atlas (Paxinos & Watson, 1998) were selected for experimentation.

2.3 Methodology and preparation of reagents and experiments

2.3.1 Artificial cerebrospinal fluid (aCSF) solution

The artificial cerebrospinal fluid (aCSF) used in experiments here is arguably the most important preparation of the entire process, as it is the medium within which all *in vitro* procedures take place: dissection of the brain, slicing, idling and washing of slices, dye staining, recuperation after staining, as well as the experiment perfusions themselves. As a result, and as the first step on each day of experimentation, a detailed protocol was followed with great care. The aCSF described here consists of ultra-pure distilled water (purified at 18.2 MΩ resistance, Purite, Thame, UK) to which specific salts and glucose concentrations were added, mostly mimicking those found in actual cerebral spinal fluid *in vivo*, with some minimal alterations. It is absolutely crucial to ensure that the aCSF precisely contains the required salt concentrations, as deviations from the concentrations listed below can have a drastic effect on slice health, or even neuronal dynamics.

Reagent	g/L	Concentration (mM)
Krebs stock solution		
KCl	1.90	25.49
KH_2PO_4	1.15	8.45
$MgSO_4 \cdot (H_2O)_7$	2.25	9.13
NaCl	49.75	851.30
Final volume: 2000 mL dH_2O		
Sodium bicarbonate stock solution		
$NaHCO_3$	25.00	297.59
Final volume: 2000 mL dH_2O		

Stock solutions were prepared fresh every 14 days, and kept in a fridge at 4°C at all times

Table 1: *Krebs and Sodium bicarbonate stock solutions contents*

In addition to providing the slice with salts and sugars, the aCSF solution also functions as a vehicle medium for solubilised oxygen (O_2) and drugs (such as specific receptor blockers, anaesthetics and bioactive peptides, see below), a pH buffer as well as, a temperature repository, thanks to the high specific heat capacity of water (Sturtevant, 1977). **Table 1** shows the list of ingredients and specific quantities used in the stock solutions, which were made up fresh at the start of every other week. Because several different ingredients are required in very specific quantities, the use of concentrated stock solutions saved a lot of time on experiment days, and prevented errors. In making up the final aCSF solution, specific volumes were taken (330 mL from the Krebs and 200 mL from the sodium bicarbonate stock

solutions), added to a 2 L glass bottle and topped with distilled water up to a total of 2260 mL, yielding the final concentrations listed in **Table 2**.

Reagent	Concentration (mM)
KCl	3.7
KH_2PO_4	1.3
$MgSO_4 \cdot (H_2O)_7$	1.3
NaCl	124.0
$NaHCO_3$	26.0
$CaCl_2$ dihydrate	2.0
D-(+)-Glucose	10.0
Final volume: 2260 mL dH_2O	$[Mg^{2+}] = 0.13$ $[Ca^{2+}] = 0.65$

Final solution was prepared fresh every day, and kept at room temperature

Table 2: Final aCSF solution; calcium chloride and glucose were added to the final solution on the day of the experiment in order to avoid the growth of microbes and mould, and the production of calcium carbonate precipitate, which would cloud the solution.

For every aCSF solution, the pH was adjusted to 7.4 ± 0.2 after the full dissolution of all required ingredients. All salts, as well as di-4-ANEPPS and most other drugs, used throughout this thesis were acquired from Sigma-Aldrich Ltd. (Dorset, England, UK), unless stated otherwise. It is also important to note that sodium bicarbonate also acts as a natural buffering salt in biological fluids, which helped shield slices under investigation from small pH changes. Whether in the dissection pot, the slicing stage, the bubbler pot or the bath within the imaging rig, the aCSF solution was at all times bubbled with a mixture of 95% O_2 – 5% CO_2 in order to

ensure appropriate levels of oxygenation within the aCSF, crucial to the survival of slices over several hours.

2.3.2 Drug solutions

All drug solutions were made as stocks: drugs were dissolved in dH_2O at concentrations of either 5 or 10 mM (depending on the final concentrations to be used), aliquoted into 1-2 mL Eppendorf tubes (Eppendorf UK Ltd., Stevenage, UK) and kept at -30.0 ± 0.5°C until required. If the drugs were not water-soluble (as was the case for etomidate, see **Chapter 4**), they were first dissolved in small volumes of DMSO, with final DMSO proportions never reaching more than 0.1% v/v in final drug perfusions. During the recording of baseline conditions (see **Section 2.7.4.d** and **Figure 9** 'Recording protocols' below), an aliquot of the required drug was quickly thawed and added in appropriate quantities to 60 mL of aCSF for preparation of final drug solutions. These solutions were then left to equilibrate for up to 5 minutes before the start of their own perfusion.

2.3.3 Rig maintenance

At the end of each month, or at the end of a set of experiments, the entire rig would be cleaned in order to ensure the agents used in one set of experiments would not affect future experiments. This maintenance included replacing all tubing within the rig, as well as a thorough clean of the metal tubes of the perfusion heater. Once all the tubing (Altec Products Ltd., St Austel, UK) was replaced, a thorough clean of the rig surfaces was undertaken, using a spray of 70% v/v ethanol in dH_2O followed by rinsing with dH_2O alone.

2.4 Harvesting of brain slices

2.4.1 Animals

All experiments carried out in this thesis were undertaken on 14 day-old (p14) male Wistar rats (Charles River, Margate, England, UK). These rats are young and not fully developed, however it was found that the responses evoked from stimulation of their cortical tissues produced much more extensive assemblies (in magnitude of evoked fluorescence) compared to young adults (p35-40; data not shown), yet retaining identical response profiles, suggesting a higher signal-to-noise ratio could be achieved in p14 rats.

2.4.2 Anaesthesia and Schedule I culling

Rats were placed inside a glass chamber (20 x 15 x 15 cm, floored with a metal wire mesh covering a layer of cotton) and anaesthesia was induced using 15-20 mL 100% w/w of the volatile anaesthetic isoflurane (Isothesia, Henry Schein, Abbott Laboratories, Illinois, USA), applied to the cotton bed flooring. First, anaesthesia depth was estimated by visual monitoring of breathing rate, which is normally quite rapid for rodents. Once the breathing rate appeared to have slowed down by approx. 50%, full anaesthesia was confirmed by pinching the hind paw of the rat – if the withdrawal reflex that such a pinch would normally trigger was absent, the depth of anaesthesia was considered adequate. Rats were then taken out of the anaesthesia chamber and had their necks quickly dislocated in accordance with the instructions of the Home Office legislation on the humane Schedule I killing of animals (https://www.gov.uk/government/uploads/system/uploads/attachment_data/file/229022/0193.pdf).

2.4.3 Surgical procedure

Once the neck had been clearly dislocated, the brain was quickly extracted from the skull in ice-cold aCSF: using a guillotine, rats were decapitated and the scalp exposed using small scissors. Using cuticle nippers, an opening was made at the back of the skull via the foramen magnum which allowed for removal of the skull shielding the cerebellum. The nippers were then used to uncover the cerebral hemispheres, from the opening made at the caudal end of the skull, by carefully inserting them between the pial surface of the dorsal cortices and the underside of the skull. A cut was made along the sagittal suture and both sides of the parietal bone were removed. Being careful not to pinch or drag any meninges and/or membranes surrounding the brain, a second cuticle nipper cut was made to remove the frontal bone and expose the entire dorsal surface of the brain. Next, small scissors were used to cut all membranes within which brains were lodged. Once all membranes were removed, a small spatula was used to sever nerve fibres linking the brain to the rest of the skull before pushing the brain out, into the ice-cold aCSF.

2.4.4 Slicing of brain for isolation of specific sub-regions of interest

The brain was left in ice-cold, oxygenated aCSF for approximately 30-40 seconds while the animal carcass was disposed of (stored at -80°C), and the slicing procedure initiated: for coronal slices, a simple vertical cut was done through the back of the cerebral hemispheres, while for thalamocortical slices, a small custom-made stage designed to allow for a cut with the specific angles required for a thalamocortical slice to be exacted in a systematic way (see **Figure 5B**). The coordinates of slices of interest within rat brain will be summarised here:

- **AIC**: 4 to 5 slices found between +3.70 and +2.20 mm from bregma
- **S1BF**: 4 to 5 slices found between-1.60 and -3.14 mm from bregma
- **Thalamocortical slices**: 2 to 3 slices cut using custom-made stage
- **Basal forebrain**: 2 to 3 slices found between +1.00 and 0.00 from bregma (see **Figure 6** below)

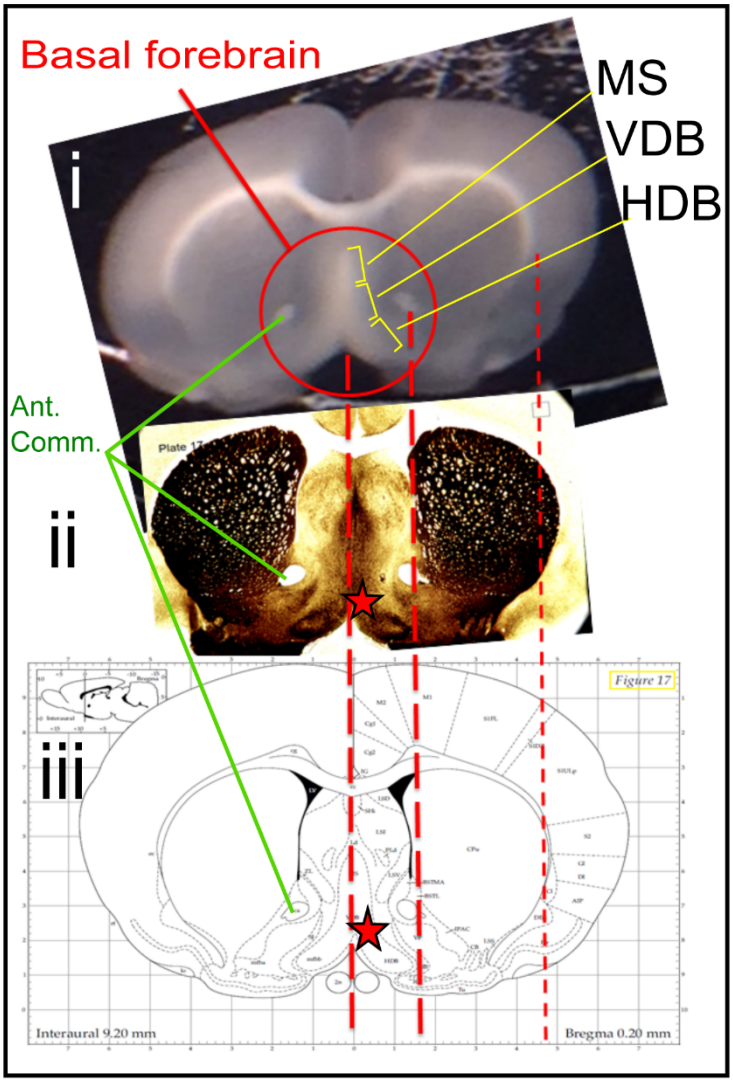

Figure 6: Identification of the basal forebrain's medial septal-diagonal band of Broca (MS-dBB) complex in coronal slices. This cluster of sub-cortical nuclei is composed of the MS, VDB and HDB, located on the ventro-medial edge of coronal slices through the basal forebrain. The MS-dBB was identified by a typical and noticeable difference in

the composition of neuronal tissue (**i**): appearing whiter than its surrounding in a conveniently obvious shape which fit that of the nuclei of interest. Comparison with anatomical pictograms and diagrams from (Paxinos and Watson, 1998) confirms the correct location of the slice, as per the presence of the anterior commissure ('ant. comm.') and general slice morphology. Figure adapted from (Badin et al., 2016).

Brains were then stuck onto a small metal stage using superglue, and placed within a Vibratome (Leica VT 1000S) illuminated using a CLS 100X light source (both from Leica Microsystems, Milton Keynes, UK): the stage containing the brain was placed on an ice bed within the Vibratome, and the stage itself filled with fresh ice-cold aCSF. Speed (when the brain is taken out of solution) as well as conscientiously keeping the brain at temperatures close to 0°C in solution, during the entire dissection and slicing procedure are key requirements for the harvesting healthy slices. In total, from the moment where the neck was dislocated until the moment the slicing began, the process never took more than 5 minutes. For coronal slices (AIC, S1BF, BF), the Vibratome blade speed was set at mark 6-7 while the frequency of blade vibration was set at mark 8-9. For thalamocortical slices, since the aim was to conserve as many of the delicate long-range connections linking two relatively distant parts of the slice, slower cutting parameters were used in order to reduce stress to the tissue, with blade speed down to mark 3-4 and frequency down to about mark 4-5. All slices were cut with thickness of 400 μm. Harvesting of slices took between 4 and 6 minutes for coronal slices, while slicing took between 8 and 10 minutes for thalamocortical slices.

2.5 VSD staining

Slices were left to recuperate for a minimum of 1 hour post-slicing before being prepared for staining with di-4-ANEPPS. Stock di-4-ANEPPS solutions were stored in a small box filled with desiccant stones at room temperature (21 ± 2°C). Sigma-

Aldrich sends the VSD in small pre-packaged dark-glass vials containing 5 mg of di-4-ANEPPS each. Upon making up the VSD stock solution, 3 mL of 7% v/v Cremophore EL in DMSO was added per 10 mg di-4-ANEPPS vial and vortexed thoroughly for up to 2 minutes, yielding a 6.93 mM di-4-ANEPPS stock solution; this was all carried out in a dimly-lit room where just enough light was available to conduct the manipulation. On the day of the experiment, and only about 5 minutes before staining, the final dye solution was made up by adding 80 μL of di-4-ANEPPS stock solution to 1.5 mL of 50% v/v oxygenated aCSF in fetal bovine serum (FBS): providing a final solution of 1.58 mL aCSF, Cremophore EL in DMSO containing a final di-4-ANEPPS concentration of 350 μM, before application.

After applying the dye solution to slices, they were placed inside a custom-made high-humidity chamber filled with aCSF (see **Figure 7A**) and bubbled with pressurised 95%O_2/5% CO_2 for 30 minutes (Badin et al., 2013; Hill & Greenfield; 2014). At the end of the 30-minute staining period, tweezers were used to drag the piece of filter paper (supporting all the stained slices) out of the staining solution, and into a beaker containing 70 mL of oxygenated aCSF for rinsing. Slices were then immediately transferred to the main bubbler pot (see **Figure 7C**), using a paint brush, for recuperation for at least 1 hour.

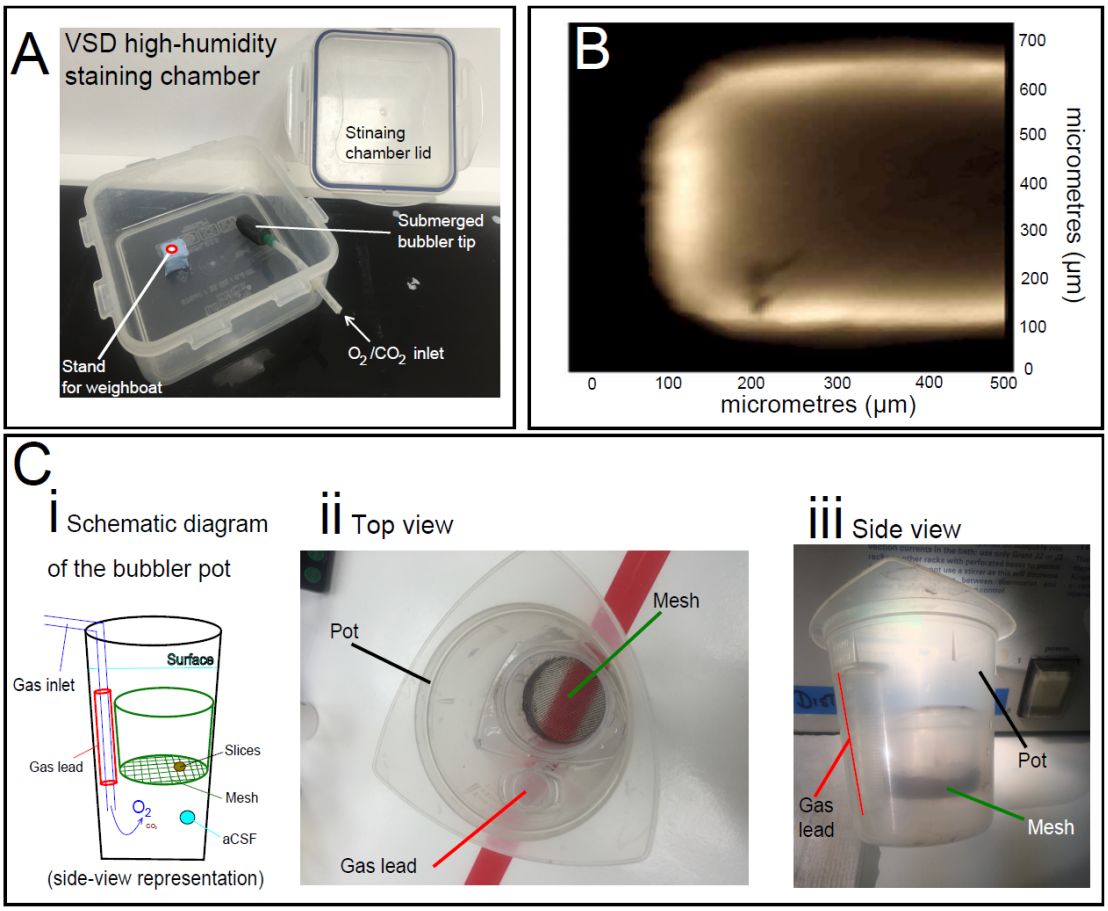

Figure 7: Staining and recuperation of brain slices with VSD di-4-ANEPPS. **A**. Picture of the VSD high-humidity staining chamber, which features a small blu-tack stage on which the slices-containing weigh-boat would be placed. aCSF would then be poured into the chamber such that the surface would rise up to a) the level of the top of the stage and b) a level where the bubbler tip would be totally submerged. Then, a Carbogen (95% O_2, 5% CO_2) lead would be connected to the O_2/CO_2 inlet and the lid would be firmly locked atop the chamber. Such an arrangement allowed for a high-humidity environment to be created within the chamber, where increased pressure would force oxygen into the dye solution (in the weigh-boat) to improve slice health over the staining period. **B**. Cross-section through a 600 µm brain slice showing the penetration of di-4-ANEPPS within the tissue. From this experiment (n=6), adapted from (Hill & Greenfield, 2014), it was concluded that the dye penetrates up to 100 µm into the tissue after a 30-minute staining period (white outline): the staining protocol used to stain the slice shown in **B** is identical to the one employed to stain slices used in experiments presented here. **C**. schematic representation (**i**) of the bubbler pot used to keep slices in oxygenated aCSF at room temperature. Actual pictures of the bubbler pot used in experiments presenting a top (**ii**) and side view (**iii**): the important principle here is that bubbling oxygen at the bottom of the bubbler pot (via the gas lead) creates a circular current which increases oxygenation of slices.

2.6 Neuroanatomical studies using DAPI

Following VSDI recording, frontal and sensory slices from the same rats were chosen for staining of neuronal cell bodies using DAPI, 4',6-diamidino-2-phenylindole (Invitrogen, Paisley, UK), and fixed with 4% Paraformaldehyde in PBS for a minimum of 30 minutes and then stored in aCSF until use. Slices were then stained in 1:1000 DAPI (4',6-diamidino-2-phenylindole, Invitrogen, Paisley, UK) for 5 minutes for identification of gross anatomical structures and cortical layers. Slices were then set in 4% agarose (Bioline, London, UK) and resectioned coronally to 70µm on a Leica VT1000S vibrating microtome. Images were acquired using a Leica DMR fluorescence microscope with DC500 camera and Leica Firecam software (Leica Microsystems, Milton Keynes, UK), and Zeiss LSM 710 confocal microscope (Carl Zeiss Microimaging, NY, USA). Images were analysed using Adobe Photoshop CS5 (Adobe Systems Inc., CA, USA).

2.7 Experiment preparation

2.7.1 Rig setup

In the setup used here, a Minipuls 3 peristaltic pump (Gilson U.K., Luton, Bedfordshire, UK) delivered artificial cerebrospinal fluid (aCSF) at a flow rate of 1.5 mL/min to the bath, well volume: 7–8 mL, located on a plastic stage. Once aCSF perfusion reached the stage, it first flowed through a stage heater which warmed the perfusate to 30 ± 1°C, a temperature which was monitored using a bath thermometer. Sample slices were submerged in the bath solution and placed atop a small piece of filter paper, to allow oxygen- and nutrient-rich aCSF to reach the tissue on the under-side of the slice, helping to maintain overall slice health for extended periods of

time. Electrodes (i.e. stimulating and recording LFP electrodes) and the CMOS camera were then positioned within and above the slice respectively, in a manner that favoured optimal data acquisition according to the intent of the experiment.

2.7.2 Stimulating electrode

For all experiments carried out in this study, neuronal assemblies were evoked using a bipolar, concentric tungsten micro-electrode (CBARC75, FHC, Bowdoin, USA) with impedance of 500 kΩ (measured at 1 kHz). The tip of the electrode consisted of a central pole (25 µm in diameter) made up of a platinum and iridium alloy, and inserted within a stainless steel tube providing the final diameter of the electrode tip at 125 µm, as can be seen, along with all other dimensions relevant to this electrode type, in **Figure 8** below. At the end of each day's experimentation, stimulating electrodes were carefully removed and rinsed in dH_2O. In the present thesis, electrodes were placed, with the help of a white light stereoscope (4.5x magnification, Micro Instruments Ltd, Oxford, England) and manual micro-manipulators (Marzhauser Wetzlar, Wetzlar, Germany), just a few micrometres (10-30 µm) into slice neuronal tissue.

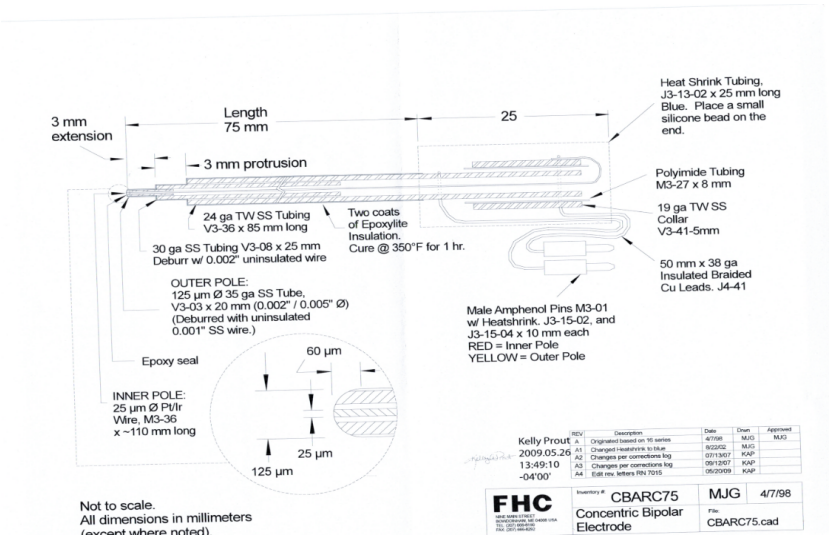

Figure 8: Specific parameters of the stimulating electrode, from FHC (CBARC75, FHC, Bowdoin, USA).

2.7.3 Electrophysiology

After placement of the electrodes and camera, a few quick stimulations were carried out in order to ensure the slice was healthy and functional. If a good enough response was evoked in the area of interest, the slice was left in complete darkness for a minimum of 30 minutes to acclimate to the bath perfusion.

a. Pulling of electrode micropipettes

Recording LFP electrodes were pulled from borosilicate glass capillaries (model: GC120F-10, standard wall with inner filament; Clark Electromedical Instruments, Pangbourne, Reading, England) using a flaming/brown micropipette puller (model: P-87; Sutter Instrument Co., Novato, California, United States) with the following pull settings: **Heat** = 402, **Pull** = blank, **Velocity** = 30, **Time** = 150. For every new batch of pulled micropipettes, a minimum of 4 capillaries were pulled first before collecting any micropipettes to be used subsequently for LFP experiments in order to offset the fact the P-87 puller seemed to require a few cycles before it could reliably pull micropipettes with adequate tip hole-diameter and taper length.

b. Local field potential recording setup

Working back from the sample slice to the acquisition software, glass electrode micropipettes were filled with an internal solution containing 1 M NaCl with 2% w/v Pontamine sky blue 5BX (BDH Chemicals Ltd., Poole, England). Once filled, a small (approx. 100 μm in diameter) AgCl filament was inserted into the lumen of the glass micropipette and placed on a manual micro-manipulator, the same type that were used to manipulate stimulating electrodes (see above). The AgCl wire was

connected to small electric cables connected to the head-stage amplifier (Cygnus Technology, Delaware Water Gap, United States). The head-stage also received a baseline signal from another (reference) bath Ag/Cl electrode for resolution of LFP deflections; this signal was then pre-amplified and relayed to a larger Neuro Data IR-283 amplifier (10x amplification; Cygnus Technology, Delaware Water Gap, United States). Finally, the signal was amplified once more in a custom-built amplifier (100x amplification; Martin Preston, Department of Pharmacology, University of Oxford, England) which also performed low-pass filtering with AC/DC input coupling, making this a three-step amplification process (totalling a x1000 amplification of original signal) with low-pass filtering at 1000 Hz for final amplified signal. It is this signal which was then transferred to the Micro 1401 mkII AD/DA converter (Cambridge Electronics Design, Cambridge, England) for digitisation.

c. Local field potential acquisition software

Signal electrophysiology software (Cambridge Electronic Design, Cambridge, UK) was used to acquire all LFP data reported here. Data were acquired at a sampling rate of 16 kHz over 800 ms-long recording frames with a 600 ms pre-stimulus baseline (see **Figure 9B**). One of the most helpful features of Signal software is the ability to quickly create stimulation protocols using a graphical pulse generator, providing a visual representation of the stimulation protocol. In the experiments presented here, electrophysiology was constantly running data acquisition loops: that is, as soon as the stability testing started (see below in **Section 2.7.4.d**), stimulations would be constantly delivered (and recorded onto disk) until the end of the experiment – this is in contrast to VSDI which only recorded data for specific periods of time within the experiment (see 'Combining electrophysiology and VSDI', **Section 2.7.4.d** below).

Signal software was used to synchronise the delivery of the stimulation with BrinVision Analyzer, i.e. with VSDI data acquisition. This synchronisation included: i) start of LFP recording (Signal software), ii) opening of the light shutter, iii) start of VSDI recording (BrainVision Analyzer), iv) trigger stimulation (Signal software), v) terminating the recording epochs in both Signal software and BrainVision Analyzer and finally vi) closing the light shutter; see **Figure 9B**. At the end of each experiment, all recorded frames were exported from Signal software to a single Notepad file containing all frames in terms of time vs mV data for offline analysis.

2.7.4 VSD Imaging

a. Imaging setup

As previously stated, the imaging setup used throughout this thesis, the MiCam Ultima, was purchased from BrainVision Inc. (Tokyo, Japan), it utilises a high-speed CMOS sensor based-camera mounted upon the optics setup (see point **b** below) fixed on a revolving arm located within the rig. CMOS sensors transform incoming photons (light) reflected from the slice into electrons (electrical signal) which are directly fed into the MiCam Ultima processor and AD converter. This method provides data with 14-bit resolution and is increased to 16-bit after digital processing. Its CMOS sensor is 10x10 mm in dimensions composed of a 100x100-pixel array, well-depth 10 000 000 *e*, and actual quantum efficiency of 63% at 550 nm wavelength while this efficiency remains at 45% at 700 nm. The dark noise for this camera is 80 *e* for its 100x100-pixel array measured with 1 ms exposure time. This MiCam Ultima system features a maximum spatial resolution, as used in this thesis, down to 40x40 μm (pixel size) and a maximal temporal resolution of down to 0.1 ms per frame; yet despite this very high temporal sampling resolution, that

which was used in the experiments presented in this thesis was set at 1 ms per frame (1 kHz frame rate acquisition).

b. Optics

The optics used here for all experiments consisted of an up-right arrangement of lenses within a metal tube, with the camera placed at the top, looking down onto the sample in the stage bath (**Figure 4B**). Within the vertical tube, two lenses were placed in succession: the first was a x1.6 magnification lens (reversed, therefore magnification is x0.625) followed by a x2.0 magnification lens at the bottom extremity of the optical setup, see **Figure 4C**. This arrangement produced a final magnification of x1.25 yielding a final pixel size of 40x40 μm. The setup was equipped with an excitation band pass filter focused at 530 ± 5 nm and an emission high-pass filter isolating light with wavelength >590 nm. Between the two lenses, a dichroic mirror was positioned in a way to reflect generated light down onto sample (reflecting >90% of wavelengths $520<\lambda<560$ nm), while filtering the light bouncing back from the sample into the optics >590 nm (with >85% of light passing through at 600 nm).

c. Acquisition software

Data was acquired with BrainVision Analyzer, a software provided with the MiCam Ultima and featuring a user-friendly interface which allows for easy data acquisition and coarse-grain, fast analysis of acquired data (filtering and data visualisation). In setting up experiments, BrainVision Analyzer offered a method of user input which relies on loading setup files into its sequencer: the setup files contain information about the imaging system and sampling protocol (such as for example: frame rate, pixel size, duration of stimulation and camera type), and were executed by

BrainVision Analyzer upon trigger from Signal software (see **Figure 9B**). When this trigger was received, BrainVision Analyzer sent a signal directly to a shutter-control box (Model SSC-1, BrainVision Inc., Tokyo, Japan) responsible for triggering the opening of the shutter inside the HL-151 light source (Moritex Corp., Saitama, Japan). The data was quickly visualised with BrainVision Analyzer in order to get a preview of the evoked response (see **Section 2.8.3**), however once the experiment started, the data was stored onto disk for off-line analysis. Both MatLab (Mathworks, Cambridge, UK) and Mathematica (Wolfram, Illinois, United States) were used for this off-line analysis, as the versatility of these programs and the possibilities they offer in terms of data analysis and calculations far exceed the capabilities of BrainVision Analyzer.

d. Data export

BrainVision Analyzer stored every single recorded VSDI frame individually in the form of multiple raw data files, which were subsequently exported to MatLab for off-line analysis: see **Figure 11** for full methodology disclosure of the MatLab '*vsdi*' script processing.

2.7.5 Stimulation protocols

Upon starting a recording (see method of electrode placement within slice above in **Section 2.6.2**), a simple sequence of protocols we observed:

a. Confirmation responses could be robustly evoked (slice health)

Script: '***Initial monitoring***' – 5 repeats of a single stimulations with 8 second ISI. These very short test trials were designed only to confirm slices were healthy and featured sufficiently large responses. In order to do so, and because these trials were very short by nature, both electrophysiology and VSDI were performed simultaneously, keeping moments of illumination to a minimum.

b. Confirmation of slice stability

Script: '***Stability testing***' – 10 minutes during which single shock stimulations (0.1 ms in duration) with 15 seconds ISI (i.e. producing 40 frames in total); these tests were only performed using electrophysiology as it provided a sufficient measure of slice stability, preventing any unnecessary slice illumination. Signal software was used to measure the maximum deflection amplitude of the LFP data for every frame, and instantly plotted this as a function of frame number in a separate window to yield a trend graph of maximum amplitude over frames (i.e. time). Using this 10-minute data graph, a quick calculation was performed to assess whether maximum deflection amplitude from the last 10 recorded frames (averaged together) varied by more than 15% from the average amplitude from the first 10 frames of the record. In the (few) cases where more than a 15% fluctuation was found compared to initial responses, the stability test was run a second time – at the end of this second stability run, if the response was found to fluctuate once again by more than 15%, the slice was disposed of and replaced with another one, otherwise, the experiment was initiated.

c. Stimulation used for experiments data sampling

Script: '***Experimental stimulation***' – 15 minute during which single shock stimulations with 30 seconds ISI (i.e. producing 30 frames in total). Experimental stimulations were performed with both electrophysiology and VSDI.

d. Combining electrophysiology and VSDI

Electrophysiology LFP records, as previously stated, were initiated at the beginning of each experiment recording epoch (first data frame of baseline condition), continuously delivering stimulations, as well as triggering BrainVision Analyzer (when the sequencer was manually engaged), every 30 seconds. This provided a full record of LFP throughout the experiment: during VSDI recording epochs (baseline, drug condition/epoch 1, drug condition/epoch 2 etc… washout) as well as during the perfusion non-recording periods (between recording epochs) and where no imaging data was therefore recorded (see **Figure 9B**).

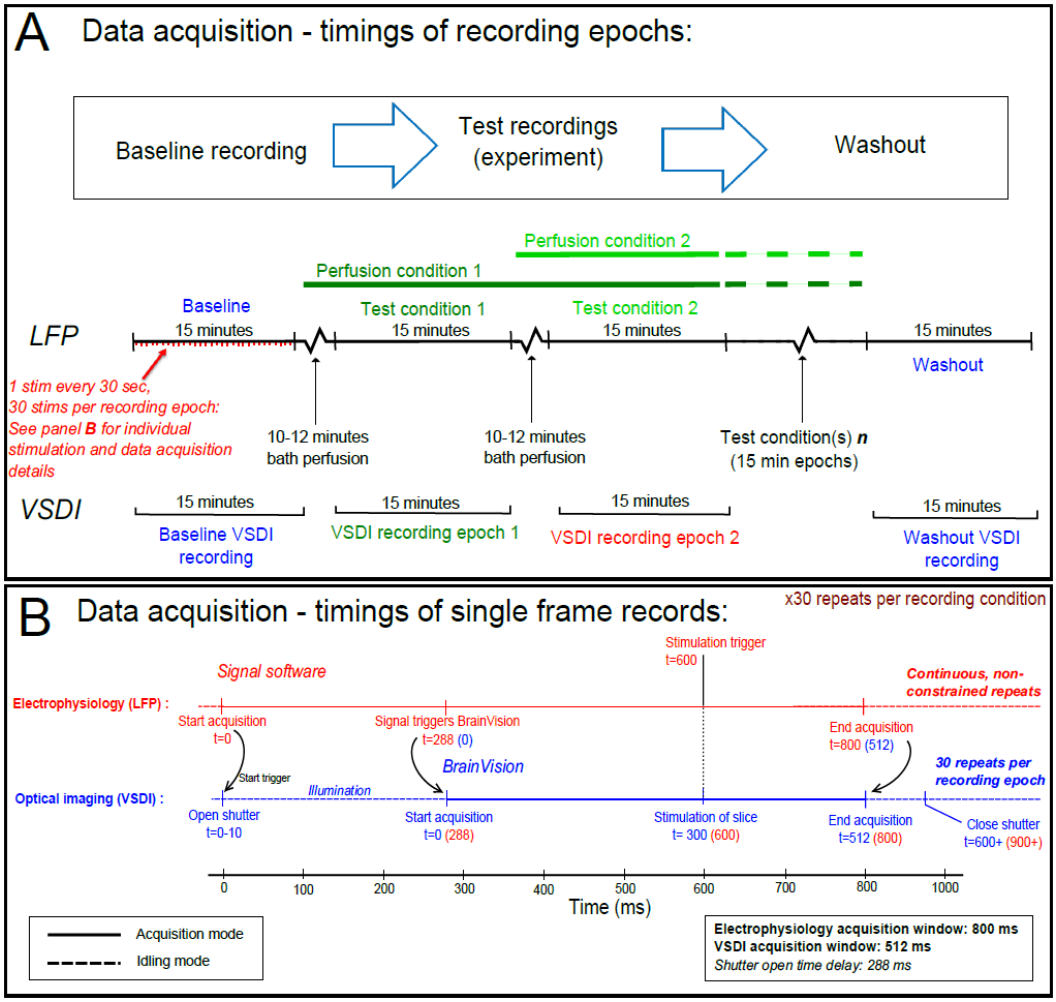

Figure 9: Perfusion and data acquisition protocols and timings. **A**. Synchronisation of recording epochs between VSDI and LFP: having performed a successful stability test, data acquisition would begin with a 15-minute recording epoch (baseline recording) – at the same

moment, LFP and VSDI recordings were triggered, in time with stimulations, however whereas LFP records indefinitely take place, every 30 seconds, VSDI recordings (including illumination) are halted after 30 stimulations. This marks the end of the baseline recording, and if performing an experiment using a drug, it would start to be perfused at this moment (green bar). The next recording epoch would be triggered with VSDI and synchronised to LFP ('Test condition 1'), just as the 'Baseline' condition was triggered. This process was iterated for as many recording epochs were necessary for the experiment at hand. As such, VSDI recordings produced discrete data, grouped into files relating to 15-minute-long epochs of data acquisition whereas LFP recording produced a single continuous file with 30 second ISI. **B**. Synchronisation of single frame records: for each stimulation, both Signal software (for LFP) and BrainVision Analyzer (for VSDI) started acquiring data several hundred milliseconds before stimulus delivery. This was done to establish a robust baseline with both software, as well as in the case of VSDI, providing enough time for the shutter to open (0-10 ms) without introducing vibrational noise in the recording. At the end of the total 800 ms, both software would go back into idling mode until the next single frame record.

At the end of this baseline condition, the perfusate was switched from aCSF to aCSF containing a soluble substance of interest (drug, or nothing if experiments were meant as control runs) and left to perfuse at four times the normal perfusion rate (i.e. 6 mL/min) for 10-12 minutes, allowing for the new perfusion to gather in the bath and replace the drug-free aCSF (see **Figure 9A**). A 'soaking' step was also undertaken as soon as the new perfusate reached the bath, whereby a small piece of tissue paper was gently introduced in the bath solution, away from the slice and electrodes in order to guarantee their immobility, such that approximately half of the bath solution was immediately soaked up into the tissue paper. This was then quickly replaced by the new, incoming perfusate over the following 10 minutes. This process was aided by the mixing induced by the bath air-inlet and rapid perfusion rate. At the end of this 10-12 minutes perfusion period, the pump speed was turned back down to 1.5 mL/min before triggering BrainVision Analyzer to start the next recording epoch.

2.8 Analysis and presentation of data

2.8.1 Calculation and presentation of LFP data

The absolute value of maximum deflection amplitudes from zero were calculated from LFP data, see **Figure 10**. Every 4 recorded deflections were averaged together to provide a single value, which were then plotted on trend graphs of *'Mean response amplitude (mV)'* against '*Frames*' in order to highlight drug effects over a period of continuous sampling (**Figure 10B**).

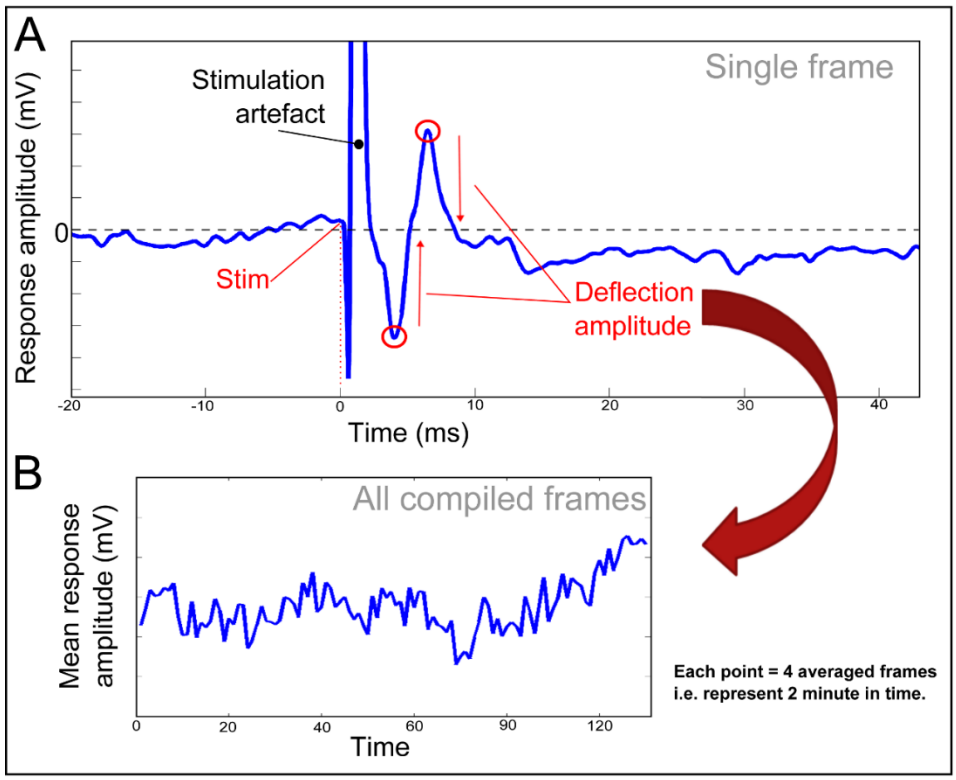

Figure 10: acquisition and presentation of LFP data. **A**. Example of general LFP record time series showing the pre-stimulus baseline (-20 to 0 ms), the moment of stimulation (0.1 ms electric pulse), the resulting stimulus artefact and evoked population activity. For each recorded frame, the largest deflection within 10 ms following the stimulation artefact was selected (either positive or negative) and the absolute value of the maximum amplitude of the deflection (mV) was recorded. **B**. Trend graph of average deflection amplitudes (each point = average of 4 deflections as seen in **A**) over time (frames).

2.8.2 Method for analysis of 3-dimensional VSDI data

A recent publication (Bourgeois et al., 2014) has provided a solution to the apparent problem of analysis variability arising from the use of custom-made analysis methods using a range of mathematical software. In this paper, the authors demonstrate the capabilities of a data handling and analysis toolbox designed to process any type of VSDI data, i.e. regardless of dye or imaging system employed, in a systematic fashion. Central to the purpose of such analytical software, is the convenient functionality of transforming any kind of three-dimensional data set, say for a VSDI 'movie' composed of i) fluorescence activity within ii) a background image (i.e. neuronal tissue) over iii) time, into a two-dimensional array, in a process known as rasterisation (Gharachorloo and Gupta, 1989); thereby concentrating much of the crucial information on a single and more accessible 2-dimensional figure of emitted fluorescence (see **Figure 13**).

In the present thesis, the VSDI toolbox was utilised for rasterisation and visualisation of VSDI movies to produce images of biologically-relevant fluorescence activity over space and time – a type of graphical representation termed throughout this thesis as 'space-time map' of fluorescence (see **Figure 13**).

2.8.3 Processing of BrainVision files into average files

A custom-made Matlab script, when called in MatLab, prompted a dialogue box demanding for the specific increments of analysis parameters (see **Figure 11B**). Once all were entered, Matlab ran fast loops of code which converted all BrainVision raw data files into recording-epoch average files (see **Figure 11** legend for details); these files were subsequently used for epoch-specific analysis of data. During this processing step, a spatial filter (Savitzky-Golay smoothing method) was applied to the data as well as a high-pass filter (using a zero-phase filtering method).

Zero-phase method filters the data in the forward direction before reversing the filtered data and running it back through the filter (Oppenheim and Schafer, 1975), and importantly, this method adequately reduces noise within acquired data, all the while retaining the salient features in exactly the same conformation as these features appear in unfiltered data (Gustafsson, 1996).

This represented the 'First processing stage' (**Figure 11**), where the resulting data was presented in the analysis summary plots automatically generated at the end of the script (see left and right bottom graphs in subplots – **Figure 11Cii**). The last line of the script instructed MatLab to save these average files within the experiment data folder for further processing.

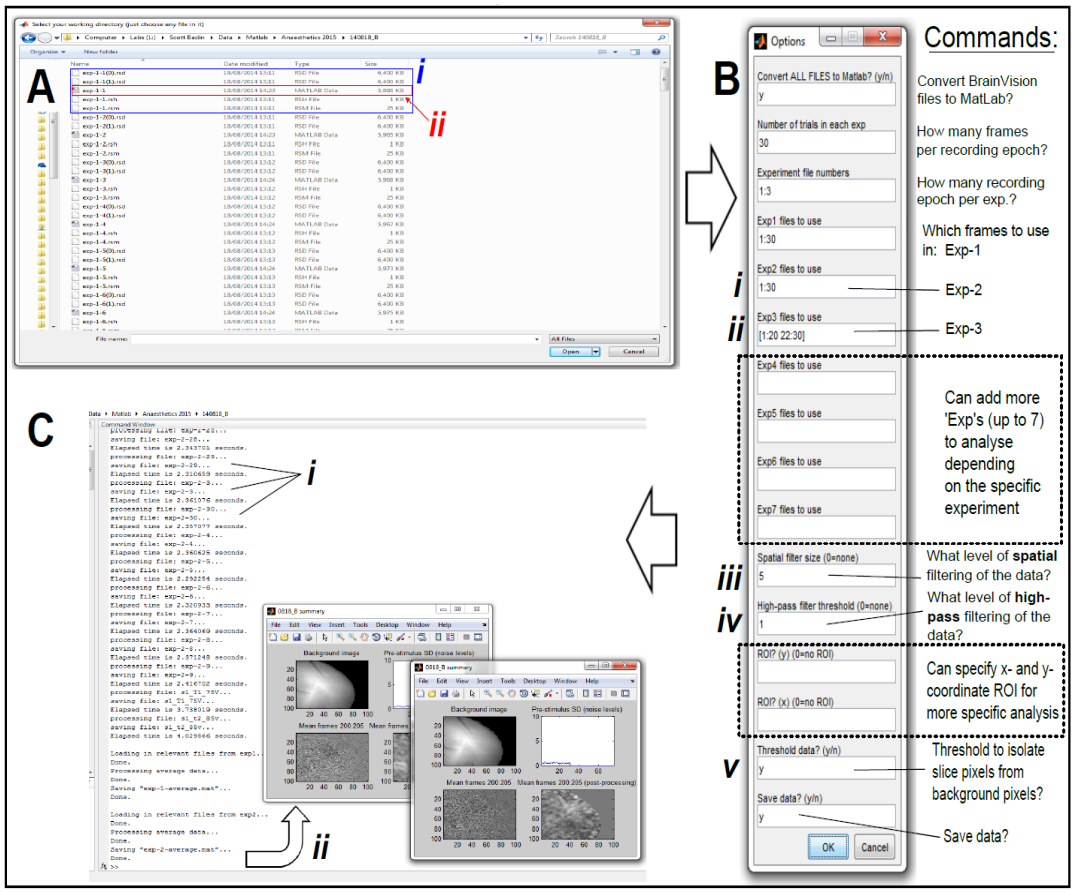

Figure 11: Illustration of the conversion (**A**), processing and filtering (**B**) and averaging (**C**) of raw VSDI data using '*vsdi*' script: **A**. BrainVision raw data files in the format 'exp_(recording epoch #)_(data frame #).extension', and for each data frame produces 4 raw data files (**i**) in 3 different formats: '_.rsd' (2 files), '_.rsm' (1 file), and '_.rsh' (1 file). **B**. Once the directory was chosen (in **A**) MatLab opened a dialogue box, here showing the

specific parameters used for analysing VSDI data: options **iii** and **iv** show where the 'First processing stage' takes place with application of spatial (**iii**) and high-pass filters (**iv**) was required, with increments 5, and 1 respectively. Note: spatial filtering increments could only be an odd number, therefore '5' represents only the third increment from 0 (no spatial filtering). The coordinates of a square ROI were also demanded, however this did not represent an essential input element (could be left blank) and was only used for selection of fast, off-hand analysis of specific square ROI's: as shown in the time-series graphs in **Figure 12** below. **C**. MatLab commands show the workings of the conversion loop, turning 4 raw data files into a single MatLab file (**i**) at the end of which, once all data frames from all recording epochs within the experiment had been converted, all MatLab data frames files from a same recording epoch were averaged together (**ii**) and summary graphs of each averaged recording epoch data were generated showing: a bright-field image of the slice (*top-right of subplot figure*), a graphical representation of the pre-stimulus standard deviation of the signal (*top-left of subplot figure*), which served as a measure of noise per data frame (which could be used to remove noisy frames). The subplot figure also included an average of the first 6 raw data frames (i.e. ms) after stimulus delivery (*bottom-left*) as well as that same averaged data shown post-processing (*bottom-right*).

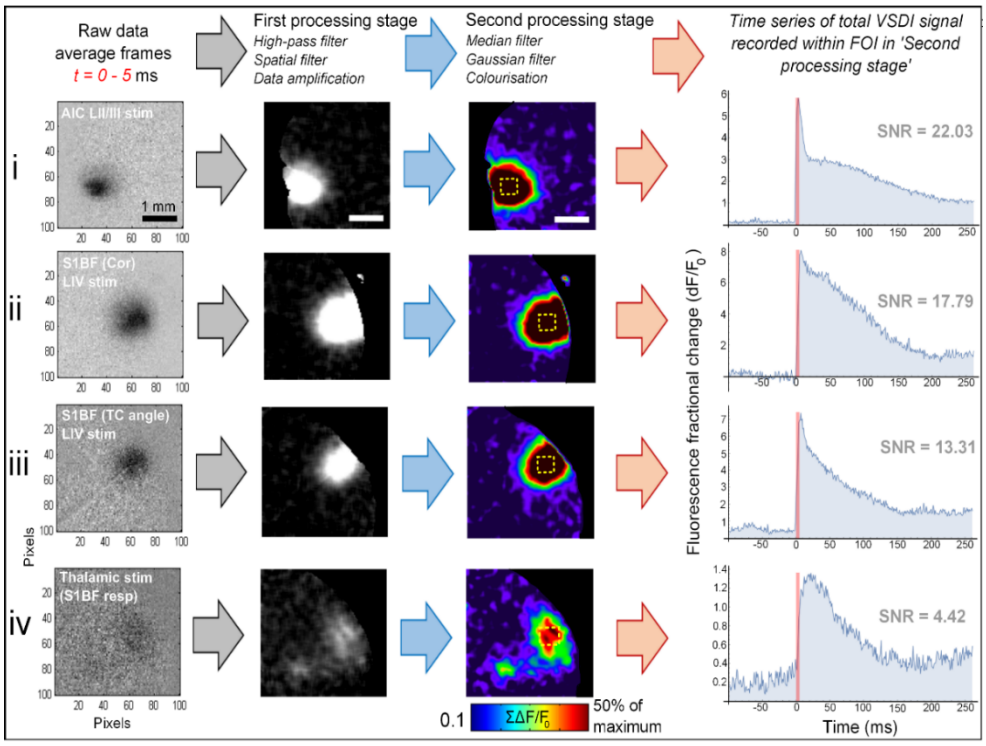

Figure 12: Quick-hand characterisation of data. '*vsdi*' produced the black and white images shown in the left column; using Mathematica, both a high-pass and spatial filter were applied to the data and produced clear maps of activity, which were then amplified using '*vsdi*' script

('First processing stage'; middle column). For image visualisation only, this data could be filtered further (median and Gaussian filter) to smooth the signal before colourisation ('Second processing stage'; right column). This data could be used to generate FOI-specific (field of view) time-series of fluorescence (yellow dotted squares in right columns): this analysis provided robust time-series yet leaving out a lot of the rest of the response. Processing stages are shown here for assemblies generated in AIC Layer II/III (**i**), S1BF Layer IV (**ii**), S1BF thalamocortical slice angle Layer IV (**iii**) and thalamocortical activation of S1BF (**iv**). For each example data, averaged still-frames and time-series display averages of the first five milliseconds (frames) after stimulus delivery over an entire experiment (30 recording frames), i.e. the average signal extracted from the time-frame equivalent to the vertical red bar in the time-series (right). Simply for visualisation purposes in this example, threshold for max intensity on the heat-map scale was set at 50% of the actual max of the response, in order to highlight the full reach of assemblies evoked in each experimental paradigm. Note: within this time frame, thalamocortical activation shows only minor activation due to the lag of remote activation.

As shown in **Figure 12**, epoch-specific average files generated by the script could be visualised as images presenting arrays of 100x100 pixels of recorded fluorescence (left column). This data needed to be clarified further however, using first a high-pass and spatial filter (first processing stage) and then a median and Gaussian filter (second processing stage); these steps were undertaken using Mathematica for the creation of still-frame images only, the main purpose of which was to help visualise and thus characterise evoked assemblies.

2.8.4 Rasterisation of averaged epoch-data files using a pre-drawn geometry

a. Generation of space-time maps

For a more rigorous analysis of the data, one that would allow for a systematic method of analysis, constrained within ROIs, and comparable across experiments, the data was rasterised into space-time matrices (Bourgeois et al., 2014), as shown

in **Figure 13** below. First, specific slice ROI geometries could be drawn and applied to each average epoch-specific data file (**Figure 13A**). Once drawn, the whole ROI was divided into segments with mid-length width constrained at 0.12 mm (for cortical tangential geometries) and 0.08 mm (for radial geometries, see **Chapter 3**) in width at their centre. Each of these segments then became mini-ROIs, from which the respective fluorescence activity over the recording time-window was averaged and organised in a matrix of fluorescence per segment over time.

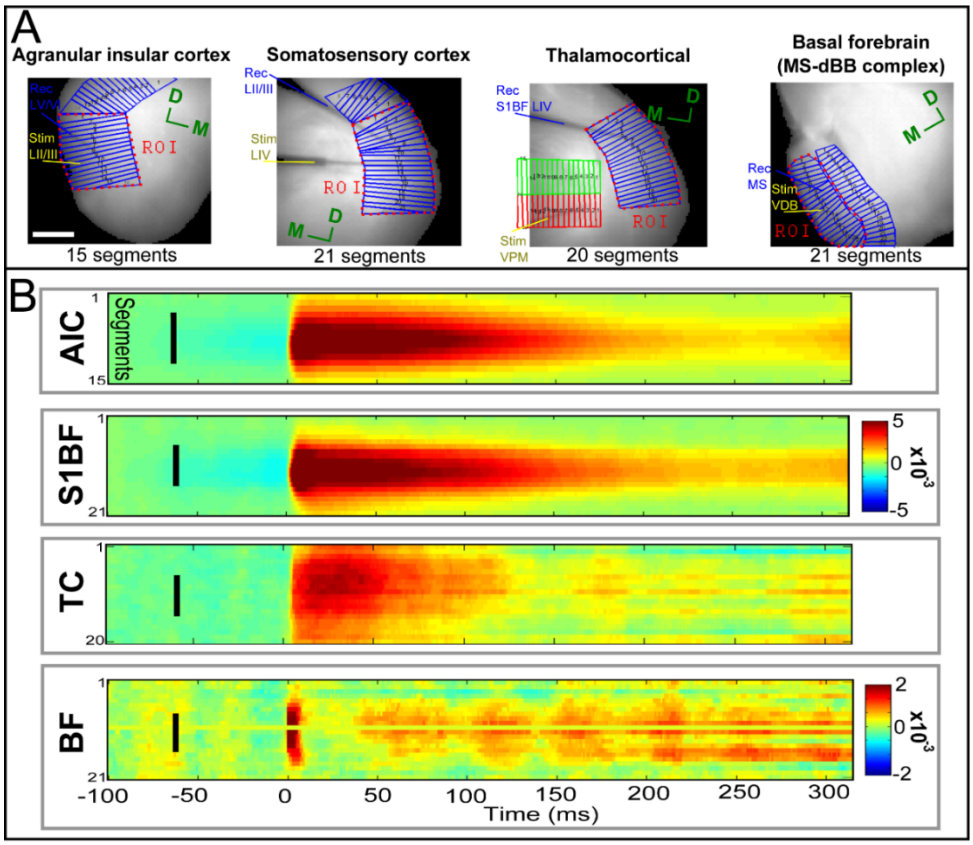

Figure 13: Presentation of ROI geometries and methodology of rasterisation. Example data extracted from a full recording epoch of assemblies evoked in each of agranular insular cortex (AIC, LII/III stimulation), somatosensory barrel field cortex via direct (S1BF, LIV stimulation) and remote (thalamocortical, TC, thalamic stimulation of the ventroposterior medial, VPM, nucleus) activation and basal forebrain (BF, vertical limb of diagonal band, VDB, stimulation), with a 0.1 ms 30 V electrical shock to tangential regions of interest (blue segments), except for TC slices, where thalamocortically-activated assemblies were triggered using a 60 V pulse of the same duration. Each data file was analysed using the functionalities of the VSDI toolbox (Bourgeois et al., 2014), whereby a geometry of a fixed ROI was drawn over the slice (dotted red areas, **A**). This fixed ROI was then divided into segments of equal area (with fixed mid-length width of 120 µm, blue regions, **A**) from which

data was collected over the entire recording window. Each segment's data was then pooled and displayed as a heat-map of fluorescence over space (y-axis: segments, i.e. space) and time (x-axis, ms, stimulation delivered at t=o ms), as displayed here (space-time maps, **B**). Fluorescence scale bar shown in S1BF box, right. Black vertical scale bars in space-time maps all represent 1 mm in length. Coordinates in **A**: D = dorsal, M = medial.

This data was then filtered using a single medial spatial filter (MSF, **Figure 14**). The MSF was attempted at three different increasing increments: 0 (none), 2 and 3. Data presented with no MSF is intended to demonstrate the need for this final step in spatial filtering (**Figure 14B1**), at increment 1 (data not shown), the space-time maps did not show sufficient improvement in data smoothing, however at increments 2 and 3, the space-time maps showed very clear active versus inactive areas. Since the goal here was to produce clearly discernible maps of activity over space and time, as well as this being the only further filtering step (after those applied during the data processing script), the higher increment (3) was chosen as the filtering level for all experiments included in this thesis, as it produced very clear data with little loss of detail.

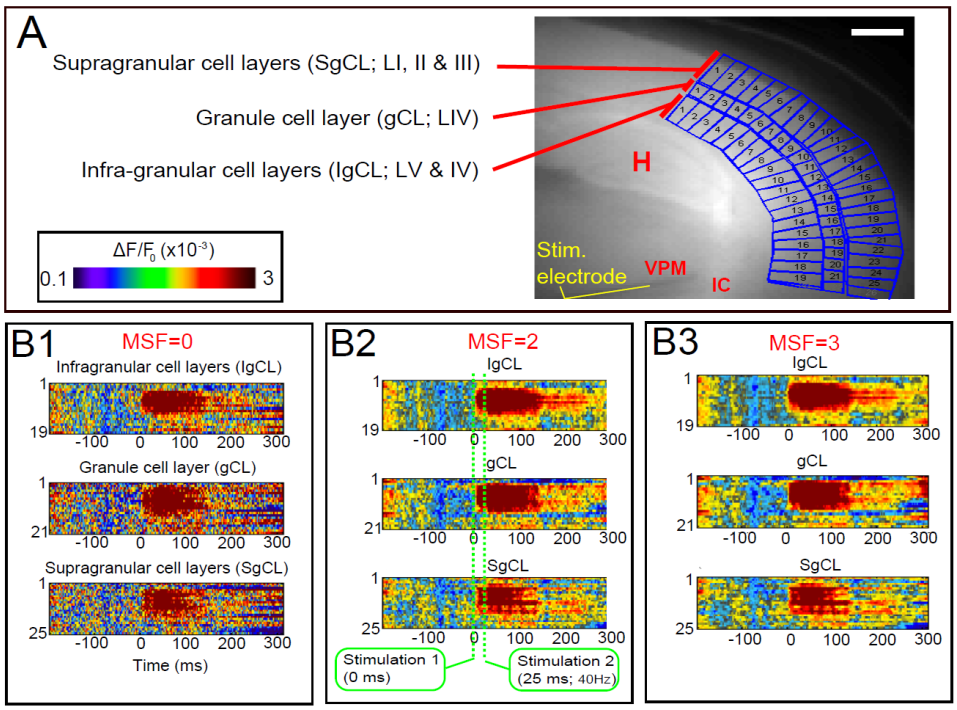

Figure 14: Final filtering stage using the VSDI toolbox. Example experiment (single 15 minute recording epoch, 30 repeat stimulations: paired-pulses at 40 Hz, each pulse 0.1 ms in duration at 60 Volts delivered to the VPM) showing the rasterised visualisation of data processed using '*vsdi*' script (also shown as still frames in **Figure 12**, left column). **A**. shows a large bright-field view of the thalamocortical slice, with the location of the stimulating electrode in the VPM, as well as the custom-made layer-specific geometry focusing on LI & II/III (supragranular cell layers, SgCL), LIV (granule cell layer, gCL) and LV/VI (infragranular cell layer, IgCL). Paired-pulses delivered to the VPM produced wide depolarisation within the cortex, with the greatest amount of fluorescence being emitted from deep layers (infragranular cell layers, IgCL), and the least from superficial layers (supragranular cell layers, SgCL). IC – internal capsule; H – hippocampus; white scale bar: 500 μm. **B**. Visualisation of the data with increasing increment of median spatial filter (MSF), blue areas: no depolarisation, red areas: depolarisation, heat-map colour bar in panel **A**. **B1**. No MSF was applied, producing a very grainy and unclear data representation (colourised representation of data shown in **Figure 12**, left column). **B2**. MSF applied at increment 2, shows a clearer response discrimination from background. **B3**. MSF applied at increment 3, shows an even clearer image of the evoked response compared to background, and where it becomes increasingly obvious that the largest fluorescence reading was recorded in the deep layers, with the weakest signal, relatively, recorded from superficial layers. For the rest of this thesis, MSF at increment 3 was used for raster data visualisation and presentation.

b. Normalisation of space-time map data

Space-time maps were presented either as 'real' (**Figure 15A** below) or as normalised values (see **Figure 15B**), as previously performed for such data (Jin and Collins, 2007), depending on the intent of the presentation. For normalisation of space time maps, the 'real', or 'absolute', maximum within the overall measured fluorescence from that recording epoch was isolated from its final raster file following which all other values within the matrix data file (i.e. the epoch-average space-time map) were divided by this max amplitude value, producing a space-time map with all values normalised to their absolute maximum, see **Figure 15B** below.

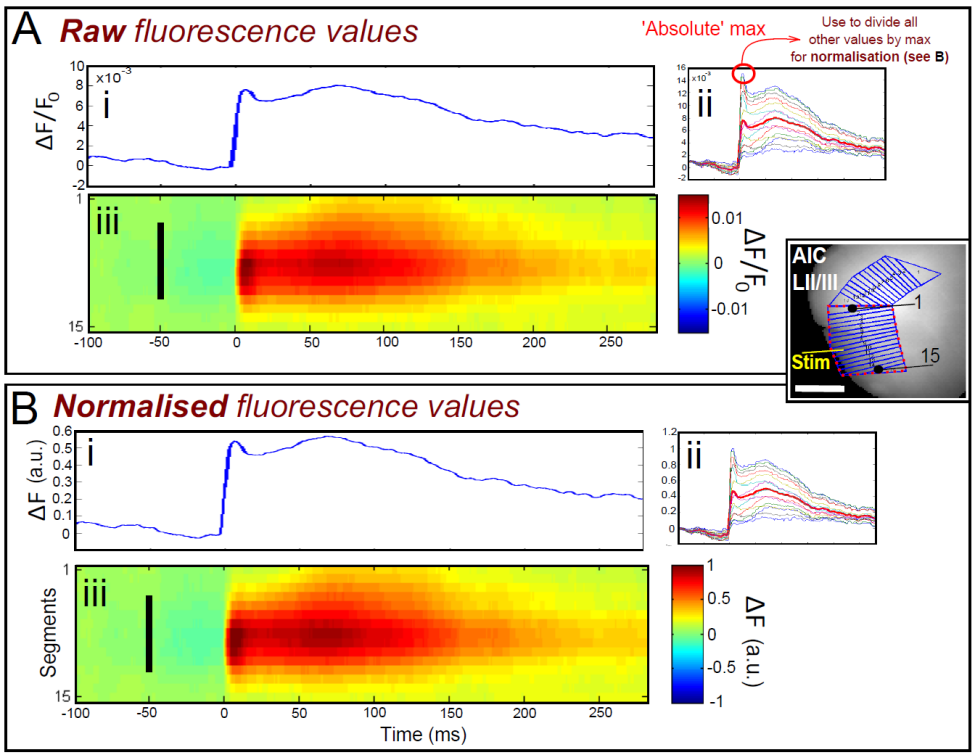

Figure 15: Example data from a single trial showing normalisation of space-time matrix. Stimulation in LII/III of agranular insular cortex (AIC) generated rasterised, 3-dimensional matrices of fluorescence data, i.e. over space and time **A**, from which the absolute maximum fluorescence reading could be extracted ('Absolute' max, inset time-series graph of individual segment data **A**) and used to normalise ever other fluorescence (**B**); black vertical scale bar on space-time maps represents 1 mm in space. Inset shows a bright-field view of the coronal slice containing AIC, the shape of the geometry ROI (dotted red square) used to analyse this specific stimulation paradigm (0.1 ms, 30 V shock), and the arrangement of the segments (blue rectangles). Colour bar represents fluorescence readings, while the (white) scale bar (in slice geometry view, inset) measures 1 mm.

c. Isolation of active pixels from space-time map data

Using either the original space-time map data produced by the VSDI toolbox or its normalised equivalent, a threshold was applied to the data matrix whereby any data point exhibiting fluorescence values less than 20% of the 'peak' maximum fluorescence data point recorded within its respective space-time map had their value converted to 0, while all those above this threshold (active pixels) were

converted to 1, producing a binary matrix data set of active or inactive pixels. Data values of active pixels were then replaced in the binary matrix, producing space-time maps of active pixels over 20% of max response (**Figure 16**, middle space-time map row). This method of applying a minimal threshold for detection and isolation of active pixels clarified the data by removing any background or unspecific activity, and allowed for a much clearer discrimination of evoked responses; such an approach has in fact already been utilised in previous VSDI investigations (Devonshire et al., 2010b).

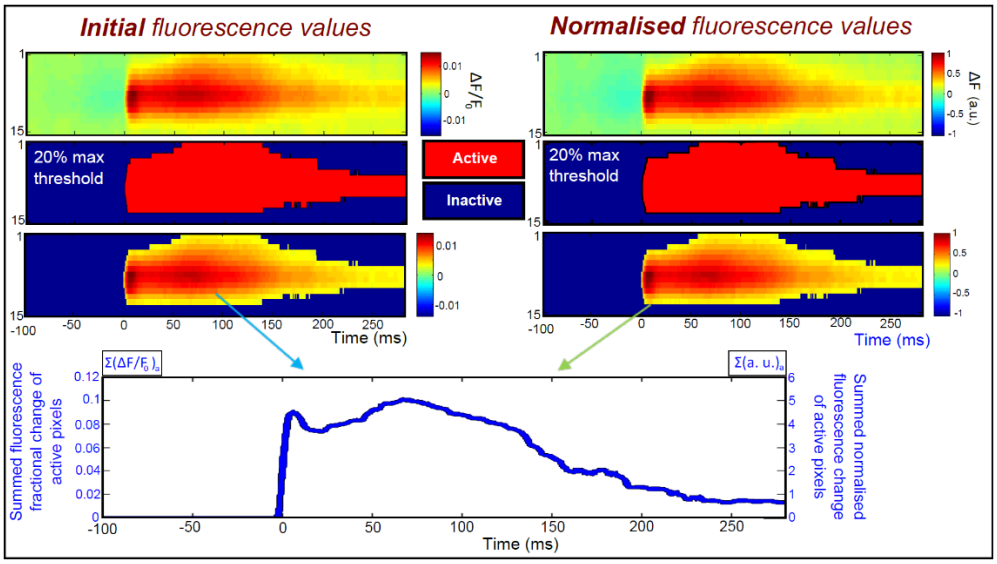

Figure 16: Demonstration of the isolation of active pixels within space-time data sets. With both raw and normalised values, a threshold could be applied which isolated all pixels exhibiting 20% or more of the fluorescence emitted from the absolute maximum amplitude within the data set (middle row). All inactive pixels (below the threshold) had their value turned to 0. When re-colourised (bottom row), the crucial evoked assembly profile of active pixels becomes evident. Finally, in order to quantify the signal originating only from the evoked response (the measurement of interest), the summed fluorescence of active pixels only ($\Sigma(\Delta F/F_0)_a$ for fluorescence values or $\Sigma(a.u.)_a$ for normalised values) was calculated, yielding the time series of activity shown at the bottom of the figure. Both in the case of raw and normalised data, and once adjusted for axes values, both time-series showed the exact same profile, as can also be seen from their respective space-time map profiles.

d. Acquisition of measureable parameters from rasterised epoch-data files for signal quantification and graphical representation

- *Generation of time-series of fluorescence over time (data units: $\Delta F/F_0/ms$)*

Time series were drawn by graphing the average fluorescence over time. This was done in three ways: first, the conventional method of graphing fluorescence time-series, whereby all emitted fluorescence is averaged and graphed indiscriminately. Second, time-series of active pixels only, whereby a threshold was applied to the data (isolating pixels showing fluorescence readings greater than 20% of the peak fluorescence recorded, **Figure 17A**). Finally, active pixels could be normalised to the previously-mentioned peak amplitude, to produce space-time maps of normalised fluorescence of active pixels (see **Figure 16**).

- Quantification of active-pixel-specific summed fluorescence data (units: $(\Sigma\Delta F/F_0)_a$) and quantification of layer-specific origin of signal (% fluorescence emitted from specific locations within ROI)

The summed fluorescence was calculated by summing the average amount of fluorescence emitted from active pixels (i.e. those above 20% of the peak fluorescence recorded) per millisecond (**Figure 17D**).

- *Quantification of tangential (lateral) spread of assemblies (units: mm)*

Lateral spread was estimated by measuring the largest tangential distance between active pixels (>20% of maximum response) within the ROI (**Figure 17C**).

- *Quantification of any time-course of active pixels (units: ms)*

The time-course of activity was estimated by calculating the time-point at which the time-series activity profiles of individual assemblies crossed the 20% of max threshold (**Figure 17B**).

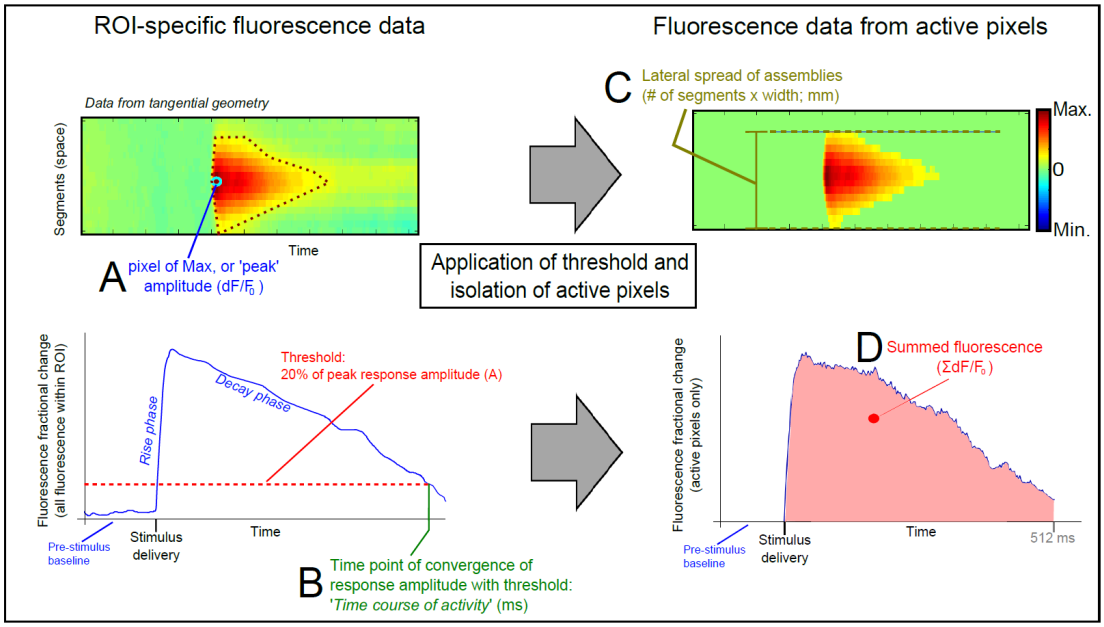

Figure 17: Calculation of quantifiable parameters of assembly dynamics. Initially, data can be visualised either as a space-time map of total fluorescence (top-left), or averaged into a time series (collapsing the spatial dimension, i.e. space-time map y-axis). From the space-time map, the peak fluorescence reading is isolated (**A**), and used to apply a 20% threshold of activity (bottom-left) to the data set. The dotted area surrounding the assembly represents the shape of the active-pixels (top right panel), and highlights the level of non-specific data acquired even when taking in account ROI-specific fluorescence (as is the case here, with tangential geometries). The time-point at which the time-series profile of activity crosses the 20% threshold (**B**) represents the end of the activity time-course of the assembly.

Additionally, active pixels-only data could be graphed out in a similar way as the original data, yielding space-time maps (top right) and time-series (bottom right) of fluorescence emanating from active pixels only. Using the space-time map, the lateral spread of individual assemblies were estimated (**C**) by measuring the lateral spread of active pixels, while the time-series were used to sum all fluorescence detected above-threshold (area under the curve, **D**).

2.8.5 Statistical testing

All data are listed and graphed (whether histograms of time series) as average value with standard error of the mean (S.E.M), calculated as the standard deviation of the data divided by the square root of the number of repeat trials. Statistical testing of data was carried out in order to test for significant differences between measured samples in all specific comparisons described in the following chapters. All data were plotted on a quantile-quantile (Q-Q) plot (Razali and Wah, 2011) in order to gauge for normality, see **Chapter 3**, **Section 3.4.2.c**. For clarity, statistical test results are not listed within the text of the results, rather they are collectively listed within statistical tables found in each result section as appropriate. All statistical tests (paired/un-paired t-tests, one-/two-way ANOVAs and extra sum-of-squares F-tests) were performed using GraphPad Prism 6 v6.05 (July 2014; San Diego, California, USA) and consisted entirely of quantification testing of discrete values (for summed fluorescence values or peak amplitude values).

Chapter 3: RESULTS I

Characterisation and quantification of evoked neuronal assemblies in selected cortical and sub-cortical structures.

3.1 Introduction

In this chapter, investigations focus on the characterisation and quantification of neuronal assemblies evoked in selected cortical and sub-cortical structures: within the cortex, attention is given to the S1BF, a region already thoroughly studied both *in vitro* and *in vivo*, where assemblies were triggered via both direct and remote (thalamocortical) stimulation. Additionally, assemblies were evoked within a less-well studied region of the frontal cortices (Badin et al., 2013), the AIC, found within orbitofrontal areas of rodent brain. Finally, assemblies evoked in VPM were investigated, as well as those evoked in the BF; to the best of my knowledge this thesis represents the first qualitative and quantitative description of neuronal assembly dynamics evoked in this latter sub-cortical area using VSDI in combination with extracellular electrophysiology.

Importantly however, and except for remote assembly activation in S1BF and VPM (thalamocortical activation), all other brain structures of interest were activated using direct stimulation, as there are no accepted methods for slice preparations of 'remote' stimulation of the AIC or BF. It was the goal of this chapter to highlight any conspicuous differences in the way each preparation expressed their evoked responses (assemblies), in particular between: i) direct and remote (thalamocortical) stimulations of the S1BF, ii) direct stimulations of cortical networks in granular (S1BF) and agranular cortices (AIC), and iii) direct stimulations in sub-cortical

structures (VPM and BF). These goals provide a way of characterising mesoscopic activity patterns across brain areas, and assessing the impact of physiological manipulations such as locus of stimulation (i.e. within superficial or deep layers or stimulated remotely) and target area (cortical or sub-cortical): such experiments should provide more information regarding the dependency of dynamic mesoscopic activity profiles to the underlying cytoarchitecture.

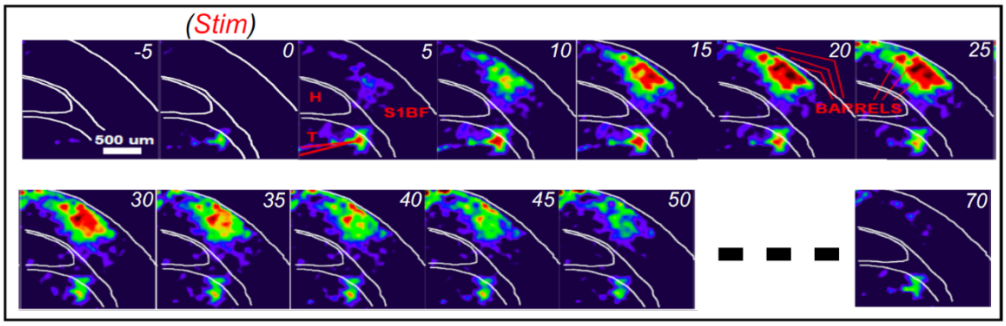

Figure 1: Sequential display of activity evoked with a single 30 Volts electrical pulse to activate fibres originating from the VPM nucleus of the thalamus (T) and targeting the S1BF in a thalamocortical slice. The 0.1 ms electrical pulse is delivered to the VPM at t=0 (time labels are visible in italic in the top-right of each image) – it takes less than 5 ms for the activated fibres to carry the impulse to the S1BF, however this single activation then triggers an assembly which lasts up to 70 ms in this particular slice. Note: As the assembly spreads in the first 15 ms (i.e. between t=5 and t=20), three hotspots of activity spanning Layers IV and II/III become easily distinguishable, and correspond to three barrel columns within the slice (labelled at t=20 and t=25 ms), which receive and amplify afferent stimuli in order to gate the spread of the signal to the rest of the cortex, in accordance with the mechanism of excitatory signal flow proposed by (Rinkus, 2010) in **Chapter 1**, **Figure 8**. It was noticed that cortical assemblies could be more robustly evoked with increasing stimulation voltage, reaching a ceiling effect from 60 Volts stimulation. Panel adapted from (Badin et al., 2017).

3.1.1 Cortical structures

a. The agranular insular cortex (AIC)

The AIC is a sub-region of the orbitofrontal cortex (OFC), a large area part of the mammalian frontal cortices mostly involved in higher cognitive processes such as reward expectancy as well as playing a role in modulating emotional responses to stimuli in humans (Elliott et al., 2000; Kringelbach and Rolls, 2004; Rolls, 2000) and primates (Bechara et al., 2000; Rudebeck et al., 2007; Tremblay and Schultz, 2000). In the evolutionarily-simpler rodent brain, the OFC has concurrently been linked to managing adaptive behaviour (Pickens et al., 2003; Schoenbaum and Roesch, 2005; Schoenbaum et al., 2006a; Schoenbaum et al., 2006b), as well as playing a role in viscerosensation, i.e. integrating and processing afferent cardiovascular, cardiopulmonary, gastrointestinal, gustatory and related sensory information (Cechetto and Chen, 1990; Zhang and Oppenheimer, 1997). In the rat specifically, the AIC can be found ventro-laterally, on the orbital surface of the frontal cortices: a region of cortex traditionally investigated *in vivo* using highly invasive electrophysiology only, due to the difficulty in accessing this region for imaging experiments, yet only a handful of reports focusing on *in vitro* experiments using optical imaging in these frontal cortices have been published to date (Bandyopadhyay et al., 2005; Bandyopadhyay and Hablitz, 2007). The AIC is an interesting area of cortex as it is not a primary sensory region, as is the case for the majority of the rodent cortex, the most significant result of which is that it features an atypical laminar organisation: i.e. lacking a Layer IV. This specific layer is also referred to as the 'granule cell' layer, hence the name of the cortical region: the agranular insular cortex, see **Figure 2** below. Cortical layers can be differentiated with respect to their profile of neuronal types and inter-connections, in turn this provides them with specific integration and processing abilities, to a similar degree to that which is induced by columnar (vertical) network organisation (Brecht, 2007).

A simplified circuit diagram of the main inter- and intra-laminar connections in granular and agranular cortex is given in **Figure 2C**.

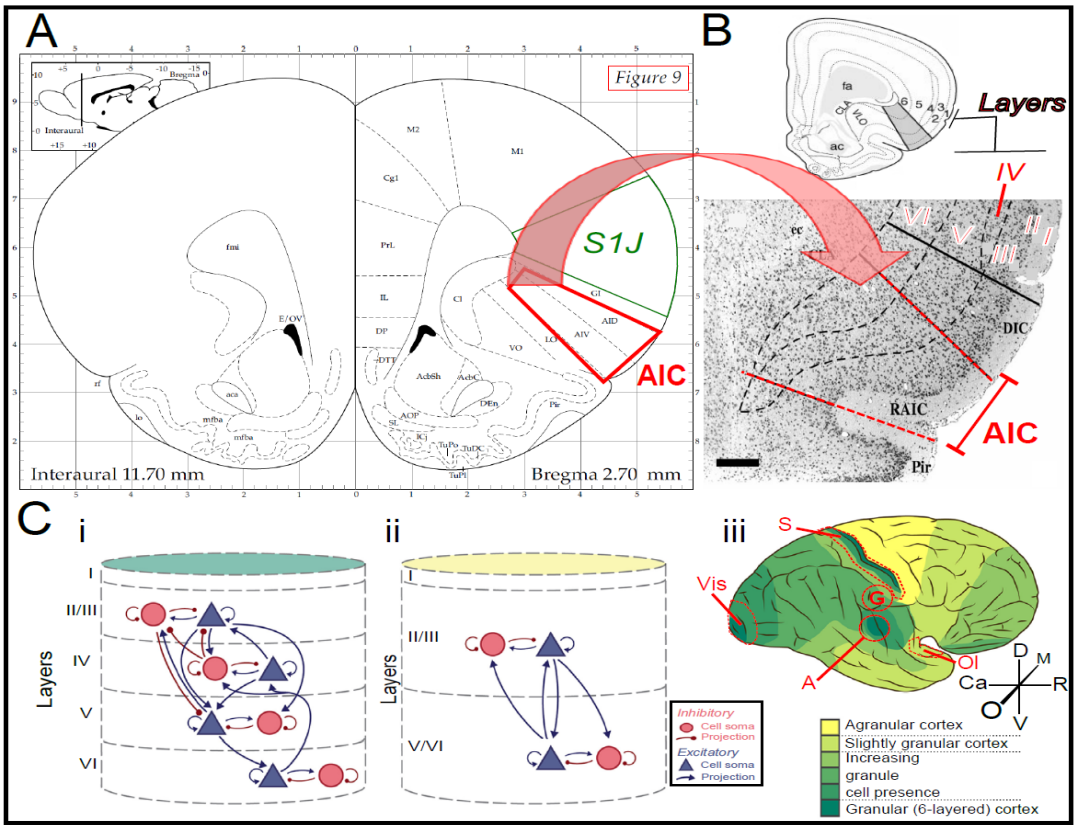

Figure 2: Schematic representation of the rodent orbitofrontal frontal cortex, with special attention given to the agranular insular cortex (AIC) and its differing columnar cytoarchitecture. **A**. Slide taken from (Paxinos & Watson, 1998) displaying a schematic representation of a rat coronal brain slice, highlighting the location of rodent AIC and primary somatosensory (jaw area; S1J) cortical areas within prefrontal cortex. **B**. Low-power photomicrograph focusing on coronal rat brain slice containing AIC, area highlighted in schematic of slice (see inset, top), providing an indication of the laminar distribution within this sub-region of cortex. Note the disappearing LIV at the border of S1J and dysgranular insular cortex. Figure labels: dysgranular insular cortex (DIC), agranular insular cortex (AIC), rostral agranular insular cortex (RAIC), piriform cortex (Pir). Black scale bar: 500 µm. Note: laminar depiction in **B** is taken approx. 0.64 mm more rostrally than the schematic slice representation in **A**. **C**. Schematic representation of signal flow and processing via interlocked inhibitory and excitatory networks within 6-layered (**i**; c.f. Chapter 1, Figure **8**) and agranular (**ii**) cortical columns. Note the absence of inter-layer inhibitory connections in agranular cortical columns; this diagram is only tentative and represents a vast oversimplification of the real network architecture and composition which can be found in either of those two areas of cortex, yet highlights key differences (Beul & Hilgetag, 2014). (**iii**) Schematic representation of human brain showing the graded approximate areas of

granular (dark green), slightly granular and dys/agranular (yellow) cortical areas, showing that the presence and thickness of LIV within cortical tissue is variable across the cortical mantle and that its emergence appears to be a defining feature of regions primarily involved in sensory processing, i.e. primary somatosensory (**S**), visual (**Vis**), auditory (**A**) gustatory (**G**) and olfactory (**Ol**) cortices. Orientation labels: dorsal (**D**), medial (**M**), rostral (**R**), ventral (**V**), orbital (**O**), caudal (**Ca**). Panel **B** is adapted from (Burkey et al., 1999); panel **C** is adapted from (Beul & Hilgetag, 2014).

The AIC receives afferent cortico-cortical connections from its contralateral homotopical counterpart – these projections originate from Layer V predominantly. Additionally, AIC receives cortico-cortical projections from medial prefrontal cortex, which mainly target Layers I, III and VI (Beckstead, 1979). Further cortico-cortical afferent projections from perirhinal cortex have been reported though with no clear distinction regarding target layers (Haberly and Price, 1978) while olfactory bulb afferents, originating from posterior primary olfactory cortex (Gerfen and Clavier, 1979), target Layer I of AIC directly.

Sub-cortically, the AIC receives input from the amygdala, which targets both Layers II and V and providing emotional context to ongoing cortical processing (Krettek and Price, 1977a), while major thalamocortical afferent innervation, originating from the mediodorsal thalamic (MD) nucleus, synapses with cells in Layers I and III (Krettek and Price, 1977b). The AIC also receives a prominent monoaminergic innervation from brainstem nuclei such as the anterior ventral tegmental area (VTA, dopaminergic afferents), as well as the dorsal raphe nucleus (serotonergic) and the locus coeruleus (noradrenergic) projections (Gerfen & Clavier, 1979), which all provide strong modulatory control of frontal cortical activity (Bandyopadhyay and Hablitz, 2007; Robbins and Arnsten, 2009). The rat frontal cortices, and in particular the OFC, represent the main cortical target of dopaminergic systems (Tassin et al., 1978), which induces a very sensitive control of prefrontal cortical activity (Bandyopadhyay & Hablitz, 2007; Bandyopadhyay et al., 2005). After integration

and processing of incoming information within the AIC, it is then relayed onto a number of other brain sub-regions, with efferent projections mainly targeting the dorsal raphe nucleus (from LV), the ventral striatum (from LV), the basolateral amygdala (from LIII and V), the lateral hypothalamus (from LIII and V), the parabrachial nucleus (from LV/VI), the VTA (from LV), the medullary nuclei (from LV) and the mediodorsal thalamus (from LVI) (Gabbott et al., 2005).

The AIC therefore represents a highly connected sub-region which integrates information already processed in other cortices (perirhinal and medial prefrontal cortices) with sensory information from the MD and olfactory bulb all the while modifying its output with respect to emotional context by way of influence from the amygdala, among other sub-cortical influences. Therefore, once processed, information transmitted out to the long-distance targets of AIC primarily affect sub-cortical regions (amygdala, thalamic and brainstem nuclei) which may in turn induce a profound modulatory impact on brain these structures, which mediate information transfer and control brain state.

b. The somatosensory barrel field cortex (S1BF)

Contrary to the AIC, the S1BF is the most extensively studied primary sensory area in the rodent neocortex, containing a Layer IV, as it is the main sensory modality used by rodents for internal representation of their immediate surroundings (Ito, 1985). The S1BF therefore represents a powerful model system for studying sensory processing as well as for general columnar cortical computations. The very particular arrangement of cells within these anatomically-defined cortical columns produce characteristic mesoscopic cytoarchitectonic profiles: especially obvious within Layer IV, an important target for afferent fibres (Bruno and Sakmann, 2006), where the aggregation of spiny stellate cells, symmetric and asymmetric pyramidal as well as classic pyramidal neurons (Staiger et al., 2004) form darker blotches

(approx. 400 μm in diameter) visible to the naked eye, and which are arranged in a somatotopic conformation faithfully replicating the whisker arrangement of the mystacial whisker pad on the animal's snout (Woolsey and van der Loose, 1970). This surprising cellular arrangement is referred to as the 'barrel field' cortex: the cells within the columns of this cortical sub-region are arranged in tightly knit networks within the circular walls of the columns (referred to as the septa) with less-compacted networks in their lumen. In a recent study focusing on this specific organisation, a single barrel column was estimated to contain approximately 19,000 neurons, with 88–89% of those neurons being excitatory while the remainder (i.e. 11–12%) are GABAergic. Providing this estimate is correct, it would mean there are approximately 2,200 interneurons per barrel column (Meyer et al., 2011; Meyer et al., 2010b).

Upon stimulus presentation, a widely accepted view is that thalamic afferents target primarily inhibitory as well as LIV stellate neurons which feed their activity forward to other spiny stellate cells as well as inhibitory basket and low-threshold spiking cells in a complex arrangement or reciprocal connections; where spiking activity is not only fed forward but also backwards among the constituting cells. Altogether, this arrangement grants LIV responses with fast excitatory dynamics under potent inhibitory control, generated within just a few milliseconds, which then sends excitatory impulses up to the superficial layers (LII/III) where they activate both excitatory pyramidal cells as well as inhibitory basket and chandelier cells, all of which also show a high degree of reciprocal interconnection among themselves in LII/III, a defining structural property of cortical networks (Kim and Ebner, 1999; Schubert et al., 2001). Pyramidal cells are of particular importance, as their specific cellular biophysical properties appear 'designed' for large-scale integration and propagation of afferent information (Spruston, 2008; Yuste, 2011). Additionally, Chandelier cells project to an estimated 1000 – 1500 pyramidal cells each, with specific targeting of sub-cellular compartments, i.e. axon initial segments (Freund

and Katona, 2007; Schubert et al., 2007). Basket cells, found in all layers, contact synaptically with somata and proximal dendrites of principal cells, and have an even greater reach than chandelier cells as their axonal arbours have been found to extend over distances of up to 1 mm, creating synaptic contacts with over 1500 pyramidal cells (Freund & Katona, 2007).

LII/III pyramidal cells send projections to LV/VI and make synaptic contacts with numerous subsets of neuronal types in the deep layers (Feldmeyer et al., 2006; Gottlieb and Keller, 1997). Important to this rather simplified model of excitatory columnar signal flow, feed-back excitation also plays an important part in maintaining a high level of excitatory potentials delivered ubiquitously to neurons present within the barrel network, driving columnar signal processing (Feldmeyer, 2012; Welker et al., 1988). In propagating this initial stimulus, network-wide activation rapidly co-activates a potent inhibitory component, which plays a major role in fine-tuning and controlling the appropriate integration and processing dynamics of the barrel (Isaacson and Scanziani, 2011; McCasland and Hibbard, 1997; Wilent and Contreras, 2004). When activity reaches superficial and deep layers, *horizontal* cortico-cortical efferent fibres also spread the activity laterally along layers and between columns to prime the surrounding barrels, granting these cortical processing units with the ability to coordinate their activity in relation to each other in real time, which is important for appropriate sensory representation (Feldmeyer, 2012). This complex configuration of neuronal networks in cortical barrels – arranged both *vertically* within barrel lumen or septa as well as *horizontally* across cortical layers (Brecht, 2007) – creates an extensive three-dimensional matrix of interconnected neuronal sub-groups forming more (septa) or less (lumen) compacted networks, the dynamic interplay of which corresponds to the 'engine' of somesthesis (Feldmeyer, 2012; Kim and Ebner, 1999). LV/VI pyramidal cells also project back to their thalamic nuclei, forming the sub-cortical afferents of the thalamocortical loops (Zhang and Deschenes, 1997), see **Chapter 1**, **Figure 3** for a

schematic representation of activation cascades proposed to take place within S1BF cortical columns.

The S1BF also receives a powerful monoaminergic innervation from sub-cortical nuclei: serotonergic afferents originating from the Raphe nucleus make up the densest monoaminergic input throughout the cortex, including the S1BF, with relatively uniform innervation profiles through all cortical layers, and is indeed so extensive that it is believed serotonergic terminals may synapse with the vast majority of all cortical cells (Foote and Morrison, 1987; Lidov et al., 1980). Noradrenergic afferents (from the Locus Coeruleus) target all layers of the neocortex within the S1BF, yet with some preference in targeting Layer I (Beaudet and Descarries, 1978; Loughlin et al., 1982; Morrison et al., 1978). Serotonergic activity and modulation in the neocortex has been strongly correlated with behavioural state while that of noradrenergic neurons show a more phasic profile best associated with 'attentiveness' (Foote and Morrison, 1987). In addition to these systems, cholinergic innervation of the S1BF is extensive and also induces a potent modulatory effect on network activity, associated with arousal state. Contrary to the extensive and dense distribution of serotonergic, noradrenergic and cholinergic terminals through the cortex and all its layers, dopaminergic fibres feature a relatively weak innervation of the rodent S1BF (Berger et al., 1974; Lewis et al., 1987), contrasting with its comparatively dense innervation of frontal cortices (see above).

c. The somatosensory mystacial organ and thalamocortical (TC) system

- *Sensory information flow in the CNS: relay via thalamic nuclei*

Upon stimulation of whisker follicles, information is relayed to the brainstem trigeminal nuclei, which specifically consist of the principalis (PrV), the oralis, the interpolaris (SpV), and the caudalis, via the trigeminal nerve (Ma, 1991; Petersen, 2007), before being relayed onto thalamic nuclei: the ventral posteromedial nucleus (VPM) and the posteromedial complex of the thalamus (POm) (Hoeflinger et al., 1995; Landisman and Connors, 2007). The "lemniscal" pathway is that which relays single-whisker information from the PrV to the barreloids of the VPM (Diamond et al., 1992), and then to barrel lumen within the S1BF via thalamocortical projections (Cruikshank et al., 2010): a specific pathway referred to as '*lemniscal 1'* (Haidarliu and Ahissar, 2001; Hoogland et al., 1987; Varga et al., 2002). The *lemniscal pathway 2* also originates from the PrV, but bifurcates from the path of lemniscal 1, and is relayed in the thalamus via a distinct area of the VPM barreloids from those utilised by the lemniscal pathway 1, and from which thalamocortical efferents project to the septal region separating cortical barrels, the specific networks of which have been reported to process multi-whisker information (Furuta et al., 2009; Petersen, 2007; Urbain and Deschenes, 2007), see **Figure 3**. Additionally to the lemniscal pathways, trigeminal nuclei also project in a separate and diffuse fashion to the VPM (from the caudal SpV, the *'extralemniscal'* pathway) and POm (from the rostral SpV, the *'paralemniscal'* pathway), where the paralemniscal pathway shows topographical whisker arrangements in the POm (barreloids) but not the rostral SpV, while the extralemniscal pathway shows the same topographical arrangement in the caudal SpV (barrelets) but not in the VPM (Ma, 1991), see **Figure 3**.

Interestingly, both the VPM and POm show notable discrepancy from the usual architecture of cortical networks, in particular in the absence of intrinsic inhibitory interneurons. These nuclei contain exclusively excitatory cells which project to the cortex, and that are kept under inhibitory control via afferent inhibitory fibres from a third, essential, nucleus within the thalamus, and central to the functioning of the thalamocortical system: the reticular nucleus of the thalamus (Rt). A network arrangement befitting of a region operating a key role in fast information relay. The Rt induces a powerful activity-dependent and recurrent feedback inhibition to the VPM and POm, which plays a central role in controlling the general activation, oscillatory behaviour, receptive field focus, burst frequencies and spindle wave generation of thalamocortical projections (Diamond et al., 1992; Lavallee and Deschenes, 2004; Steriade et al., 1985). Similarly, the Zona Incerta projects to the POm and also exert a powerful inhibition upon the activity of this paralemniscal thalamic nuclei; this relationship has been shown by inhibiting the Zona Incerta, which results in a significant increase in POm output (Trageser and Keller, 2004).

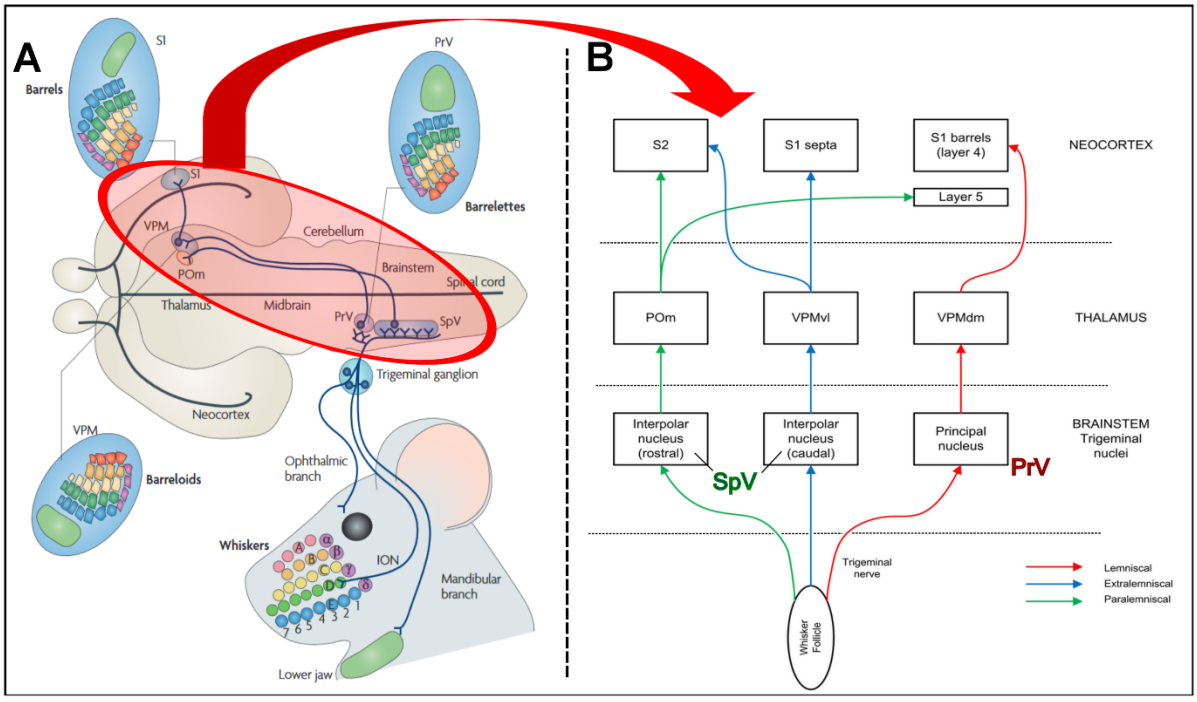

Figure 3: Rodent somatosensory communication via the trigeminal and lemniscal pathways – from peripheral sensory receptors to cortical perception. **A**. Schematic diagram displaying a dorsal view of rodent brain (top) and head (inset, bottom), highlighting the *trigeminal pathway*, with the location of peripheral mechanoceptors within whisker follicles ('**whiskers**', bottom) and simplified projection paths linking them first to the brainstem nuclei ('**PrV**' & '**SpV**', top), then projecting to the thalamic nuclei ('**VPM**' & '**POm**', top) and finally the cortex ('**S1**'); note the specific tissue organisation of the different brainstem and thalamic nuclei, as well as that of S1 cortical field faithfully reproducing the arrangement of rows of whiskers on the mystacial pad. **B**. Flow diagram (bottom to top) focusing on the lemniscal pathways inter-linking the brainstem nuclei with the different cortical sub-regions involved in somesthesis. **VPM** – ventroposterior medial nucleus of the thalamus; **vl** – ventrolateral; **dm** – dorsomedial; **POm** – posteromedial nucleus of the thalamus; **S2** – secondary somatosensory cortex; **ION** – infraorbital branch of the maxillary nerve.

- *Thalamic innervation of cortical barrels*

Within the paralemniscal pathway, thalamocortical axons originating from the POm target the S1BF barrel septa (Herkenham, 1980; Wimmer et al., 2010), relaying multi-whisker information (Veinante and Deschenes, 1999; Williams et al., 1994), as well as targeting the secondary somatosensory cortex (S2). Extralemniscal axons originate from the VPM and also target the barrel septa with secondary connections projecting to the S2. The more concentrated septal neuronal networks and those of the lumen are therefore simultaneously innervated by afferent projections from multiple sources including projections from the lemniscal 2 pathway, as well as para- and extralemniscal afferents: extensive integration of multi-modal information must therefore take place within these barrel septa (Alloway, 2008). Thalamocortical neurons in the more traditionally studied lemniscal 1 pathway show a complex and diffuse profile of synaptic connections within barrels (White, 1978), with additional specific targeting of cortical neurons in the lumen of Layer IV barrels (Feldmeyer, 2012; Jones and Powell, 1970; Lorente de No, 1922). This view was formed by early studies which reported sparsely distributed thalamocortical afferent synapses in all layers of the S1BF, and significant axonal arborisation in LVI and I (Killackey, 1973). In turn, the dynamics of this system have been reported

to arise primarily as a result of Layer IV activation (Bruno and Sakmann, 2006), from which activity then spreads to superficial and deep layers (Armstrong-James et al., 1992; Douglas and Martin, 2004), as described previously. Yet, thalamocortical synapses have been reported to be located wherever their axons overlap with the dendritic arbours of cortical cells throughout columns, and that overall, thalamocortical terminals make simultaneous active connections with nearly all cells present in the height of the column (Peters, 1979; White, 1979). Thalamocortical synapses may therefore occur on a much greater array of cortical boutons than initially thought, which may indeed be sparsely dispersed throughout the entire height of the barrel column, yet with greater amounts of specific thalamocortical connections in the layers originally thought to be exclusively targeted: LVb and IV for VPM efferents, LVa and I for POm efferents (Lorente de No, 1922; Meyer et al., 2010a) – see **Chapter 1**, **Figure 3**. As a result of this complex innervation, afferent information is delivered to most neurons within the column in a near-simultaneous fashion, albeit via synaptic contacts of varying strengths: evidence for such a whole-column activation scenario has been gathered using whole-cell, juxtasomal and extracellular electrophysiology recording paradigms in rodent S1BF columns (Ahissar et al., 2000; Brecht et al., 2003; Manns et al., 2004). This theory of simultaneous column-wide activation posits that incoming sensory information initially activates a wide range of cortical cells throughout all six layers, thereby generating an immediate representation of tactile stimulus throughout the thickness of the cortex, rather than that which would radiate out from the granule cell layer in a sequential layer activation (Meyer et al., 2010a), albeit on similar timescales.

More specifically, in a series of detailed studies focusing on the specific micro-scale innervation of cortical barrels by thalamic nuclei (Meyer et al., 2010a; Wimmer et al., 2010), it was established that: a) all excitatory neuronal types present within the column are potentially innervated by thalamocortical afferents in the order of 100-

600 boutons per neuron, i.e. there is no specific 'target cell' for thalamocortical afferents; b) pyramidal neurons located in Layers V–III receive dual input from both VPM and POm which, at least for LV pyramidal neurons, may be of similar potency (i.e. approx. 300 contacts from either afferents); and c) pyramidal cells in Layers V and III each possess up to four separate thalamocortical innervation domains which are found in different layer compartments and usually associated with their dendritic arbours.

- *Corticothalamic projections and thalamocortical loops*

The deep layers (LV & LVI) also constitute the 'output' layers, as one of their specialisation is that they possess significant amounts of efferent fibres which project back to thalamic nuclei (Deschenes et al., 1998; Veinante et al., 2000). In turn therefore, cortical activity also triggers downstream corticothalamic efferents, which are nearly 10 times as numerous as their upstream reciprocal thalamocortical counterparts (Jones, 2002; Liu and Tsien, 1995), transmitting activity back to the VPM and POm nuclei (Monconduit et al., 2006). More specifically, the ventral posterior nucleus (VP; which includes the VPM) receives projections from LVI from pyramidal cells, while the POm receives input from both LVI and LV (Killackey and Sherman, 2003). These reciprocal axonal projections interlinking the trigeminal nuclei to the S1BF play a major role in shaping and controlling the activity within the thalamus via i) their direct monosynaptic excitatory feedback as well as ii) polysynaptic inhibitory feedback via activation of GABArgic neurons in the Rt (Gibbs et al., 2000). The stimulation of thalamocortical loops, during active sensory perception, has been reported to trigger high frequency activity which varies between 20 and 80 Hz, depending on functional state.

In addition to those of the somatosensory system, thalamocortical loops have been identified in auditory (Liu et al., 2011; Theyel et al., 2010), visual (Nita et al., 2003;

Van Essen, 2005) and motor systems, as well as between the cortices found in the frontal lobe and their thalamic nuclei (Alexander et al., 1990; Kelly and Strick, 2003), highlighting the central role of this highly efficient and widespread mode of information processing to appropriate brain functioning. In spite of those similarities, investigations in the present thesis focus on the mechanisms of assembly generation (i.e. the recruitment of neuronal populations into active, dynamic assemblies) and maintenance in the primary somatosensory thalamocortical system (VPM/POm–S1BF).

3.1.2 Sub-cortical structures

a. The ventroposterior medial (VPM) and posteromedial nuclei (POm)

Thalamic relay nuclei of the lemniscal pathway, see above.

b. The basal forebrain nuclei (BF)

In the rat, the 'basal forebrain' (BF) refers to a collection of nuclei located on the ventral surface of the brain, from the 3rd ventricle in the rostral direction, and lining the medial septal walls between the cerebral hemispheres: its activity has been reported to be central in modulating key behavioural functions including memory, learning, attention and arousal (Nunez, 1996; Sarter and Bruno, 2002; Vanderwolf et al., 1993). This complex of nuclei has been grouped together with regard to their extensive set of long-range projections, which are mostly cholinergic and together include the nucleus accubens (NAcc), the nucleus basalis (NB), the diagonal band of Broca (dBB) comprising both the vertical (VDB) and horizontal diagonal band (HDB) of Broca, the substantia innominate of Meynert (SI) and the medial septal nuclei (MS), among others (Divac, 1975).

- *Local networks and efferent long-range connectivity*

As is the case with most sub-cortical structures, such as the VPM and POm, the BF features a strikingly different neuronal network architecture from that of laminated cortical areas, which could be seen as 'tailored' to their respective function; be it of fast information relay (in the case of the sub-cortical structures considered here) or integration and processing (in the case of cortex). Importantly in the BF, 2 complexes have been repeatedly grouped in the literature combining a) the MS and the dBB as the MS-dBB complex and b) the SI and NB as the SI-NB complex (Rye et al., 1984). Each of these constituting nuclei are composed of a heterogeneous and complex mix of glutamatergic, GABAergic and nitric oxide (NO) synthase-positive neurons forming putative local networks within which longer-projecting cholinergic (mostly) but also glutamatergic and GABAergic cells originate (Sotty et al., 2003; Wang et al., 2006). Glutamatergic and GABAergic long-range connections have been reported to target the auditory cortex (Metherate and Ashe, 1995), the paralimbic cortex (Gritti et al., 1997) and neocortex in general (Henny and Jones, 2008; Porter et al., 1999). The vast majority of long-range axonal projections originating from the BF nuclei however, are cholinergic, making the BF the main source of cholinergic innervation to the entire brain (Amaral and Kurz, 1985; Semba et al., 1988). The main targets of BF cholinergic long-range projections include sub-cortical regions such as the amygdaloid complex (Emson et al., 1978; Rye et al., 1984), the thalamus (Hallanger et al., 1987; Levey et al., 1987) and multiple nuclei within the brainstem: the reticulopontine, pedunoculopontine and laterodorsal tegmental nuclei, the pontine reticular formation, locus coeruleus, the vestibular nuclei, the dorsal raphe nucleus, the motor and sensory trigeminal nuclei (such as the sensory Prv and SpV nuclei mentioned above), as well as the cerebellum (Semba et al., 1988). Additionally, BF projections (cholinergic and otherwise) potently

innervate regions of allocortex such as the olfactory bulb (Rye et al., 1984; Semba et al., 1988) and the hippocampus (Lewis and Shute, 1967; Segal and Landis, 1974), as well as neocortex (Johnston et al., 1979; Lehmann et al., 1980; Mesulam et al., 1983a; Sikes et al., 1983). An additional reason for the functional relevance of the BF is its seemingly selective degeneration in the context of Alzheimer's disease (Hefti and Weiner, 1986), which has been implicated as a major cause giving rise to the emergence of many deficits in cortical processing associated with disease pathology (Coyle et al., 1983; Lin et al., 1998).

More specifically, cholinergic fibres from the BF have been ordered into 4 main distinct sub-groups classified with respect to their long-range targets: 'Ch1' projections originate from the MS and target the hippocampal formation primarily; 'Ch2' axons originate from the VDB and also innervate the hippocampal formation; 'Ch3' neurons found in the HDB project to the olfactory bulb; while 'Ch4' efferents from the SI-NB target specific neocortical areas (Mesulam et al., 1983a; Rye et al., 1984). Neocortical areas innervated by cholinergic afferents from the BF include the anterior cingulate cortex (by Ch4 neurons but also some from Ch2 and Ch3) and insular cortex (from Ch4), as well as sensory cortices such as the visual cortex (from Ch3), the somatosensory cortex (from Ch4) and auditory cortex (from Ch4) (Mesulam et al., 1983b). In addition to this, there also exists reciprocal connections between areas of prefrontal cortex and cholinergic cells within the BF (Zaborszky, 2002), with recent investigations attributing increases in acetylcholine release in the frontal cortices (on the temporal scale of seconds) with cue detection; to the contrary of increases in overall cortical acetylcholine release which is mostly attributed to overall arousal state (Parikh et al., 2007).

- *Afferent long-range connections to the BF*

In addition to excitatory connections from cortical areas (Sarter and Bruno, 2002), the BF features a significant number of afferent inputs originating from monoaminergic midbrain nuclei such as the ventral tegmental area (dopaminergic), the locus coeruleus (noradrenergic) and the raphe nucleus (serotonergic), which have been found to be so extensive that they represent the main extra-thalamic relay network to the neocortex (Jones and Cuello, 1989). Such a potent innervation of the BF by modulatory amines highlights the very precise control of cholinergic systems required for appropriate behavioural function.

3.2 Materials and methods

All experiments were carried out here as described previously: for experiment preparation, recording and data analysis, refer to **Chapter 2**. However: some methods specific to the experiments carried out in this chapter will be mentioned in more detail or will be added if not previously mentioned. These brief supplementary methods include information about pharmacological drugs used to highlight certain aspects of population activity (**Section 3.2.1**) as well as greater detail about the geometries used here for rasterisation and analysis of VSDI data (**Section 3.2.2**).

3.2.1 Drugs used for investigating internal assembly dynamics

a. Tetrodotoxin – *Voltage-gated sodium-channel blocker*

Tetrodotoxin (TTX, **Figure 4A**) is a complex molecule often attributed to the puffer fish, however it is also found in other cousin species of the Tetraodontiform fish family. It was then found that TTX was not produced from the fish themselves, but

from symbiotic bacteria which infect the fish, including Pseudoalteromonas, Pseudomonas and Vibrio bacteria. TTX is a very potent neurotoxin, reversibly binding to voltage-gated sodium- (Na^+-) channels in neuronal cell membranes, mostly responsible for the rise-phase of action potentials, inhibiting their action and preventing sodium ions from crossing the membrane, thereby shunting all spiking activity (Bane et al., 2014). More specifically, TTX has been shown to bind to an extracellular site on Na^+-channels referred to as *site 1* (Moczydlowski, 2013), a binding site associated with inhibition of this voltage-gated channel protein where several other toxins bind, such as several conotoxins (snail venom) and saxitoxin, and which all disable its activity. With respect to TTX pharmacology, two different voltage-gated Na^+-channel proteins exist, exhibiting different binding kinetics of TTX with site 1: TTX-resistant Na^+-channels are found in cardiac tissue and bind TTX with at 1-10 µM concentrations, while TTX-sensitive Na^+-channels bind the toxin at concentrations 1000 times lower, i.e. 5-15 nM, and are found throughout the body, in particular in the brain. In turn this accounts for the very high toxicity of TTX which can effectively halt all neuronal impulse conduction with nanomolar concentrations at the target, resulting in a lethal dose required to kill 50% of the population (LD_{50}) for TTX of 334 µg/kg in rats; for comparison purposes only, the LD_{50} dose of potassium cyanide (a highly toxic cyanide salt) in mice is more than 25 times larger (8.5 mg/kg). In the experiments presented here where the goal was to confirm recorded activity resulted from physiological neuronal firing, TTX was perfused in aCSF at 15 µM, which would in any case insure a potent inhibition of impulse propagation.

b. **CNQX** – *AMPA receptor blocker*

6-cyano-7-nitroquinoxaline-2,3-dione, more commonly known as CNQX (**Figure 4B**), is a pharmacological agent which selectively blocks the activity of some

ionotropic glutamate receptors (Garthwaite et al., 1989), competing for the same binding site as glutamate. These ionotropic glutamate receptors are important since they represent the 'fast' component of glutamatergic EPSPs, the main excitatory process in the CNS. In addition to ionotropic glutamate receptors sensitive to α-amino-3-hydroxy-5-methyl-4-isoxazolepropionic acid (AMPA), two other kinds exist which are selectively sensitive to kainate (KA) and *n*-methyl-D-aspartate (NMDA); CNQX blocks both AMPA and KA receptor sub-types. These latter two receptors are not highly involved in fast excitatory glutamatergic transmission, as KA receptors are only slightly involved in synaptic transmission, instead playing a major role in longer-term synaptic plasticity (Song and Huganir, 2002); more information is provided about the nature and function of NMDA receptors in **Chapter 4**, **Section 4.1.3.b**. Almost all of the fast glutamatergic transmission in the CNS occurs via activation of AMPA receptors, therefore using CNQX provides an efficient way of gauging the dependence of any neuronal activity of interest on fast glutamatergic transmission: in experiments presented here, CNQX was perfused at 20 μM.

c. **Bicuculline** – *$GABA_A$ receptor blocker*

Gamma-Aminobutyric acid (GABA) is the principle inhibitory neurotransmitter acting on fast ionotropic receptors ($GABA_A$ receptors), which are permeable to chlorine (Cl^-) and hydrogen carbonate (HCO_3^-) ions. Bicuculline (**Figure 4C**) blocks the actions of GABA at its binding sites on $GABA_A$ receptors specifically – thereby sharing its mechanism of action with that of CNQX in competitively antagonising the endogenous transmitter. This gives rise to highly disinhibited network states (Sloviter and Brisman, 1995). Just like TTX, bicuculline occurs naturally, as it is synthesised by certain plants, i.e. Dicentra Cucullaria, Fumariaceae and several species of Corydalis. The concentration of bicuculline required to induce a 50%

inhibition of $GABA_A$ receptor-mediated effects (IC_{50}) is reported to be 3 µM, and was used in the experiments presented here at 10 µM. At this concentration, bicuculline is reported to give rise to epileptiform network activity as a result of inhibition of fast GABAergic neurotransmission (Jones and Barth, 2002). Interestingly, it has been reported for the bicuculline methiodide salt (as used here) that this action could also in part be due to the blocking actions of bicuculline on calcium (Ca^{2+})-sensitive potassium (K^+) channels (Khawaled et al., 1999), as well as KCNQ-containing K^+-channels (Yue and Yaari, 2004).

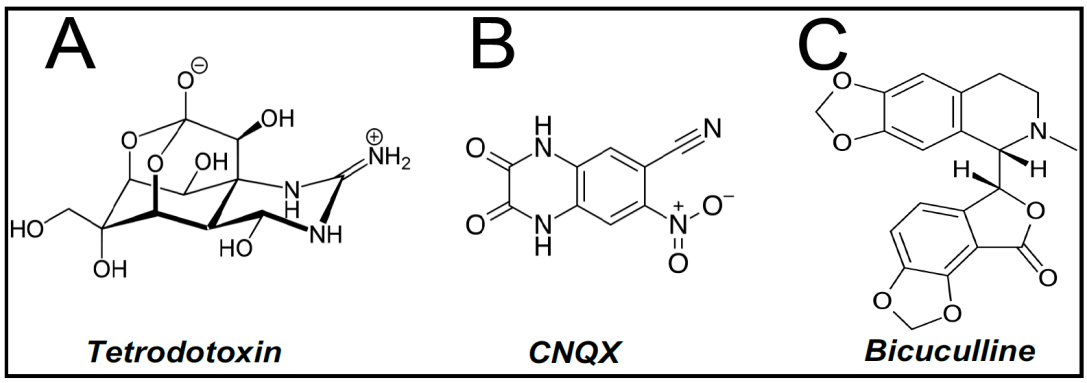

Figure 4: Molecular structures of pharmacological agents used in experiments in this chapter including the sodium channel blocker tetrodotoxin (TTX, **A**), the AMPA receptor-selective competitive antagonist CNQX (**B**) and the $GABA_A$ receptor-selective competitive antagonist bicuculline (**C**).

3.2.2 Radial and tangential geometries for analysis of VSDI data

In order to investigate the propagation of assemblies in both the tangential (i.e. along layers) and radial (i.e. across layers) orientation, different geometries were drawn for each cortical area and layer-specific stimulation, see **Figure 5** below. This is because in order to turn a three-dimensional data set into a rasterised image, the VSDI toolbox collapses 2-dimensional space by averaging the data within segments

into a single dimension. In the case of 'tangential' geometries, segments (mid-point width: 120 µm, i.e. encompassing 3 camera pixels, i.e. 2-3 putative mini-columns) run along the orientation of cortical columns (vertical, from LI to LVI), thereby providing an overall indication of the lateral spread of activity across successive segments/columns. 'Radial' geometries on the other hand feature segments which stretch across cortical columns and along layers (horizontal orientation) with mid-point width of 80 µm, i.e. encompassing 2 camera pixels. Tangential geometries consist of unified ROIs, as their purpose was to encompass the entire assembly, while radial geometries feature 2.0-2.4 mm-wide ROIs which are divided in two at the middle, with stimulations delivered to the green ROI. This ROI conformation was chosen because the purpose of radial geometries was to assess the columnar (vertical) spread of activity (green ROI), as well as the lateral spread of activity (red and blue ROIs). All radial and tangential geometries used in this thesis are shown below in **Figure 5**.

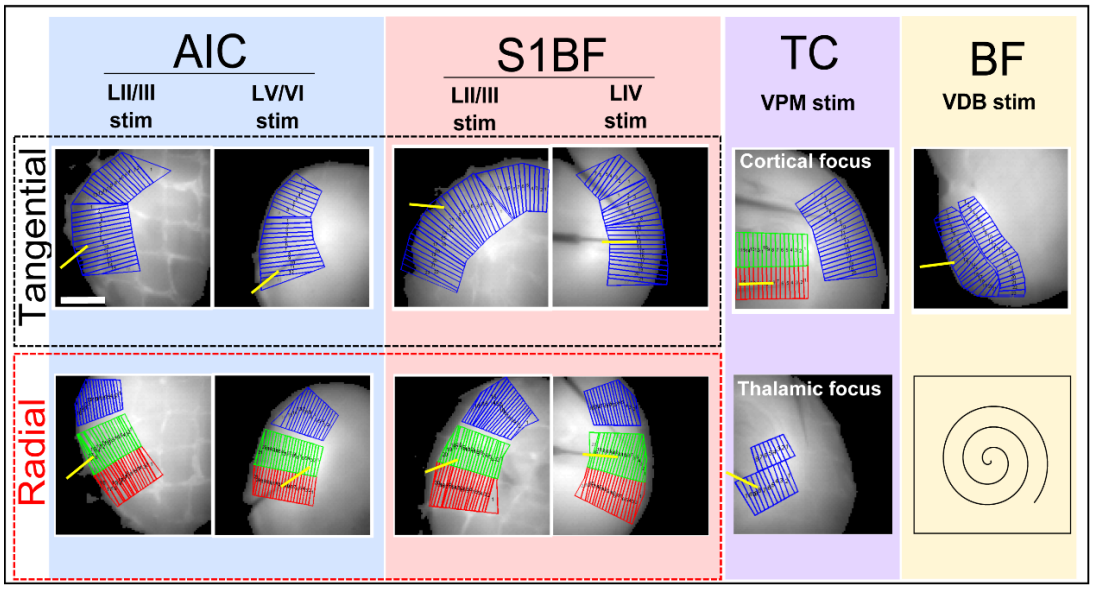

Figure 5: Example geometries for rasterisation of data for analysis of assemblies along layers (tangential) and across layers (radial). AIC: agranular insular cortex; S1BF: primary somatosensory barrel field cortex; S1BF-TC: primary somatosensory barrel field cortex, thalamocortical slice angle; TC: thalamocortical slice; BF: basal forebrain. Yellow lines indicate location and orientation of stimulating electrode tip. 'Radial' geometries all included a double-region ROI in order to highlight columnar spread as well as lateral

facilitation, whereas 'tangential' geometries took in account all layers and focused on the maximum lateral spread of evoked assemblies. BF was only analysed using a tangential ROI since the sub-regions considered here (MV, VDB, HDB) are morphologically thin, therefore not providing enough space for a radial ROI to be drawn, in addition to the fact that the BF, like VPM, does not feature a layered neuronal population organisation. For all slices, the dorsal side of the brain slice is located at the top of the image. Scale bar: 1 mm.

3.3 Results

3.3.1 Somatosensory cortex

a. Direct stimulations to S1BF LIV

Initially, the commonly reported coronal somatosensory cortical slice preparation (S1BF, with LIV stimulation) was investigated. Electrodes were placed between 400 and 450 μm from the pial surface (**Figure 6A**), within the thin band of slightly darker tissue which was often visible under the light microscope when the bath and slice were slightly illuminated from below, i.e. designating the approximate location of LIV. Single-pulse stimulations (30 V, n=7 slices from 4 animals) triggered very fast rises in fluorescence (peak 7-10 ms after stimulation) followed by a slower decay (**Figure 6B**), consistently spreading over a millimetre of tissue tangentially and spanning the entire thickness of the cortex; indicating a facilitated radial spread (**Figure 6Cii vs iii**).

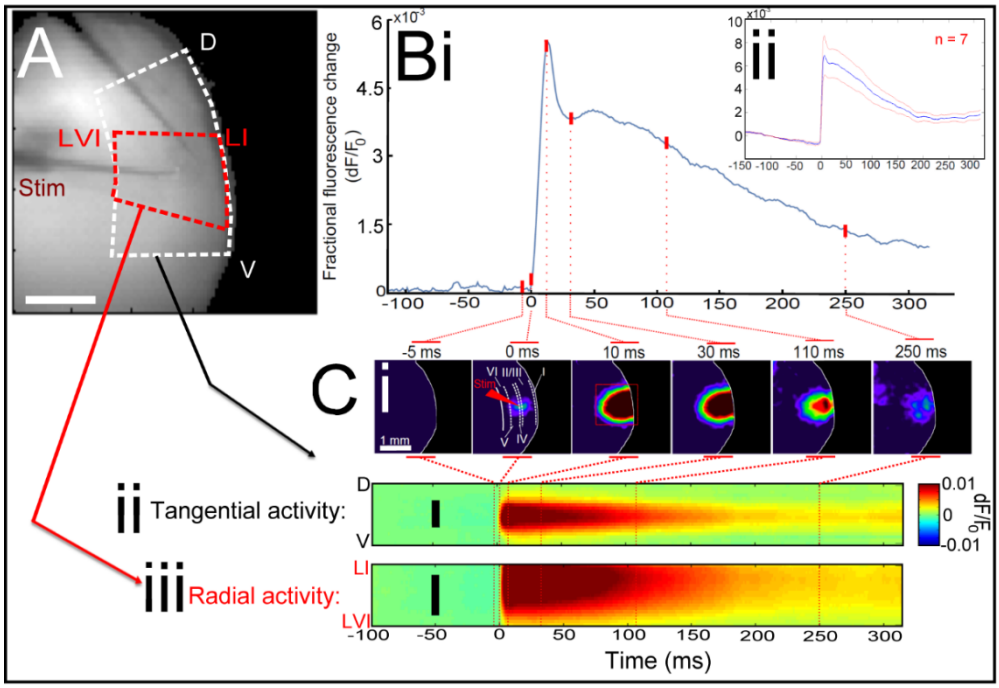

Figure 6: Primary somatosensory cortex response to direct LIV stimulation. **A**. Bright-field view of slice showing the location of the electrode (positioned 400-450 µm from the pial surface), an electrophysiology recording electrode positioned in LII/III as well as the position of the tangential (white) and radial (red) geometries used for analysis. LI – layer I, LVI – layer VI, Stim – stimulation, D – dorsal, V – ventral. Scale bar: 1 mm. **B**. **i**. Single experiment average response evoked from the example slice shown in **A**. **ii**. Overall average response in n=7 experiments (blue trace, S.E.M drawn in red), generated using the tangential (white) geometry in **A**. **C**. **i**. Still-frame visualisation of example VSDI data (captured at 1 kHz frame rate) at key time-points with approximate location of layers (0 ms); red box indicates ROI used to extract trace shown in **Bi**. This same data was then analysed using the VSDI toolbox geometries and compiled into space-time maps of tangential (**ii**) and radial activity (**iii**). Vertical scale-bars represent 1 mm in space.

b. Direct stimulations to S1BF LII-III

In order to investigate layer-specific differences in cortical processing within S1BF, identical experiments were carried out with stimulations delivered in LII/III, where electrodes were placed 100 to 250 µm from the pial surface (**Figure 7A**). Assemblies generated in this fashion (n=8 slices from 5 animals) generated activity patterns which very much resembled those evoked in LIV (**Figure 7B**), both in time course (**Figure 7C**) and spread, yet with less prominent radial spread (**Figure 7Ciii)**. For

data averages of measured values for summed fluorescence, spread and time course of activity, see **Table 4** below.

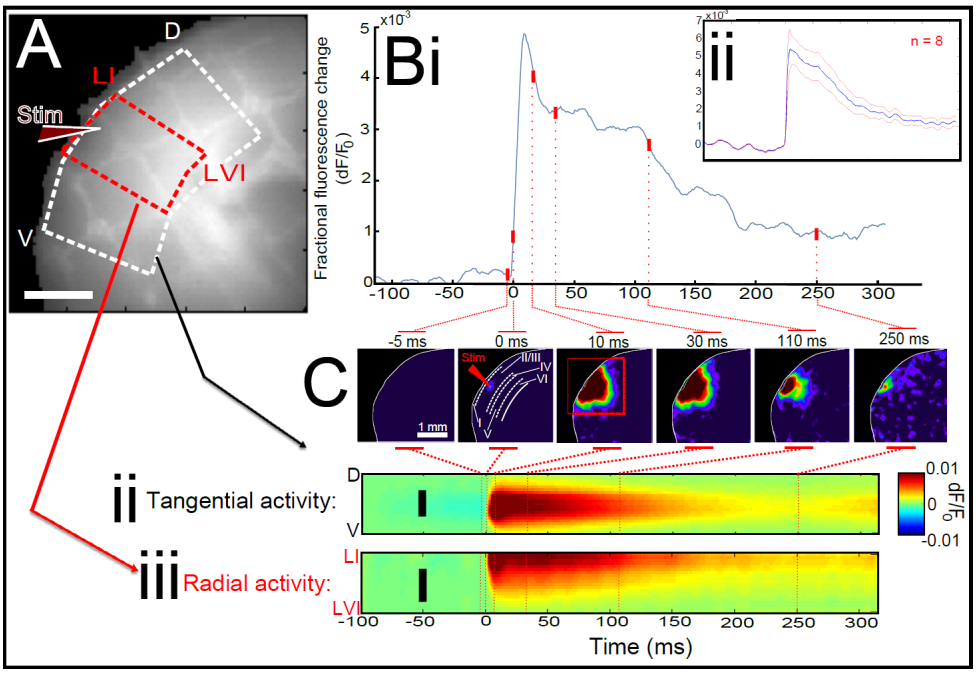

Figure 7: Primary somatosensory cortex response to direct LII/III stimulation. **A**. Bright-field view of slice showing the location of the electrode (positioned 100-250 µm from the pial surface) as well as the position of the tangential (white) and radial (red) geometries used for analysis. LI – layer I, LVI – layer VI, Stim – stimulation, D – dorsal, V – ventral. **B**. **i**. Single experiment average response evoked in the example slice shown in **A**. **ii**. Overall average response in n=8 experiments (blue trace, S.E.M drawn in red), generated using the tangential (white) geometry in **A**. **C**. **i**. Still-frame visualisation of example data at key time-points with approximate location of layers (0 ms); red box indicates ROI used to extract trace shown in **Bi**. This same data was then analysed using the VSDI toolbox geometries and compiled into space-time maps of tangential (**ii**) and radial activity (**iii**). Vertical scale-bars represent 1 mm in space.

c. Thalamically-evoked (remote) assemblies in S1BF

S1BF assemblies were also evoked remotely via thalamic stimulation, using a specific slice angle which conserves functional long-range connectivity. In order to do so, electrodes were placed in the thalamus, within the VPM (**Figure 8A**): it was

not always easy finding this small nucleus within thalamic tissue, only the slight striation of small white matter tracks entering the VPM through the internal capsule and the Rt allowed for identification of the correct location. In order to achieve this, up to three electrode placement trials were performed within a small area (approx. 1.5 x 1.5 mm) in an attempt to produce a robust cortical activation; if no cortical activation could be elicited in this manner, on the fourth trial, the electrode was placed within the white matter of the internal capsule. In such cases, slices gave rise to cortical responses with indistinguishable dynamics from those evoked from VPM: of the 11 experiments presented here in thalamocortical slices (from 9 animals, **Figure 8**), 8 were performed via successful VPM stimulation, while 3 were carried out using white matter stimulation.

S1BF assemblies triggered via remote thalamic stimulation gave rise to distinct profiles of cortical assembly from those evoked via direct stimulation (**Figure 8B**), i.e. consistently activating large areas of cortex (on average reaching over 2 mm laterally along the cortex), featuring multiple hot-spots of activity, often becoming obvious for short time-frames: these were concentrated along LIV, see **Figure 1** above and **Figure 8Ci**, and can be putatively attributed to barrel-center activation. For data averages of measured values for summed fluorescence, spread and time course of activity, see **Table 4** below.

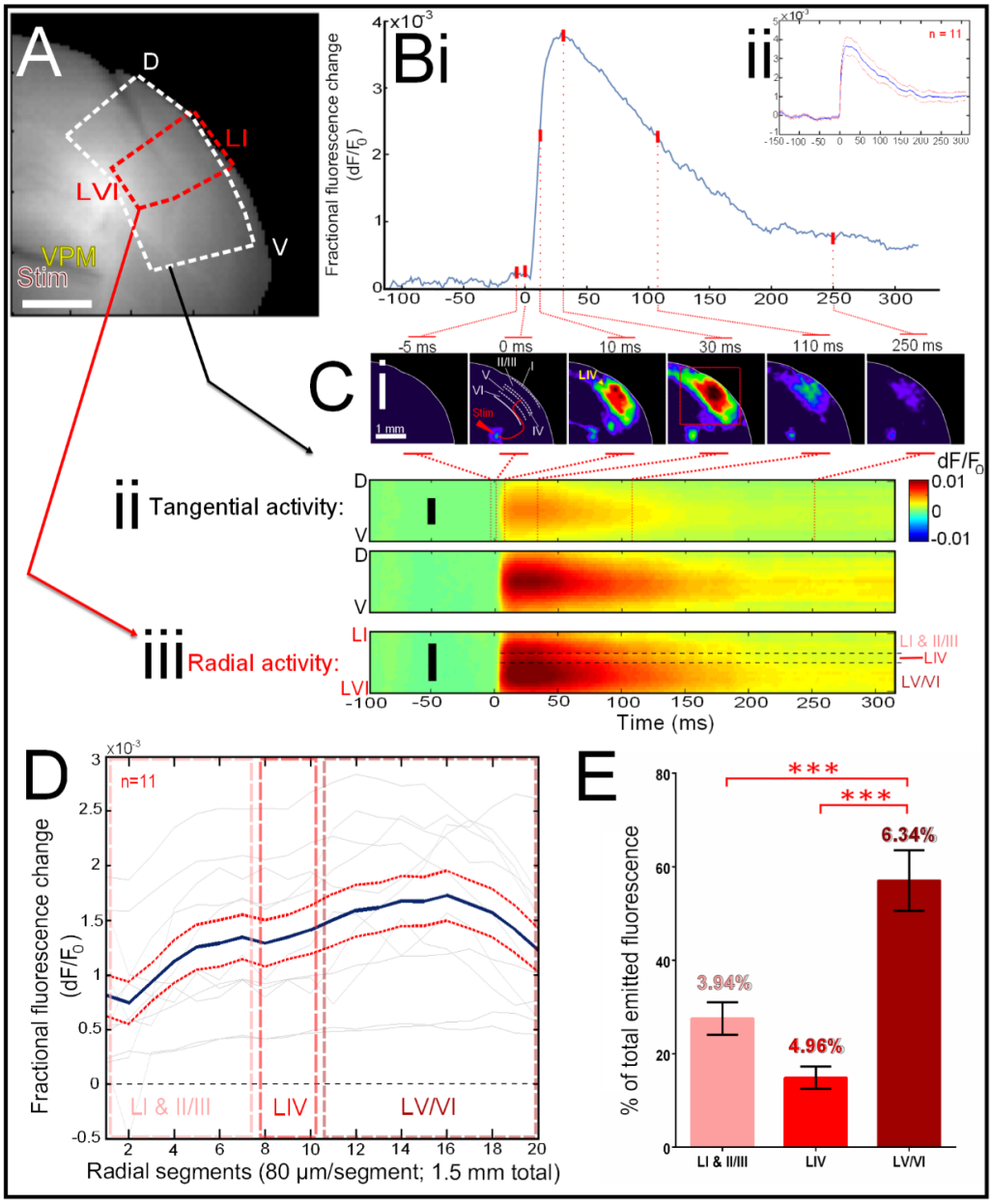

Figure 8: Primary somatosensory cortex response to remote thalamocortical stimulation. **A**. Bright-field view of slice showing the location of the electrode (positioned in VPM), an electrophysiology electrode positioned in LIV (300-350 µm from the pial surface), as well as the position of the tangential (white) and radial (red) geometries used for analysis. LI – layer I, LVI – layer VI, Stim – stimulation, D – dorsal, V – ventral. Scale bar: 1 mm. **B**. **i**. Single experiment average response evoked in the example slice shown in **A**. **ii**. Overall average response in n=11 experiments (blue trace, S.E.M drawn in red), generated using the tangential (white) geometry in **A**. **C**. **i**. Still-frame visualisation of data at key time-points with approximate location of layers (0 ms); red box indicates ROI used to extract trace shown in **Bi**. This same data was then analysed using the VSDI toolbox geometries and compiled into space-time maps of tangential (**ii**) and radial activity (**iii**) with approximate location of LIV (white dashed lines). Note: in **ii**, the same data is shown on two different colour-scales,

the top map is identical to previously-shown data (±0.01 dF/F_0), while the bottom map shows data on half that scale (±0.005 dF/F_0). Vertical scale-bars represent 1 mm in space. **D**. Overall radial profile of activity over space (visualised across layers). Each segment represents 80 μm in radial space. **E**. Histogram of layer-specific fluorescence emission, with average percentage emitted fluorescence per segment showing a greater contribution of deep layers to the overall signal.

- *Responses evoked in S1BF from direct LIV, LII-III and remote thalamic stimulation*

With regards to the temporal profile of remotely activated assemblies, it was found to consist of a fast rise followed by a slower decay phase, yet featuring a lower slope of initial rise phase in addition to a lower overall response amplitude, smoother (more rounded) peak response, and longer time-course (**Figure 9A**). Further differences also became apparent when taking in account the spatial profile of assemblies: whereas direct stimulations produced high-amplitude hotspots of activity around the point of contact of the electrode, and sharp decay with distance, stretching just over a millimetre across, thalamocortical assemblies on the other hand featured wide-reaching, low-amplitude activity with multiple hotspots and a longer duration. Furthermore, when considering radial profile of thalamocortical assemblies: a bi-phasic spatial pattern of activity can be seen where a significantly greater proportion of fluorescence was found to arise from the deeper layers (LV/VI) compared to both superficial (LI & II/III) and granular layers (LIV; **Figure 8D** & **E**; comparison ID: **3.3.1.c.i** – **Table 1**).

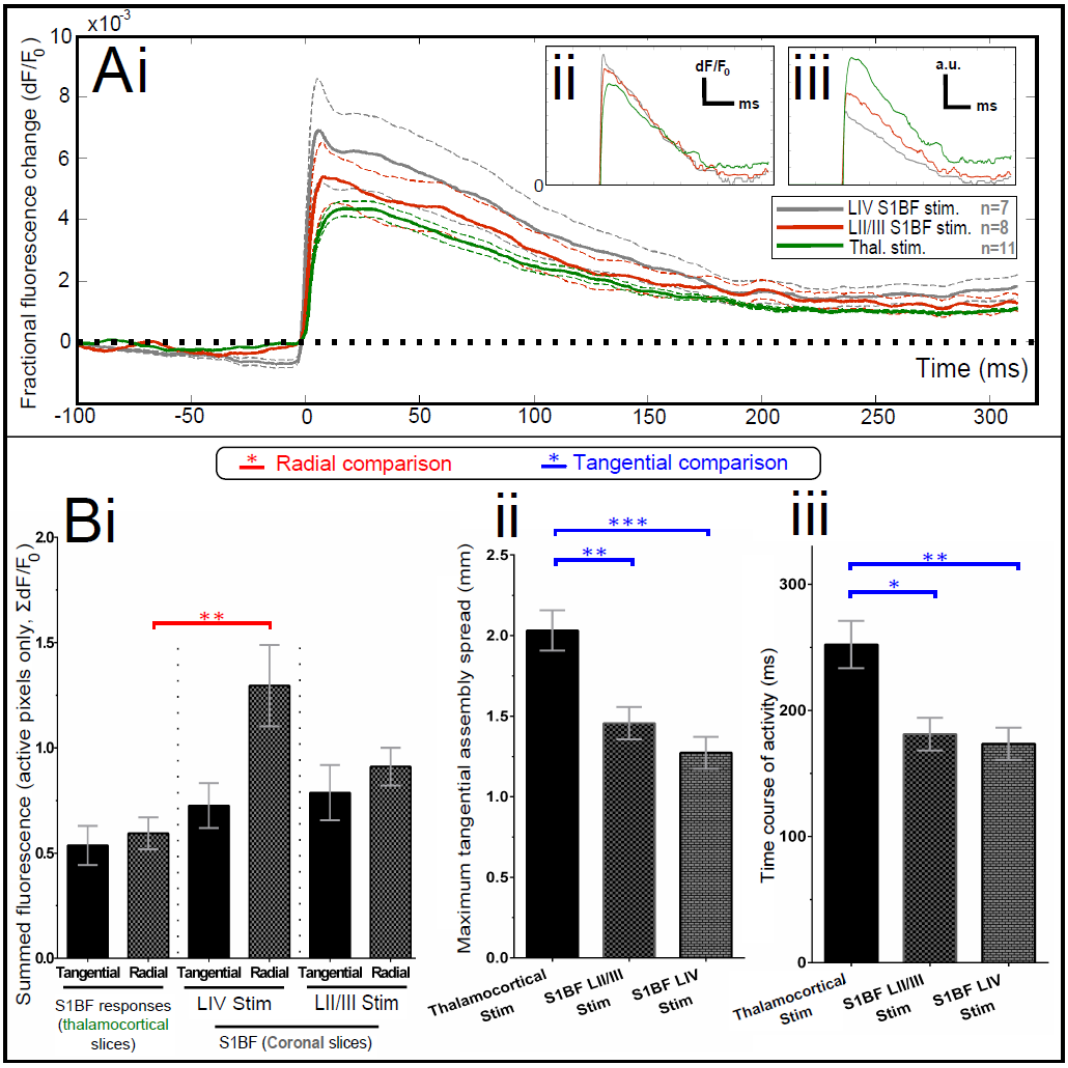

Figure 9: Comparison of activity profiles evoked in Primary somatosensory cortex resulting from direct and remote activation. **A**. Summary time-series of VSDI responses: **i**. Overall average responses evoked via direct LIV, LII/III, and remote VPM stimulation; S.E.M. drawn in dashed lines. **ii**. Traces showing active pixels-only data (threshold: 20% of absolute maximum from respective data sets); scale bars – $1x10^{-3}$ dF/F_0 vertically, 50 ms horizontally. **iii**. Same traces shown once normalised to their respective maxima; scale bars – 20% normalised signal from absolute max vertically, 50 ms horizontally. **B**. Quantification of evoked responses analysed using radial and tangential geometries in S1BF using direct stimulations versus thalamocortical: **i**. Summed fluorescence emitted from active pixels only. **ii**. Lateral spread of assemblies. **iii**. Time course of activity.

For the purpose of directly comparing activity profiles, fluorescence data time series are displayed in three formats: first as an overall average of space-time map fluorescence data (**Figure 9Ai**), secondly as 'active pixels' (**Figure 9Aii**, see

Section 2.7.1.2), and thirdly as normalised (**Figure 9Aiii**), prior to the averaging step. When comparing direct to remote stimulations of the S1BF, thalamocortical activation showed the lowest amount of evoked fluorescence compared to both direct stimulations in tangential and radial geometries, with significant differences found only between the radial activity of LIV direct stimulation and thalamocortical activation (**Table 1,** comparison ID: **3.3.1.c.iii**, **Figure 9Bi**). In addition to this, tangential spread analysis showed that thalamocortical assemblies evoked activity over much greater areas of tissue compared to both LII/III and LIV direct stimulations (**Table 1**, comparison ID: **3.3.1.c.iv**; **Figure 9Bii**). Altogether these observations indicate that assemblies activate preferentially along the columnar axis, while both direct stimulation paradigms gave rise to assemblies featuring higher intensity and lower lateral spread than thalamocortical assemblies. In addition to this, thalamocortical assemblies were indeed found to spread over a much wider area of cortex all the while exhibiting lower fluorescence values than direct stimulations, i.e. featuring a more diffuse cortical activation.

Finally, it was found that both LII/III and LIV assemblies were significantly shorter in duration compared to thalamocortical assemblies (**Table 1,** comparison ID: **3.3.1.c.v**; **Figure 9Biii**), while direct stimulation responses did not differ significantly in time course among themselves (**Table 1,** comparison ID: **3.3.1.c.v**; **Figure 9Biii**). Furthermore, a small number of thalamocortical experiments (2 out of 11) produced assemblies that were found to remain active for a longer period of time than the recording window provided (312 ms+), and that both of these occurrences took place only in experiments where the VPM (rather than the white matter) was stimulated; these observations hinted at the possible presence of functional thalamocortical loops reciprocally linking the S1BF to the VPM.

- *Characterisation of functional thalamocortical and corticothalamic connections*

Upon more rigorous scrutiny of the VPM and resulting cortical VSDI traces (**Figure 10Bi**), peculiar deflections can be seen within their response time series which appeared in phase and recurring at approximately 20 Hz, with 5 apparent in-phase oscillations during the first 250 ms following stimulation at t=0 (**Figure 10Bi**, red rectangles). The possible presence of recurrent excitation via activation of thalamocortical loops could also explain the much increased average time course of thalamocortical activity compared to that of direct stimulations. This representation however remains only a very coarse-grain and imprecise detection of the possible presence of active and reciprocal thalamocortical loops, and the focus here was more on identifying and characterising the origin of connections which successfully innervate the cortex (thalamocortical) and the thalamus (corticothalamic projections), rather than to study their precise inter-dependent dynamics.

In so doing, active thalamocortical slices were stimulated with a cortical 30 Volts pulse both in their respective LV/VI (n=6 slices, from 6 animals) and LIV (n=6 slices, from 5 animals). Additionally, coronal slices (LV/VI stimulation, n=5 slices, from 5 animals) were used as a control to confirm the activity seen in thalamocortical slices was specific to the thalamic innervation or arose as a result of artefactual effects related to stimulation delivery in the bath, and in all cases with attention given to thalamic responses (see geometries utilised in **Figure 10Aiii–vi**). Thalamic geometries were designed to encompass both the VPM and POm, as cortical efferents target both regions. All preparations except from coronal slices triggered activity within the thalamus (**Figure 10Bii**), confirming that this activity was indeed brought about by the presence of functional corticothalamic efferents activated either ortho- or antidromically. More specifically, LV/VI stimulation in active thalamocortical slices produced VPM responses (summed fluorescence:

0.237 ± 0.037 $\Sigma dF/F_0$; time-course: 243.7 ± 21.1 ms) which appeared lower in magnitude of emitted fluorescence as well as showing a faster return to baseline than in direct-VPM stimulation, yet none of those differences were found to be significant (n=8, summed fluorescence: 0.370 ± 0.050 $\Sigma dF/F_0$; time-course: 245.5 ± 19.8 ms; **Table 2,** comparison IDs: **3.3.1.c.vi** and **3.3.1.c.xi**; **Figure 10Ci** & **Cii**). In all cases, VPM responses featured low amplitude, as shown by the need to half the colour-scale (from ±0.01 to ±5x10^{-3} dF/F_0, **Figure 10Biii–vi**) for the spatio-temporal responses (space-time maps) to become apparent compared to cortical spatio-temporal data; this was true for remotely as well as directly activated VPM assemblies, suggesting a lower ceiling effect in the magnitude of evoked assemblies in VPM. Activity evoked via LIV stimulation (0.128 ± 0.023 $\Sigma dF/F_0$; **Figure 10Ci**) showed responses in only 5 of the 6 tested slices which, overall, emitted significantly lower fluorescence than direct stimulations to the VPM (**Table 2,** comparison ID: **3.3.1.c.vi**, **Figure 10Ci**), but not significantly different compared to LV/VI thalamocortical slices stimulation (**Table 2**, comparison ID: **3.3.1.c.vi**, **Figure 10Ci**), despite a visibly less robust response. The time-course of activity evoked in VPM by LIV stimulation in thalamocortical slices (118.8 ± 13.4 ms; **Figure 10Ci**) however was found to be significantly shorter than those induced in both direct VPM, and remote LV/VI stimulation (**Table 2**, comparison ID: **3.3.1.c.ix**, **Figure 10Ciii**), suggesting fewer corticothalamic afferents were stimulated in this manner. Finally, it was confirmed that these active connections functioned using excitatory glutamatergic transmission via AMPA receptors, with significant reductions in both summed fluorescence (**Table 2**, comparison ID: **3.3.1.c.vii–x Figure 10Cii**) and time-course of VPM responses (**Table 2**, comparison ID: **3.3.1.c.xii–xv**, **Figure 10Civ**) as a result of CNQX perfusion in all experimental paradigms tested with the exception of coronal LV/VI stimulations, where no VPM responses were elicited. Altogether these results confirm that active corticothalamic projections were present in the thalamocortical slices preparation used here, and that VPM activity was more

easily triggered when stimulating LV/VI directly rather than stimulating LIV, suggesting a greater presence of corticothalamic cell bodies in these particular layers.

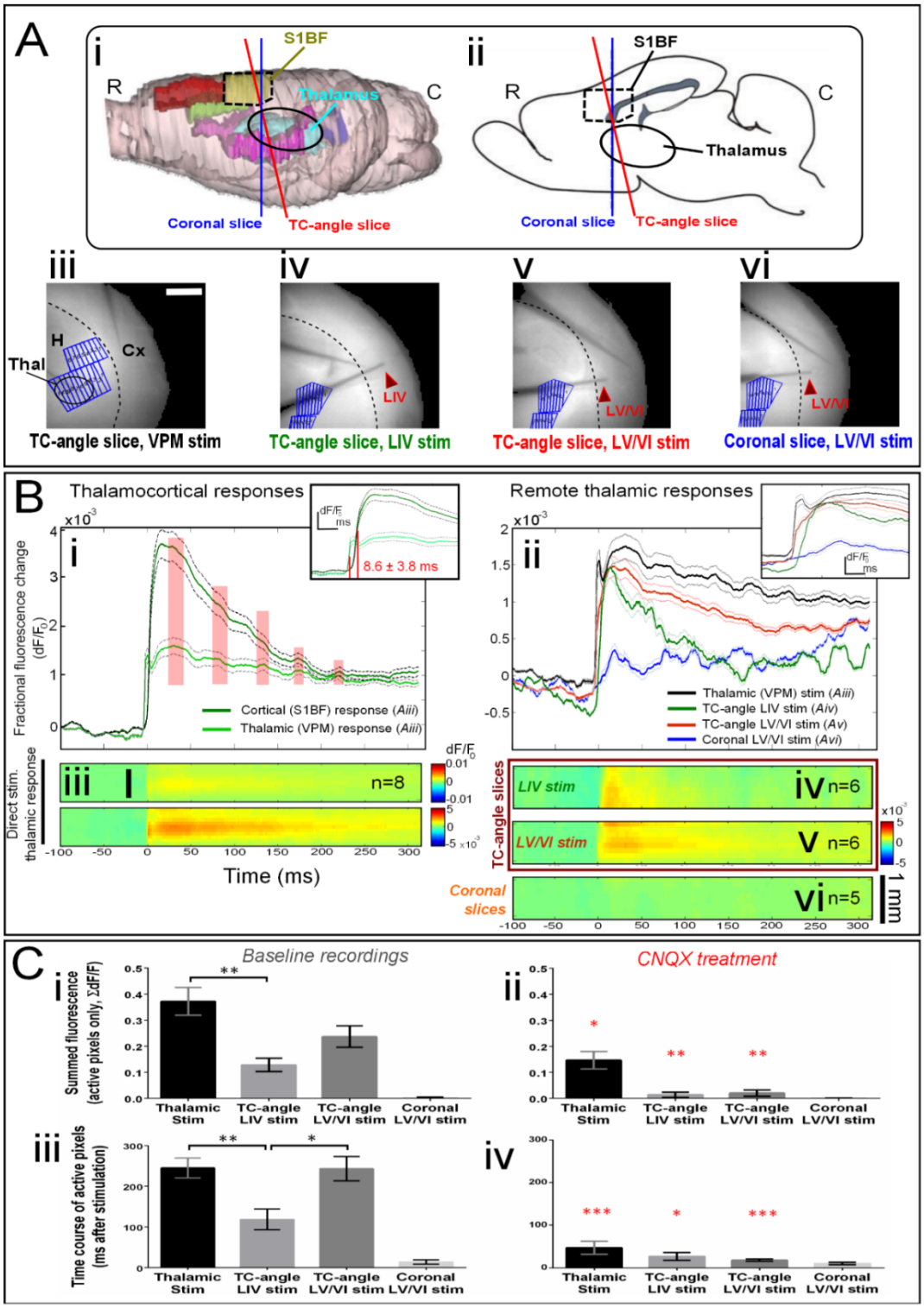

Figure 10: Investigation of the thalamocortical system. **A**. **i**. 3-D representation of rat brain with key areas such as the primary somatosensory cortex (S1BF, yellow) and thalamus (blue); adapted from (He et al., 2012). 'R' – rostral, 'C' – caudal. **ii**. Schematic representation of rat brain indicating the approximate locations of S1BF and Thalamus. Blue line represents coronal plane; red line represents the thalamocortical-slice plane. **iii-vi**. Bright-field view of slices: **iii**. Thalamocortical slices with VPM stimulation; **iv**. Thalamocortical slices with cortical LIV stimulation. **v**. Thalamocortical slices with LV/VI stimulation. **vi**. Coronal slice with LV/VI stimulation. Each were analysed using the same specially-designed thalamus analysis geometry for comparison. **B**. **i**. Responses evoked from a single 60V stimulus applied directly either in VPM (n=8) (light-green time-series) and resulting S1BF activation (n=11: n=8 evoked from VPM, n=3 evoked from white matter stimulation; dark green time-series), note the bumpy time-series oscillations which appear in phase. Inset: close up view of responses' rise and plateau, including annotation of the average half-maximum time-points (red) between thalamic and cortical responses (n=8); vertical scale bar: $1x10^{-3}$ dF/F_0, horizontal scale bar: 15 ms. **ii**. Time series of responses evoked in thalamus (VPM) from either direct or remote cortical stimulation in different preparations (see **A**). Inset: close up view of responses' rise and plateau; vertical scale bar: $0.5x10^{-3}$ dF/F_0, horizontal scale bar: 15 ms **iii**. Space-time map relating to the thalamus data (light-green trace) shown in **i** (left space-time maps) and **ii** (right space-time maps). Note: the same data is shown on two different colour-scales, the top map is identical to previously-shown data (±0.01 dF/F_0), while the bottom map shows data on half that scale (±0.005 dF/F_0). Of the n=11 thalamocortical experiments, only 8 were used for the VPM response analysis as the others were stimulated in the white matter rather than the VPM. Vertical scale bar indicates 1 mm in space. **C**. **i**. Quantification of summed fluorescence evoked in each preparation listed in **A** (baseline conditions). **ii**. Quantification of summed fluorescence from each preparation following CNQX (20 μM) application. **iii**. Quantification of the time-course of active pixels detected in each preparation listed in **A** (baseline conditions). **iv**. Quantification of time-course of active pixels detected in each preparation. Black stars represent statistical comparisons between preparations in their baseline condition, while red stars indicate significant differences of each preparations' baseline levels with their CNQX treated response.

- **Section 3.3.1,** parts **a, b** & **c** – *Statistical analysis and parameters*

Thalamocortical responses and comparison against S1BF LII/III- & LIV-evoked responses									
Comparison ID	**Figure panel**	**Data set comparison**	**Test parameter(s)**	**Statistical test employed**	***p* value**	**Geometry**	***F*- or *t*-statistics**	**Post-hoc test (adjusted) *p* value**	**Significance level**
3.3.1.c.i	8E	**Thalamocortical: LI & II/III vs LIV fluorescence**	% of total fluorescenec emission	one-way ANOVA	$p < 0.0001$	Radial	$F(2, 30) = 23.66$	$p = 0.1256$	n.s.
		Thalamocortical: LI & II/III vs LV/VI fluorescence	% of total fluorescenec emission					$p = 0.0002$	***
		Thalamocortical: LIV vs LV/VI fluorescence	% of total fluorescenec emission					$p < 0.0001$	***
3.3.1.c.ii	9Bi	**S1BF LII/III stim vs TC**	Summed fluorescence	one-way ANOVA	$p = 0.2300$	Tangential	$F(2, 23) = 1.568$	$p = 0.4169$	n.s.
		S1BF LIV vs TC	Summed fluorescence					$p = 0.2523$	n.s.
		S1BF LII/III stim vs LIV stim	Summed fluorescence					$p = 0.9272$	n.s.
3.3.1.c.iii	9Bi	**S1BF LII/III stim vs TC**	Summed fluorescence	one-way ANOVA	$p = 0.0017$	Radial	$F(2, 23) = 8.565$	$p = 0.1935$	n.s.
		S1BF LIV vs TC	Summed fluorescence					$p = 0.0011$	**
		S1BF LII/III stim vs LIV stim	Summed fluorescence					$p = 0.1259$	n.s.
3.3.1.c.iv	9Bii	**S1BF LII/III stim vs TC**	Lateral spread	one-way ANOVA	$p = 0.0002$	Tangential	$F(2,23) = 12.30$	$p = 0.0041$	**
		S1BF LIV vs TC	Lateral spread					$p = 0.0004$	***
		S1BF LII/III stim vs LIV stim	Lateral spread					$p = 0.5627$	n.s.
3.3.1.c.v	9Biii	**S1BF LII/III stim vs TC**	Time-course of active pixels	one-way ANOVA	$p = 0.0033$	Tangential	$F(2, 23) = 7.400$	$p = 0.0129$	*
		S1BF LIV vs TC	Time-course of active pixels					$p = 0.0080$	**
		S1BF LII/III stim vs LIV stim	Time-course of active pixels					$p = 0.9508$	n.s.

Table 1: Significance statistics for data parameters recorded in S1BF in direct vs remote thalamocortical stimulations. For all ANOVAs performed, Dunnett's multiple comparisons test were performed as post-hoc analysis.

Thalamic responses, comparisons of directly and remotely-evoked activity									
Comparison ID	**Figure panel**	**Data set comparison**	**Test parameter(s)**	**Statistical test employed**	***p* value**	**Geometry**	***F-* or *t*-statistics**	**Post-hoc test (adjusted) *p* value**	**Significance level**
3.3.1.c.vi	10Ci	**Thalamic stim vs TC-angle LIV (VPM response)**	Summed fluorescence	one-way ANOVA	*p* = 0.0002	Tangential	F(3,21) = 14.32	***p* = 0.0018**	**
		Thalamic stim vs TC-angle LV/VI (VPM response)	Summed fluorescence					***p* = 0.2894**	**n.s.**
		TC angle LIV vs TC-angle LV/VI (VPM response)	Summed fluorescence					***p* = 0.1337**	**n.s.**
3.3.1.c.vii	10Cii	**Thalamic stim response CNQX treatment**	Summed fluorescence	two-tailed paired t-test	***p* = 0.0249**	Tangential	*t* (7) = 2.844	n/a	*
3.3.1.c.viii	10Cii	**TC-angle LIV stim thalamic response CNQX treatment**	Summed fluorescence		***p* = 0.0046**	Tangential	*t* (5) = 4.861	n/a	**
3.3.1.c.ix	10Cii	**TC-angle LV/VI stim thalamic response CNQX treatment**	Summed fluorescence		***p* = 0.0016**	Tangential	*t* (5) = 6.225	n/a	**
3.3.1.cx	10Cii	**Coronal LV/VI stim response CNQX treatment**	Summed fluorescence		***p* = 0.4731**	Tangential	*t* (4) = 0.7913	n/a	**n.s.**
3.3.1.c.xi	10Ciii	**Thalamic stim vs TC-angle LIV**	Time-course of activity	one-way ANOVA	*p* = 0.0055	Tangential	*F* (2, 17) = 7.190	***p* =0.0082**	**
		Thalamic stim vs TC-angle LV/VI	Time-course of activity					***p* = 0.9986**	**n.s.**
		TC angle LIV vs TC-angle LV/VI	Time-course of activity					***p* = 0.0144**	*
3.3.1.c.xii	10Civ	**Thalamic stim response time-course CNQX treatment**	Time-course of activity	two-tailed paired t-test	***p* = 0.0005**	Tangential	*t* (7) = 6.091	n/a	***
3.3.1.c.xiii	10Civ	**TC-angle LIV stim thalamic response time-course CNQX treatment**	Time-course of activity		***p* = 0.0100**	Tangential	*t* (5) = 4.030	n/a	*
3.3.1.c.xiv	10Civ	**TC-angle LV/VI stim thalamic response time-course CNQX treatment**	Time-course of activity		***p* = 0.0007**	Tangential	*t* (5) = 7.413	n/a	***

Table 2: Significance statistics for data parameters recorded in thalamus from direct and remote activation (corticothalamic investigations), under control and CNQX treatments. For all ANOVAs performed, Dunnett's multiple comparisons test were performed as post-hoc analysis.

- **Section 3.3.1**, part **d** – *Statistical analysis and parameters*

S1BF responses evoked by direct stim in TC-angle slices and comparison against coronally-evoked responses									
Comparison ID	**Figure panel**	**Data set comparison**	**Test parameter(s)**	**Statistical test employed**	***p* value**	**Geometry**	***F-* or *t*-statistics**	**Post-hoc test (adjusted) *p* value**	**Significance level**
3.3.1.d	11F	**Cor LII/III v Cor LIV**	ROI2/ROI1 fluorescence ratio	one-way ANOVA	p < 0.0001	Tangential	*F* (2, 23) = 16.52	***p* = 0.6410**	**n.s.**
		Cor LII/III v Thalamocortical	ROI2/ROI1 fluorescence ratio					***p* = 0.0006**	***
		Cor LIV v Thalamocortical	ROI2/ROI1 fluorescence ratio					***p* < 0.0001**	***

Table 3: Statistical tests table for columnar spread statistical analysis. For all ANOVAs performed, Dunnett's multiple comparisons test were performed as post-hoc analysis.

- *Preferential spread across cortical columns*

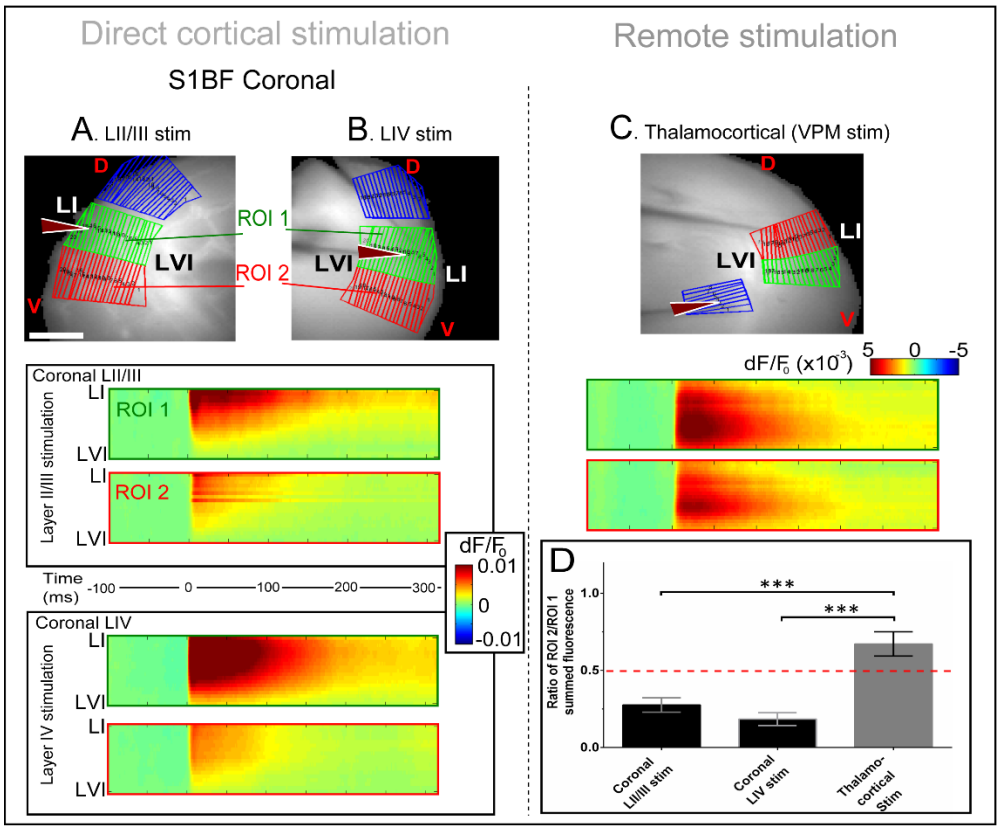

Figure 11: Analysis of layer-specific spread of activity. Two radial geometries (approximately 1 mm in width and 1.6 mm in length) were used to sample the evoked summed fluorescence within a region encompassing the site of stimulation (ROI 1, green) in comparison to an adjacent, ventral location (ROI 2, red) of cortex where assemblies were triggered via stimulation of coronal S1BF slices LII/III (**A**) and LIV (**B**), and VPM (**C**). Scale bar (**A**) represent 1 mm in space. LI – Layer I; LVI – Layer VI. Furthermore, fluorescence values were expressed as a percentage of ROI2/ROI1 overall fluorescence (**D**) in order to assess the extent of variability of lateral assembly spread in these preparations. Red dotted line represents 50% level of fluorescence in ROI2 compared to ROI1.

Since the lateral spread of assemblies seemed to be the crucial factor in differentiating between the overall fluorescence emission of assemblies, a further analysis was carried out in order to establish the proportion of fluorescence emitted from a radial geometry located over the locus of stimulation (ROI 1, green region, **Figure 11**) in relation to a second ROI of equal size positioned adjacent to ROI 1 in the ventral direction (ROI 2, red region). Such an operation provided an indication of the amount of fluorescence transmitted to neighbouring columns within the slice,

with respect to that which was emitted in the columns primarily targeted by direct stimulation. Assemblies generated in slices via direct stimulation of the S1BF produced the lowest percentage, as suggested in previous findings indicating lower levels of lateral spread (see **Figure 11**), with assemblies generated in LII/III and LIV both emitting approximately 15-30% of their respective ROI 1 fluorescence within their adjacent ROI 2 (LII/III: 27.6 ± 5.8%; LIV: 18.4 ± 6.2%). Most remarkably however, were the proportional spread of assemblies evoked via remote VPM stimulation (67.1 ± 9.8%), corroborating previous findings that this preparation produced the largest-spreading assemblies. This relative proportion of transmitted fluorescence was so extensive that it was found to be significantly different, unsurprisingly, from that of assemblies evoked in direct LII/III (**Table 3**, comparison ID: **3.3.1.d**, **Figure 11F**) and LIV stimulation (**Table 3**, comparison ID: **3.3.1.d**). This data representation highlights the very different nature of assemblies triggered via either neuronal or electrical stimulation, i.e. remote or direct activation, respectively.

3.3.2 Agranular Insular Cortex

a. Direct stimulations LII-III

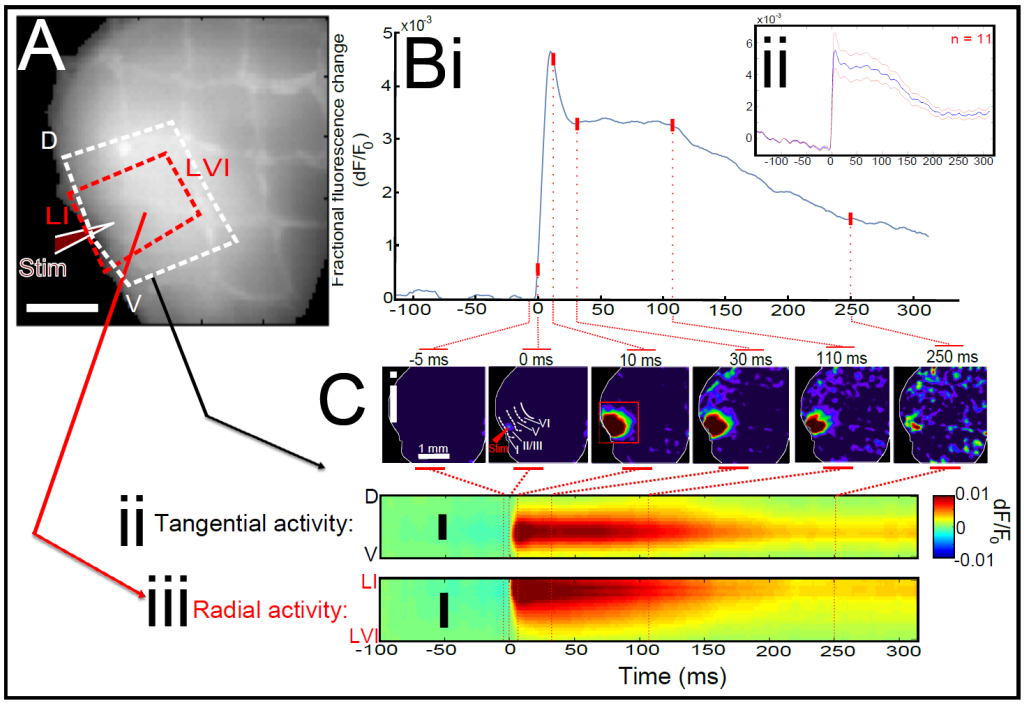

Figure 12: Agranular insular cortex response to direct LII/III stimulation. **A**. Bright-field view of slice showing the location of the electrode (positioned 100-300 µm from the pial surface) as well as the position of the tangential (black) and radial (red) geometries used for analysis. LI – layer I, LVI – layer VI, Stim – stimulation, D – dorsal, V – ventral. **B**. **i**. Single experiment average response evoked in the example slice shown in **A**. **ii**. Overall average response in n=7 experiments (blue trace, S.E.M drawn in red), generated using the tangential (white) geometry in **A**. **C**. **i**. Still-frame visualisation of data at key time-points with approximate location of layers (0 ms); red box indicates ROI used to extract trace shown in **Bi**. This same data was then analysed using the VSDI toolbox geometries and compiled into space-time maps of tangential (**ii**) and radial activity (**iii**). Vertical scale-bars represent 1 mm in space.

For stimulation of LII/III in AIC, electrodes were placed 100-300 µm from the pial surface, and approximately 200 µm from the rhinal fissure (in a dorsal direction, **Figure 12A**). Assemblies evoked in this fashion produced characteristic assembly patterns, as previously observed using direct stimulation, consisting of a fast rise (6-12 ms) followed by a gradual decay (**Figure 12B**). Summed fluorescence readings for assemblies were, as expected, larger in the radial compared to tangential

orientation (see **Table 4**, below for quantification of mean values). However, in the case of this particular stimulation site, interestingly, assemblies did not reach their maximum lateral spread until 50-100 ms after stimulus delivery, and following which responses quickly subsided (**Figure 12C**). This plateau in AIC activity, where all other (S1BF) profiles of activity show slow decreases, is apparent on the resulting time-series, which show a second 'peak' in activity between 70-120 ms (92.4 ± 19.8 ms) after stimulation (**Figure 12B**) – these experiments were repeated a few extra times (n=11 slices, from 8 animals) in order to confirm that this was a true effect rather than due to some outliers, the majority of which showed this same profile.

b. Direct stimulations LV/VI

For LV/VI stimulation in AIC (n=6 slices, from 4 animals), electrodes were placed 450-600 μm from the pial surface, approximately 200 μm from the rhinal fissure (in the dorsal direction). Assemblies evoked from deep layers (LV/VI) showed a more familiar profiles of rise (5-11 ms) and decay, i.e. with no plateau/rebound excitation in the response, yet featuring some of the highest summed fluorescence values recorded so far, both in the tangential and radial geometries (**Figure 13**). These large fluorescence readings did not arise as a result of an increased time-course of assembly dynamics which remained correlated to those of other assemblies, but rather as a result of the large spread exhibited by LV/VI assemblies. For data averages of measured values for summed fluorescence, spread and time course of activity, see **Table 4** below.

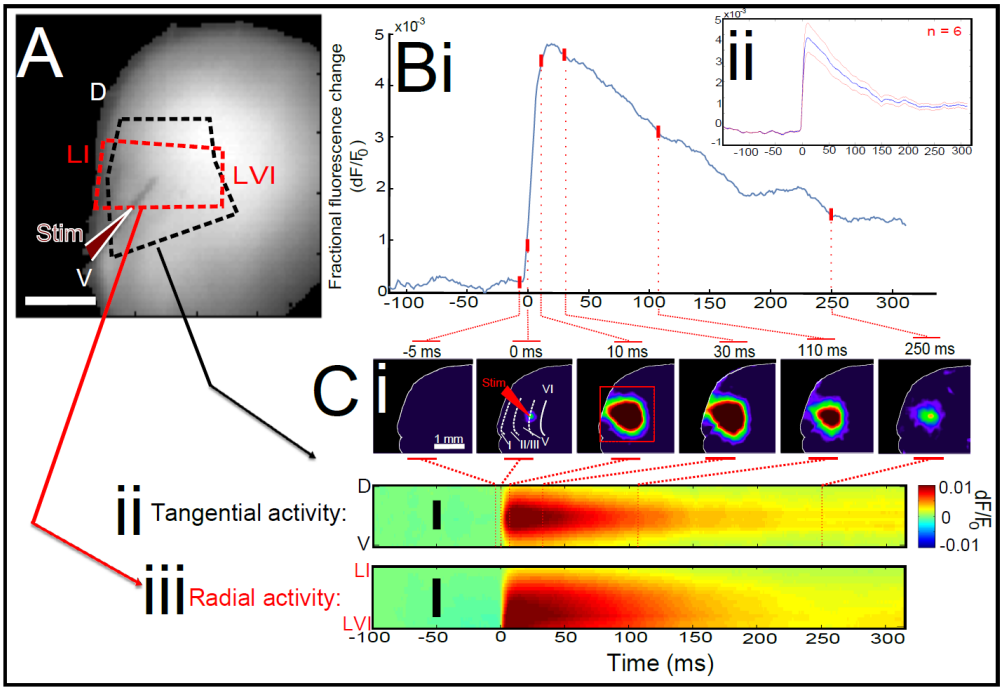

Figure 13: Agranular insular cortex response to direct LV/VI stimulation. **A**. Bright-field view of slice showing the location of the electrode (positioned 550-750 µm from the pial surface) as well as the position of the tangential (black) and radial (red) geometries used for analysis. LI – layer I, LVI – layer VI, Stim – stimulation, D – dorsal, V – ventral. **B**. **i**. Single experiment average response evoked in the example slice shown in **A**. **ii**. Overall average response in n=7 experiments (blue trace, S.E.M drawn in red), generated using the tangential (black) geometry in **A**. **C**. **i**. Still-frame visualisation of data at key time-points with approximate location of layers (0 ms); red box indicates ROI used to extract trace shown in **Bi**. This same data was then analysed using the VSDI toolbox geometries and compiled into space-time maps of tangential (**ii**) and radial activity (**iii**). Vertical scale-bars represent 1 mm in space.

Preparation	Repeat trials (*n*)	Geometry	Mean summed fluorescence (dF/F0)	S.E.M.	Mean lateral spread (mm)	S.E.M.	Mean Time course (ms)	S.E.M.
S1BF (coronal) LIV stim	7	Tangential	**0.727**	0.085	**1.27**	0.09	**173.6**	8.4
		Radial	**1.296**	0.154				
S1BF (coronal) LII/III stim	8	Tangential	**0.787**	0.097	**1.46**	0.09	**181.3**	12.2
		Radial	**0.911**	0.066				
Thalamocortical S1BF activation	11	Tangential	**0.537**	0.089	**2.03**	0.12	**252.3**	17.9
		Radial	**0.594**	0.073				
AIC LII/III stim	11	Tangential	**0.868**	0.051	**1.44**	0.11	**231.5**	12.6
		Radial	**1.152**	0.079				
AIC LV/VI stim	6	Tangential	**0.989**	0.113	**1.85**	0.14	**197**	8
		Radial	**1.071**	0.054				

Table 4: Mean and S.E.M. measurements for summed fluorescence (tangential and radial geometries), lateral spread and time course of activity. Data parameters were only recorded from tangential geometries (except for summed fluorescence where radial measurements are also included).

- *Comparison of assemblies evoked via direct stimulation in S1BF and AIC*

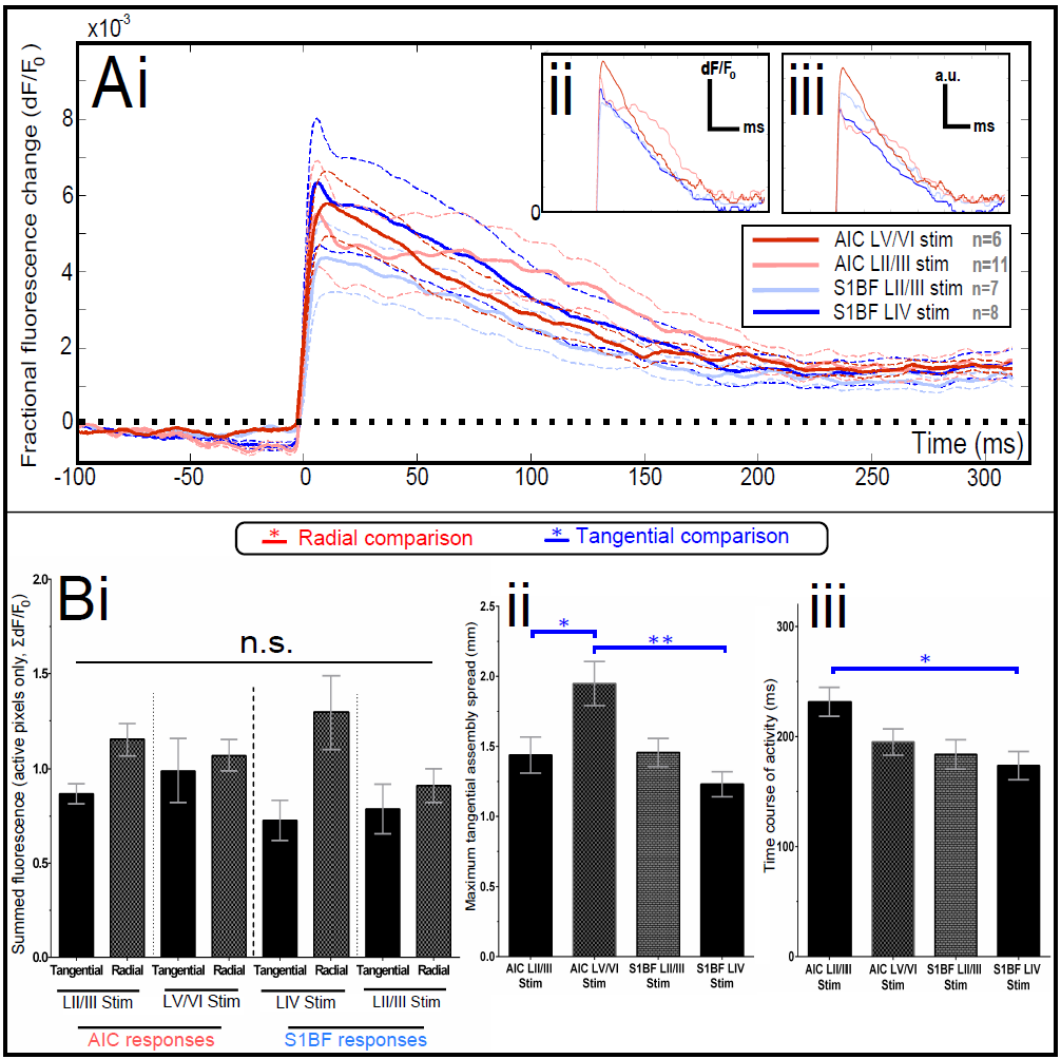

Figure 14: Comparison of activity profiles evoked in Primary somatosensory (S1BF) and agranular insular cortex (AIC) cortices. **A**. Summary time-series of VSDI responses: **i**. Overall average responses evoked via direct LII/III & V/VI (AIC, blue traces) and LII/III & LIV (S1BF, red traces) stimulation; S.E.M. drawn in dashed lines. **ii**. Traces showing active pixels-only data (threshold: 20% of absolute maximum from respective data sets); scale bars – $2x10^{-3}$ dF/F_0 vertically, 50 ms horizontally. **iii**. Same traces shown once normalised to their respective maxima; scale bars – 20% normalised signal from absolute max vertically, 50 ms horizontally. **B**. Quantification of evoked responses analysed using radial and tangential geometries evoked in coronal S1BF versus AIC: **i**. Summed fluorescence emitted from active pixels only. **ii**. Lateral spread of assemblies.

When comparing the activity profiles of assemblies evoked in coronal S1BF and AIC slices (**Figure 14Ai**), all were found to evoke similar levels of fluorescence, however when isolating active pixels, both LII/III and LV/VI AIC traces show higher readings than S1BF, yet none are significantly different (**Table 5**, comparison ID: **3.3.2.a.i**, **Figure 14Bi**). **Figure 14Aiii** shows this higher trend of emitted fluorescence remains even when the data is normalised, indicating a higher amount of fluorescence per pixel in LV/VI assemblies. Lateral spread analysis however, revealed that assemblies evoked in AIC LV/VI displayed significantly higher spread than those triggered in AIC LII/III (**Table 5**, comparison ID: **3.3.2.a.iii**, **Figure 14Bii**) and S1BF LIV (**Table 5**, comparison ID: **3.3.2.a.iii**, **Figure 14Bii**), with comparisons between AIC LV/VI and S1BF LII/III also nearly reaching significance ($p = 0.0671$; **Table 5**, comparison ID: **3.3.2.a.iii**, **Figure 14Bii**), these findings provide a possible explanation for the slightly increased overall emitted fluorescence from AIC assemblies compared to those evoked in S1BF. Finally, with regards to those of AIC LII/III assemblies, responses were found to last significantly longer than those evoked in S1BF LIV (**Table 5**, comparison ID: **3.3.2.a.iv**, **Figure 14iii**), providing a further explanation for the overall increased fluorescence recorded compared to S1BF (**Figure 14Bi** vs **Biii**). Together, these observations indicate that population responses in S1BF and AIC arise as a result of a similar over-arching process of columnar and macro-columnar activation, yet in doing so exhibit intricate region-specific differential dynamics, which are evident in both superficial and deeper layers, and characterised by a greater time-course of activity in the former, and a larger lateral spread in the latter.

- **Section 3.3.2**, parts **a** and **b** – *Statistical analysis and parameters*

S1BF and AIC responses evoked by direct stim in Layers II/III & IV and II/III and V/VI (respectively)									
Comparison ID	**Figure panel**	**Data set comparison**	**Test parameter(s)**	**Statistical test employed**	***p* value**	**Geometry**	***F*- or *t*-statistics**	**Post-hoc test (adjusted) *p* value**	**Significance level**
3.3.2.a.i	14Bi	**AIC LII/III v LV/VI**	Summed fluorescence	one-way ANOVA	$p = 0.0035$	Tangential	$F(3, 28) = 0.9783$	$p = 0.8559$	n.s.
		AIC LII/III v S1BF LIV	Summed fluorescence					$p = 0.7423$	n.s.
		AIC LII/III v S1BF LII/III	Summed fluorescence					$p = 0.9443$	n.s.
		AIC LV/VI v S1BF LIV	Summed fluorescence					$p = 0.3839$	n.s.
		AIC LV/VI v S1BF LII/III	Summed fluorescence					$p = 0.6269$	n.s.
		S1BF LIV v LII/III	Summed fluorescence					$p = 0.9791$	n.s.
3.3.2.a.ii	14Bi	**AIC LII/III v LV/VI**	Summed fluorescence	one-way ANOVA	$p = 0.1710$	Radial	$F(3, 28) = 1.795$	$p = 0.8623$	n.s.
		AIC LII/III v S1BF LIV	Summed fluorescence					$p = 0.9446$	n.s.
		AIC LII/III v S1BF LII/III	Summed fluorescence					$p = 0.3054$	n.s.
		AIC LV/VI v S1BF LIV	Summed fluorescence					$p = 0.6252$	n.s.
		AIC LV/VI v S1BF LII/III	Summed fluorescence					$p = 0.8392$	n.s.
		S1BF LIV v LII/III	Summed fluorescence					$p = 0.1602$	n.s.
3.3.2.a.iii	14Bii	**AIC LII/III v LV/VI**	Lateral spread	one-way ANOVA	$p = 0.0081$	Tangential	$F(3,28) = 4.795$	$p = 0.0370$	*
		AIC LII/III v S1BF LII/III	Lateral spread					$p = 0.9994$	n.s.
		AIC LII/III v S1BF LIV	Lateral spread					$p = 0.6166$	n.s.
		AIC LV/VI v S1BF LII/III	Lateral spread					$p = 0.0671$	n.s.
		AIC LV/VI v S1BF LIV	Lateral spread					$p = 0.0052$	**
		S1BF LII/III v S1BF LIV	Lateral spread					$p = 0.6030$	n.s.
3.3.2.a.iv	14Biii	**AIC LII/III v LV/VI**	Time-course of active pixels	one-way ANOVA	$p = 0.0338$	Tangential	$F(3, 28) = 3.329$	$p = 0.3476$	n.s.
		AIC LII/III v S1BF LII/III	Time-course of active pixels					$p = 0.0972$	n.s.
		AIC LII/III v S1BF LIV	Time-course of active pixels					$p = 0.0412$	*
		AIC LV/VI v S1BF LII/III	Time-course of active pixels					$p = 0.9606$	n.s.
		AIC LV/VI v S1BF LIV	Time-course of active pixels					$p = 0.8016$	n.s.
		S1BF LII/III v S1BF LIV	Time-course of active pixels					$p = 0.9665$	n.s.

Table 5: Significance statistics for comparisons of data parameters recorded in S1BF and AIC in direct coronal stimulations. For all ANOVAs performed, Dunnett's multiple comparisons test were performed as post-hoc analysis.

3.3.3 Basal forebrain

a. Basal forebrain response

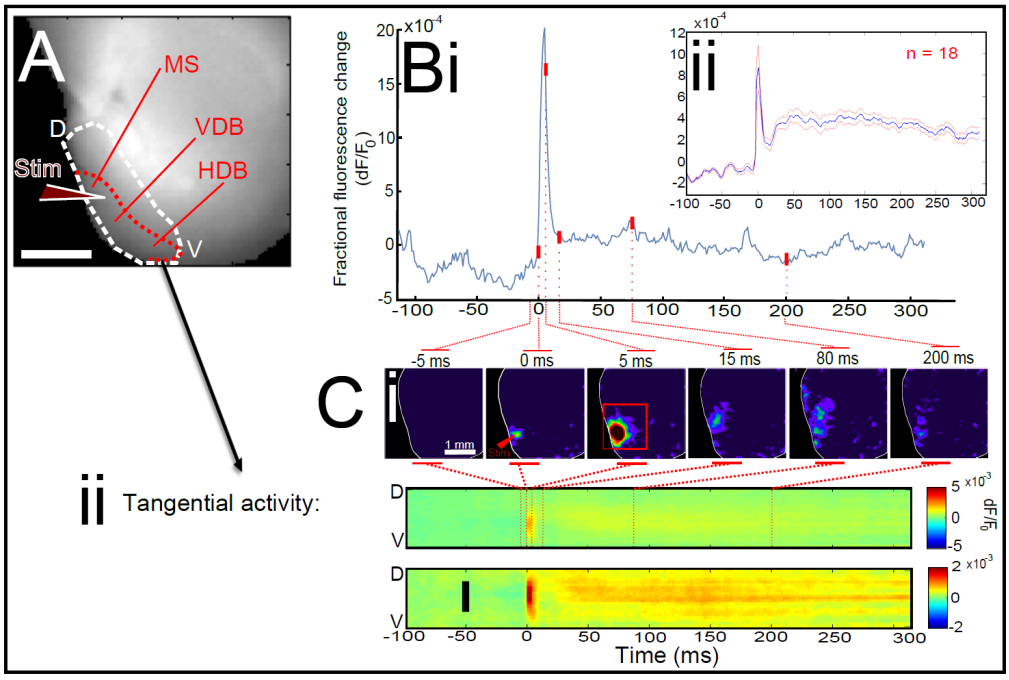

Figure 15: Basal forebrain response to direct stimulation within the horizontal band of broca (HDB). **A**. Bright-field view of slice showing the location of the electrode (positioned 50-100 µm from the pial surface) as well as the position of the tangential geometry used for analysis. Stim – stimulation, D – dorsal, V – ventral. **B**. **i**. Single experiment average response evoked in the example slice shown in **A**. **ii**. Overall average response in n=18 experiments (blue trace, S.E.M drawn in red), generated using the tangential (white) geometry in **A**. **C**. **i**. Still-frame visualisation of data at key time-points with approximate location of the MS-dBB sub-nuclei (0 ms); red box indicates ROI used to extract trace shown in **Bi**. This same data was then analysed using the VSDI toolbox geometries and compiled into space-time maps of tangential (**ii**) activity; the activity evoked in basal forebrain was of very low amplitude, and therefore space-time maps are shown with very narrow colour-bar scales ($\pm 5 \times 10^{-3}$ dF/F_0 – top, and $\pm 2 \times 10^{-3}$ dF/F_0 – bottom space-time map). Vertical scale-bars represent 1 mm in space.

Responses evoked via VDB stimulations (n=18 slices, from 14 animals), with stimulating electrodes placed 20-100 µm from the pial surface, evoked responses which showed a very different profile from that usually evoked in other preparations. That is, instead of a fast rise followed by a slower decline, fluorescence

readings in BF assemblies featured a fast rise which was immediately mirrored by an equally-fast decay, then followed by a long-latency rebound in activity (**Figure 15B**). This activity was characterised by a fast depolarisation spreading circularly from the locus of stimulation, with peak active pixel spread of 1.14 ± 0.08 mm, before quickly receding back, leaving behind isolated loci of activity appearing sporadically within the MS-dBB (**Figure 15Ci**). Moreover, basal forebrain assemblies consistently produced low-amplitude fluorescence deflections, well below the usual range for cortical assemblies (Badin et al., 2016). This was further highlighted to be a key difference when displaying space-time maps, where the colour-scale had to be reduced to a range of $\pm 2 \times 10^{-3}$ (from an already reduced level of $\pm 5 \times 10^{-3}$, see **Figure 10** above) for the spatio-temporal assembly response to become apparent in this data representation (top vs bottom space-time map, **Figure 15Cii**). These responses were found to last 242.3 ± 12.8 ms, with 2 of the 18 experiments showing activity patterns which lasted longer than the recording window (truncated at 312 ms). Basal forebrain data was only analysed using a tangential geometry with reduced segment mid-width (80 μm), as the physical thickness of the MS-dBB complex is small (<500 μm from pial surface to edge of MS-dBB) as well as the fact this brain sub-region is not organised into layers, but rather as an aggregation of smaller nuclei and cell clusters (Sotty et al., 2003; Wang et al., 2006).

b. Comparison of sub-cortical evoked responses

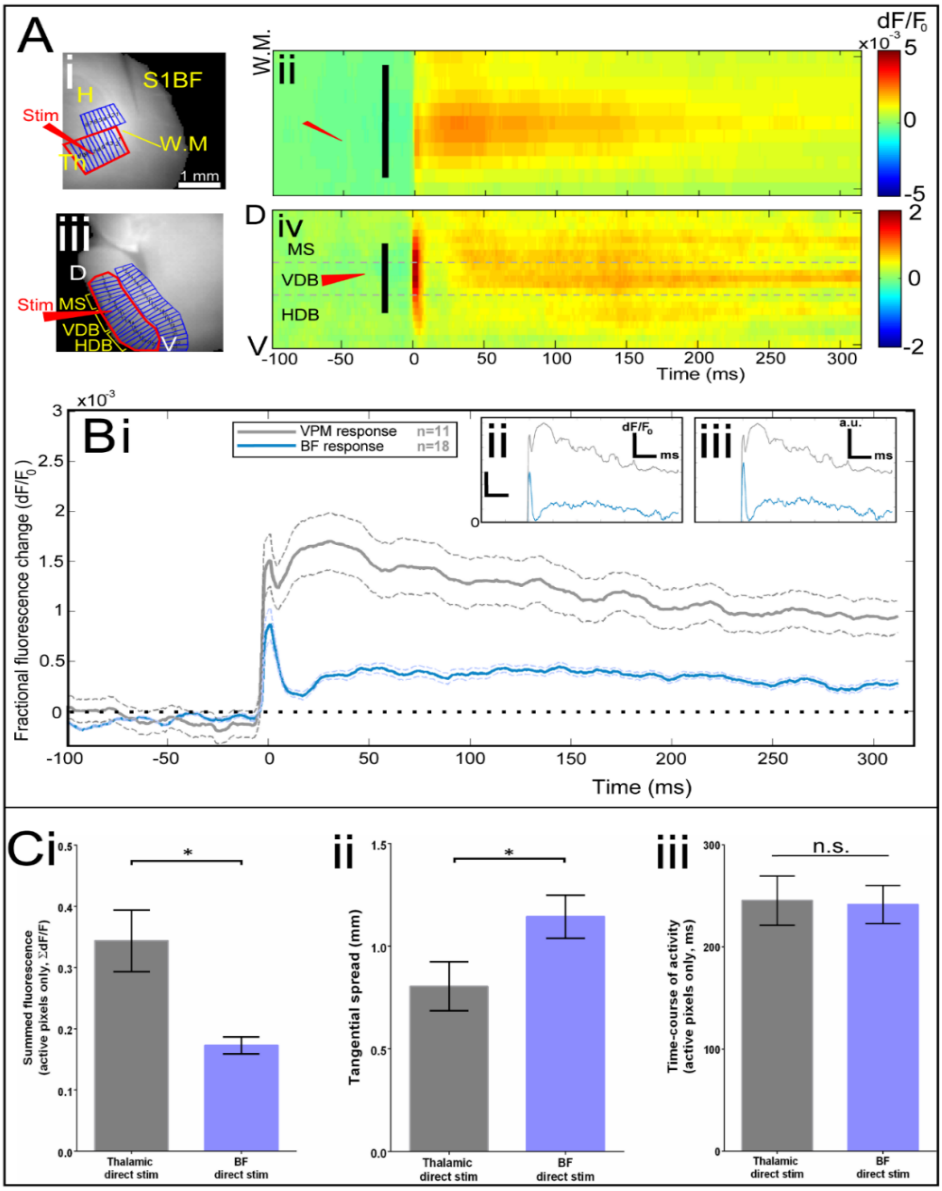

Figure 16: Comparison of assemblies evoked in basal forebrain (BF) and VPM. **A**. Space-time maps showing spatio-temporal profile of activity evoked in VPM (**i** & **ii**) and basal forebrain (**iii** & **iv**) plotted using different colour-scales to show clear evoked response – both brain sub-regions produced much reduced activity profiles compared to cortical responses. **B**. Summary time-series of VSDI responses: **i**. Overall average responses evoked via direct HDB (BF, blue trace, n=18) and VPM (grey trace, n=8) stimulation; S.E.M. drawn in dashed lines. **ii**. Traces showing active pixels-only data (threshold: 20% of absolute maximum from respective data sets); scale bars – $4x10^{-4}$ dF/F_0 vertically, 50 ms horizontally. **iii**. Same traces shown once normalised to their respective maxima; scale bars – 20% normalised signal from absolute max vertically, 50 ms horizontally. **C**. Quantification of evoked responses evoked in BF versus VPM: **i**. Summed fluorescence emitted from active pixels only. **ii**. Lateral spread of activity. **iii**. Time-course of activity.

Comparison of assembly parameters recorded from BF and VPM assemblies showed that overall, BF stimulation evoked even lower levels of summed fluorescence than VPM (**Table 6**, comparison ID: **3.3.3.i**, **Figure 16Bi**). These differences were not found to arise as a result of a longer time-course of assembly activity (**Table 6**, comparison ID: **3.3.3.iii**, **Figure 16Biii**), yet controversially showed a greater spread in BF (**Table 6**, comparison ID: **3.3.3.ii**, **Figure 16Bii**). The overall spatio-temporal profile of evoked assemblies also differs greatly, with VPM assemblies showing a sustained response over the entire recording window, while BF assemblies show a return to baseline 15-25 ms after stimulus delivery, then followed by diffuse rebound in activity. Together these observations highlight fundamentally-different dynamics of population activity in these two sub-cortical regions, and even greater differences compared to cortical responses.

- **Section 3.3.3** – *Statistical analysis and parameters*

Comparison of activity evoked in sub-cortical structures (basal forebrain vs VPM									
Comparison ID	**Figure panel**	**Data set comparison**	**Test parameter(s)**	**Statistical test employed**	***p* value**	**Geometry**	***F*- or *t*-statistics**	**Post-hoc test (adjusted) *p* value**	**Significance level**
3.3.3.i	16Ci	**Direct BF vs direct VPM responses**	Summed fluorescence	two-tailed un-paired t-test (with Welch's correction)	***p* = 0.0108**	Tangential	$t(8.097) = 3.291$	n/a	*
3.3.3.ii	16Cii	**Direct BF vs direct VPM responses**	Lateral spread		***p* = 0.0474**	Tangential	$t(17.76) = 2.131$	n/a	*
3.3.3.iii	16Ciii	**Direct BF vs direct VPM responses**	Time-course of activity		***p* = 0.9001**	Tangential	$t(15.53) = 0.1276$	n/a	**n.s.**

Table 6: Significance statistics for data parameters recorded in basal forebrain and VPM using direct tissue stimulations.

- **Section 3.3.4** – *Statistical analysis and parameters*

Pharmacological characterisation of neuronal assembly dynamics									
Comparison ID	**Figure panel**	**Data set comparison**	**Test parameter(s)**	**Statistical test employed**	***p* value**	**Geometry**	***F*- or *t*-statistics**	**Post-hoc test (adjusted) *p* value**	**Significance level**
3.3.4.a.i	17Di	**AIC vs S1BFstim (TTX treatement)**	Summed fluorescence	one-way ANOVA	*p* = 0.0458	Tangential	$F(2,13) = 3.946$	***p* = 0.3867**	**n.s.**
		AIC vs Thalamocortical stim (TTX treatement)	Summed fluorescence					***p* = 0.3786**	**n.s.**
		S1BF vs Thalamocortical stim (TTX treatement)	Summed fluorescence					*p* = 0.0369	*
3.3.4.a.ii	17Dii	**AIC vs S1BFstim (TTX treatement)**	Lateral spread	one-way ANOVA	*p* = 0.0052	Tangential	$F(2,13) = 8.112$	***p* = 0.8552**	**n.s.**
		AIC vs Thalamocortical stim (TTX treatement)	Lateral spread					*p* = 0.0205	*
		S1BF vs Thalamocortical stim (TTX treatement)	Lateral spread					*p* = 0.0072	**
3.3.4.a.iii	17Diii	**AIC vs S1BFstim (TTX treatement)**	Time-course of activity	one-way ANOVA	*p* = 0.0005	Tangential	$F(2,13) = 14.55$	***p* = 0.8244**	**n.s.**
		AIC vs Thalamocortical stim (TTX treatement)	Time-course of activity					*p* = 0.0008	***
		S1BF vs Thalamocortical stim (TTX treatement)	Time-course of activity					*p* = 0.0025	**
3.3.4.b	18C	**AIC vs TC response (Bic treatement)**	Summed fluorescence	two-tailed un-paired t-test	*p* = 0.003	Tangential	$t(9) = 5.590$	n/a	***

Table 7: Significance statistics for comparison of data parameters recorded in AIC LII/III stimulation and S1BF via direct LII/III and remote VPM stimulations during treatment with TTX and Bicuculline. For all ANOVAs performed, Dunnett's multiple comparisons test were performed as post-hoc analysis.

3.3.4 Characterisation of neuronal activity within assemblies

In an attempt to characterise further the molecular substrates governing the population activity patterns seen here, classic experiments involving specific blockers were carried out. For these experiments, a single preparation from each cortical area under investigation was chosen (AIC LII/III, S1BF LIV and thalamocortical), with the assumption that any drug-related effects seen could be readily extrapolated to assemblies evoked in other layers.

a. Dependence on sodium channel activity

First, TTX was used in order to abolish all impulse conduction along nerve fibres. In all cases, TTX treatment produced near-total silencing of evoked assemblies with on average 89.6 ± 7.3% (AIC), 81.8 ± 9.1% (S1BF) and 95.2 ± 3.9% (thalamocortical) decreases in summed fluorescence compared to control for assemblies evoked in each of AIC LII/III (n=5 from 3 animals), S1BF LIV (n=5 from 4 animals) and thalamocortical preparations (n=6 from 5 animals; **Figure 17Di**). The silencing actions of sodium channel blockade were characterised by reduced spread, with 81.4 ± 5.3% (AIC), 78.3 ± 6.2% (S1BF) and 97.5 ± 1.6% (thalamocortical) decreases in tangential reach of evoked assemblies compared to control (**Figure 17Dii**). These differences were further echoed in the decreases seen in the time course of evoked assemblies (**Figure 17Diii**): 33.1 ± 5.8% (AIC), 38.8 ± 4.9% (S1BF) and 78.2 ± 10.1% (thalamocortical) decreases from control. Additionally, thalamocortical activation of the S1BF was found to be more extensively inhibited by CNQX than those measured for direct stimulation parameters (**Figure 17Di–iii**; **Table 7**, comparison ID: **3.3.4.a**). Together with the results presented for CNQX action (**Figure 10C,** above), these observations

demonstrate that assemblies arise from action potential propagation along nerve fibers, communicated to post-synaptic cells mainly via fast glutamatergic transmission at the micro-scale, giving rise to the meso-scale assemblies.

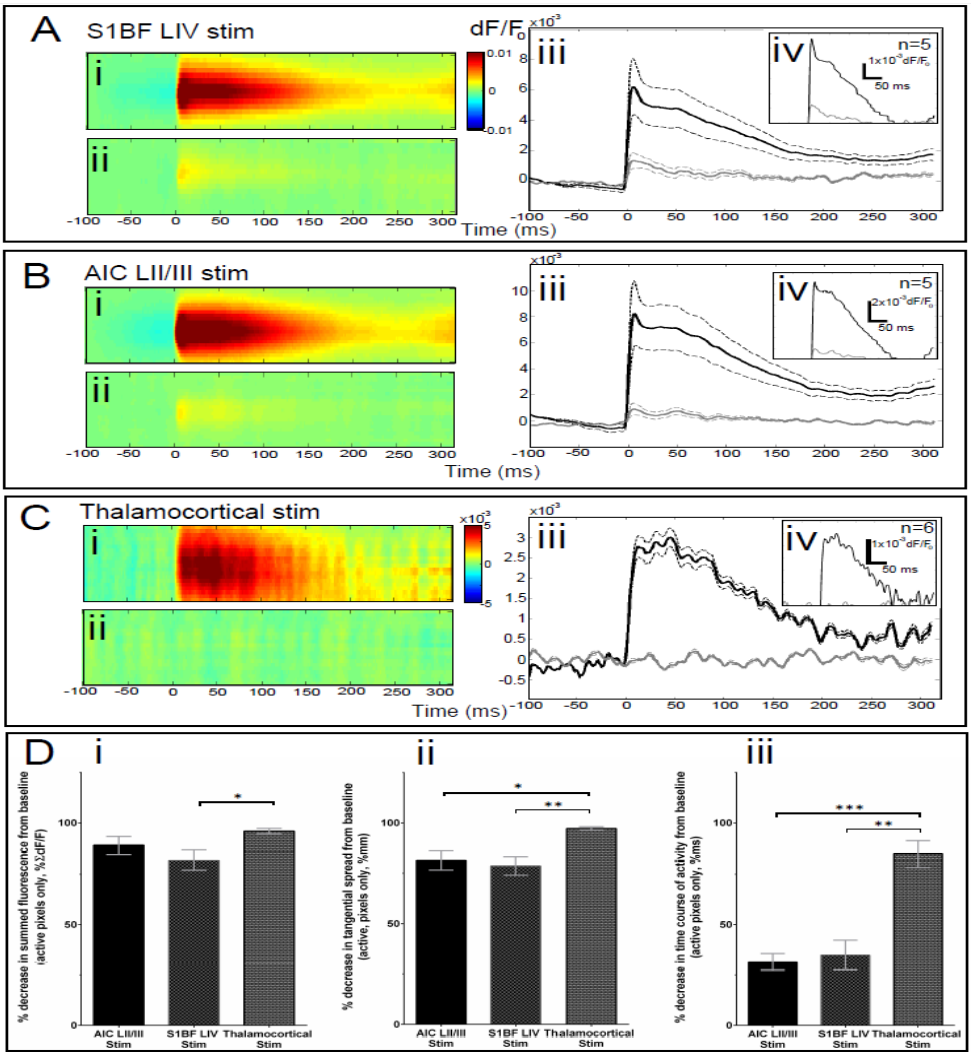

Figure 17: Effect of tetrodotoxin (TTX) on assembly dynamics. **A**. S1BF experiments (n=5) showing a standard baseline response from LIV stimulation (**i**) and that elicited under TTX (15 μM) treatment (**ii**). This data is recapitulated as time-series (**iii**), with S.E.M. drawn in dashed lines: black is baseline response, grey represents the response in the presence of TTX, while inset (**iv**) represents the time series active pixels only. **B**. Identical experiments as shown in **A** carried out via AIC LII/III stimulation: baseline response (**i**) is almost totally abolished under TTX treatment (**ii**), as can also be seen from the time series (**iii**) as well as those of active pixels (**iv**). **C**. Identical sets of experiments carried out with thalamocortical slices, where in this case both the space-time maps (**i** & **ii**) and time series (**iii** &**iv**) show no activity at all upon TTX treatment. **D**. Quantification of the percent decrease in TTX-treated response parameters relative to their respective baseline levels in AIC LII/III, S1BF LIV and TC in (**i**) overall summed fluorescence, (**ii**) lateral spread and (**iii**) time course of activity.

b. Local network activity is shaped by fast GABAergic control

Further to the identification of cellular machinery essential for the generation and propagation of neuronal communication, experiments were also conducted in order to assess the mechanisms involved in controlling, shaping and terminating neuronal communication: GABAergic inhibition (Isaacson & Scanziani, 2011). To do so, slices were perfused with aCSF containing bicuculline (Bic, **Figure 18**). Many studies have already investigated the effects of disinhibition in S1BF, in particular with stimulations delivered directly to LIV (Berger et al., 2007; Petersen & Sakmann, 2001) which all showed large, aberrantly-spreading activity, it was therefore attempted to reproduce this disinhibited response profile here using AIC and thalamocortical preparations (**Figure 18A** and **B**, respectively). Bic induced surprising changes to the dynamics of evoked assemblies: AIC LII/III stimulation produced assemblies which emitted 396 ± 24% more fluorescence than in their control responses (**Figure 18C**), yet activity was seen to propagate slower across slices (**Figure 18Ai** vs **ii**), and did so with preferential dorsal spread, as could be seen already in the control response.

Thalamocortical responses on the other hand showed even greater increases in evoked assembly magnitudes, with an average 713 ± 53% increases in summed fluorescence from control level (**Figure 18C**); here too the propagation of activity in the cortex was slowed down compared to control responses (**Figure 18Bi** vs **ii**). The delayed responses of both preparations becomes even more obvious when taking in account their VSDI time-series, which showed clear delays between onset of control (black traces) and Bic responses (red). The drastic increases in fluorescence signal were shown to arise as a result of much increased amplitudes of voltage changes, as well as with the emergence of epileptiform activity within the

LFP records (**Figure 18D**, arrows) of nearly all AIC Bic-treated slices (green trace) compared to control (blue). None of the Bic-treated slices produced assemblies which remained confined within the analysis ROI or that subsided within the recording epoch, therefore neither of those parameters could be measured.

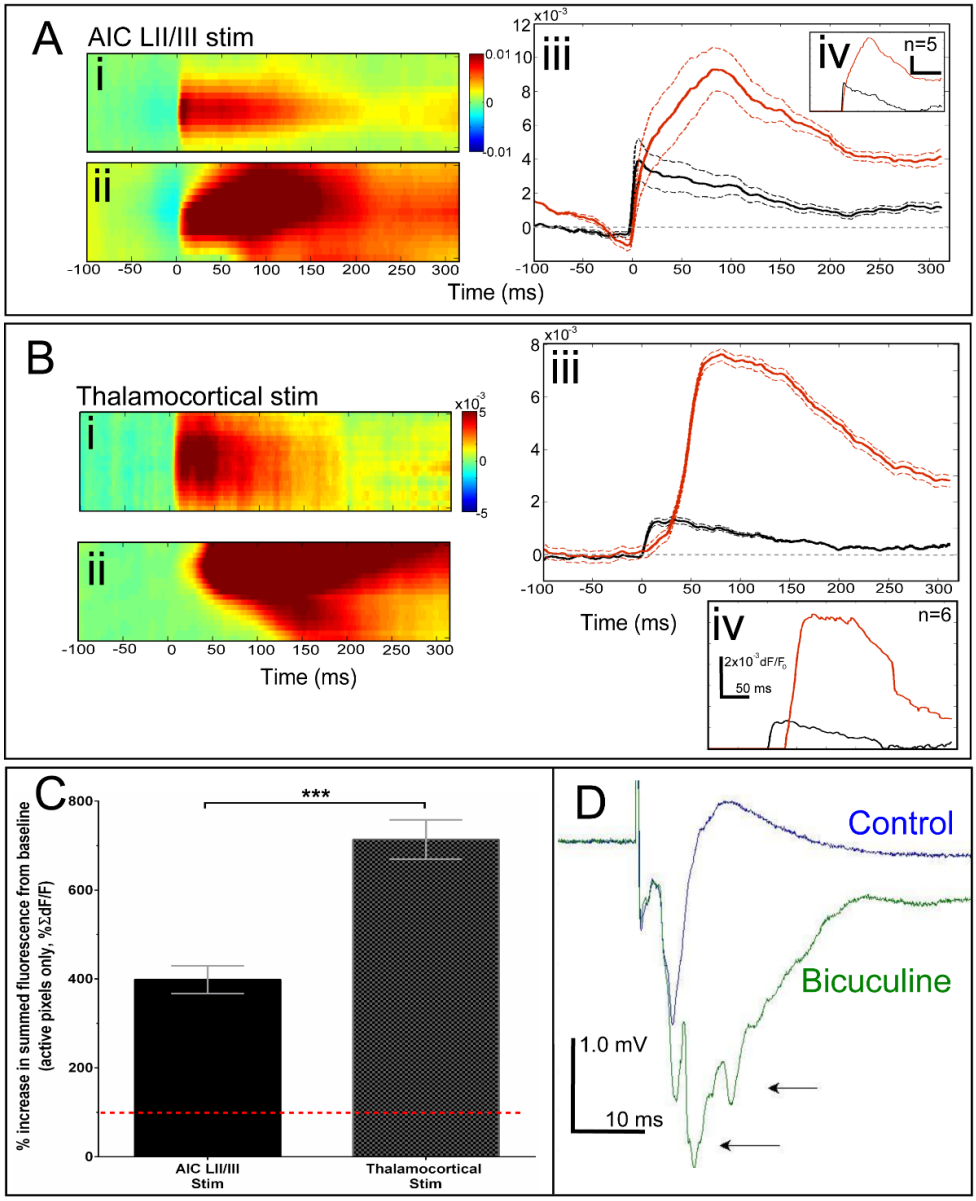

Figure 18: Effect of disinhibition on assembly dynamics. **A**. AIC experiments (n=5) showing a standard baseline response from LII/III stimulation (**i**) and that elicited under bicuculline (10 μM) treatment (**ii**). This data is recapitulated as time-series (**iii**), with S.E.M. drawn in dashed lines: black is baseline response, red represents the response in the presence of bicuculline, while inset (**iv**) represents the time series active pixels only. Note the enhanced preferential spread in the dorsal direction under bicuculline treatment, a phenomenon already occurring in a more controlled manner in baseline recordings. **B**.

Identical experiments as shown in **A** carried out in thalamocortical slices via VPM/white matter stimulation: baseline response (n=6; **i**) is greatly modified and increased several folds under bicuculline treatment (**ii**). This data is recapitulated as time-series (**iii**), with S.E.M. drawn in dashed lines, as well as with active pixels only (**iv**). Note the delayed onset and spreading of VSDI responses under bicuculline treatment compared to their respective baseline responses (**A** & **B**) suggesting networks activate much more robustly yet with significantly reduced propagation speed. **C**. Quantification of the percent decrease in bicuculline-treated summed fluorescence relative to their respective baseline levels for either slice preparation treated. **D**. The conspicuous increase in activity induced by disinhibition of slices was investigated further with field potentials (LFP), as seen here in AIC LII/III stimulation and LV/VI record, also showing an obvious increase in baseline evoked potentials (blue trace), characterised by greater initial responses followed by even greater troughs of epileptiform activity (green trace, arrows), suggesting the sustained activity seen in VSDI responses may arise as a result of fast recurrent network activation.

In order to characterise the dynamics of Bic-treated assembly propagation further, a sample thalamocortical experiment showing a typical response was chosen for presentation as a sequential activation (**Figure 19B**). What is immediately intriguing is the latency taken for VPM stimulations to activate the cortex, as can be seen at t=10 and 15 ms frames, where the control response reaches its peak activity (**Figure 19Bi** and **ii**). By comparison, it takes a total of 80 ms for the Bic-treated response to reach peak activity, and by this time, the activity has already spread beyond the boundaries of the S1BF into neighbouring cortical areas. This finding suggests bicuculline slows down conduction velocity both along thalamocortical fibres as well as within network activation all the while increasing the reach of wave propagation. Furthermore, it indicates GABAergic control is not only restrictive in nature, but also highly involved in the effective recruitment of neurons into the dynamic activity of assemblies. Control thalamocortical activity is shown here to remain confined, and subsides after ≈173 ms, yet with bicuculline treatment the entire cortical mantle is highly active at least for 312 ms after stimulus delivery. Interestingly, when looking at VPM responses specifically, those seen in control

often showed longer-lasting activity while these became very much attenuated under Bic treatment.

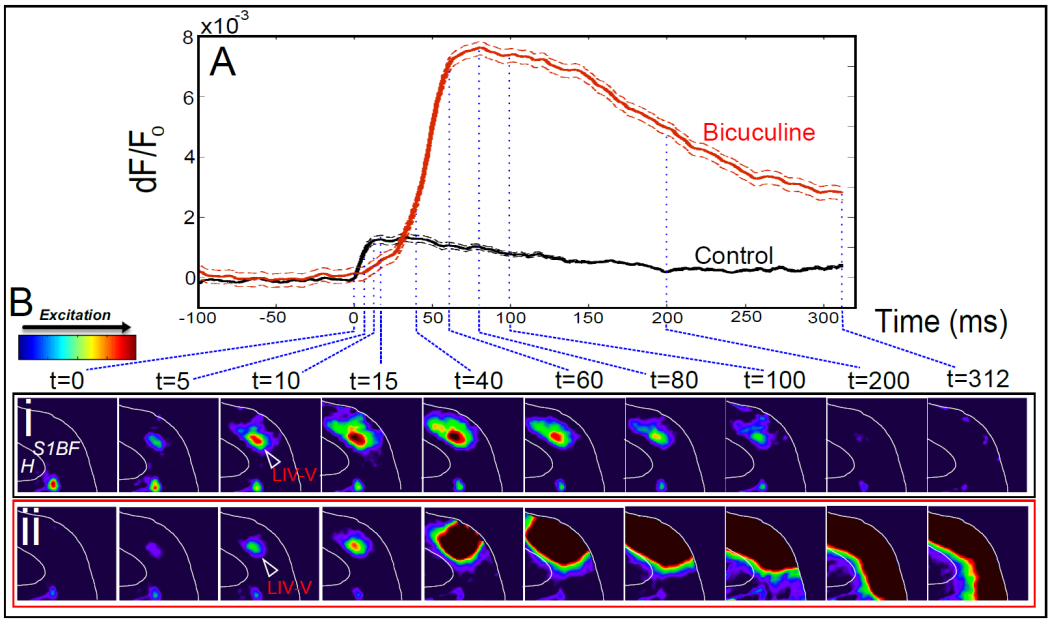

Figure 19: Characterisation of assembly disinhibition. **A**. Average VSDI time series (n=6) of control and bicuculline-treated responses in thalamocortical slices showing both a delayed onset of assembly activation and a much greater response and decay; S.E.M drawn in dotted lines. **Bi**. Sequential activation of an example experiments where stimulation was delivered in the white matter, below the cortex, giving rise to normal activation of the S1BF. Note the emergence of activity primarily in a region corresponding to LV/VI and spreading outwards, with a greater lateral than radial spread. **ii**. The same experiment under bicuculline treatment shows a much lower activity in the VPM followed with a delayed response in the cortex which slowly propagates to all layers in a radial manner followed by an overwhelming propagation to the entire cortical mantle, well beyond the limits of the somatosensory cortex, within 200 ms of stimulus delivery. Note: in both cases activity was initiated in cortical LV and IV, before spreading radially to all layers, and for Bic-treatment this activity remained sustained for the entire recording period for all 6 experiments.

c. Electrical potential vs fluorescence changes

Comparison of selected typical responses seen with VSDI and LFP provided further insights into the dynamics of neuronal assemblies. LFP responses to direct cortical stimulations gave rise to downward deflections in both AIC preparations (grey/black traces, **Figure 20A**) comparable to those recorded in coronal S1BF preparations

(**Figure 20B**), which often showed more complex responses featuring both upward and downward deflections (blue traces). Electrophysiological recordings in TC-angle slices also showed a similar profile: fast population voltage changes (LFP deflections, t=2-15 ms) followed by long periods of slow returns to baseline (t=15-50 ms). Of particular interest, is the apparent similarity in phase change between VSDI and LFP traces: grey bars highlight the peak VSDI responses with respect to their relative LFP responses, allowing for this discrimination to be made between temporal profiles. The rise phase of fluorescence signals reaching peak amplitude (between 7 and 10 ms) often corresponds to the majority of fast deflection phases in LFP traces. This can be seen in the 'time to peak' response histograms (**Figure 20iv & v**), showing that LFP responses reach peak response before VSDI signals. Following the VSDI peak response, the signal starts to decay slowly and this corresponds to the onset of low amplitude, slow LFP deflections. In turn, the observation that LFP and VSDI signals bear some relevant temporal correspondence between their respective fast and slow phases may provide further indications of the sequence of events taking place within neuronal assemblies.

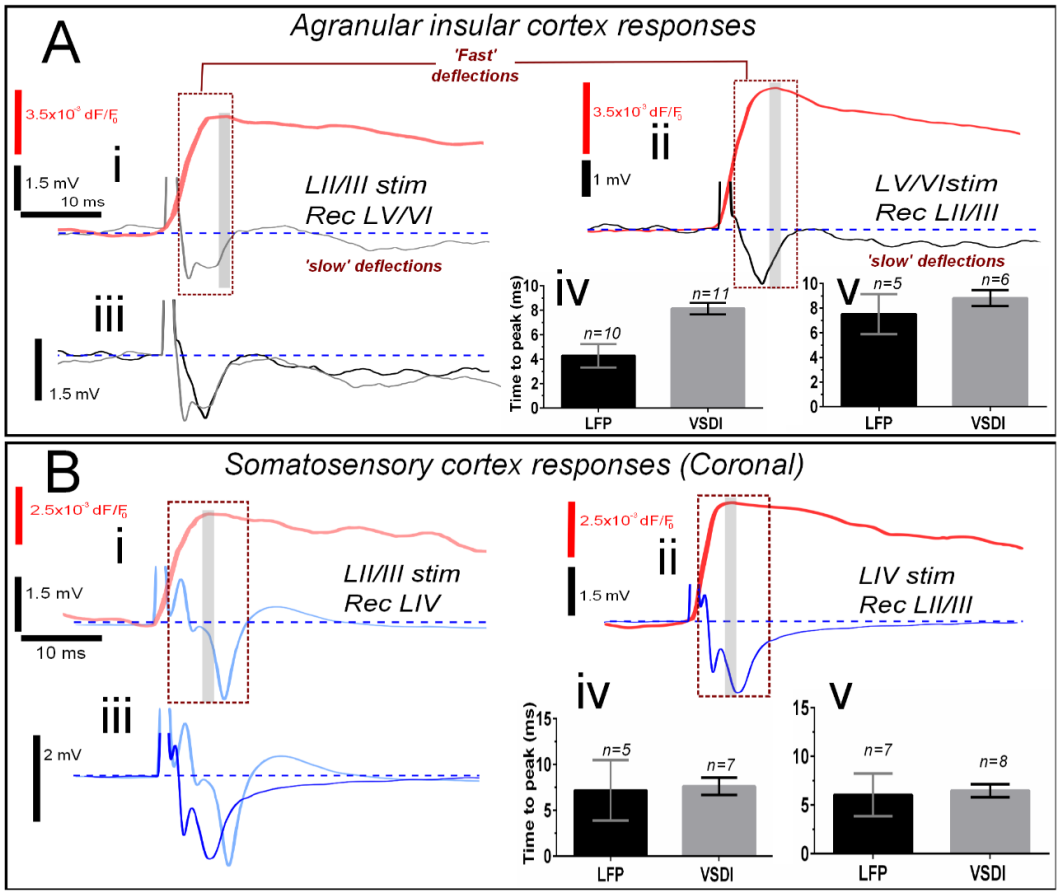

Figure 20: Comparison of VSDI and LFP responses for cortical direct stimulation experiments. Example VSDI (red) and LFP (coloured) time series from **A**. AIC in response to (**i**) LII/III stimulation, recorded in LV/VI and (**ii**) LV/VI stimulation, recorded in LII/III. **iii**. Traces are overlaid on same scale for comparison, with quantification of time delay required for peak deflection amplitude for LII/III (**iv**) and LV/VI stimulation (**v**). **B**. S1BF (coronal) in response to (**i**) LII/III stimulation, recorded in LIV and (**ii**) LIV stimulation, recorded in LII/III. **iii**. Traces are overlaid on same scale for comparison, with quantification of time delay required for peak deflection amplitude for LII/III (**iv**) and LIV stimulation (**v**). VSDI data was compiled from a 5x5 pixels square (i.e. 200x200 µm) centred on the location where the LFP recording electrode entered the slice.

The above-mentioned features, relating LFP and VSDI signals, were found to be most easily discriminated when comparing those evoked from thalamocortical assemblies (**Figure 21Ai–iii**), which showed a clear correspondence of the fast LFP deflections with the rise phase of the optical signal. Since thalamocortical activation of the cortex represents a more physiological stimulation of target networks than when stimulated with direct electrical stimulation, these observations corroborate

the theory that fast LFP deflections reflect activity taking place during the rise phase of VSDI records with the peak response usually indicating a change in network dynamics. In the case of the basal forebrain (**Figure 21B**), VSDI responses often peaked during the fast deflection phase of the LFP response, in a similar way as with direct cortical stimulations. LFP deflections in basal forebrain all showed small upward deflections (approximately 20-30 μV in amplitude), which correlate with the small amplitude of VSDI signals recorded in this particular preparation. Together these observations highlight close correlations between VSDI and LFP signals of intrinsic assembly dynamics, both in temporal profiles and relative magnitudes, reflecting the activity of functional neuronal networks at the meso-scale of brain organisation.

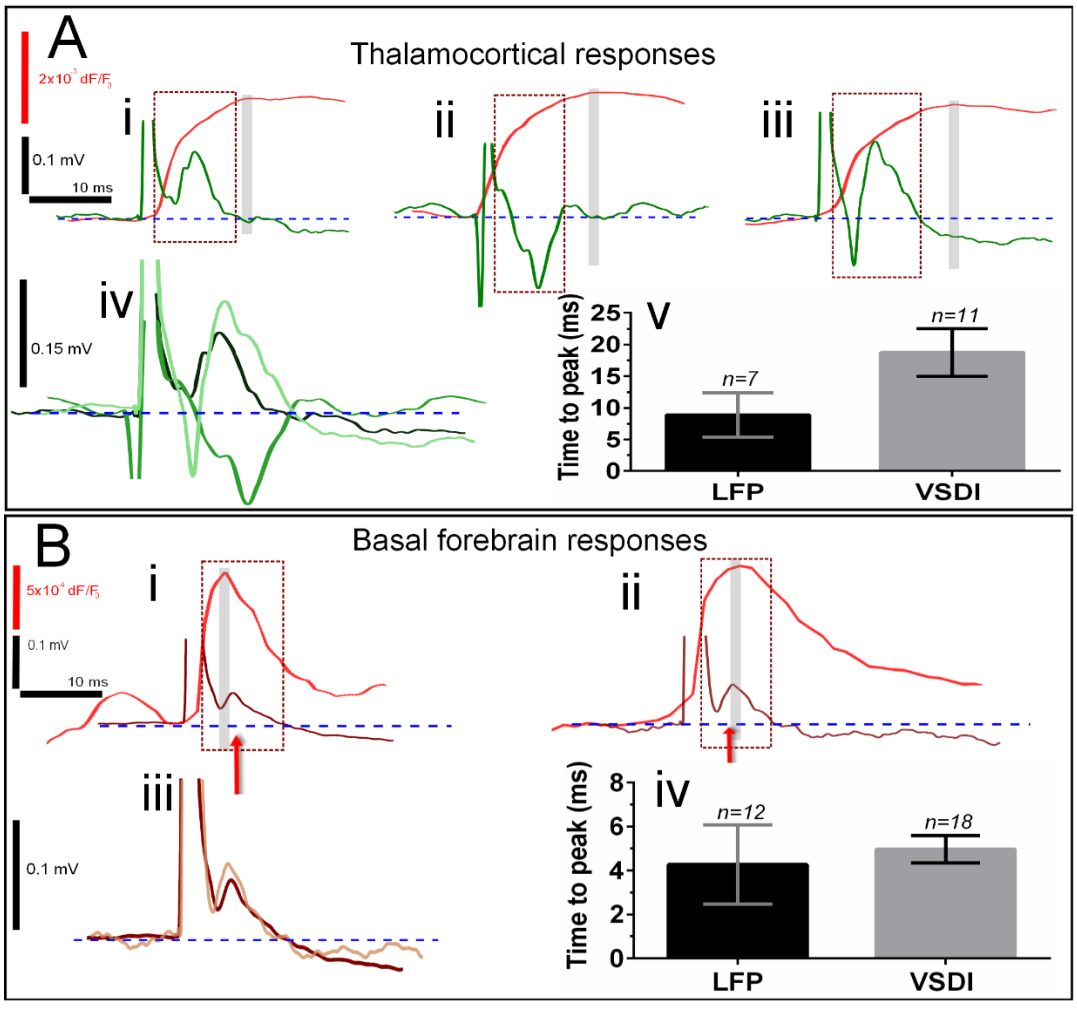

Figure 21: Comparison of VSDI and LFP responses for remote thalamocortical and direct basal forebrain stimulation experiments. Example VSDI (red) and LFP (coloured) time series from **A**. S1BF in response to remote VPM stimulation, recorded in LIV showing different profiles of response with upward deflections (**i**, n=4 of 7), downward deflections (**ii**, n=1 of 7) and time series showing both a positive and negative deflection (**iii**, n=2 of 7). **iv**. Traces are overlaid on same scale for comparison, with quantification of time delay required for peak deflection amplitude (**v**). **B**. Basal forebrain in response to HDB stimulation, recorded in MS showing typical low amplitude upward deflections (**i** & **ii**, red arrows, n=12). **iii**. Traces are overlaid on same scale for comparison, with quantification of time delay required for peak deflection amplitude (**iv**). VSDI data was compiled from a 5x5 pixels squared (i.e. 200x200 μm) centred on the location where the LFP recording electrode entered the slice.

3.4 Discussion

3.4.1 Generating cortical assemblies using direct electrical stimulation

a. Stimulation of neuronal cellular elements

In all experiments presented here, single-shock stimulations were delivered to neuronal tissue as a means of triggering population responses in live slices; such a stimulation paradigm has been used as the gold standard for eliciting and studying population activity (Frostig et al., 2017; Nowak and Bullier, 1997; Stett et al., 2000), producing robust responses which have been shown to be representative of those evoked with train stimulation paradigms under pharmacological treatment (Bandyopadhyay & Hablitz, 2007). The sudden change in electrical gradient resulting from extracellular cathodal stimulation depolarises nearby axons, both along shafts and at initial segments (Bostock et al., 1983; Coburn, 1989). It has been shown here that assembly generation is highly dependent on sodium channel activity, the substrates of neuronal impulse conduction, with their blockade abolishing all activity within slices (**Section 3.3.4.a**), confirming electrical stimulation triggers assemblies via a sodium-channel-dependent pathway. In support of this mechanism, somato-dendritic depolarisation has been reported to be less likely to take place under these circumstances, owing to low voltage-gated sodium channel membrane content. Indeed, unmyelinated axonal membranes in vertebrate neurons have been reported to contain approximately 100-200 sodium channels/μm^2, while this proportion can reach up to 1200 channels/μm^2 at the nodes of Ranvier of myelinated axons (Pellegrino et al., 1984; Ritchie and Rogart, 1977; Ritchie et al., 1976): these concentrations are found several orders of magnitude greater than those of somato-dendritic membranes, estimated between 3 and 7 channels/μm^2 (Nowak and Bullier, 1997). In light of these previous findings, and in

order to prevent over-activation of neuronal elements, the data presented here were acquired using short 0.1 ms stimulation pulses.

b. Stimulation intensity and nature of evoked mesoscopic responses

Stimulus-response relationships were investigated in AIC LII/II and S1BF LIV (**Figure 22**, below), and revealed both a relatively low threshold of stimulus intensity (>5 Volts) required to trigger assembly generation, and a ceiling effect reached from 30 Volts stimulation upwards. This narrow range in assembly gain (approximately 25 Volts) was consistently observed in all experiments across cortical regions (**Figure 22B**), and highlights the manner in which assembly dynamics behave as 'all-or-none' responses (Hsieh et al., 2000; Metherate and Cruikshank, 1999; Wu et al., 2001; Wu et al., 1999). Very small injections of current (down to 10 µAmperes during a 0.2 ms pulse) have been shown to directly activate up to 38 neurons at high-threshold (spiking) within the vicinity of an electrode placed within cortical tissue, and another 2000 neurons at low-threshold (Tehovnik et al., 2006). The electrical current delivered to slices in the experiments presented here can be estimated according to Ohm's law ($V=IR$): the resistance (R, units: Ohms, Ω) is the tricky variable to estimate in this particular case, and describes that of the entire setup including slice, stimulating electrode and wires. Within the stimulation setup employed here, 30 V stimulations can thus be estimated to deliver 60 µA of current for 0.1 ms, as the resistance of the slice and wires is estimated to be very low, with the main contribution arising from the stimulating electrode itself (Barry W. Connors, personal communication, 29th of March 2013), see **Chapter 2**, **Section 2.7.2**. According to this estimate, 10 µA of currents would have been delivered using 5 V stimulations, and did not evoke any measureable response, yet

only doubling this to 20 µA (10 V stimulation) did (**Figure 22**), highlighting the 'all-or-none' nature of assembly generation.

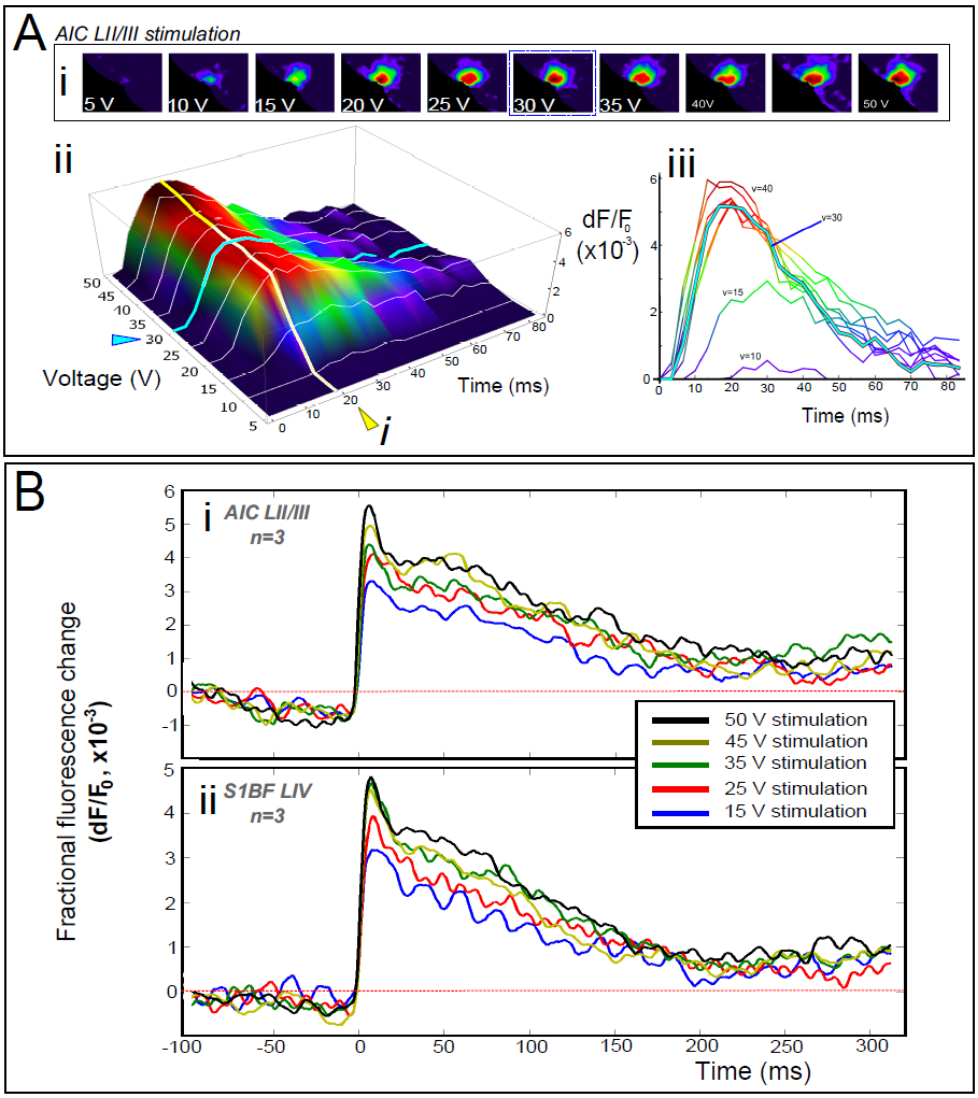

Figure 22: Voltage-response relationship for assemblies evoked in AIC and S1BF via direct cortical stimulation. **A**. Example experiment demonstrating the very narrow range of assemblies evoked in AIC; assemblies showed surprisingly similar profiles of stimulus intensity in both cortical regions. **i**. Sequential activation of peak activity frames from each stimulation intensity (5-50 Volts in 5 Volts steps). **ii**. a 3-D plot showing a sharp rise in activity between 5 and 20 Volts stimulation, highlighting the 'all-or-none' nature of assembly activation, then followed by a slower rise up to 30 Volts where responses reach a ceiling effect (intersection of the blue and yellow traces). Blue trace and arrow indicate the chosen stimulation intensity for experiments. Yellow arrow and band indicate the relative data points used to compile the sequential activation frames in **i**, above. **iii**. Time series further highlighting the steep slope of the stimulus-response relationship of cortical assemblies; 30 Volts trace highlighted in blue. For all graphs and images (**i–iii**) warmer colours indicate depolarisation while cooler colours indicate baseline level. **B**. Average time series of evoked assemblies from AIC LII/III (n=3, **i**) and S1BF LIV (n=3, **ii**) at selected stimulation intensities, highlighting similarly narrow response ranges to increasing stimulation intensity in both cortical areas, as shown in **Aiii**. S.E.M traces omitted from data for clarity.

c. Antidromic vs orthodromic impulse propagation

Extracellular electrical stimulation of nerve fibres can lead to the activation of antidromic nerve impulses: action potentials travelling in the opposite direction to orthodromic propagation, i.e. from distal axonal compartments towards the cell soma (Gerard, 1931). The majority of the VSDI signal can be attributed to orthodromic impulse propagation, as has previously been shown for similar experimental methods (Contreras & Llinas, 2001): perfusion of slices with Ca^{2+}-free aCSF (replaced with Mg^{2+}, 4 mM) before the start of experiments nearly completely abolished the generation of assemblies from electrical stimulation. Calcium is an essential ion in the process of action potential firing and synaptic transmission (Berger et al., 2007) and the reported impact of its absence in perfused aCSF provides evidence of the very high reliability of assembly dynamics on initial amounts of spiking activity triggering orthodromic impulse propagation.

d. Optimising 'direct' and 'remote' stimulation paradigms

Furthermore, neuronal activity at multiple levels features high trial-to-trial variability (Kisley and Gerstein, 1999), this is believed to arise from multiple factors, including: the combination of stimuli with pre-existing spontaneous activity, at the micro-scale from alterations in neuronal membrane properties of individual cells (Henze and Buzsaki, 2001; Tehovnik and Slocum, 2004) , or even from alterations in current densities delivered by the stimulating electrode, since the number of neurons activated by an electric pulse is directly proportional to input current (Tehovnik, 1996; Tehovnik et al., 1994). Highly variable dynamic activity patterns, such as those recorded *in vivo* using a range of macro-scopic recording

techniques, require much greater data sets for averaging, in order to isolate salient data. For the purposes of avoiding this high variability, as well as attempting to keep animal numbers to a minimum, a stimulus intensity of 30 Volts (approximately 60 μA) was chosen for triggering assemblies: this intensity ensured robust responses would be consistently elicited at (or close to) their maximum response magnitudes, yet without over-stimulating slices.

When stimulating the VPM at this intensity (for thalamocortical activation of the S1BF), cortical assemblies were not as reliably evoked: the largest assemblies were found to be evoked with 60 Volts pulses, after which the magnitude of thalamocortical assemblies were also found to reach a ceiling effect (data not shown). This may be due to the increased difficulty of targeting cells involved in cortical assembly dynamics (thalamocortical afferents) from remote VPM compared to direct cortical stimulations, or from the inevitably limited number of afferent excitable fibers available for impulse propagation.

e. Final conclusions from comparisons of evoked assemblies

One of the most important findings so far resulting from the comparison of assemblies evoked in S1BF and AIC is that though specific parameters of their activation dynamics were found to be different, the overall profile of response were extremely similar. This shared profile of fast rise followed by a slower decay lasting up to 300 ms was also seen when stimulating remotely (thalamocortical activation or S1BF), confirming that it did not arise as a result of the direct stimulation paradigm. Additionally, this profile was not repeated for experiments carried out in VPM or BF: it follows that this specific profile may be an intrinsic feature of cortical tissue which may play a crucial role in its physiological function. More studies will

be needed however to confirm whether neuronal assemblies retain this profile in all cortical aresas.

3.4.2 Measurement of data parameters of assembly dynamics

a. Interpretation of VSDI time-series

In the results presented here, data is first displayed as time series and/or space-time maps for characterisation of evoked responses, as well as quantified in terms of summed fluorescence intensity, lateral spread and time course of active pixels (**Section 2.7.1.2.d**). Where the process of isolating active pixels presents obvious advantages over the standard averaging of overall fluorescence data sampled within an ROI, the third step of normalisation of active pixel data may present less obvious advantages. However, this normalised version of salient data is in fact very telling: once normalised, time series show the average activity with respect to that data set's specific fluorescence range - in essence providing a description of the 'uniformity' of the evoked response. This data presentation therefore helps characterise key differences in evoked responses between direct and remote cortical activation: that is, thalamocortical activation produced wide-reaching assemblies with low, but more homogenous fluorescence values, whereas direct stimulations produced highly variable fluorescence readings within a comparatively smaller area, i.e. triggering high fluorescence values at the epicentre surrounding the electrode tip and showing a drastic decrease in fluorescence with distance from their epicentre.

Cortical processing depends on the synchronous and coherent activity of multiple inter-connected neuronal networks involving hundreds of thousands of cells, with distinct sensory receptive fields to represent all aspects of a given stimulus (Movshon et al., 1978). As a result, this information is encoded in space over time

within cortical tissue: it was therefore crucial to assess not just the magnitude of evoked responses (summed fluorescence and its temporal profile), but also gather data to characterise the ways in which summed fluorescence readings were found to differ between preparations and pharmacological treatments. Such discrimination was achieved by measuring the most obvious spatio-temporal parameters of evoked assemblies: i. lateral spread and ii. time course of active pixels.

b. Use of tangential vs radial geometries

Tangential geometries, featuring ROI segments oriented perpendicular to the pial surface, highlighted potential differences in lateral spread of propagation (**Figure 5**, upper panels), i.e. a means of appreciating the entirety of the response and thereby represented the main method of analysis employed in this thesis. Further analysis was conducted with a greater emphasis on the columnar activity evoked from the stimulation site however, using radial geometries – where ROI segments were instead oriented parallel to the pial surface – allowing for analysis of trans-laminar spread (**Figure 5**, lower panels). This combination of approaches produced very similar results with identical conclusions, i.e. that assemblies evoked using direct stimulation were significantly less extensive in space compared to thalamocortical assemblies (**Table 1** vs **5**, comparisons: **3.3.1.c.iv** vs **3.3.1.d**).

c. Statistical testing of parameters

- *Assessing the normality of parameter data sets*

Quantile-quantile (Q-Q) plots were used here to gauge the normality of data: this method ranks data points in ascending order of magnitude, plotted against an expected axis of quantiles according to the normal distribution. If the data is normally distributed, the resulting plot features a tightly-clustered, linear

relationship with a slope of 1. Some deviation from the line can be assumed, as the variable nature of sample data ultimately induces some deviations, but these variations must remain small, with data closely correlated with the line $y=x$. Minor deviations arising at the tails of the distribution (top right and bottom left of each graphs) are common and in fact expected when plotting normally distributed data sets. All tangential geometry data from each parameter, i.e. summed fluorescence, lateral spread and time course of response, were pooled and graphed on their respective Q-Q plots (see **Figure 23**, below), showing only minor deviations, providing strong evidence that the data recorded here were normally distributed. In all cases, if the correlation factor (r^2) of the data to the line $y=x$ was greater than 0.95 (i.e threshold: $r^2>0.95$), the data was considered to be sufficiently normally distributed. As a result, statistical comparisons were undertaken in each case using parametric tests: either using Student's *t*-tests or, if more than two data sets were compared, one-way analysis of variance (ANOVA) using Tukey corrections to accommodate for multiple comparisons. In all cases $p<0.05$ was considered significant, however since *p*-values represent the *probability* that two data sets arise from distributions featuring distinct parameters, the real meaning of a *p*-value is that the smaller its value, the more probable it is that the sample distribution indeed differs statistically from another. Therefore, *p* values reported between $0.08<p<0.05$ (see for example **Table 5** comparison ID: **3.3.2.a.iii**) were deemed to 'approach a high level of significant difference' and were therefore concurrently, yet less prominently, considered with statistically significant data (where $p<0.05$).

In conclusion, the parameters measured in the investigation of assemblies evoked in multiple brain regions provided a general pattern, where summed fluorescence highlighted differences between regions performing highly distinct functional roles (i.e. cortex vs sub-cortex), while parameters like spread and time course provided

more specific information, highlighting more intricate differences in assembly dynamics.

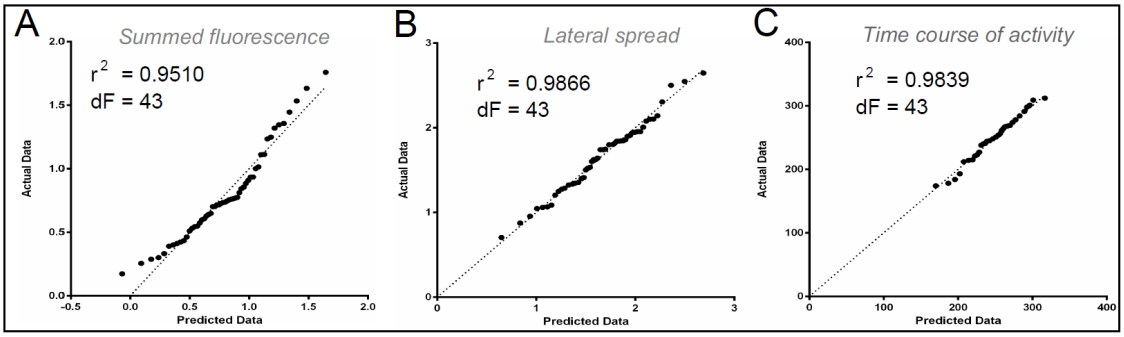

Figure 23: Probing the normal distribution of the data. Quantile-quantile plots of the data presented here for each of the three parameters: tangential geometry summed fluorescence (**A**), lateral/tangential spread (**B**) and time course of activity (**C**), in all cortical preparations (S1BF, thalamocortical and AIC). These graphs show that the data falls within reasonable measures of the x=y line between observed ('actual') and predicted ('expected') data, i.e. $r^2 > 0.95$: the data is assumed to be normally distributed.

- *Statistical testing of geometry-specific data sets*

Statistical tests were carried out between data sets compiled using like-geometries only (i.e. tangential vs tangential or radial vs radial), as the nature of the data produced by each geometry were too different as a result of their respective focus on selected subsets of recorded data. All data parameters were measured from tangential geometries (as these encompassed the entire response), except for summed fluorescence measurements which were measured in both orientations. In all results of cortically-evoked assemblies presented here, radial data were only found to differ significantly in a single comparison: that between S1BF LIV direct and remote thalamocortical stimulations. In turn the similarity between radial activity of direct stimulation paradigms (i.e. focusing on columnar activity) suggests internal cortical dynamics obeyed similar network-wide rules of activation and decay upon identical stimulation, in all cortical areas tested, i.e. in AIC and S1BF, coronal and TC-angle. As mentioned above, the greater differences detected were between direct and remote activation of the S1BF: thalamocortical slice stimulation

inevitably differs greatly from that of direct electrical stimulation, both in spatial distribution and sub-cellular selectivity of inputs as well as in the intensity of this input activation: it was therefore expected for remote and direct stimulations to give rise to highly disparate data distributions (Badin et al., 2017).

- *Effect size of data*

Experiments carried out to probe assembly patterns presented here were each repeated a minimum of 6 times for use in statistical testing of assembly parameters. A quick calculation was made to estimate the minimum required sample size to achieve satisfactory statistical power ("Cohen's *d*", at threshold: $d>0.9$, see **Table 8** below), which revealed that the relatively small S.E.M.s of the data presented here required only few repeats of experimental trials (n=3-4) to achieve reliable statistics when considering summed fluorescence and lateral spread data. When considering time course of activity data however, the means were more often found to be relatively close in value with increased S.E.M.s, increasing the minimum required sample size to 6 repeat trials per experiment in order to ensure robust statistical testing. **Table 8** shows example calculations of three data comparisons presented here which all show high *d* values, confirming that all statistical comparisons reported here provide a true representation of observed differences.

Data parameter	Comparison	Means	Standard deviation	Repeat trials (*n*)	*d* statistic	Statistical power
Summed fluorescence	(i) LIV S1BF vs (ii) thalamocortical (radial summed fluorescences)	(i) 1.30	(i) 0.51	(i) 8	1.76	95%
		(ii) 0.594	(ii) 0.24	(ii) 11		
Lateral spread	(i) LIV S1BF vs (ii) thalamocortical	(i) 1.27	(i) 0.238	(i) 7	2.836	100%
		(ii) 2.2	(ii) 0.398	(ii) 11		
Time course of activity	(i) LIV S1BF vs (ii) AIC LV/VI	(i) 173.6	(i) 22.22	(i) 7	1.26	68.70%
		(ii) 195.0	(ii) 19.6	(ii) 6		

Table 8: Mean values, standard deviations and *d* statistic for example summed fluorescence, lateral spread and time course data where it is shown that in each of these three cases the statistical power of the comparison was high. Examples are shown for 1 comparison in each of the three parameters of interest, however all comparisons presented here featured *d* statistics which were greater than 1 – i.e. giving rise to high statistical power for all comparisons. In order to test statistical power, the parameters (mean and standard deviation) were fed in an on-line statistical power calculator (Research, 2016; Stangroom, 2016) and the power was tested for two-tailed hypotheses with a 5% alpha error level.

3.4.3 Mesoscopic population activity as a sensitive index of brain function

a. Assemblies evoked in somatosensory cortex

The results presented here largely replicate those previously published in the literature: in S1BF LIV (**Section 3.3.1.a**), stimulations gave rise to wide-spreading assemblies featuring high activity in the centre of the response and decaying signal with distance lasting for hundreds of milliseconds. Such sustained activity results from local recurrent excitation (Douglas et al., 1995; McGuire et al., 1984) via feed-forward and feed-back impulse propagation to both excitatory and inhibitory cells in layer-specific synaptic contacts (Povysheva et al., 2006; Welker et al., 1988). This activity is commonly reported to feature preferential spread in the radial direction (across cortical layers), i.e. initially restricted to the target column, and shortly

followed by lateral spread in LII/III (Petersen & Sakmann, 2001; Berger et al., 2007). These dynamics arise in most part from the local network architecture: with the radial organisation of cells, i.e. projecting their apical dendrites up towards the pial surface and their axons down towards LVI and the sub-plate (**Figure 24**; Douglas & Martin, 2004). The lateral spread which ensues may be accounted for by i. lateral cortico-cortical connections which interlink columns together in their superficial layers (Fitzpatrick, 1996; Somogyi et al., 1998), ii. divergent translaminar connections, which originate in all cortical layers and innervate superficial layers (Gilbert, 1992; Petersen and Sakmann, 2001), as well as iii. the activation of regenerative poly-synaptic cortical loops utilising both radial and lateral projections (Contreras and Llinas, 2001; Tanifuji et al., 1994). **Figure 24C**, below, shows a reconstruction of interlinked cortical columns, where the complex arrangement of neurons of all types and their connections give rise to a general radial structure with bulky neuropil in deep and superficial layers. This precise columnar arrangement represents a strong theoretical basis accounting for the initial assembly activation profile discussed above (Johnson and Frostig, 2016).

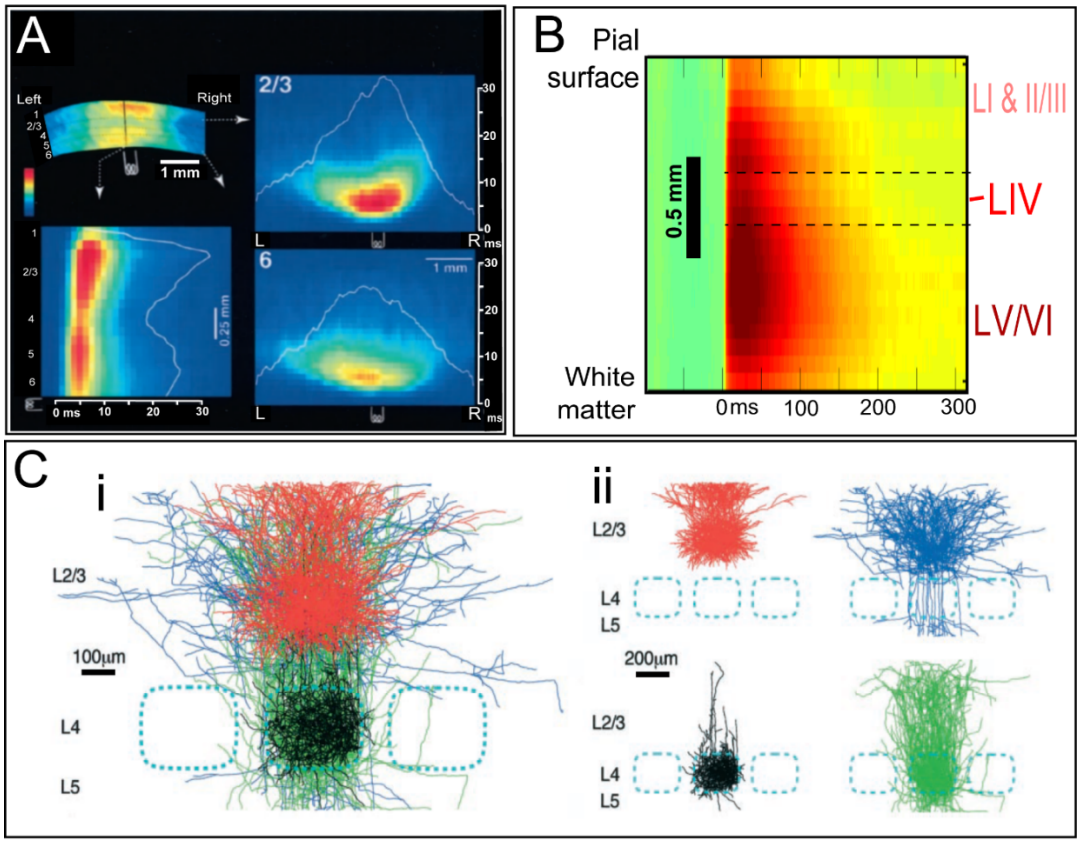

Figure 24: Representation of the spatio-temporal distribution of remote thalamocortical activity. **A**. Data presentation taken from a previous report (Contreras & Llinas, 2001) showing the signature profile of thalamocortical activity evoked in *coronal* slices from white matter stimulation. Activation of cortical afferents gives rise to two hotspots of activity in LII/III and LV/VI spreading horizontally well over 1 mm to encapsulate multiple barrel columns. Note the greater magnitude of superficial responses in this preparation compared to deep layer activity. **B**. Data from **Section 3.3.1.c**, also showing these two regions of activity, yet in the data presented here the profile of response is inverted, with greater activity in LV/VI than in LII/III. This response profile may arise as a result of the slice cut (TC-angle), which is likely to truncate superficial layers of innervated columns. **C**. Reconstruction of two of the main types of cortical neuronal sub-types found in barrel columns within superficial layers, i.e. 18 LII/III pyramidal and 18 LIV spiny stellate neurons showing their respective layer-position and morphology. (**i**) Superposition of both groups in a schematic representation of the cortical construct (showing LIV barrels and putative layer stratification). Note: the radial organization of cellular projections, which altogether give rise to a columnar mesoscopic architecture. *LII/III pyramidal neurons*: red dendrites (projecting locally, i.e. within column **diameter**, within LII/III and I) and blue axons (projecting laterally to the LII/III domains of neighbouring barrels as well as vertically to deep layers within the column lumen), while *LIV spiny stellate neurons* are shown with their axons in green (projecting nearly exclusively up to the superficial layers, with fibres mostly confined to the column lumen with a small number of extra-columnar projections, as well as

few fibres targeting the deep layers), and their dendrites in black (projecting mostly to the local network of its LIV barrel, with a small number of projections up to superficial layers). (**ii**) Same reconstructed neurons with their dendrites and axons separately drawn on the same schematic cortical construct as in **i**, showing the above-mentioned features with greater clarity: LII/III pyramidal neurons (red dendrites/blue axons, top) mostly featuring high amounts of lateral connections in LII/III; LIV spiny stellate neurons (black dendrites/green axons, bottom) feature a dense array of local dendritic processes with axons projecting almost exclusively to superficial layers. Figure adapted from (Petersen & Sakmann, 2001).

- *GABAergic control of mesoscopic network dynamics*

Neuronal population activity depends on fast glutamatergic transmission, as suggested here (**Section 3.3.1.c**) and reported in the literature (Berger et al., 2007; Cauller and Connors, 1994; Fukuda et al., 1998; Wu et al., 2001), while the narrow gain control of mesoscopic propagating activity is most probably mediated by fast GABAergic inhibition (Markram et al., 2004). The restriction of this activity is shaped by dense networks of GABAergic interneurons (Chagnac-Amitai and Connors, 1989; Galarreta and Hestrin, 2001; Wilson et al., 1994), found throughout cortical layers (Letinic et al., 2002). Interneurons make up between 20 and 25% of all neurons in the cortex, featuring high amounts of target selectivity: 'Double-bouquet', 'Martinotti' and 'Neurogliaform' neurons have been found to target the distal dendrites of pyramidal neurons (Druga, 2009), affecting the radial integration of activity along dendritic trees, 'Basket' cells have been found to innervate cell soma and proximal dendrite (Druga, 2009; Wang et al., 2002; Gupta et al., 2000), while 'Chandelier' cells target axon initial segments (Gabbott and Bacon, 1996; Jones, 1975). All these different inhibitory neuronal types act to control the dynamics of assemblies such as to remain at first confined within their local region of sensory processing (Isaacson and Scanziani, 2011); this powerful inhibitory control was highlighted in **Section 3.3.4.b**, with perfusion of bicuculline producing sustained epileptiform cortical activity (**Figure 18D**, green arrows) – a phenomenon

previously reported (**Figure 25**) and which demonstrates the importance of appropriate GABAergic control for normal network dynamics (Petersen & Sakmann, 2001; Jin et al., 2002). Interestingly however, the aberrant population activity seen here, as well as in other reports (Petersen & Sakmann, 2001), appears to propagate with slower velocity, as observed on VSDI time-series showing a lower slope of activation compared to control (**Figure 25Ai–iii**, red arrows); this effect did not arise as a result of the direct-stimulation protocol, as this was also evident in thalamocortically-evoked assemblies (**Figure 19**). Other studies however, have presented results which contrast with such observations, instead reporting increases in assembly propagation velocity (Tsau et al., 1999), with one publication even reporting a nearly 12-fold increase in lateral cortical propagation speed, i.e. from 11 mm/s in control condition to 125 mm/s under 20 μM bicuculline treatment (Wu et al., 2001). The exact reason for this discrepancy remains unclear, however dye bleaching could play a part as a result of the excessive levels of emitted fluorescence under bicuculine treatment. This possibility can be mostly discarded however since this effect was never seen in longer experiments lasting up to 2 hours (see **Chapter 4**). Alternatively, the actions of bicuculine in blocking Ca^{2+}-sensitive and KCNQ-containing K^+ VGICs when applied at the concentrations used here may play a part (Khawaled et al., 1999; Yue and Yaari, 2004), see **Section 3.2.1.c**. This is also unlikely as the blockade of these protein effectors usually leads to heightened neuronal activity, yet these effects could nonetheless potentially trigger a complex physiological antagonism of appropriate activity propagation at the meso-scale. The similarity between results presented here and those of previously-published reports confirms the use of such experimental paradigms in acquiring data which enable the observation of real measures of physiological function, as well as representing an important validation of the methods.

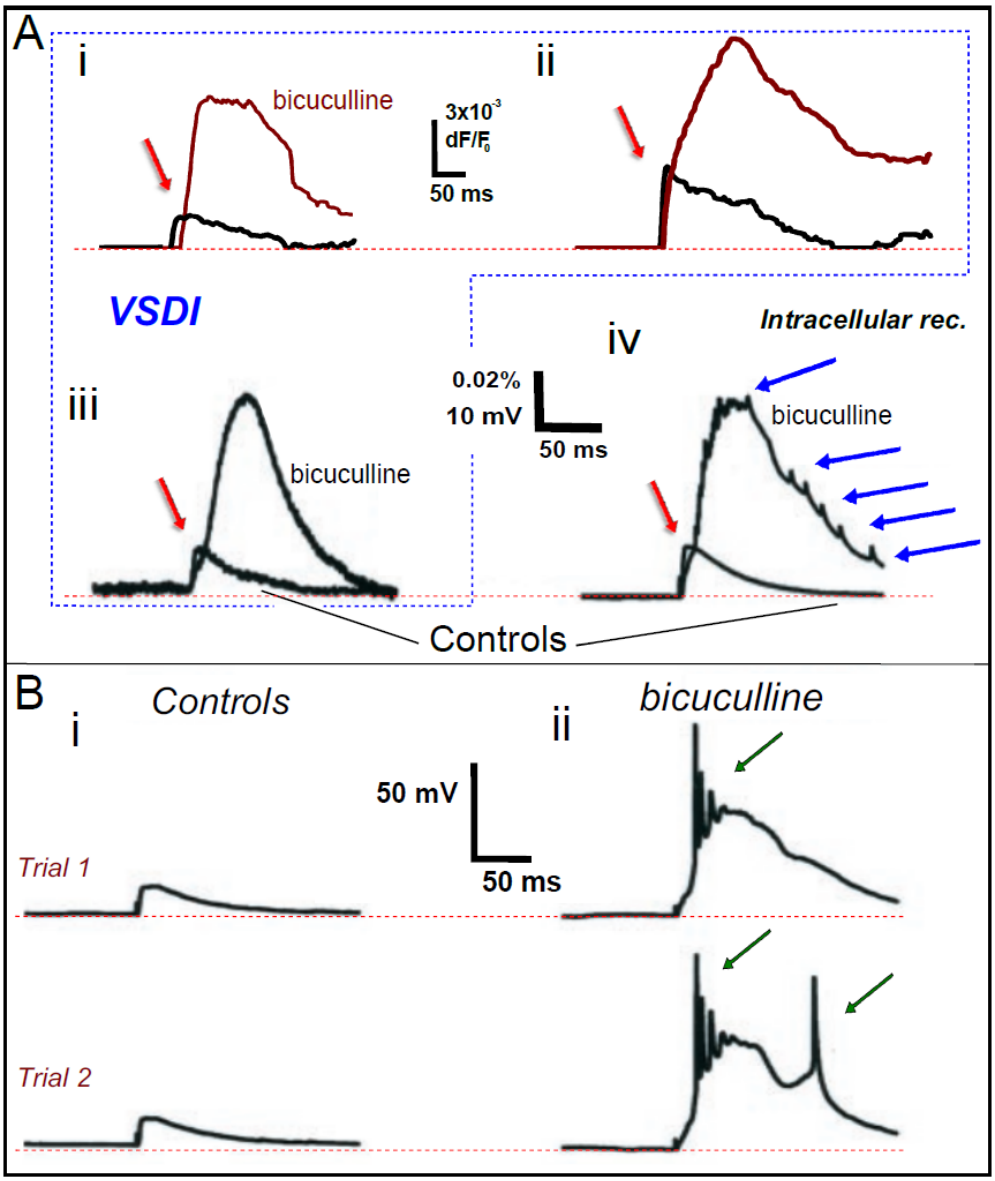

Figure 25: Bicuculline profoundly disrupts normal network dynamics. **A**. direct comparison of thalamocortical (**i**) and direct stimulation data (**ii**) presented here under control and bicuculline treatment in comparison to similar experiments reported elsewhere with concurrent VSDI (**iii**) and intracellular recordings (**iv**). Note the slower dynamics of the bicuculline-treated responses (red arrows), in addition to the much increased response magnitude (amplitude, spread and time course), characterised by ample rises in intracellular V_m giving rise to epileptiform spiking activity (truncated spikes; blue arrows). **B**. Two individual trial sweeps from the same experiments as in **Aiii** & **iv**, showing first the control condition response (note the signature EPSP trace not giving rise to any spiking activity in the control condition, **i**), then followed by the resulting traces under bicuculline treatment, again in either case showing the much increased intracellular EPSP signals accompanied by aberrant spiking (green arrows). Figures **Aii**–**iii** & **B** were adapted from (Petersen & Sakmann, 2001).

- *Remote thalamocortical activation*

Assemblies evoked in S1BF via VPM stimulation triggered network-wide activation of barrels corresponding to whiskers either C2 or D2 (Land and Kandler, 2002). Tangential ROI analysis (**Section 3.3.1.c**) revealed that among all preparations tested, thalamocortical activation produced the widest assemblies, reaching over 2 mm of cortical surface, yet showing relatively low overall fluorescence values. The distinct activation dynamics of remote and direct cortical activation paradigms may reflect the specific method of stimulation: remote activation of thalamic efferents diffusely innervate multiple loci (barrels) along the cortical mantle (White, 1978), giving rise to low levels of activity over larger distances compared to when applied in a single locus, such as with direct cortical stimulations. Further considerations must be taken in account regarding the fact direct stimulations activate all processes within the immediate vicinity of the stimulating electrode, in addition to possibly activating neuromodulatory fibres, such a stimulation does not take in account the ordered successive activation of processes which occurs with thalamocortical stimulation; this may in turn contribute further to the difference in activity profile seen here between the two preparations.

- *Corticothalamic connections originating from deep layers*

In addition to functional thalamocortical projections, the presence of corticothalamic connections was also confirmed. It was found that the greatest activity was evoked via LV/VI cortical stimulation in TC-angle slices, as would be expected since that is where corticothalamic cell bodies have been reported to originate (Reichova and Sherman, 2004). Responses were also evoked when stimulating in LIV, yet showed weaker thalamic responses: this observation would suggest that LV/VI pyramidal cells which project back to the thalamus may have

been activated in an ectopic manner via activation of their axon collaterals which reach up into LIV. The detection of active corticothalamic loops within slices confirms further the health of the preparation and the validity of the methods.

- *Thalamocortical activation of the S1BF: functional relevance*

Thalamocortical responses are often reported to feature a biphasic spatial profile in the radial orientation, containing two peaks of activity, evident in the deep layers V/VI and superficial layers II/III (Hill & Greenfield, 2014; Llinas & Contreras, 2001). The data presented here shows this biphasic profile, with a greater amount of fluorescence recorded from the deep cortical layers compared to that of superficial layers, and that this greater activity did not solely arise from a greater area of cortex dedicated to layers V/VI, but also as a result of a more intense fluorescence compared to that of superficial layers (**Figure 8E**). The VPM was the target of stimulations and these particular efferents preferentially target layers VI and IV (Lu and Lin, 1993) while those of POm are reported to activate both deep and superficial layers, i.e. with pronounced and direct innervation of deep cortical layers (Constantinople and Bruno, 2013). This biphasic response profile could thus be explained by slight inaccuracies in stimulation loci: the VPM was difficult to clearly delineate from the POm, meaning some thalamocortical stimulations are likely to have activated fibres originating from both nuclei. Such stimulations could have driven stimulation of LVI-IV with high intensity compared to superficial layers. The differences seen here in the radial distribution of activity in S1BF compared to those normally recorded *in vivo*, often showing more equal distributions of activity (Devonshire et al., 2007; Di et al., 1990; Jellema et al., 2004), could also arise as a result of the *in vitro* preparation, i.e. from both i) the lack of otherwise significant presence of neuromodulators affecting cortical networks (Rorig and Sutor, 1996;

Waterhouse et al., 1980), as well as ii) alterations to normal network organisation resulting from the thalamocortical slice angle. While the former possibility cannot be fully discounted, previous demonstration of *in vitro* activity profiles resembling those recorded *in vivo,* with thalamocortical afferent activation of *coronal* S1BF slices (Contreras & Llinas, 2001) and where networks are thus equally deprived of neuromodulatory influences, indicates the latter possibility, i.e. slice angle cut, may be the more influential factor in altering thalamocortical assembly dynamics.

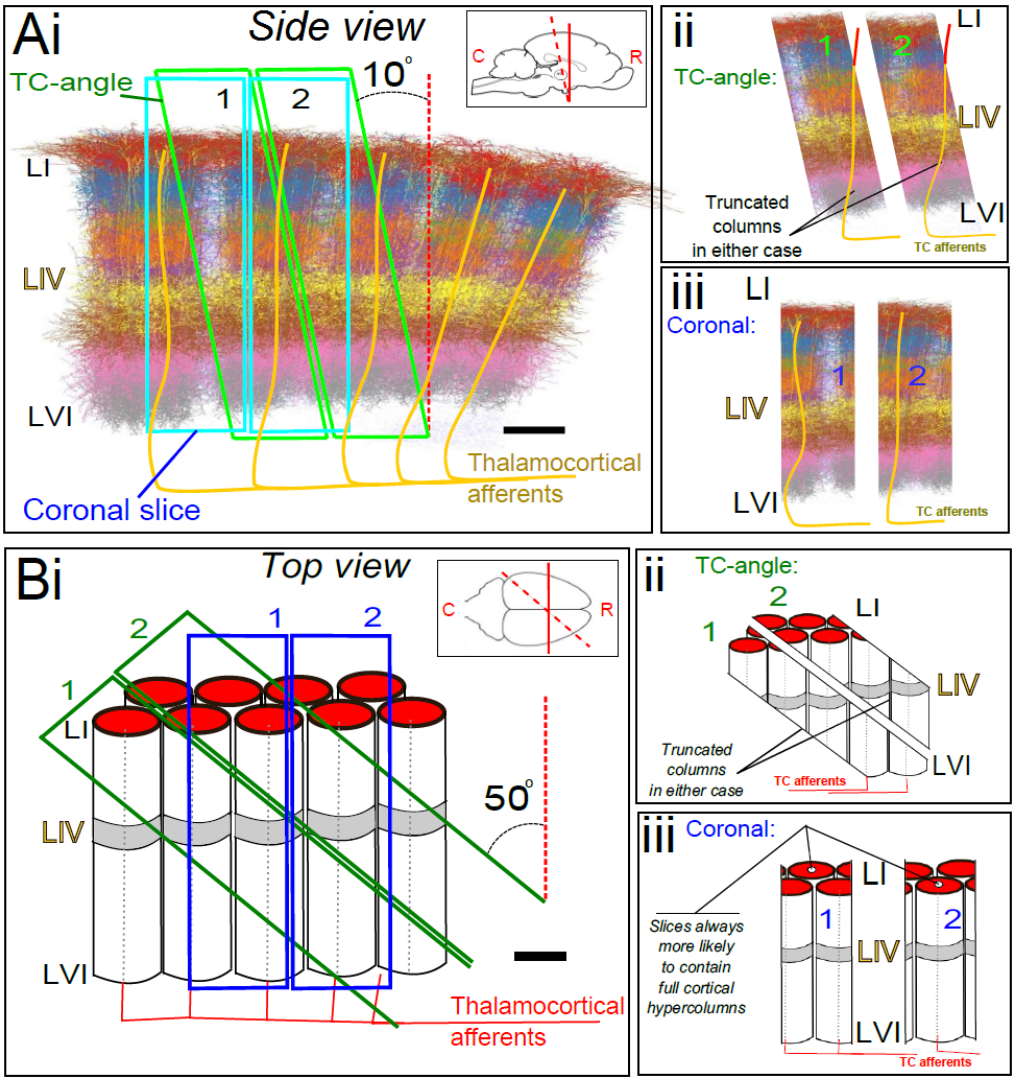

Figure 26: Schematic diagram attempting to depict the effect of slice angle cuts on mesoscopic columnar organisation. **Ai**. Representation of the impact of a 10° angle cut, compared to the vertical coronal plane, on the structure of cortical columns within slices. Blue boxes indicate putative coronal slices, green boxes indicate thalamocortical angle, and orange lines represent general thalamocortical afferent tracts reaching up to superficial layers (i.e. both from VPM and POm). **ii**. Isolation of thalamocortical slices extracted from

their respective positions in **i**. Note the inevitable truncation of some radially-oriented thalamocortical afferents within LII/III (red lines). **iii**. Similar display for coronal slices showing both the inclusion of an entire column within the thickness of the slice as well as the preservation of columnar architecture across the cortical thickness. Scale bar: 250 μm. **B**. Same representation as in **A** this time presenting the effects of a 50° angle cut from the lateral coronal plane on the structure of cortical columns. Dotted vertical lines within schematic columns represent possible thalamocortical afferents. **ii**. Slices shown in **i** for thalamocortical angle cut (green boxes) display an even greater degree of truncation of cortical columns, as well as the inclusion of a greater number of cortical columns within slices. **iii**. Coronal slices shown in **i** (blue boxes) showing a similar integral profile of columnar architecture as shown in **Aiii**. Scale bar: 250 μm.

As seen in the thalamocortical slice cut (**Figure 26**), it is highly probable that many sub-cortical afferent fibres, which effectively link the VPM to the entire height of their respective cortical column within the thickness of the slice (Lu & Lin, 1992), may innervate columns featuring variable levels of truncation. This would be especially true for columns forming the edges of the slice and where the majority of the VSDI signal originates. Ablation of superficial columnar networks (**Figure 26Aii** & **Bii**), would in turn also result in truncation of thalamocortical afferents in superficial layers, i.e. POm afferents primarily, reducing the higher expected manifestation of LII/III activity. The even lower levels of fluorescence recorded from LIV, specifically, are reported to arise as a result of the simultaneous activation of significant local inhibition via LVI poly-synaptic pathway targeting excitatory granule cells (Bolz and Gilbert, 1986), resulting in yet greater control of excitation (Hill and Greenfield, 2014; Contreras and Llinas, 2001; Fukuda et al., 1998). Together, the findings presented here highlight complex yet organised assembly dynamics resulting from remote S1BF activation, with high levels of processing taking place in two separate local networks organised radially into columns and laterally into layers (Constantinople & Bruno, 2013), segregated by tightly-controlled activity within LIV mediated by fast GABAergic inhibition.

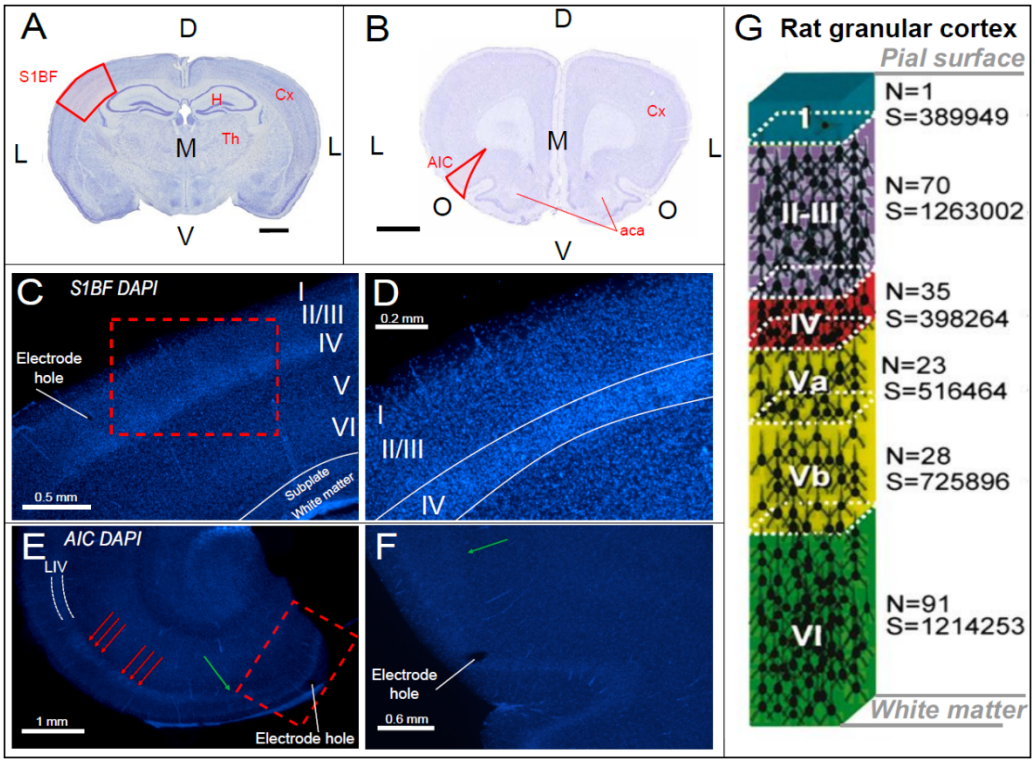

Figure 27: Laminar organization of primary somatosensory (S1BF) and agranular insular cortices (AIC) in the coronal plane. **A**. Pictogram of a nissle-stained coronal slice containing S1BF, adapted from (DeFelipe, 2011). Scale bar: 1mm. Orientation labels: *D* – dorsal; *M* – medial; *V* – ventral; *L* – lateral. Brain region labels: *H* – hippocampus; *Th* – thalamus (including VPM and POm); *Cx* – cortex. **B**. Pictogram of nissle-stained coronal slice containing AIC, adapted from (Gruter et al., 2015). Scale bar: 1 mm. Orientation labels are displayed as in **A**, except with the addition of '*O*', which represents the '*orbital*' cortical surface, found in close proximity to the ventral surface of the brain, making this area difficult to study in *in vivo* imaging experiments. Brain region labels: *Cx* – cortex; *aca* – anterior part of the anterior commissure. **C**. Pictogram of a DAPI-stained coronal S1BF slice used in LII/III stimulation experiments: the hole made by the stimulating electrode can be seen on the left of the image, while the more intense LIV can be seen approximately 400 from the pial surface as a thick and intense band of cells. Dotted red box indicates the field of view shown in panel **D**. Note the greater thickness of LV/VI compared to LVI-I, occupying nearly two thirds of the entire cortical thickness – matching the radial thalamocortical spatial profile of activity **Figure 23B**. **D**. Pictogram of the same slice under greater magnification, showing the clear demarcation of LIV from deep and superficial layers. **E**. Pictogram of a coronal slice containing AIC: Dotted red box indicates the field of view shown in panel **F**. green arrow shows LIV disappearing in the ventral direction, marking the start of agranular cortex. Red arrows show the presence of barrels in the frontal cortices, most probably within primary somatosensory (jaw area; S1J) cortex, which is reported to extend to the lateral cortical

surface found in coronal slices taken at 2-3 mm from bregma (Paxinos & Wattson, 1998), see **Section 3.3.1.a**, **Figure 2A**. Electrode hole is labelled in the bottom left of the image. **F**. Pictogram of a magnified view of the agranular insular cortex, taken from a deeper cut of the same slice shown in **E**, showing the disappearing LIV (green arrow, top of image) and the resulting homogeneous appearance of the cortex, contrasting with that of S1BF. **G**. Schematic representation of the mesoscopic architecture of rat primary somatosensory cortex, including layer-specific measurements of the number of neurons (N) and synapses (S) present in 50x50 µm cubes of cortical tissue, from the pial surface to the white matter. Note the high neuron density of superficial layers II/III and VI, compared to the sparseness of layer I which nonetheless contains almost as many synapses as LIV. Adapted from (DeFelipe, 2011).

b. Assemblies evoked in agranular insular cortex

The AIC lacks a granular cell layer and therefore presents a much more homogeneous laminar organisation than seen for example in S1BF (**Figure 27D** vs **F**); for this reason, the AIC represents a good test preparation to compare against the comparatively well-studied S1BF. Assemblies evoked in AIC produced characteristic patterns of population activity, yet showing intricate differences in population dynamics. Since LIV was absent, assemblies were evoked in superficial LII/III layers as well as deep LV/VI layers for comparison with S1BF assemblies, and in both cases showed (non-significantly) increased overall summed fluorescence relative to S1BF (**Section 3.3.2**). Closer analysis of the data revealed that assemblies evoked from LII/III stimulation gave rise to more sustained time courses of assembly activity, while when evoked in LV/VI, assemblies featured wider spread of activity compared to S1BF LIV assemblies.

In either case, though differences in overall response profile were detected, the AIC produced typically extensive assemblies, lasting hundreds of milliseconds; akin to those recorded in S1BF. The differences in spatio-temporal assembly dynamics could be explained however, by a more diffuse organisation and/or concentration of inhibitory interneurons within agranular cortical networks, overall amounting to a

less rigid control of dynamic activity (Beul and Hilgetag, 2014; Kawaguchi and Kubota, 1997). In S1BF, LIV inhibitory systems as well as the columnar orientation of inter-laminar connections induce a segregation in the activity of superficial and deep layers (Petersen and Sakmann, 2001), as discussed previously (**Section 3.4.1c**). In AIC, this 'barrier' does not exist, allowing for a more homogeneous propagation of assemblies, with less restrictive spatial control (**Section 3.3.2.a**). In support of this theory, it was shown that assemblies evoked in AIC superficial layers lasted longer than S1BF assemblies, particularly when compared to those evoked in S1BF LIV (**Section 3.3.2.b**); a profile which could indeed arise as a result of less stringent overall GABAergic control of network dynamics. This effect has already been reported in disinhibited prefrontal cortical slices (Bandyopadhyay et al., 2005). This theory is further supported by evidence from previous studies in agranular cortices describing less complex connectivity patterns of layer-specific networks (see **Figure 2C**, in **Section 3.3.1.a** above), one of the simplifications being the absence of inter-layer inhibitory connections (Katzel et al., 2011; van Haeften et al., 2003). The more homogeneous and possibly less restricted nature of agranular cortical activity may be of some relevance to its reported associative role (Schoenbaum et al., 2003): providing greater computational capacity and longer time-frames for signal integration, and in contrast to sensory cortices – which specialise in organising and processing dynamic sensory information. Together, these subtle differences in assembly dynamics could represent quantifiable measures of the functionally-distinct roles operated by frontal agranular and somatosensory cortices with respect to overall brain function.

c. Assemblies evoked in basal forebrain

In addition to the AIC, assemblies evoked in basal forebrain also represented novel observations: the activity profiles recorded in this sub-cortical region were

characterised by fast rise and decay dynamics. In addition to this, and in even starker contrast to cortical assemblies, basal forebrain responses were found to emit significantly lower summed fluorescence readings, nearly one order of magnitude below those recorded in cortical preparations (**Section 3.3.3.a**). Following the initial response, the diffuse fluorescence detected in basal forebrain, though displaying low amplitude, indicated that direct stimulation of this sub-cortical area triggered some level of network activity, as confirmed with LFP (**Section 3.3.4.c**). This could be due to the vast GABAergic influence in this particular brain region, restricting the expression of evoked activity. These observations were surprising at first, yet corroborated further the theory that the dynamics of mesoscopic activity profiles represent sensitive indicators of regional neuronal processing, and therefore function.

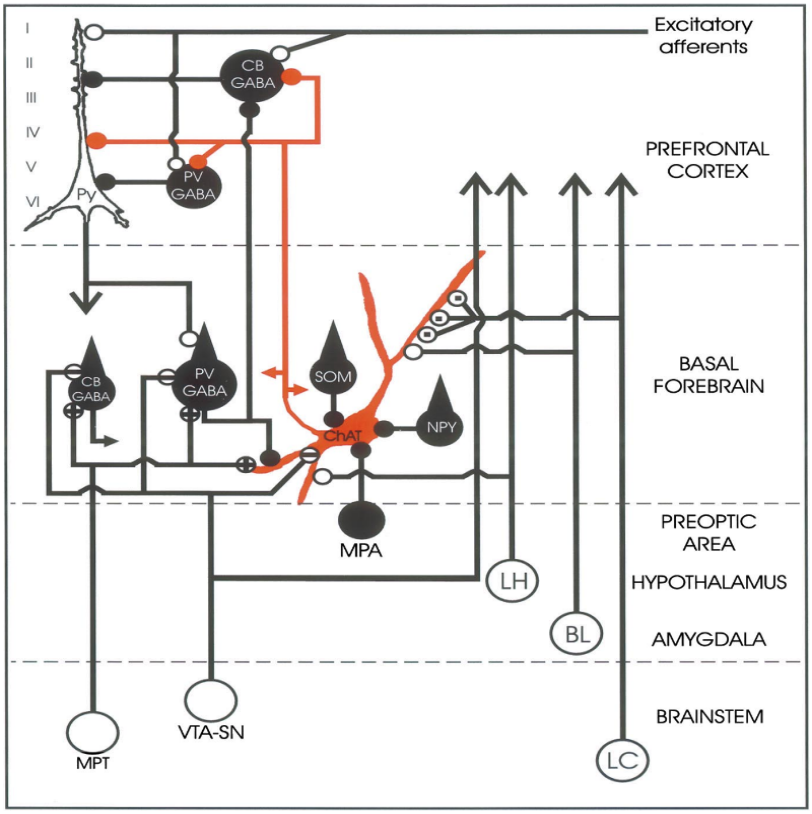

Figure 28: Schematic diagram representing the simplified termination of several major afferent connections to the basal forebrain as well as some of its internal circuitry. Most afferent connections to the BF originate from up-stream sub-cortical structures and target GABAergic and cholinergic (ChAT, orange) projection neurons, transducing signal

impulses and targeting the cerebral cortex. Note the selective targeting of glutamatergic afferents from the basolateral amygdala (BL) (Zaborszky et al., 1984), noradrenergic afferents from the locus coeruleus (LC) (Zaborszky and Cullinan, 1996; Zaborszky et al., 1993) and lateral hypothalamic (LH) axons (Zaborszky et al., 1991) terminating on the distal dendrites of cholinergic cells in the basal forebrain. On the other hand, somatostasin (SOM), neuropeptide Y (NPY) (Zaborszky and Cullinan, 1989), GABAergic (Zaborszky et al., 1986), medial preoptic (MPA) (Cullinan and Zaborszky, 1991) and dopaminergic fibres (Gaykema and Zaborszky, 1996) from the ventral tegmental area/substantia nigra (VTA-SN) all innervate cell soma and proximal dendrites of cholinergic neurons. Therefore, it appears as though the majority of the processing takes place *within* neurons rather than *between* neurons: a mechanism befitting the signal transduction and relay functions of the basal forebrain, compared to the much wider network activity dynamics of cortical tissue (compare circuit diagram to **Chapter 1**, **Figure 3**), more suited for the representation of multiple aspects of a same stimulus, and integration with spatially-competing assemblies. Adapted from (Zaborszky and Duque, 2000).

The basal forebrain, as explained in **Section 3.1.2.b**, is a sub-cortical region consisting of an aggregation of neuronal clusters which act similarly both as a signal transducers and relay stations, as displayed in the simplified circuit diagrams of **Figure 28** representing the general mesoscopic connectivity in these sub-cortical nuclei. The highly heterogeneous mix of cells in basal forebrain are not primarily arranged into local recurrent connections designed to process information, such as in the cortex (Douglas & Martin, 2004). Rather, basal forebrain consists mostly of large projection neurons which receive information, and relay it to distant brain regions, transducing initially glutamatergic excitatory signals by virtue of their neurochemical identity; particularly in the form of cholinergic (Armstrong et al., 1983) and GABAergic (Freund and Meskenaite, 1992) modulation of distant brain regions. As a result of this greatly simplified network organisation compared to that of cortical tissue, extensive population activity cannot be sustained (Golomb and Amitai, 1997; Wu et al., 1999), giving rise to the inconspicuous basal forebrain assemblies presented here. These observations are further supported by the finding that upon 60 Volts VPM stimulation, only minor levels of activity were elicited in

this sub-cortical nucleus: the VPM also acts as a relay station, yet not as a 'transducer', i.e. information arrives and is relayed in the form of glutamatergic transmission. Similarly therefore, both the basal forebrain and VPM feature much simpler network organisation than cortical tissue, which is reflected in the temporal dynamic signatures of the expression of their respective neuronal assemblies.

d. Conclusions and selection of representative cortical preparations

From the direct comparison of cortical and sub-cortical response discussed here, it can be concluded that those evoked in cortex are characterised by large activation dynamics taking place over relatively large spatio-temporal scales of millimetres and hundreds of milliseconds, in accordance with the need for large and longer-lasting cortical network activation required for integration and processing functionalities (Singer, 1993; Wu et al., 2001). It was also found that as expected, the manner of stimulation (direct or remote) of S1BF gave rise to strikingly different assemblies: this is further corroborated by the finding that assemblies evoked from direct LII/III or LIV stimulations did not give rise to strikingly dissimilar dynamics, confirming that it is indeed the *manner* in which the stimulus was delivered to the cortex which was responsible for the highly heterogeneous assembly expression profiles. Though no major differences were seen, assemblies evoked in LIV featured slightly more restricted lateral spread compared to those evoked in LII/III, and this can be attributed to the lack of lateral connections in LIV (Petersen and Sakmann, 2001), meaning activity must first spread to superficial or deep layers in a poly-synaptic manner before spreading horizontally. Similarly, the spatio-temporal profiles (as seen on space-time maps) and specific parameters of assembly dynamics were also found to differ somewhat between S1BF and AIC. These findings highlight the close correlation between VSDI signal and relevant mesoscopic

neuronal activity, which has been shown here to successfully discriminate between responses evoked i) via different stimulation paradigms, and ii) from structurally distinct cortical. Sub-cortical structures on the other hand, display comparatively lower amplitude responses featuring fast dynamics, as would be expected from structures specialised in fast relay of neuronal information. These observations further confirm the high precision of VSDI in recording the entirety of relevant responses, which electrophysiology could not provide fully.

Because of the similarity in overall assembly dynamics recorded across cortical preparations, it was decided that pharmacological treatments would be performed only on a single representative preparation from each cortical area, i.e. LII/III AIC and LVI S1BF stimulations, in addition to thalamocortical slice preparations. LIV stimulations in S1BF were selected as this experimental preparation has been used as the gold standard for studies of dynamic columnar activity, as well as for the putative role of LIV as the 'input' layer of information to primary cortices, driving otherwise naturally-evoked columnar activity. In AIC, afferent fibres have been reported to target both superficial and deep layers (Jasmin et al., 2004) with no precise discriminatory rule establishing a target layer for afferent information. Assemblies evoked in LII/III were thus chosen since of all cortical responses, these presented spatio-temporal profiles (time-series) which were the most dissimilar from those evoked in S1BF LIV.

3.4.4 Complementarity of VSDI and LFP and origin of recorded signals

a. Origin of VSDI and LFP signals

VSDs are lipophilic molecules which aggregate in fatty cell membranes: it has been reported that dye molecules have a heightened propensity to embed in (and thus

reflect activity from) the neuropil, where the complex arrangement of densely-packed cell membranes of dendritic processes equate to a greater concentrations of stainable membrane (Denk et al., 1990; Yuste et al., 1997). This is not to say that cell-body- and axon-rich regions do not contribute to the overall signal, yet may do so at a reduced intensity; this is in part due to the lower surface area of available excitable membrane as a result of the large volumes of cell bodies and the myelination of axons (Palkovits et al., 1986). Dendrites form elongated structures which frequently extend across vast areas of cortical tissue, and this plays a part in the discrepancy seen in spatial reach of VSDI response with that of CaSD imaging for example (Tsytsarev et al., 2014; Zecevic et al., 2003). The functionally-relevant and voltage-dependent nature of VSDI signal, such as is presented here, has indeed been confirmed electrophysiologically (Ross et al., 1977; Cohen et al., 1978; Salzberg et al., 1977; Cauller and Connors, 1994). The vast majority of the VSDI response reflects sub-threshold population V_m changes (Chen et al., 2012; Berger et al., 2007; Petersen & Sakmann, 2001), and in particular those originating from post-synaptic sites, which feature much larger surface area of highly excitable membrane compared to pre-synaptic terminals (Gandolfi et al., 2015). Evidence from experiments presented here and reported elsewhere (Berger et al., 2007; Cauller and Connors, 1994) using AMPA receptor blockers, which induce a block of assembly generation, corroborates the hypothesis that VSDI signal reflects post-synaptic changes in V_m.

Additionally, when considering the specific experimental methods utilised here for VSD staining of slices, the penetration of dye into the tissue under consideration must also be taken into account. Indeed, using di-4-ANEPPS and employing the methodology described here has been reported to only stain 70 and 100 μm of tissue from the surface of the slice (Hill and Greenfield, 2014). As discussed previously in **Chapter 1**, such a depth from which data can be acquired would therefore include,

if recorded radially within cortex (such as in slice preparations), the width of several inter-connected mini-columns. The signal is therefore only indicative of the activity taking place in that volume of brain slice, or from the superficial layers (LI and II/III) *in vivo* (Grinvald et al., 1988). In both approaches however, the VSDI signal only reflects part of the overall activity: electrical stimulations are likely to activate networks throughout the slice yet only record from the surface, while *in vivo* recordings emphasise the activity in superficial layers only. Either case present some level of restriction to the acquisition of the entire evoked cortical response, yet overall, VSDI retains the ability to provide a unique window on highly sensitive measures of cortical functioning.

An explanation of the crucial neuronal elements and events of interest, with respect to LFP recordings, has already been given in **Chapter 2**, **Section 2.1.2**: pyramidal cell synapses have been reported to feature heavily in the overall response (Johnston and Wu, 1995; Mitzdorf, 1985; Rall, 1962), similarly to VSDI signals. In all cases, the data featured a typical overall format of response consisting of i. 'fast', high-amplitude deflections lasting up to 20 ms after stimulus deliver, then followed by ii. 'slow', low-amplitude deflections lasting dozens of milliseconds. LFP deflections often showed a high level of trial-to-trial variability, both between and within different slice preparations, yet maintaining this general response architecture (**Figure 20** & **21**). In turn this activity is expected to reflect mainly the depolarisation of pyramidal cells, attributable to the large LFP deflections, leading to more subtle and latent, downstream changes in network activity (slow deflections) (Berger et al., 2007; Jin et al., 2002; Wu et al., 1999).

b. Complementarity of VSDI and LFP data

Relating electrophysiological and optical imaging data may initially present a difficulty, in particular when attempting to grasp the relevance of LFP records in the context of 2-dimensional VSDI data. But since the main advantage of VSDI is to provide V_m measurements from a continuous plane of locations (pixels), averaging together the VSD signal originating from an area approximately equivalent to that of the LFP reach (< 2 mm in radius) indeed demonstrates a close relationship in recorded signal between the two techniques (**Chapter 2**, **Figure 3**), as well as further confirmation of the functional relevance of each. To do so, all pixels within a small area befitting the putative size of the reach of the LFP receptive field (here selected as 5x5 pixels, i.e. 200x200 µm) were averaged together: this analysis yielded VSDI time series which could be compared to those of LFP on an identical time axis (**Figure 20** & **21**). Co-analysis of simultaneously obtained LFP and VSDI data could therefore provide unique insights into the internal dynamics of neuronal assemblies. Indeed, comparison of VSDI responses with their respective LFP signals present a possibly telling temporal symmetry: first detectable between the fast LFP deflections and the rise phase of the VSDI signal (both taking place within the first 15–20 ms after stimulus delivery in all tested preparations), and then between the onset of the slow optical signal decay phase and slower LFP deflections (>10 ms), if any were visible (**Section 3.3.4.c**). In turn the signal amplitude difference between the two techniques may reflect the size of their respective spatial receptive field, as well as their sensitivities. Since LFP is more sensitive to sizeable changes in local population V_m (Linden et al., 2011; Nowak and Bullier, 1997), this would indicate the majority of supra-threshold neuronal events take place in the first few milliseconds of assembly generation, and only within assembly hotspots of activity, while the rest of the response may represent sub-threshold activity only (Berger et al., 2007; Yuste et al., 1992). Indeed, the number of spiking cells at any

one moment within an assembly has in fact been estimated to be between 5 and 7% of all neurons involved in the event (Wu et al., 1999). This theory is further supported by the finding that performing identical experiments while imaging calcium-sensitive dyes (CaSD), indicative of action potential firing, shows a concentrated response confined to the immediate surroundings of the locus of stimulation (Kerr et al., 2007; Stosiek et al., 2003).

This apparent temporal binding of fast and slow responses in concurrent VSDI and LFP responses seems almost always detectable (Berger et al., 2007; Jin et al., 2002; Carlson and Coulter, 2008; Hill and Greenfield, 2014), and has already been proposed as describing the initially evoked spiking activity followed by long-lasting network-wide sub-threshold effects (Wu et al., 2001). Combining simultaneously-acquired VSDI and LFP data therefore provides an effective way of gathering information about the input activation of neuronal networks: where VSDI provides conspicuous records of the intensity, spatial reach and overall time course of network-wide sub-threshold effects initially triggered by small amounts of spiking activity which can be more easily appreciated within in a specific location using LFP.

3.4.5 Conclusions

In the present chapter, experiments were the dynamics of assemblies in a range of different brain regions under identical experimental conditions were investigated further. Within cortical preparations, responses showed comparable activity profiles bearing nonetheless some differences in their dynamic parameters, which can be explained in terms of differences in network architecture. When stimulated via remote thalamocortical activation, cortical activity patterns showed strikingly different dynamics, featuring wide and diffuse activity, in accordance with this more physiological method of stimulation. Sub-cortical structures showed much more

modest responses in comparison, which also differed greatly between VPM and basal forebrain. These activity profiles are correlated to the nature of their underlying networks: these experiments therefore provide further confirmation of the high dependence of recorded signal on the physical processes which generated it, especially that acquired using VSDI. The combination of this relatively new technique of optical imaging with more traditional electrophysiology allowed for a thorough characterisation of evoked activity. It was found that the fast propagation of assemblies upon stimulation coincides with large population and spiking activity, as detected by field potentials, followed by gradual decay back to baseline dominated by sub-threshold potential changes. Such a strategy can hence be applied to the study of the drug action at the meso-scale, in particular for clinical agents used routinely for which the exact mechanism the subject of much controversy: anaesthetics.

Chapter 4: RESULTS II

Anaesthetic action on mesoscopic dynamics of cortical and sub-cortical neuronal assemblies

4.1 Introduction

In the present chapter, investigations focus on the effects induced by anaesthetics on assemblies evoked in S1BF, both with direct and thalamocortical stimulations, and AIC. The interest in this field of research is two-fold: first, providing a comprehensive description of anaesthetic effect on mesoscopic brain dynamics remains an under-explored field of anaesthesia research (Antkowiak, 2002), and secondly such research could implement a useful intermediate level of description linking the vast body of knowledge already acquired on both the cellular and systemic actions of anaesthetics, at the micro- and macro-scales respectively. Furthermore, anaesthetics represent a very interesting class of drugs as the property which unifies them into a same drug 'family' is not physical (i.e. structural), chemical (i.e. molecular composition) or pharmacological (i.e. biological targets): rather, anaesthetics are loosely grouped together as a result of their shared potential in inducing analgesia (pain relief) and loss of consciousness (LOC), mainly.

The initial intent of the present investigations focuses on assessing the similarities and differences in inhibition induced by each of pentobarbital, etomidate and ketamine in different areas of cortex: AIC and S1BF, using direct stimulations. Secondly, the effects of anaesthetics in S1BF assemblies will be compared between direct and remote (thalamocortical) stimulation paradigms. In doing so, the effects of each agent on specific parameters of assembly dynamics, such as summed fluorescence, lateral spread and time course of activity, will be compared. Thirdly,

effects of anaesthetics on LFP recordings will be discussed in light of those acquired using optical imaging. Finally, the effects of each anaesthetic on basal forebrain assemblies will be characterised, and compared to those induced in cortical assemblies.

The process by which anaesthetics induce LOC remains unclear to this day (Kopp Lugli et al., 2009) yet two questions in particular, can be addressed in the present investigations: i) does an anaesthetic drug induce a homogenous profile of inhibition across brain sub-regions or are there regional differences in sensitivity? And ii) can VSDI help differentiate more clearly what protein targets are responsible for the inhibition seen upon application of clinically-relevant anaesthetics concentrations? The former question has implications for general anaesthesia, as the profile of anaesthetic action across the brain may help understand more clearly their respective clinical effects, while the latter could shed more light on which protein effectors are most relevant to anaesthesia at the meso-scale of brain organisation. First however, an introduction to the history of the use of anaesthetics in clinical practice, as well as to the current status of research into the mechanisms of anaesthesia will be provided.

4.1.1 A brief history of the discovery of anaesthetic drugs

Since the Middle Ages, it had been known that diethyl ether (or just 'ether') possesses significant mind-altering properties which include a potent analgesic effect, altogether inducing a state of delirium described as 'ether frolics'. Another substance of note: opium, which contains a range of active opioid compounds the main effectors of which are codeine and morphine, was used since the antiquity also both as a popular recreational drug as well as for analgesic purposes. In the early

19th century, Friedrich Sertürner isolated and purified morphine from opium giving birth to the first strong analgesic drug. Shortly after, Humphrey Davy publicised the use of both ether and nitrous oxide (N_2O) for clinical practice, emphasizing their beneficial effects in destroying painful sensation. A few decades later, in 1847, the Scottish obstetrician James Young Simpson used chloroform to induce anaesthesia in a patient needing dental surgery with great success; chloroform initially received very wide public appeal, but was quickly found to also be highly toxic. Although these first inhalational drugs had some beneficial effects as analgesics, their overall clinical effectiveness remained limited, mostly due to their high toxicity, which prompted the continued search for better anaesthetic agents (Lopez-Munoz et al., 2005). The discovery and cataloguing of anaesthetic drugs marked a significant milestone in clinical research, and indeed the end of the 'dark ages' of medicine, as the only meagre reassurance a surgeon could provide his patient prior to their discovery was speed – in those days, many patients needing surgery would unfortunately opt for certain death rather than to risk undergoing traumatic operations.

In 1903, the physician Joseph von Mering and chemist Hermann Emil Fischer discovered the hypnotic (i.e. induction of a state of unresponsiveness and loss of consciousness (Campagna et al., 2003)), effects of diethyl barbituric acid, later known as barbital; a discovery which paved the way for the subsequent synthesis of many derivatives which all showed varying degrees of antiepileptic, hypnotic and sedative effects. The first intravenous anaesthetics, sodium thiopental and pentobarbital, were discovered and synthesized by Ernest Volwiler and Donalee Tabern in the early 1930's (Lopez-Munoz et al., 2005). Following this, a large number of different anaesthetic compounds were further synthesized in the second half of the 20th century (Carter, 1951), many of them credited to Paul Janssen, founder of Janssen Pharmaceutica, who also first synthesized etomidate in 1964.

Among a long list of structurally- and chemically-distinct molecules possessing anaesthetic properties discovered in the late 20th century, ketamine, synthesised by Calvin Stevens in 1962 at Wade State University, is of notable importance: contrary to barbiturates or other classical anaesthetics, this drug induces a 'dissociative' anaesthesia, i.e. where the patient remains conscious but dissociated from events occurring in the operation theatre. This type of anaesthesia did not affect blood flow/pressure or respiration rate, making it the anaesthetic agent of choice for 'emergency anaesthesia', as well as becoming a popular drug of abuse from the 1970's onwards. Ketamine is a peculiar agent, as it shares many of the molecular targets as traditional group 2 anaesthetics (such as Xenon and N_2O), yet produces a qualitatively different type of anaesthesia. As a result, of the thousands of drugs ever synthesised that were found to possess anaesthetic properties, only a handful have ever been used clinically (**Figure 1**).

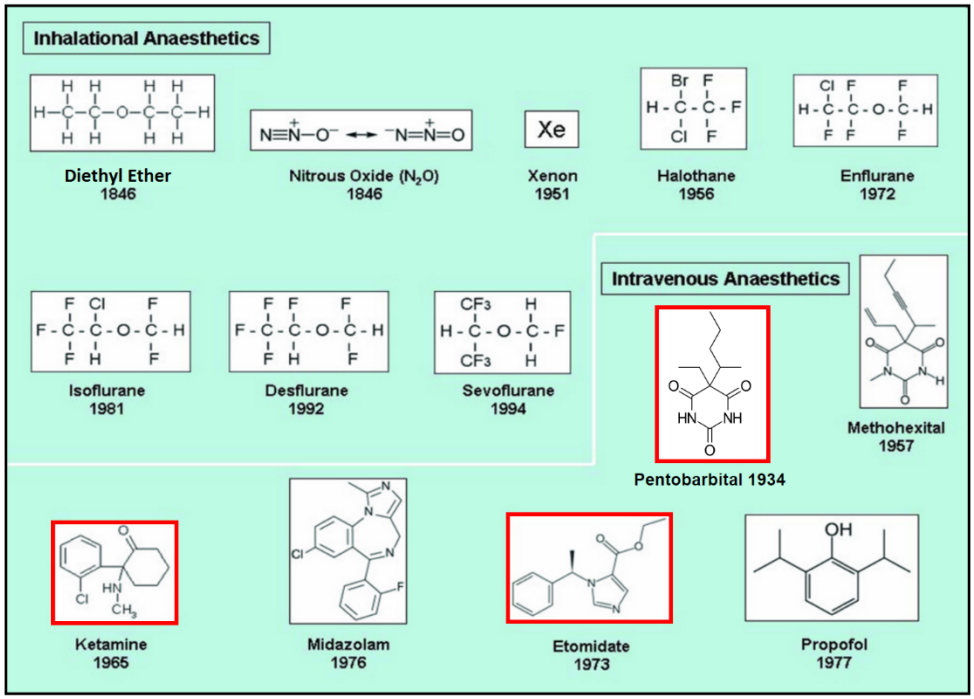

Figure 1: Molecular structures of common anaesthetic drugs. Anaesthetics are most traditionally inoculated via inhalation (top panel) or intravenously (bottom panel). The names of the drugs are given below their molecular structure, also displaying the year they were first used in clinical practice. Note the high heterogeneity in molecular structure, size and chemical species exhibited by these particular anaesthetics yet, importantly, all induce

altered mental states (once) adequate for the purposes of anaesthesia. Drugs used in the present investigations are highlighted in red squares. Adapted from (Lugli et al, 2009).

- *Choice of anaesthetic drugs: intravenous agents*

In the present chapter, three anaesthetic agents were chosen in order to conduct experiments: pentobarbital, etomidate and ketamine (see **Figure 1**). First of all, a well-studied barbiturate drug was chosen (pentobarbital), as this family of anaesthetic drugs are among the oldest intravenous drugs used for general anaesthesia in clinical settings, and have been extensively studied – providing ample data regarding their effects at a range of relevant target proteins. More specifically, pentobarbital was chosen over thiopental, which is nowadays preferred in human anaesthesia, for its availability in our lab as well as for its still important use in animal anaesthesia. Etomidate was also chosen as a test agent since it is still currently used as an anaesthetic of choice in clinical settings (Fengler, 2008). Propofol, nowadays the anaesthetic of choice, was omitted from this study as its pure form does not solubilise well in water, meaning it must to be tested using its emulsified formulation, the appearance of which is a thick milky white. Some experiments were run with this propofol emulsion within the perfusate, however only low concentrations could be tested: at medium and high concentrations, optical imaging data acquisition was affected by the increased opacity of the resulting test perfusion. Compared to all other experiments presented in this thesis, these particular propofol trials produced excessively noisy recordings (data not shown), suspected to arise as a result of an increased scattering of photons within the bath solution, i.e. shot noise, and highlights an important limitation of VSDI when studying this particular drug. Finally, a group 2-like anaesthetic ketamine, which has also been extensively studied in the context of both clinical and toxicological

research, was tested both for investigation purposes as well as for comparison against group 1 anaesthetics mentioned previously.

4.1.2 The mode of action of anaesthetic drugs

a. The necessity of clarifying the actions of anaesthetics

Studying anaesthetic action represents an attractive area of research, as even though thousands of people each day undergo successful anaesthesia, the specific cellular (micro-scale) and population-wide (meso-scale) mechanisms responsible for the overall behavioural effect (anaesthesia, macro-scale) remain one of the greatest un-solved mysteries of modern neuropharmacology (Urban, 2008). Moreover, in some instances, accidental awareness during general anaesthesia (AAGA) may occur, even when significant doses of anaesthetic drugs are inoculated, prompting the need for a better understanding of the exact mode of action of anaesthetics to help avoid this phenomenon (Pandit et al., 2013).

b. Early theories of anaesthetic action

Over the years, different theories positing a general mode of action of anaesthetic drugs have been advanced: one in particular, the 'Meyer-Overton correlation', found that there was a strikingly close correspondence between anaesthetic potency and solubility in olive oil (Lugli et al., 2009), positing the lipophilicity of anaesthetic agents (i.e. their solubility in fatty media) as a key factor in determining their respective potency. This finding implicated neuronal cell membranes as the target of anaesthetic action: by this mechanism, drugs were believed to dissolve preferentially in phospholipid compartments, altering the internal homeostasis of neuronal cell membranes and increasing their overall fluidity, leading to reduced cellular function. This was considered an attractive theory as it provided a simple

thermodynamic basis for the common overall action of a wide range of molecules featuring often very dissimilar structures and compositions. This theory has largely been discounted in the last 30 years however, due to it conflicting with other physiological observations, for example the fact that high body temperature (which also disrupts membrane fluidity) does not give rise to states of anaesthesia.

It was later discovered that anaesthetics could affect the delicate functionality of proteins: in particular, it was shown that incubation of the enzyme luciferase (which fireflies use to create flashes of light) with increasing concentrations of anaesthetic produced dose-dependent impairments in the ability of the enzyme to produce light (Franks and Lieb, 1984; Moss et al., 1991). Additionally, it was found that the potencies of these effects in inhibiting luciferase coincided with those predicted by the Meyer-Overton correlation; these experiments implicated membrane proteins, rather than the membranes themselves, as a target of anaesthetic drugs (Lugli et al., 2009). These findings prompted novel interest in identifying which proteins could be involved in, and how this mechanism took place.

c. Proteins as targets of anaesthetic drugs

Investigators soon turned to the use of electrophysiology to probe the activity of ion channel proteins using novel advances in molecular cloning techniques, allowing for the expression of pure protein populations (for example in Xenopus oocytes): such approaches provided model systems of receptor function in the presence of specific drugs of interest, making abstraction of the multitude of confounding processes at play within native neurons, and effectively isolating the dynamics of interest. In addition to the implication of a large number of different types of ion channels as possible targets, anaesthetics could therefore also potentially affect proteins involved in many other functions than just regulation of transmembrane

ionic conductances. For example, they have been found to significantly affect the function of protein kinase C (PKC), an essential enzyme for the correct homeostasis of neurotransmitter release and ion channel activity (Gomez et al., 2003; Hemmings and Adamo, 1994); anaesthetics have also been found to affect the appropriate functioning of mitochondrial proteins (Zaugg et al., 2002), protein pumps, G proteins, phosphatases and SNARE (soluble *N*-ethylmaleimide-sensitive factor attachment protein receptor) proteins, involved in neurotransmitter exocytosis (Salaun et al., 2005). It is believed therefore, that anaesthetics actually affect a range of proteins involved in many distinct locations and aspects of intracellular functioning, modulating brain processes over several time scales, the most conspicuous impact of which is that induced on transmembrane channel proteins, as these actions have a direct and fast effect on cerebral (and therefore behavioural) function, i.e. induction of anaesthesia.

Over the years, it has been found that proteins, including the all-important trans-membrane ionic channel proteins, contain structural irregularities (cavities) which, due to the biochemical nature of the amino acid residues which form the surface of these cavities, create specific electrochemical micro-domains (Brunori et al., 2000). These crevices can be either hydrophilic, where they are filled with water – helping to stabilise the hydration shell of the protein, or hydrophobic – repulsing water molecules. The lipid solubility of anaesthetics makes hydrophobic cavities a preferential target site, however hydrophilic crevices have also been implicated. Indeed, these water-filled regions along the surface of channel proteins may represent necessary spaces to allow for the adequate movement associated with a change in conformation which accompanies gating of the channel: it has been shown that anaesthetics, by preferentially infiltrating these crevices, can in turn interact with the protein to favour the stabilisation of structural conformations *other* than the usual resting state (Urban, 2008), thereby modulating the probability of channel

gating. More generally, cavities may feature a range of specific chemical and physical milieus combining charge, hydrophilicity, size and shape, which act as selectivity filters for anaesthetic drugs and in turn as allosteric interaction sites. The binding of drugs within protein cavities increases the probability of altering the electronic distribution within the protein, favouring the stabilisation of distinct macro-molecular structural rearrangements, which could account for some of the actions of anaesthetics at the micro-scale.

In all cases, it is the interaction of anaesthetic drugs with channel proteins which has been found to be the key mechanism in the overall effect these drugs induce on the discharge dynamics of central neurons (Campagna et al., 2003; Rudolph and Antkowiak, 2004), yet the diversity of anaesthetic binding sites which were subsequently found supplied a further difficulty. These findings suddenly turned the field of anaesthetic research from one of overwhelming uncertainty (of possible mechanisms), to one offering too many possible targets.

4.1.3 Trans-membrane ion channels relevant to anaesthesia

With regards to the drugs selected for experimentation in this chapter, i.e. etomidate, pentobarbital and ketamine, it is well known that the former two agents act primarily via actions at $GABA_A$ receptors (Bieda and MacIver, 2004; Garcia et al., 2010; Zimmerman et al., 1994), while the anaesthetic actions of ketamine have been attributed more prominently to its interactions with NMDA receptors (Belelli et al., 1999; Franks and Lieb, 1984; Krasowski and Harrison, 1999). Therefore, a brief introduction to the structure, function and possible role in the mechanism of anaesthesia played by each of these two channel proteins is provided in parts **a** and **b**. Furthermore, a description of the role played by other transmembrane ion channel

protein targets of anaesthetic drugs, which are now known to be central to mechanisms of anaesthesia (Chen et al., 2009; Friederich and Urban, 1999; Rudolph and Antkowiak, 2004; Zhang et al., 2014), is given in part **c**. Finally, the concentrations at which ketamine, pentobarbital and etomidate are reported to modulate the functions of these relevant protein targets is presented in part **d**.

a. The $GABA_A$ receptor

$GABA_A$ receptors mediate the fast inhibitory component of neuronal communication (within just a few milliseconds); the slower component of GABAergic inhibition on the other hand, is mediated via metabotropic G-protein-coupled receptors (GPCRs, i.e. $GABA_B$). Another type of ionotropic GABA receptor exists, which is entirely composed of ρ (rho) subunits: this '$GABA_A$- ρ' receptor activates with slower yet more sustained dynamics compared to those of $GABA_A$ (Zhang et al., 2001), but are insensitive to common allosteric modulators such as barbiturates and benzodiazepines, and as such will not be considered further. $GABA_A$ receptors are most usually localized at synapses within post-synaptic densities, with some isoforms preferentially found extra-synaptically (Wei et al., 2003): anaesthetics positively modulate $GABA_A$ receptors, with the magnitude of their effects at extra-synaptic receptors remaining an open question in the context of anaesthesia (Orser, 2007).

$GABA_A$ receptors consist of the assembly of 5 separate sub-units, which span the entire thickness of the membrane, protruding both intra- and extracellularly, and come together to create a pentameric channel protein (Olsen and Sieghart, 2009). $GABA_A$ receptors are members of the "*Cys*-loop" superfamily of LGICs, which include nicotinic acetylcholine receptors (nAChRs), serotonin-3 ($5\text{-}HT_3Rs$), glycine and $GABA_A$ receptors (Thompson et al., 2010). The subunits which make up the

receptors of this superfamily consist of single amino acid chains which extend to form 4 α-helical trans-membrane (TM) domains with both carboxy- and amino-termini situated extracellularly, featuring a typical cysteine-to-cysteine di-sulphide bond creating a loop (*Cys*-loop) in their extracellular domain close to the N-terminus: a structure which is highly conserved across all cys-loop receptors (**Figure 2**). Upon receptor gating, an anion-selective (negative ions, such as chlorine, Cl^-) channel opens in their centre which lets in brief (few milliseconds) currents of Cl^- ions, flooding the intracellular space down their electrochemical gradient, and giving rise to inhibitory post-synaptic potentials (IPSCs) which hyperpolarize the cell (Colquhoun and Sivilotti, 2004). As a result of their mediation of IPSCs, $GABA_A$ receptors are generally attributed the role of the inhibitory component in neuronal communication however in some instances, curiously, this mechanism has been found to give rise to neuronal *depolarization* (Ben-Ari et al., 1989), the most common of those occurrences being when inhibitory neurons target other inhibitory neurons (Anaclet et al., 2015; Freund and Meskenaite, 1992) – thereby removing the inhibitory block on downstream excitatory processes.

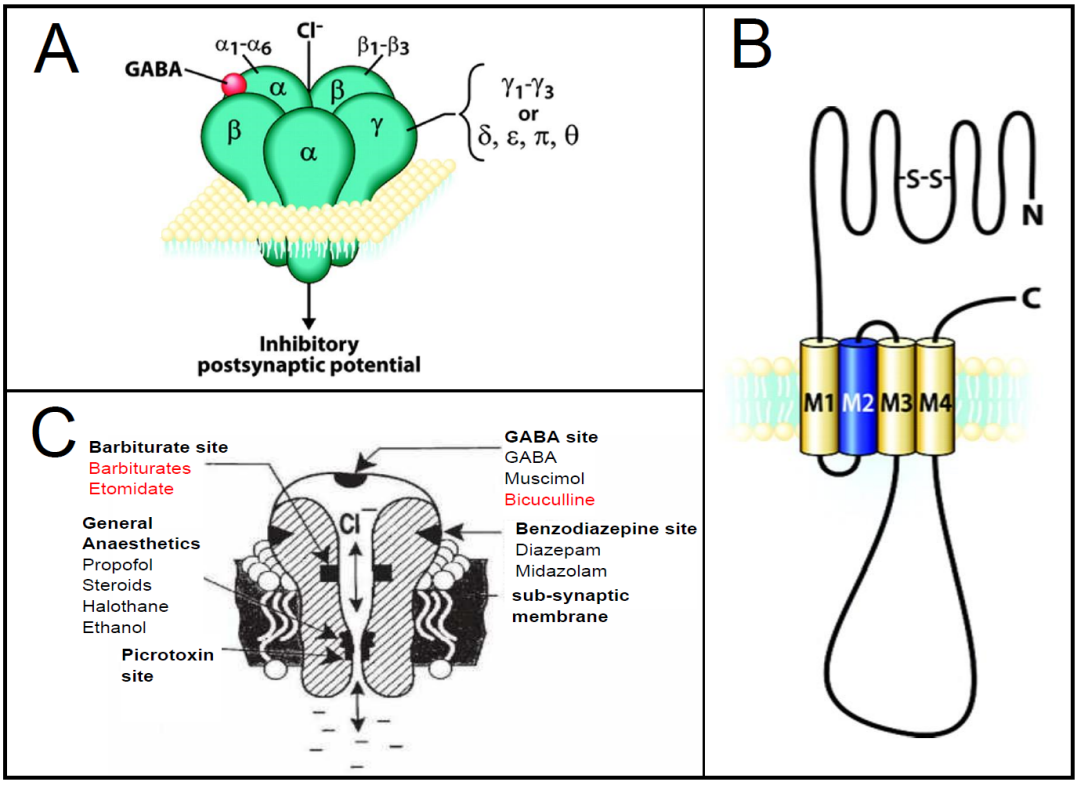

Figure 2: The $GABA_A$ receptor structure, function and pharmacology. **A**. Diagram representing a general functional receptor complex quaternary structure which includes the assembly of 5 subunits, which include at least 2 α- and 2 β-subunits with a 5th subunit of either the δ, γ, ε, π or θ sub-type – each possessing specific chemical, physiological, structural and pharmacological properties (Colquhoun & Silvetti, 2004; Olsen & Sieghart, 2009). In all cases however, $GABA_A$ receptors bind their endogenous agonist, GABA, on two separate binding sites located at the intersection of α- and β-subunits – both binding sites must be occupied for the receptor to open. Upon gating of the channel, short bursts of Cl^- ions are allowed into the cell through an anion-selective pore, owing to the nature of the amino acid residues on the M2 TM domain which lines the lumen of the channel, i.e. mediating the channel's ion selectivity. The high Cl^- conductance of this receptor (IPSCs) leads to hyperpolarization of the cell. Panel adapted from (Uusi-Oukari et al., 2010). **B**. Schematic showing the general structure of a single receptor subunit: large extracellular domain from the amino terminus (top), featuring a disulphide bond (*cys*-loop) which leads to 4 α-helical TM domains (M1-4, embedded within cell membrane), with a longer intracellular domain formed by an extensive M3-to-M4 chain (bottom), ending with a shorter extracellular carboxy terminus. The TM α-helices aggregate together inside the membrane with M2 (blue cylinder) positioned such as to line the lumen of the channel in the quaternary protein structure. **C**. $GABA_A$ receptor pharmacology: GABA receptor subunits possess a number of binding domains for allosteric agents. So far relevant to anaesthesia, it has been found that benzodiazepine drugs bind to an allosteric site on the extracellular domain of receptor subunits, additionally, barbiturates have been reported to bind within the receptor

pore, general anaesthetics bind close to the channel lumen, as does picrotoxin – each of these agents induce a potent modulation of the gating dynamics of the receptor channel, yet do so in distinct ways. For example, binding of diazepam (benzodiazepine) to the receptor has the overall effect of increasing the probability that the channel will open when GABA binds; barbiturates, like pentobarbital for example, act by stabilizing the open conformation of the receptor channel, meaning that the probability the channel opens remains largely unchanged, but once the channel does open it remains so for longer periods of time, giving rise to much increased IPSCs (Bianchi et al., 2009; Eghbali et al., 1997). Etomidate also acts by increasing GABAergic burst duration, yet has also been shown to possess the ability to gate the receptor into an open-channel conformation all on its own, without the presence of GABA, when applied at high enough concentrations. Drugs used in pharmacological manipulations within this thesis are highlighted in red. Panel adapted from (Ingrid, 2012).

Each receptor subunit (see **Figure 2** legend) possess their own intricacies, thereby assigning specific dynamics and sensitivities to each distinct receptor stoichiometries: the site of action of benzodiazepines is only formed at the interface of α_1 and γ_2 subunits, meaning only $\alpha_1\beta_x\gamma_2$–containing channels are sensitive to benzodiazepines (Richter et al., 2012). In addition to that of benzodiazepines (Barnard et al., 1998), $GABA_A$ receptors contain a number of drug-specific allosteric binding sites (**Figure 2C**) including a barbiturate site (for drugs such as thiopental, pentobarbital and etomidate), another general anaesthetics binding site (propofol, halothane and ethanol), as well as a picrotoxin site. Each of these drugs affect the gating of receptors sensitive to their effects in distinct ways, see **Figure 2** legend, adding to the difficulty in identifying specific drug effects with respect to behavioural responses. Crucially, it was found that inhalational anaesthetics such as the noble gas Xenon, N_2O (nitrous oxide) and cyclopropane as well as (importantly) the intravenous agent ketamine do not, or only minimally, interfere with $GABA_A$ receptors (Flood and Krasowski, 2000; Franks, 2008; MacDonald et al., 1987), suggesting an alternate mechanism of action.

b. The NMDA receptor

In **Section 3.2.1.b**, a short introduction to glutamate LGIC receptors was given where the different sub-classes of receptors were listed, i.e. AMPA, NMDA and KA receptors; all three are excitatory ionotropic receptors which respond to the binding of glutamate by opening a cation-selective channel, leading to the generation of EPSPs, and ultimately cellular depolarisation. The NMDA receptor features a similar structure to that of $GABA_A$, yet with important differences: NMDA receptors consist of the aggregation of 4 subunits, i.e. 2 GluN1 and 2 GluN2 subunits, forming a TM channel at their centre (Cull-Candy et al., 2001; Wyllie et al., 2013). Though similar, GluN1 and GluN2 subunits differ in key aspects: their respective binding domains are not activated by the same endogenous ligand, GluN1 subunits bind glycine (or D-serine) while GluN2 subunits bind glutamate – both agonists must be bound before the receptor channel can open (Kleckner and Dingledine, 1988). NMDA receptor subunits are also made up of a single amino acid chain, which produce an extracellular domain (containing a modulatory domain and a ligand binding domain), 4 α-helical membrane-associated domains, with helices (TM) 1, 3 and 4 crossing the membrane, while helix 2 (TM2), instead of crossing through the entire thickness of the membrane, forms a re-entrant loop back into the intracellular space (**Figure 3A**) (Furukawa et al., 2005; Paoletti and Neyton, 2007). This M2 loop is key to the function of the NMDA receptor: it lines the lumen of the cation channel, and the nature of its residues plays a crucial role in the channel's cation selectivity (Furukawa et al., 2005), reminiscent of the selectivity filter of potassium channels. Finally, NMDA receptor subunits also form large intracellular domains featuring residues which can directly interact with phosphatases, kinases and a slew of adaptor and scaffolding proteins which have a direct effect on receptor localization, activity, dynamics and trafficking (Stephenson, 2006).

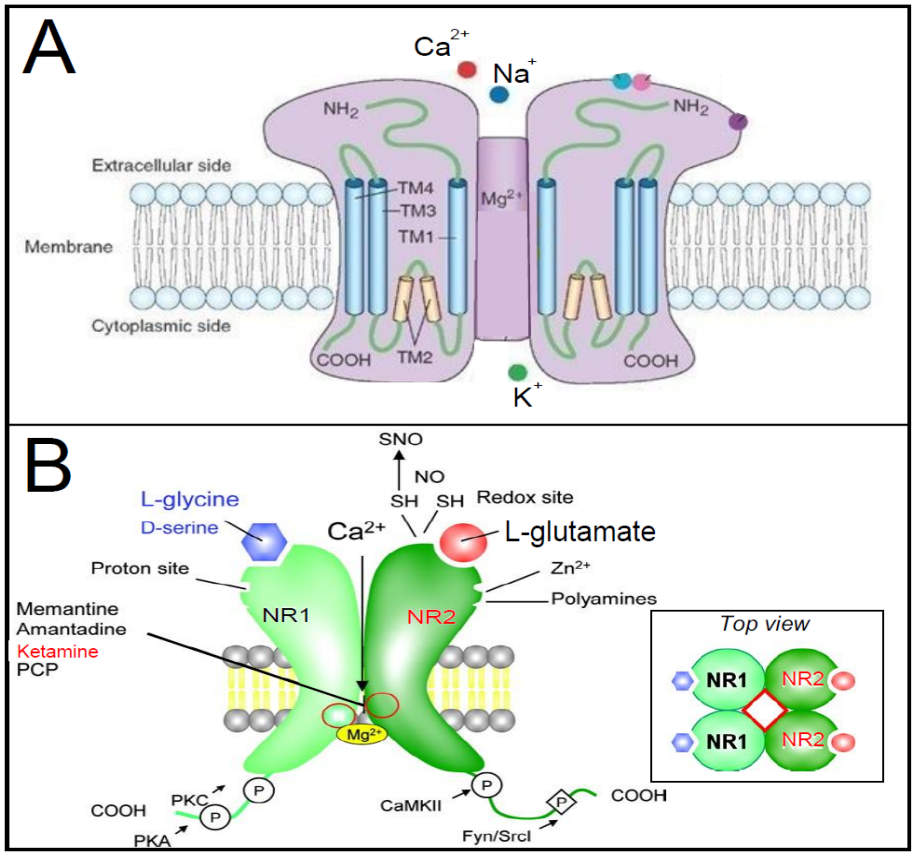

Figure 3: The NMDA receptor structure, function and pharmacology. **A**. Schematic diagram showing a cross-section through an NMDA receptor, highlighting their general architecture: quaternary structure includes the aggregation of 4 receptor subunits – 2 GluN1 (NR1) and 2 GluN2 (NR2) subunits. The successive binding of ligands to the subunits incrementally increases the gating probability of the receptor which opens an un-selective cation pore, i.e. permeable to K^+, Na^+ and, crucially, Ca^{2+} ions. Upon channel gating, cations enter neurons producing robust EPSCs, depolarizing the cell. NMDA receptor subunits are composed, like $GABA_A$ receptors, of a large extracellular amino terminus domain where the agonist binding site is located, leading to 4 α-helical domains where TM1 crosses the membrane while TM2 forms a re-entrant loop into the membrane and back into the intracellular space, followed by two more regular TM (3 & 4) domains, ending with an intracellular carboxy terminus highly involved in interacting with intracellular proteins. An intrinsic property of the NMDA receptor is that it possesses a magnesium (Mg^{2+}) binding site within its channel lumen which acts as an endogenous receptor blocker: only once certain levels of intracellular depolarisation have taken place within the post-synaptic cell is this Mg^{2+}-block alleviated, allowing for ions to pass through. Panel adapted from (Ribeiro et al., 2014). **B**. NMDA receptor pharmacology: multiple endogenous agents and drugs have been identified to target NMDA receptors at specific sites on receptor subunits, including zinc (Zn^{2+}) and polyamines binding sites on GluN2 subunits. A redox reaction site has also been identified on GluN2 subunits which, depending on its state, can have a profound effect on the excitability of the receptor. GluN1 subunits have been found to be sensitive to acidic

conditions (proton site, H^+), as well as harbouring the binding site for Mg^{2+} within the channel lumen. It was also found that drugs like Phencyclidine (PCP, 'angel dust'), Ketamine, Memantine and MK-801 also showed potent allosteric inhibition of NMDA receptors, and in the last 30 years, a specific site within the channel pore has been identified as the target binding site of these drugs, blocking the flow of ions. Inset: top view of the tetrameric quaternary NMDA receptor structure within the membrane, composed of 2 GluN1 (NR1) and 2 GluN2 (NR2) subunits. Drugs used in pharmacological manipulations within this thesis are highlighted in red.

To the contrary to $GABA_A$ and AMPA receptors, NMDA receptors do not mediate the 'fast' component of signal transmission, as a result of a number of their intrinsic properties. In addition to the existence of a peculiar re-entrant channel lumen α-helix, the TM domains of NMDA receptor subunits contain other intricacies which are central to their functionality: specific amino acid residues present within these TM domains account for the receptor's high-unitary conductance, which is un-selective to cations (i.e. allowing free passage of calcium ions, Ca^{2+}, in addition to sodium, Na^+, and potassium, K^+, ions), as well as their property of being blocked by magnesium (Mg^{2+}) and zinc (Zn^{2+}), in a voltage-dependent way, at resting V_m (Wyllie et al., 2013; Cull-Candy et al., 2001; Paoletti and Neyton, 2007). These receptors have been implicated in more physiological processes than just signal transmission: Ca^{2+} is not only a potently-charged ion, but most significantly also acts as an intracellular messenger, necessary to trigger a range of key cellular and synaptic processes (Berridge et al., 2000; Bootman et al., 2002). For example, the high Ca^{2+}-conductance of NMDA receptors is known to be of crucial importance in the initiation of long-term potentiation (LTP) and depression (LTD), shaping the adaptation of neuronal networks to on-going activity and experience (May, 2011); thereby implicating this receptor sub-class, in addition to its role in neurotransmission, as an effector in the processes of learning and memory (Riedel et al., 2003).

On the extracellular domains of GluN1 subunits (**Figure 3B**), in addition to zinc and glycine binding sites, a proton (H^+) modulatory site has been found, which grants this receptor with pH-sensing capabilities (Traynelis et al., 1995). On GluN2 subunits, a further polyamines binding site has been found, as well as a redox site rich in cysteine residues which, depending on the state of the sulphur atoms, induce a potent modulatory effect on channel gating dynamics. NMDA receptors also contain an additional binding site within their channel lumen, which is the target of several antagonists, including phencyclidine (PCP), MK-801 (Wong et al., 1986) and importantly, ketamine (Harrison and Simmonds, 1985; MacDonald et al., 1987; Martin and Lodge, 1985). Therefore, the initially puzzling finding that ketamine did not produce its main effect via some mechanism of $GABA_A$ receptor potentiation, can be accommodated for by the finding that it has a greater impact on the slower component of excitatory glutamatergic transmission (Anis et al., 1983; Irifune et al., 1992); this may also explain why ketamine, contrary to most other anaesthetics, induces a 'dissociative', rather than 'general', anaesthesia (Badin, 2004; Grasshoff et al., 2005). The term 'dissociative' anaesthesia refers to an induced state characterised by catatonia, catalepsy, analgesia and amnesia, without necessarily achieving LOC, i.e. hypnosis (Winters et al., 1972).

c. Additional ion channel targets

In addition to the above mentioned LGICs, another cys-loop receptor is involved as a target of anaesthetic action: the neuronal and muscle nicotinic acetylcholine receptors (nAChR) (Forman and Miller, 2011). This receptor is very close in structure to those of $GABA_A$ and 5-HT_3 receptors, with major differences in the selectivity of both its endogenous ligand (acetylcholine), and ionic species permeability (cations) compared to $GABA_A$ receptors. Though recent studies have only been able to conclusively demonstrate the involvement of only a few specific

receptor subtypes (including $\alpha_4\beta_2$-, $\alpha_3\beta_4$- and α_7-containing nAChRs), anaesthetic blockade of these targets has been reported to mediate some of the amnesia, analgesia (in the brain) and immobility (in the spinal cord and at the neuro-muscular junction) of anaesthesia (Tassonyi et al., 2002).

LGICs are essential to appropriate neuronal communication, however they work in tandem with a wide range of other ion channels (ligand-gated or not) in order to support appropriate neuronal membrane properties and impulse conduction. These ion channel proteins are usually ion-selective (i.e. potassium-, sodium- or calcium-selective), and if not ligand-gated, respond to changes in voltage (voltage-gated, VGIC), or both (Enyedi and Czirjak, 2010); thereby operating specific roles in action potential propagation. For example, sodium-selective (Na^+) VGICs open upon relatively small amounts of depolarisation, letting sodium ions rush into neurons down their electro-chemical gradient, depolarising the cell and thereby mediating the rising phase of action potentials. Once a region of the neuron has depolarised past a specific threshold, calcium-selective (Ca^{2+}) VGICs (which are also permeable to sodium ions, yet to a much lesser extent) also open, letting calcium into neurons. Calcium is a very potent divalent ion which therefore provokes robust cellular depolarisation, in addition to inducing multiple secondary effects, which include: altering and regulating gene expression (West et al., 2001), activating Ca^{2+}-sensitive potassium channels (Chung et al., 1991; Takahashi and Terrar, 1994) (as well as other intracellular proteins not directly involved in cellular communication), and mediating neurotransmitter exocytosis (vesicular membrane fusion) (Augustine, 2001). Finally, potassium-selective (K^+) VGICs play a part in repolarising neurons back towards the resting state as well as maintaining their hyperpolarised state (Baranauskas et al., 2003; Hoffman et al., 1997), by allowing potassium to flow in and out of neurons. Anaesthetics have been widely reported to interfere with neuronal VGICs, impacting on their gating dynamics and thereby

having a direct effect on neuronal impulse conduction. Furthermore, anaesthetics have also been reported to act on another type of ion channel called the hyperpolarisation-activated cyclic nucleotide-gated (or HCN) channel: these channels are also part of the K^+ VGIC superfamily, yet are non-selective to cations and are gated by the intracellular ligand cAMP (Biel, 2009; Wahl-Schott and Biel, 2008). They have been attributed the role of 'pacemaker' channels as they are crucial in the process of spontaneous and rhythmic neuronal impulse generation; HCN channels have also been implicated as targets of anaesthetic drugs with potential relevance to anaesthesia (Chen et al., 2009).

d. Effective concentrations of anaesthetics at transmembrane ionic channels

Table 1 lists all of the previously described potential targets, in addition to estimates of their respective effective concentrations at each of those targets, extracted from the literature.

ANAESTHETIC TARGET	KETAMINE	PENTOBARBITAL	ETOMIDATE
$GABA_A$ RECEPTORS	**No/negligible actions**	**> 50 → potentiation of $GABA_AR$ currents** (Weiss and Hablitz, 1984) **>100 → direct activation of $GABA_ARs$** (Thompson et al., 1996)	**> 1 → *potentiation of $GABA_AR$ currents*** (Hill-Venning et al., 1997) **> 40 → direct activation of $GABA_ARs$** (Rusch et al., 2004)
NMDA RECEPTORS	**10-20** (Yamamura and Kemmotsu, 1990)	**No/negligible actions**	**No/negligible actions**
K^+ VGIC	**400-450 → delayed rectifying (DR) K^+ VGICs** (Schnoebel et al., 2005)	**≈ 8 → Leak and inward rectifying (IR) K^+ VGICs** (Wan et al., 2003)	**No/negligible actions** (O'Connell et al., 2002)
K2P CHANNELS	**≈ 350** (Friederich & Urban, 1999)	**No/negligible actions** (Heurteaux et al., 2004)	**100-130** (Putzke et al., 2007)
HCN CHANNELS	**> 5** (Chen et al., 2009)	**No/negligible actions**	**No/negligible actions** (Chen et al., 2009)
NEURONAL AChRs	**> 2** (Forman et al., 2015; Moaddel et al., 2013)	**≈ 25** (Dilger et al., 1997; Roth et al., 1989)	**> 5** (Hamouda et al., 2011; Nirthanan et al., 2008)
Na^+ VGIC	**800+** (Wagner et al., 2001)	**600-1000** (Frenkel et al., 1990; Rehberg et al., 1995)	**≈0.46** (Zhang et al., 2014)
Ca^{2+} VGIC	**T-type: ≈ 2500** (Todorovic & Lingle, 1998) **L-type: ≈9.2** (Hatakeyama et al., 2001)	**> 300** (Todorovic and Lingle, 1998) (Joksovic et al., 2005)	**> 25-205** (Todorovic and Lingle, 1998) (Joksovic et al., 2005)
OTHER TARGETS	--	**5-HT_3Rs block: 135** (Barann et al., 2000; Barann et al., 1997)	--

Table 1: Effective or inhibitory dose ranges for ketamine, pentobarbital and etomidate (in μM) at some of the most widely reported protein targets involved in the induction of anaesthesia, including: $GABA_A$, NMDA and nicotinic acetylcholine receptors, two-pore-domain potassium (K2P) channels, Hyperpolarization-activated cyclic nucleotide–gated

(HCN) channels, as well as potassium, sodium and calcium voltage-gated channels. This table is only intended to provide a rough comparison of dose- and drug-specific effects on common protein targets of anaesthesia. Most of the protein targets listed in this table consist of large families of related isomeric forms: anaesthetics usually affect only some of these family members, or affect different ones at widely different concentration ranges, hence the ranges given in the table above. Furthermore, while many of these effective drug concentrations were obtained in reductionist preparations (oocytes or HEK293 cells), which undoubtedly lack the complexity and modulation of intact neuronal networks, these findings nonetheless represent valuable pieces of information from which the interpretation of mesoscopic data presented here can be discussed. These effective doses can be matched, assuming some degree of error, to the observed mesoscopic effects of ketamine, etomidate and pentobarbital in attempting to identify salient drug targets.

4.1.4 Relating impaired assembly dynamics to anaesthesia

As discussed previously in **Chapter 1**, brain computations (and therefore, functions), such as sensory processing, motor activity, cognition as well as sleep, rely on the transient and synchronous activation of spatially distributed groups of neurons, i.e. neuronal assemblies (Koch and Greenfield, 2007; Shirvalkar, 2009). Anaesthesia refers to a behavioural state in which sensory perception is lost and consciousness is abolished, it therefore suggests that the wide variety of anaesthetic drugs must affect an up-stream, fundamental brain process common to the generation of all the above-mentioned cerebral functions. One potential candidate target for this central mechanism could be the appropriate functioning and interaction of assemblies *in vivo* (Lin et al., 2006); indeed, the process of information transfer and integration in the brain requires the ability to generate both local computational units (assemblies) as well as robust long-range connectivity interlinking these spatially-segregated 'small-world networks' (Dehaene and Changeux, 2003; Sporns et al., 2004). Since synaptic activity as well as neuronal impulse conduction, both essential mechanisms for appropriate neuronal and

systemic function, are targeted by anaesthetic action (Hanchar et al., 2005; Olsen and Sieghart, 2009), impeding these precise dynamics could in turn account for a macro-scale systemic loss of function. Therefore, this hypothesis could account for the great heterogeneity of anaesthetic molecules and sites of action. Indeed, the relevance of neuronal assemblies as clinical measures of brain state has already been discussed, in particular in the context of EEG records (**Chapter 1**, **Section 1.5.3**) since it is those measures which are often used to probe for depth of anaesthesia in the clinic, such as with bispectral (BIS) index monitoring (de Deyne et al., 1998; Rosow and Manberg, 2001), or even during *in vivo* experiments (Devonshire et al., 2010b). Electrophysiology has enabled investigators to understand the microscopic effects of anaesthetics (Takahashi & Terrar, 1994; Ribeiro et al., 2014), what is needed now is a similar acquisition of data focusing on characterising and quantifying the network-level effects of anaesthetics *in vitro*, i.e. using high-resolution imaging techniques such as VSDI, for which to this day only a handful of reports have been published (Collins et al., 2007b; Kratzer et al., 2012; Kratzer et al., 2014).

4.1.5 Advantages of studying anaesthetic action at the meso-scale

Historically, studies of the inhibitory influence of anaesthetic agents have primarily concentrated on either the micro-scale using electrophysiological techniques, or the macro-scale with the use of non-invasive brain monitoring technology, electrophysiological (i.e. EEG; (Clark and Rosner, 1973; Thornton, 1991)) as well as using imaging (i.e. fMRI or PET scans) (Heinke and Schwarzbauer, 2002). In the former case, the investigative strategy employs a bottom-up approach, attempting to identify specific protein effectors responsible for higher-order systemic effects

while for the latter, a greater emphasis is given to identifying specific anaesthetic doses which give rise to reproducible overall brain states (systemic effects); i.e. a top-down approach. Yet no clear link can easily be established relating protein targets with specific doses and their resulting behavioural effects. This is because, as it was already stated in the introduction (**Section 1.2**), the gap separating the micro- from the macro-scale of brain organisation is too vast to infer causal links between molecular effector and behavioural state (such as levels of anaesthesia). Therefore, focusing on network-level (mesoscopic) effects of anaesthetics would represent a shortening of the informational gap previously separating data already acquired at the micro- with that obtained at the macro-scale. This approach has the potential of offering a method of linking protein targets to network-level effects and then to behavioural states with greater ease.

In the experimental setting presented here, the effects of anaesthetics (see **Section 4.1.1**) are tested on slice preparations of interest: the AIC (LII/III stimulations), the S1BF (LIV stimulations) and the thalamocortical system. The former two preparations provide data on the impact of anaesthetics on local cortical excitability, and possibly show differences between granular and agranular cortices, while the latter preparation provides an indication of the extent to which extra-cortical mechanisms are affected by these same clinically-relevant concentrations of anaesthetic. Additionally, the impact of effective doses applied to basal forebrain preparations will be investigated in order to probe for differential impacts of anaesthetics in this key brain region, highly implicated in modulating arousal state and attentional control.

4.2 Methods

All experiments were carried out here in S1BF coronal slices (LIV stimulation), AIC coronal slices (LII/III stimulation), thalamocortical slices (VPM stimulation) and basal forebrain slices (VBD stimulation), as they were described previously: for experiment preparation, recording and data analysis, refer to **Chapter 2**. However: some methods specific to the experiments carried out in this chapter will be mentioned in more detail or will be added if not previously mentioned. These brief supplementary methods include a description of the concentrations used for experiments with ketamine, pentobarbital and etomidate (**Section 4.2.1**), specific methods of drug solution preparations (**Section 4.2.2**) as well as analysis methods for comparison of multi-epoch data (**Section 4.2.3**).

4.2.1 Experimental anaesthetic concentrations

The dynamics of assemblies were probed using increasing concentrations of anaesthetic where first a baseline condition was recorded, acquired in an identical way as the data presented in **Chapter 3**, followed by successively increasing concentrations of either pentobarbital, etomidate or ketamine. With the purpose of studying the effects such agents have on mesoscopic dynamics upon induction of large doses of anaesthetic drugs, the first few concentrations were designed to produce only slight or no effect, followed by rapidly increasing dose ranges which reach well beyond the estimated doses used for clinical anaesthesia. The reasoning behind the concentration ranges chosen for each drug, as well as the validity of this perfusion protocol are discussed in greater detail in **Section 4.4.1**.

- **Pentobarbital** was perfused at 20, 50, 80, 150, 320 and 600 μM, where 20 μM perfusions were expected to produce only negligible effects, while at

600 μM perfusion, maximum effects were expected. In order to gather these data, experiments were run first by recording a baseline condition followed by 20, 80 and 320 μM pentobarbital, while a second set of experiments investigated the effects of 50, 150 and 600 μM solutions.

- **Etomidate** was perfused at 0.5, 2, 8, 32 and 120 μM, according to similar maximum and minimum dose-response expectations. In this case, experiments consisted of baseline followed by 0.5, 8 and 120 μM etomidate, and baseline followed by 2 and 32 μM solutions.
- **Ketamine** was perfused at 0.1, 0.5, 1, 2.5, 5, 25, 125 and 250 μM. At first, experiments were carried out with 0.1, and 1, then a further set of experiments were performed using 0.5, 2.5 and 25 μM ketamine, and finally experiments were run with 5, 125 and 250 μM.

4.2.2 Preparation of anaesthetic stock solutions

Ketamine and pentobarbital are both readily soluble in dH_2O: stock solution were therefore made, without the need for added solvents, as 20 mM solutions before being aliquoted into eppendorfs and kept at -30°C. Etomidate on the other hand is not water soluble, therefore solubilising the drug first required to dissolve it in DMSO and then slowly added to warmed (30-35°C) dH_2O, yielding a 10 mM etomidate stock solution in 1.5% DMSO, before being aliquoted. This protocol ensured the appropriate dissolving of etomidate which, once diluted down to the concentrations used for experimentation (diluted between 20 000 and 13 times), resulted in negligible levels (<0.1% v/v) of DMSO in final test perfusions; some vehicle controls experiments were run with 0.1% DMSO and showed no modulation of baseline response over a 2-hour long recording period (n=2, data not shown). Drug aliquots were kept frozen until approximately 10 minutes before rig perfusion:

eppendorfs were quickly thawed with warm water before required amounts of stock solution were added to aCSF samples (room temperature) and mixed thoroughly. Drug solutions were then left to rest for 2 to 3 minutes at room temperature, with bubbling carbogen, until the start of their perfusion.

4.2.3 Normalisation of multi-epoch data

In the experiments presented here, drug perfusions were inoculated in series starting from a drug-free baseline condition, followed by epochs of successively increasing anaesthetic concentrations. In order to prevent the contamination of data as a result of time-dependent changes in assembly dynamics and slice health, experiments were limited to a maximum of 5 successive recording epochs (total of 115-120 minutes, see **Chapter 2**, **Section 2.7.4.d**). Since modulation of evoked responses over time was inevitable, even over this time frame, a series of control experiments were run with each preparation for that same amount of time, see **Section 4.3.1**, and used for normalisation of data. The analysis of spatio-temporal data was performed as described previously, using the VSDI toolbox in order to extract and rasterise fluorescence recorded within tangential geometries (See **Chapters 2** & **3**).

a. Normalisation of VSDI epoch data

VSDI data were collected as shown in **Chapter 3**, averaging fluorescence within an ROI over 15 minute recording periods (30 individual trials), termed 'recording conditions' or 'epochs'. When subsequently running experiments using anaesthetics, the data from each recording epoch were normalised in two ways: first, within a single experimental trial, all drug conditions were normalised to their respective baseline, and second: to their respective time-locked control condition, in order to express the data as the percentage change in fluorescence from that which

is normally emitted in control experiments. These normalisation steps allowed for the isolation of drug-specific effect, making abstraction of the slowly deteriorating trend in response magnitude which, though non-significant, often become noticeable after 50-60 minutes of recording.

b. Acquisition and normalisation of LFP data

LFP data were acquired continuously throughout the experiment, therefore the average deflection amplitude was calculated (see **Chapter 2**) for baseline conditions (first 30 trials) and used to normalise the rest of the recorded amplitudes, producing normalised trend plots. Field potentials gave rise to highly variable deflections, even in control solutions, which is translated in the jitter of their resulting response amplitude trend plots (see **Figure 5A–Ci**), therefore only a single normalisation step was operated for LFP data, i.e. normalising voltage deflections to their average of baseline. The second normalisation step undertaken for VSDI data (i.e. normalisation to time-locked control level) was omitted as a result of the difficulty in exactly matching drug conditions with their respective controls, due to the continuous nature of LFP data acquisition protocols. In order to assess the extent of drug effects, the mean normalised amplitude of LFP deflections over the last 5 minutes (10 individual trials) of each drug recording condition was measured for use in analysis (see **Figure 5A–Cii**).

4.3 Results

4.3.1 Control experiments

a. Probing stability of assembly dynamics using VSDI

The initial step undertaken in the present investigations was to run control experiments in the absence of anaesthetics in the perfusate, in order to probe for any time-dependence of assembly dynamics. **Figure 4** shows the magnitude (i.e. overall summed fluorescence) of evoked responses over 2 hour-long recording periods. Though no significant changes (see **Tables 2**, comparison ID: **4.3.1.a**, two-way ANOVA, factor 1: time-dependence of response, factor 2: sample preparation) were found between any comparisons (epochs/controls 1-5, **Figure 4A**), the average magnitude of evoked responses can be seen to decrease more prominently from the third control condition onwards (after more than 1 hour of recording) in AIC and S1BF slice preparations. This differed from thalamocortical experiments which showed an initial decrease (between controls 1 and 2) followed by more stable responses, plateauing between control conditions 2 and 5. In all cases however, over a 2-hour recording period, all preparations tested showed slight decreases in response magnitude reaching a common level at the end of condition 5 with a maximum decrease of 18.75% seen in S1BF (≈12% decrease for both AIC and thalamocortical preparations). For comparison purposes, the data from the first and last recording condition are displayed in space-time maps (**Figure 4B**), showing only minor decreases in their respective spatio-temporal activity profiles. From these data, responses were considered to be adequately stable over 2 hours-long recording time scales, yet showing small decreases in response magnitude over time. This finding justified the second, time-locked normalisation step, in addition to the initial normalisation of conditions 2-5 to their respective baseline level (condition 1), between drug experiments and controls, as described in **Section 4.2.3.a**.

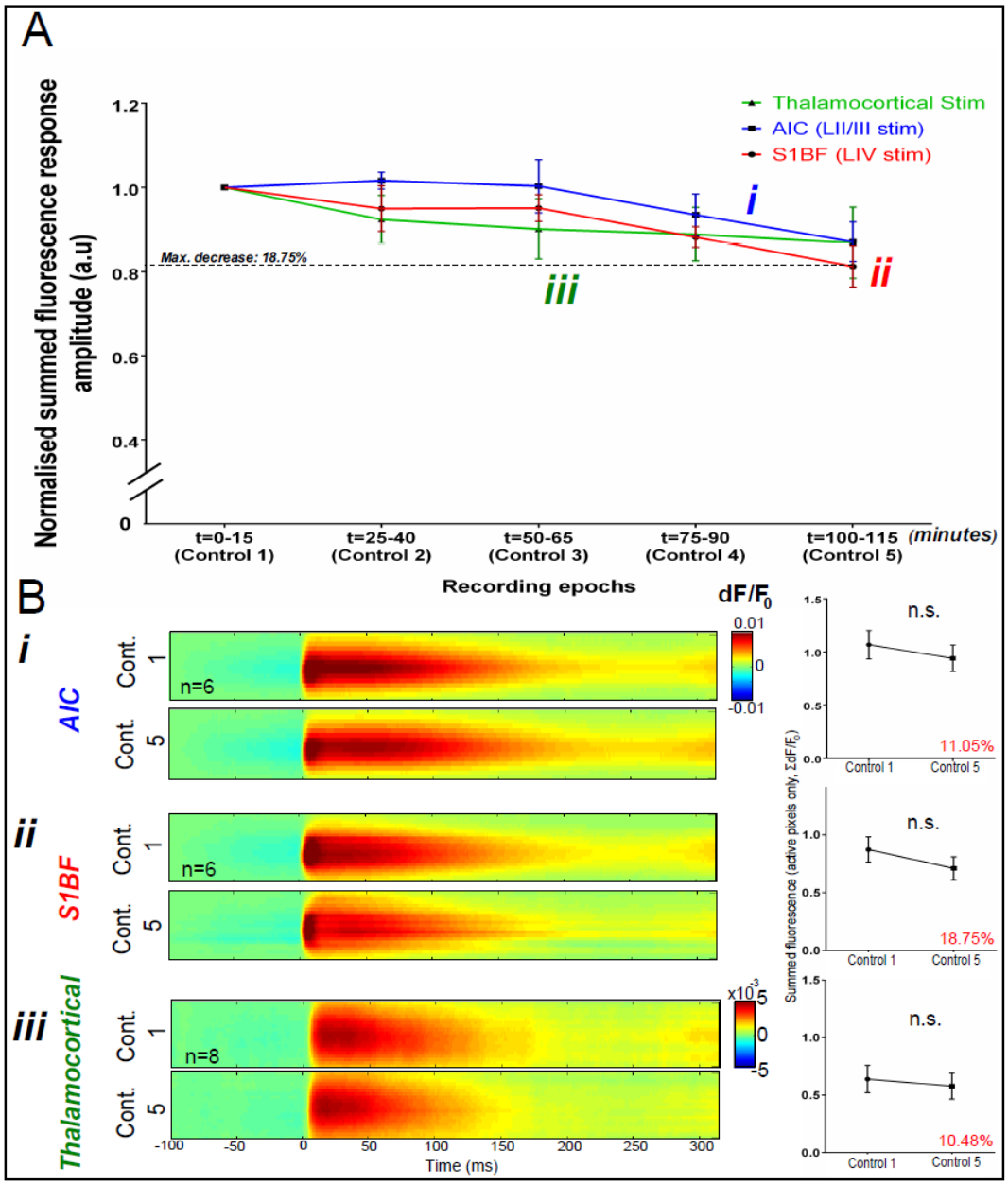

Figure 4: VSDI control experiments. The data acquisition protocol is described in **Chapter 2**: over a 2-hour period, 5 recording epochs (15 minutes in length) were acquired, with 10-12 minutes separating each epoch. **A**. Overall normalised data showing time had only a minimal impact on the emitted summed fluorescence from agranular insular cortex (LII/III stimulation, n=6, blue trace), primary somatosensory cortex (LIV stimulation, n=6, red trace) and thalamocortical activation (VPM/white matter stimulation, n=8, green trace). **B**. Average space-time maps of activity evoked in the above-mentioned slice preparations in the first recording epoch ('Control 1') and the last ('Control 5'): AIC (**i**), S1BF (**ii**) and thalamocortical (**iii**). The summed fluorescence values are quantified and compared for each preparation (right panels), with only small (<20%) non-significant decreases found over two hours of recording – for statistical comparisons, see **Table 3**, comparison ID: **4.3.1.a**.

Statistical test results of assembly magnitudes over time: ANOVA table						
Comparison ID	**Factors**	**Sum of squares**	**Dgrees of freedom**	**Mean of squares**	***F*-statistics**	***p*-values**
4.3.1.a	**Interaction**	0.03991	8	0.004989	F (8, 85) = 0.1658	***p* = 0.9948**
	Time-dependence	0.2647	4	0.06617	F (4, 85) = 2.199	***p* = 0.0758**
	Preparation	0.04891	2	0.02446	F (2, 85) = 0.8129	***p* = 0.4470**
	Residual	2.557	85	0.03009		

Table 2: Two-way ANOVA result table testing for significant effects induced either as a result of time (factor 1) or preparation (factor 2) on the stability of evoked responses (assemblies). No significant differences were found here.

b. Probing stability of assembly dynamics using LFP

When responses to electrical stimulation were probed over time using electrophysiology, similar stable responses were seen: **Figure 5** shows LFP deflection trend graphs over 2 hour-long recording periods recorded from agranular insular cortex LV/VI (**A**), somatosensory cortex LII/III (**B**) and thalamocortical LIV (**C**). Contrary to VSDI control experiments, simultaneous LFP experiments did not show slow decreases in deflection amplitude over time, but rather showed very stable if not slightly increasing amplitudes over time. LFP deflections were consistently observed to be more extensive in S1BF compared to AIC or TC slice preparations; additionally, S1BF LFP records all seemed noisier than those recorded in AIC and TC, yet this may have been due to external factors within the lab during those experimental runs rather than to physiological slice effects. For each preparation, the experiment showing the greatest LFP deflection was chosen as examples to display deflection time series (bottom panels, **ii**): in every case, the first (blue) and last (yellow) 5 frames from each trend graph (panels **i**) were averaged together to produce deflection time series (panels **ii**) which highlight the high stability in magnitude of evoked LFP deflections over time.

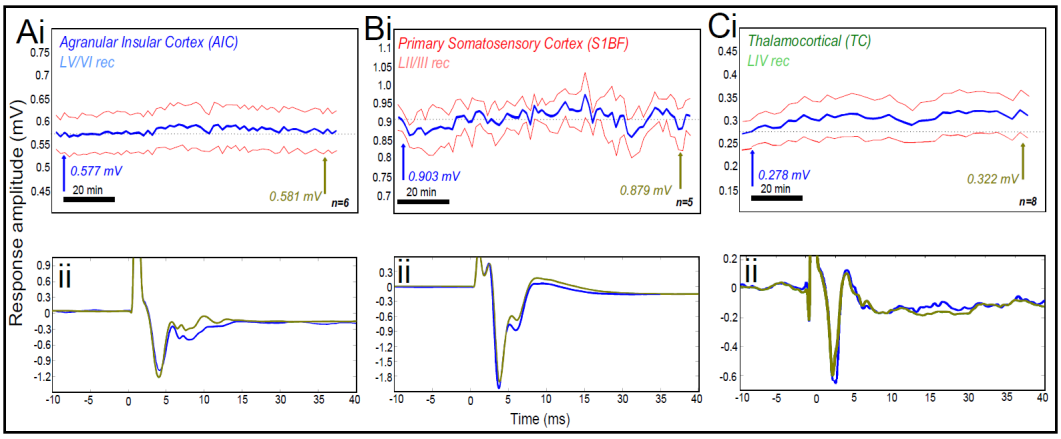

Figure 5: LFP results of control experiments. **A**. **i**. Trend graph showing the evolution of the average LFP response amplitude (blue line) measured in agranular insular cortex (AIC, n=6), with S.E.M (red lines), over a 2-hour recording window, blue and gold arrows show the time points from which data frames were averaged together (5 frames each) for representation and comparison of typical time-series (**ii**). Blue and gold labels (mV) provide a reading of the overall mean deflection amplitude obtained at the start and end of each set of control experiments. **B**. **i**. Trend graph of response amplitude (blue line) in primary somatosensory cortex (S1BF, n=5), with S.E.M (red lines), typical time-series shown in panel **ii**. **C**. Trend graph of response amplitude (blue line) in thalamocortical slices (TC, n=8), with S.E.M (red lines), typical time-series shown in panel **ii**.

Statistical test results of LFP controls: first 10 averaged frames vs last 10 averaged frames (2-hour-long recordings)							
Comparison ID	**Data set comparison**	**Test parameter(s)**	**Statistical test employed**	***p* value**	***F*- or *t*-statistics**	**Post-hoc test (adjusted) *p* value**	**Significance level**
4.3.1.b.i	LFP controls in AIC	Deflection amplitude	Two-tailed paired t-test	***p* = 0.8138**	$t(5) = 0.2482$	n/a	**n.s.**
4.3.1.b.ii	LFP controls in S1BF	Deflection amplitude		***p* = 0.7765**	$t(4) = 0.3037$	n/a	**n.s.**
4.3.1.b.iii	LFP controls in TC	Deflection amplitude		***p* = 0.5425**	$t(6) = 0.6455$	n/a	**n.s.**

Table 3: Statistical test result table for control experiments in direct and remote stimulation experiments using LFP. In all cases, the first 5 evoked deflections were averaged together and compared the last 5 evoked deflections, as shown by the blue and gold arrows in **Figure 5**.

4.3.2 Anaesthetic effect on evoked cortical responses

The first goal of the present investigation was to characterise the inhibitory effects of each anaesthetic in two different cortical sub-regions, i.e. the S1BF and AIC, using identical direct stimulation paradigms. In order to do so, investigations first focused on assembly sensitivity to anaesthetics, i.e. how are assemblies in each preparation affected by the three anaesthetics of choice, followed by a comparison of each anaesthetics' potencies with regards to their target preparation. Some differences were previously found in the normal response profiles of these assemblies (see **Chapter 3**), and anaesthetic treatment may highlight further differences in their respective population behaviour.

a. Anaesthetic effects in agranular insular (AIC) and somatosensory cortices (S1BF) using direct stimulation

- *Direct activation of agranular insular cortex (AIC)*

The normalised data points for each anaesthetic were plotted on *XY* semi-log graphs and fitted with sigmoidal 4 parameters logistic (4PL) regressions, which are mathematically identical to the Hill equation (Hill, 1910; Prinz, 2010); highlighting the clear dose-response relationships of anaesthetic effect on mesoscopic AIC assemblies and allowing for the calculation of IC_{50} value estimates for each anaesthetic agent. Perfusing slices containing AIC with increasing anaesthetic concentrations in all cases produced significant dose-dependent inhibition of assembly magnitude (measured as the summed fluorescence; see **Table 4** & **5**, two-way ANOVA, factor 1: drug concentration, factor 2: anaesthetic agent). Additionally, it was found that even at supra-clinical concentrations (i.e. maximal dose perfusions), none of the anaesthetics tested here induced a total silencing of

evoked activity (**Figure 6B**). Pentobarbital induced the most potent inhibition of assembly dynamics at maximal concentration (600 μM, 62% inhibition from normalised control), followed by etomidate (120 μM, 56% inhibition from normalised control) while ketamine induced the least inhibition (250 μM, 47% inhibition from normalised control). Following this, the concentrations equalling 50% inhibition of population activity (IC_{50} values) for each anaesthetic were calculated (see **Figure 6A**): etomidate was found to be the most potent anaesthetic (IC_{50}: 5.92 μM), followed by ketamine (IC_{50}: 10.60 μM), with pentobarbital showing the lowest potency (IC_{50}: 136.50 μM). These calculations enabled for the selection of data from drug perfusions closest to their respective IC_{50} values, i.e. etomidate: 2 μM, ketamine: 5 μM, pentobarbital: 150 μM, for display as space-time maps (**Figure 6B**).

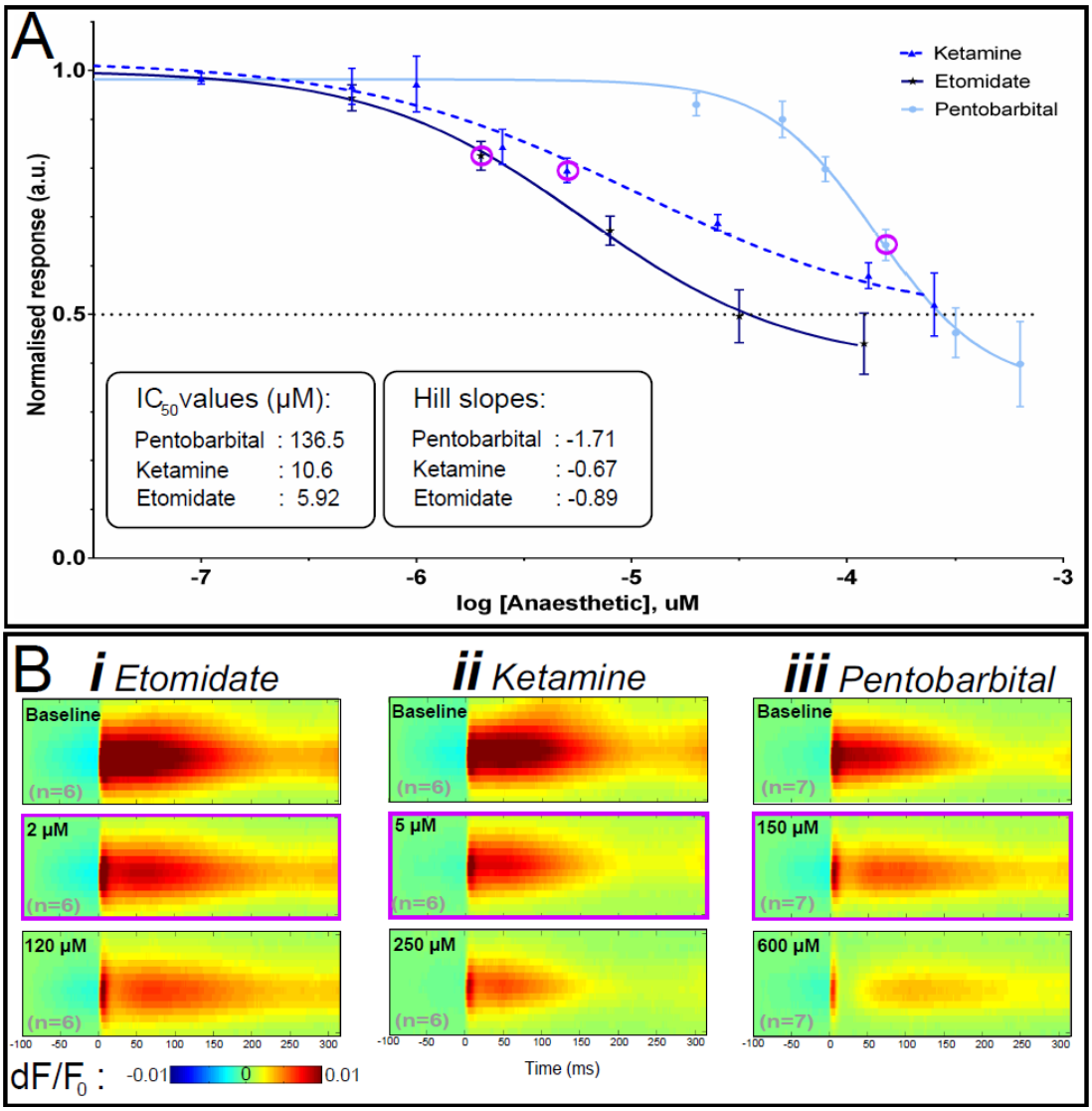

Figure 6: Anaesthetic effect on AIC network excitability. **A**. Dose-response curves for the effects of increasing concentrations of etomidate, ketamine and pentobarbital, inset: IC_{50} values for each anaesthetic as calculated from the dose-response curves. Purple circles indicate which of the anaesthetic concentrations were found to be closest to their calculated IC_{50} values: etomidate – 2 μM perfusion; ketamine – 5 μM perfusion; pentobarbital – 150 μM perfusion. These 'near-IC_{50}' drug doses are displayed in purple boxes in panel **B** space-time maps (middle row). **B**. space-time maps of activity showing baseline activity, that which is evoked near each anaesthetic's IC_{50} values as well as max inhibition for **i**. Etomidate, **ii**. Ketamine and **iii**. Pentobarbital.

- *Direct activation of primary somatosensory cortex (S1BF)*

Dose-response curves were fit to the data acquired in S1BF slices (**Figure 7A**) in exactly the same way as it is described above for slices containing AIC; these dose-response curves were then used for data analysis. All anaesthetic drugs tested were found to induced significant dose-dependent decreases in assembly dynamics (summed fluorescence, see **Table 4**, comparison IDs: **4.3.2.a.i-iii** & **4.3.2.a.iv-vi**, two-way ANOVA, factor 1: drug concentration, factor 2: anaesthetic agent), both in AIC and S1BF. Assemblies evoked in S1BF were similarly resistant to total silencing resulting from maximal anaesthetic dose perfusions: pentobarbital induced the greatest depression of activity (600 μM, 66% inhibition from normalised control), followed by etomidate (120 μM, 61% inhibition from normalised control) and ketamine, again inducing the least inhibition (250 μM, 46% inhibition from normalised control). IC_{50} values for each anaesthetic were also very similar to their respective AIC values, indicating similar potencies in either cortices: etomidate showed the greatest potency (IC_{50}: 4.73 μM), followed by ketamine (IC_{50}: 14.52 μM), with pentobarbital showing the lowest potency (IC_{50}: 125.34 μM). As a result of the similarity in the results obtained in S1BF to those of AIC, the near-IC_{50} concentrations remained the same.

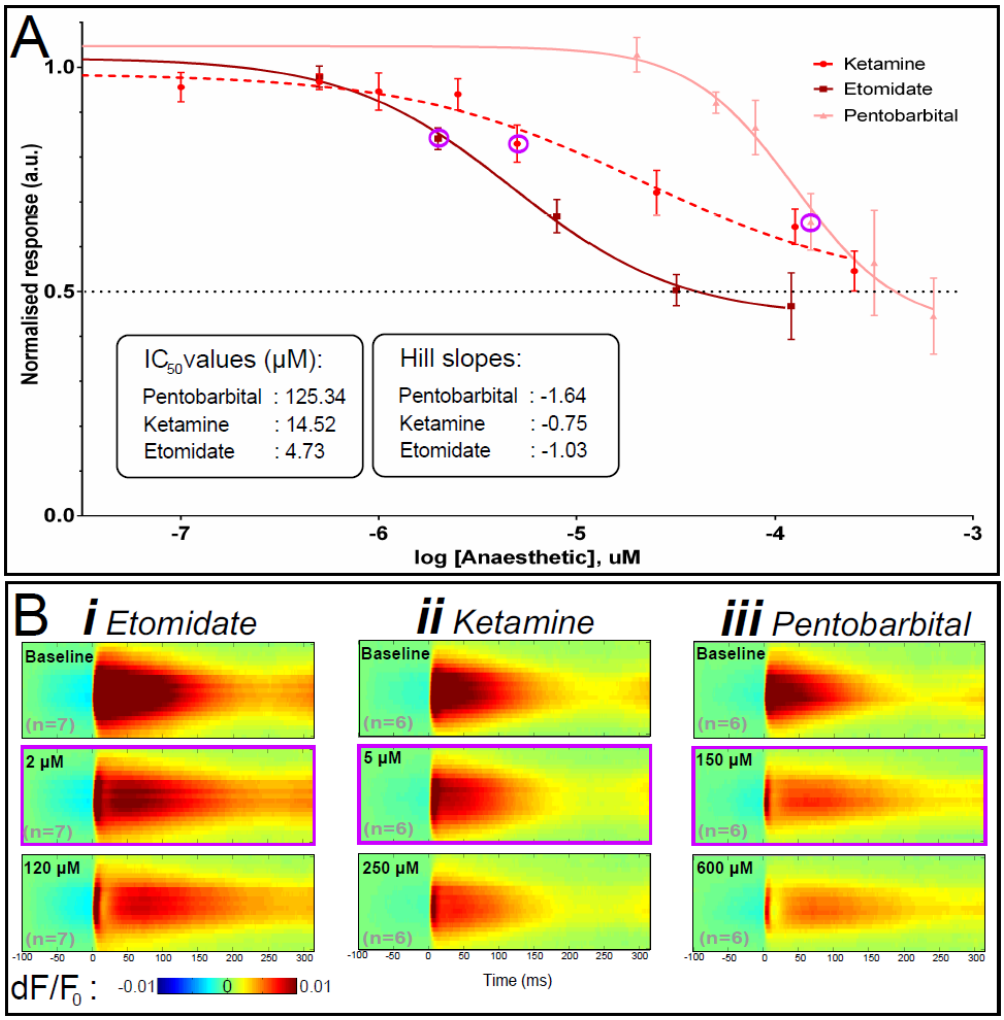

Figure 7: Anaesthetic effect on S1BF network excitability. **A**. Dose-response curves for the effects of increasing concentrations of etomidate, ketamine and pentobarbital, inset: IC_{50} values for each anaesthetic as calculated from the dose-response curves. Purple circles indicate which of the anaesthetic concentrations were found to be closest to calculated IC_{50} values: etomidate – 2 μM perfusion; ketamine – 5 μM perfusion; pentobarbital – 150 μM perfusion. These 'near-IC_{50}' drug doses are displayed in purple boxes in panel **B** space-time maps (middle row). **B**. space-time maps of activity showing baseline activity (top row), that which is evoked near each anaesthetic's IC_{50} values (middle row) as well as max inhibition (bottom row) for **i**. Etomidate, **ii**. Ketamine and **iii**. Pentobarbital.

Statistical test results of assembly magnitudes over time: ANOVA table						
Comparison ID	**AIC**	**Sum of squares**	**Degrees of freedom**	**Mean of squares**	***F*-statistics**	***p*-values**
4.3.2.a.i-iii	**Interaction**	0.4439	10	0.04439	F (10, 90) = 5.990	***p* < 0.001**
	Drug concentration	2.624	5	0.5249	F (5, 90) = 70.82	***p* < 0.001**
	Anaesthetic agent	0.7395	2	0.3697	F (2, 90) = 49.89	***p* < 0.001**
	Residual	0.667	90	0.007411		
	S1BF					
4.3.2.a.iv-vi	**Interaction**	0.627	10	0.0627	F (10, 90) = 4.858	***p* < 0.001**
	Drug concentration	2.165	5	0.433	F (5, 90) = 33.55	***p* < 0.001**
	Anaesthetic agent	0.6964	2	0.3482	F (2, 90) = 26.98	***p* < 0.001**
	Residual	1.161	90	0.01291		
	TC					
4.3.2.b.i-iii	**Interaction**	1.161	10	0.1161	F (10, 95) = 6.815	***p* < 0.001**
	Drug concentration	5.633	5	1.127	F (5, 95) = 66.14	***p* < 0.001**
	Anaesthetic agent	1.989	2	0.9945	F (2, 95) = 58.39	***p* < 0.001**
	Residual	1.618	95	0.01703		

Table 4: Two-way ANOVA result tables testing for significant effects induced either as a result of drug concentration (factor 1) or agent (factor 2) on the magnitude of evoked responses (assemblies) in AIC (comparison ID: **4.3.2.a.i-iii**), S1BF (comparison ID: **4.3.2.a.iv-vi**) and thalamocortical slices (comparison ID: **4.3.2.b.i-iii**). Highly significant effects were detected for all parameters tested, including a highly significant level of interaction, making the interpretation of this data ambiguous; see **Table 5 & 6** for details of post-hoc tests.

Statistical test results of assembly magnitudes with respect to anaesthetic treatment: post-hoc tests					
Comparison ID	**Dunnett's multiple comparisons test**	**Mean Diff.**	**95% CI of diff.**	***p* value**	**Summary**
Anaesthetic effect in AIC					
4.3.2.a.i	**Ketamine**				
	Baseline vs. Drug conc 1	0.0163	-0.1109 to 0.1435	$p = 0.9972$	**n.s.**
	Baseline vs. Drug conc 2	0.03246	-0.09471 to 0.1596	$p = 0.9482$	**n.s.**
	Baseline vs. Drug conc 3	0.02755	-0.09962 to 0.1547	$p = 0.9734$	**n.s.**
	Baseline vs. Drug conc 4	0.1563	0.02908 to 0.2834	$p = 0.0101$	*
	Baseline vs. Drug conc 5	0.2046	0.07743 to 0.3318	$p = 0.0004$	***
4.3.2.a.ii	**Etomidate**				
	Baseline vs. Drug conc 1	0.05587	-0.07130 to 0.1830	$p = 0.6887$	**n.s.**
	Baseline vs. Drug conc 2	0.1748	0.04760 to 0.3019	$p = 0.0032$	**
	Baseline vs. Drug conc 3	0.3279	0.2007 to 0.4550	$p < 0.0001$	***
	Baseline vs. Drug conc 4	0.5036	0.3764 to 0.6307	$p < 0.0001$	***
	Baseline vs. Drug conc 5	0.56	0.4328 to 0.6872	$p < 0.0001$	***
4.3.2.a.iii	**Pentobarbital**				
	Baseline vs. Drug conc 1	0.0696	-0.05757 to 0.1968	$p = 0.4919$	**n.s.**
	Baseline vs. Drug conc 2	0.09998	-0.02719 to 0.2271	$p = 0.1724$	**n.s.**
	Baseline vs. Drug conc 3	0.2022	0.07505 to 0.3294	$p = 0.0005$	***
	Baseline vs. Drug conc 4	0.3572	0.2300 to 0.4843	$p < 0.0001$	***
	Baseline vs. Drug conc 5	0.5378	0.4106 to 0.6649	$p < 0.0001$	***
Anaesthetic effect in S1BF					
4.3.2.a.iv	**Ketamine**				
	Baseline vs. Drug conc 1	0.04433	-0.1235 to 0.2121	$p = 0.9408$	**n.s.**
	Baseline vs. Drug conc 2	0.03245	-0.1354 to 0.2003	$p = 0.9836$	**n.s.**
	Baseline vs. Drug conc 3	0.05397	-0.1138 to 0.2218	$p = 0.8786$	**n.s.**
	Baseline vs. Drug conc 4	0.06	-0.1078 to 0.2278	$p = 0.8277$	**n.s.**
	Baseline vs. Drug conc 5	0.17	0.002188 to 0.3378	$p = 0.0460$	*
4.3.2.a.v	**Etomidate**				
	Baseline vs. Drug conc 1	0.02093	-0.1469 to 0.1887	$p = 0.9977$	**n.s.**
	Baseline vs. Drug conc 2	0.159	-0.008851 to 0.3268	$p = 0.0695$	**n.s.**
	Baseline vs. Drug conc 3	0.3318	0.1640 to 0.4996	$p < 0.0001$	***
	Baseline vs. Drug conc 4	0.4969	0.3291 to 0.6648	$p < 0.0001$	***
	Baseline vs. Drug conc 5	0.5322	0.3643 to 0.7000	$p < 0.0001$	***
4.3.2.a.vi	**Pentobarbital**				
	Baseline vs. Drug conc 1	-0.02817	-0.1960 to 0.1396	$p = 0.9915$	**n.s.**
	Baseline vs. Drug conc 2	0.07896	-0.08885 to 0.2468	$p = 0.6313$	**n.s.**
	Baseline vs. Drug conc 3	0.1339	-0.03390 to 0.3017	$p = 0.1621$	**n.s.**
	Baseline vs. Drug conc 4	0.3443	0.1765 to 0.5122	$p < 0.0001$	***
	Baseline vs. Drug conc 5	0.4358	0.2680 to 0.6036	$p < 0.0001$	***

Table 5: Post-hoc test results obtained using Dunnett's multiple comparisons test of anaesthetic experiments in AIC and S1BF (**Table 4**). For each preparation, the mean summed fluorescence recorded during the first recording condition (baseline) was compared to each of the following recording epochs (2-5) over 2 hours-long recording windows. Highly significant differences were found in the magnitude of evoked assemblies in response to all anaesthetic treatments.

The two-way ANOVA results indicate that increasing concentration of anaesthetic induced significantly lower emitted fluorescence from evoked assemblies, another finding is that the profile of inhibition induced by each agent was different (**Table 5**); however, since interactions were also found to be significant (**Table 4**), it remains difficult to clearly interpret these test results (Rosnow and Rosenthal,

1991). Therefore, in order to more accurately test for disparity between dose-response curves, the curve fits were compared using the extra sum-of-squares *F*-test: in both cases (AIC and S1BF), this test yielded clear results that the null hypothesis, i.e. the parameters of curve fit are the same for all three anaesthetic dose-response profiles, could be rejected (**AIC**: $F(6, 118) = 23.02$, $p < 0.001$; **S1BF**: $F(4, 121) = 31.07$, $p < 0.001$). Yet, despite clear differences between anaesthetic agents *within* either preparation, the profiles of anaesthetic inhibition *between* AIC and S1BF appear very similar, indicating comparable inhibitory effects induced by each agent in both slice preparations; this can be seen in their apparent effects on spatio-temporal profiles of assembly dynamics (**Figure 6B** and **7B**). Indeed, Hill slopes of dose-response curves were also very similar in AIC and S1BF for each anaesthetic. These observations indicate ketamine, etomidate and pentobarbital induce their respective effects on local networks in a uniform manner within cortex, even when the two areas of cortex show conspicuous differences in layer organisation.

b. Anaesthetic effects on locally- and remotely-generated cortical activity

Having established that anaesthetics induce uniform inhibitory effects in isolated cortical preparations, i.e. direct stimulations to AIC and S1BF, the focus of investigations is now shifted towards the possibility of differential anaesthetic effects induced in extra-cortical locations and processes involved in thalamocortical processing, compared to intra-cortical only (i.e. S1BF). In an attempt to shed more light on such a question, direct stimulations in S1BF LIV were compared to data acquired using thalamocortical stimulation. **Figure 8** shows the more prominent impact of increasing anaesthetic doses on thalamocortical processing, featuring highly significant changes in overall emitted fluorescence (see **Table 6**, two-way ANOVA, factor 1: drug concentration, factor 2: anaesthetic agent).

Indeed, this enhanced effect is detectable from the lowering of each anaesthetic's calculated IC_{50} concentrations compared to those calculated in S1BF; such a left-ward curve shift is indicative of an increase in potency. The calculated IC_{50} concentrations for pentobarbital and etomidate in thalamocortical slices are approximately 30% and 50% lower compared to S1BF slices, i.e. 85.8 µM and 2.42 µM respectively. For ketamine however, the IC_{50} calculated in thalamocortical slices is only ≈15% lower than that of S1BF, i.e. 12.18 µM, and is in fact higher than that of AIC. The dose-response profiles remained largely unchanged in thalamocortical slices, albeit more potent, showing great disparity between the curve fits of etomidate, ketamine and pentobarbital data (extra sum-of-squares *F*-test, $F(6, 126) = 21.04$, $p < 0.001$).

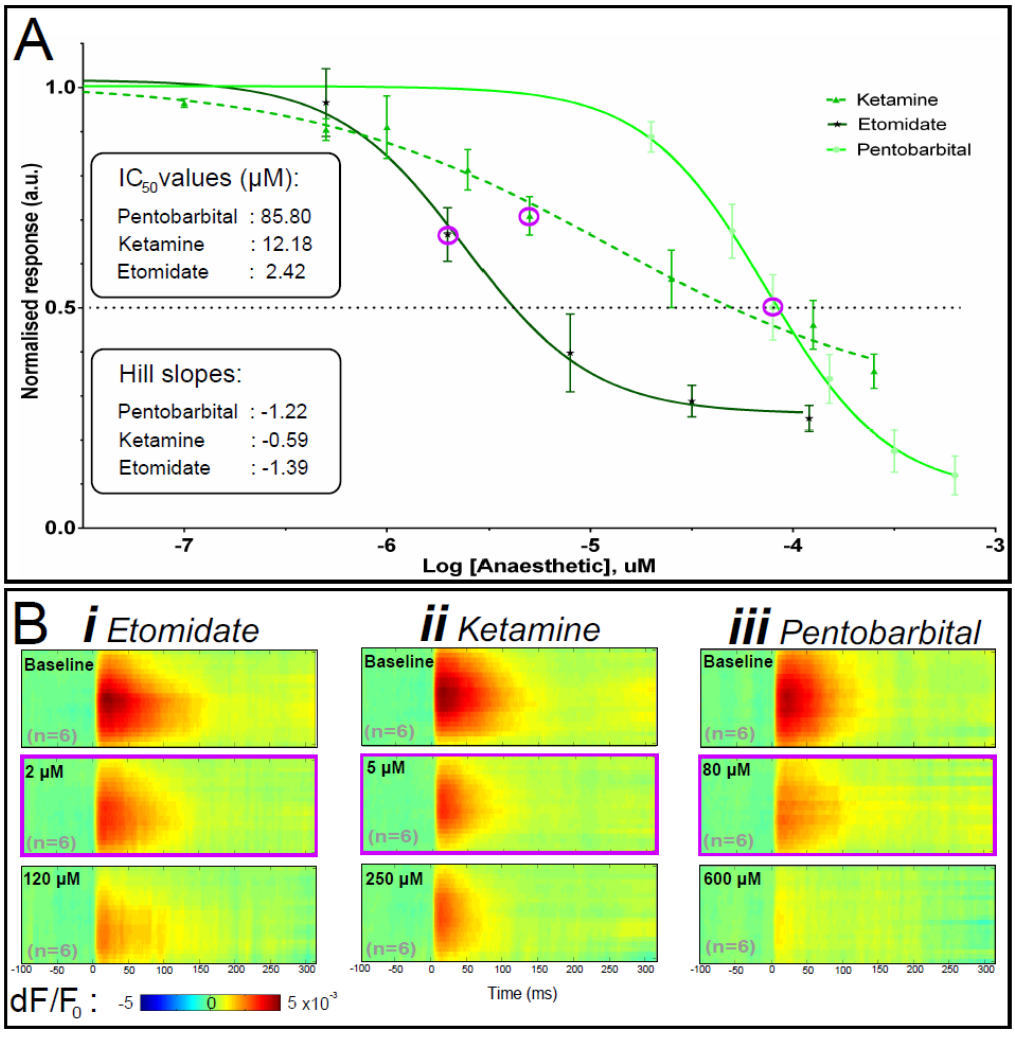

Figure 8: Anaesthetic effect on remotely-activated network excitation (TC). **A**. Dose-response curves for the effects of increasing concentrations of etomidate, ketamine and pentobarbital, inset: IC_{50} values for each anaesthetic as calculated from the dose-response curves. Purple circles indicate which of the anaesthetic concentrations were found to be closest to their calculated IC_{50} values: etomidate – 2 μM perfusion; ketamine – 5 μM perfusion; pentobarbital – 80 μM perfusion. These 'near-IC_{50}' drug doses are displayed in purple boxes in panel **B** space-time maps (middle row). **B**. space-time maps of activity showing baseline activity, that which is evoked near each anaesthetic's IC_{50} values as well as max inhibition for **i**. Etomidate, **ii**. Ketamine and **iii**. Pentobarbital.

Statistical test results of assembly magnitudes with respect to anaesthetic treatment: post-hoc tests					
Comparison ID	**Dunnett's multiple comparisons test**	**Mean Diff.**	**95% CI of diff.**	***p* value**	**Summary**
Anaesthetic effect in TC					
4.3.2.b.i	**Ketamine**				
	Baseline vs. Drug conc 1	0.03522	-0.1574 to 0.2278	$p > 0.9999$	**n.s.**
	Baseline vs. Drug conc 2	0.09525	-0.09735 to 0.2878	$p > 0.9999$	**n.s.**
	Baseline vs. Drug conc 3	0.08977	-0.1028 to 0.2824	$p > 0.9999$	**n.s.**
	Baseline vs. Drug conc 4	0.1865	-0.006053 to 0.3791	$p = 0.0753$	**n.s.**
	Baseline vs. Drug conc 5	0.2913	0.1057 to 0.4769	$p = 0.0006$	***
4.3.2.b.ii	**Etomidate**				
	Baseline vs. Drug conc 1	0.03407	-0.1515 to 0.2197	$p > 0.9999$	**n.s.**
	Baseline vs. Drug conc 2	0.3336	0.1410 to 0.5262	$p = 0.0001$	***
	Baseline vs. Drug conc 3	0.602	0.4164 to 0.7876	$p < 0.0001$	***
	Baseline vs. Drug conc 4	0.7118	0.5098 to 0.9138	$p < 0.0001$	***
	Baseline vs. Drug conc 5	0.7509	0.5653 to 0.9365	$p < 0.0001$	***
4.3.2.b.iii	**Pentobarbital**				
	Baseline vs. Drug conc 1	0.1116	-0.08098 to 0.3042	$p = 0.7091$	**n.s.**
	Baseline vs. Drug conc 2	0.3258	0.1402 to 0.5114	$p = 0.0001$	***
	Baseline vs. Drug conc 3	0.4989	0.3063 to 0.6915	$p < 0.0001$	***
	Baseline vs. Drug conc 4	0.5909	0.4053 to 0.7765	$p < 0.0001$	***
	Baseline vs. Drug conc 5	0.8246	0.6320 to 1.017	$p < 0.0001$	***

Table 6: Post-hoc test results obtained using Dunnett's multiple comparisons test of anaesthetic experiments in thalamocortical slices (**Table 4**). Just as for the comparison of AIC and S1BF in **Section 4.3.2.a**, the mean summed fluorescence recorded during the baseline condition was compared to each of the following recording epochs (2-5) over 2 hours-long recording windows. Highly significant differences were found in the magnitude of evoked assemblies in response to all anaesthetic treatments.

c. Region-specific potency of individual anaesthetic agents

Having investigated drug effects within each particular preparation, greater attention is now given to investigating the effects of anaesthetic agents across slice preparations. In order to highlight the differences in effects of anaesthetics within cortex compared to thalamocortical preparations, the dose-response curves shown above for each slice preparation were compiled this time with respect to anaesthetic agent (**Figure 9A**). It is clear that, for all agents, the influence of drug on thalamocortical activity is more profound than for other regions. This difference is greatest for etomidate but also quite marked for pentobarbital. Extra sum-of-squares *F*-tests were run twice for each anaesthetic agent: the first test included only the cortical direct stimulation preparations (AIC & S1BF), while in the second test, thalamocortical data were included before calculating for significant differences between dose-response curves (see **Figure 9B** for extra sum-of-squares test results). The effect was the same for all anaesthetic agents: when only cortical preparations with direct stimulations were taken into account (AIC & S1BF), the null hypothesis (that all considered curves are the same) was never rejected, indicating very similar dose-response profiles. However, when thalamocortical dose-response curves were included in the comparisons, the test yielded highly significant results ($p < 0.001$). These findings implicate the actions of extra-cortical mechanisms in the process of induction of anaesthesia, as seen here with the more potent effects of anaesthetics in thalamocortical preparations, and is supported by the finding that in the current experiments, anaesthetics induced a uniform profile of inhibition in local cortical assemblies (AIC and S1BF). Finally, the Hill slopes remained similar across preparations except for etomidate, which produced a steeper Hill slope in thalamocortical slices. In summary, this set of experiments shows both, that drugs differ in their actions within any one brain region, and also that for any given drug,

its action differs across preparations (with thalamocortical being the most sensitive to all agents). Given that the agents we studied act predominantly on different receptor populations, these results are consistent with the notion that different receptor subpopulations exist in each of the three brain regions studied.

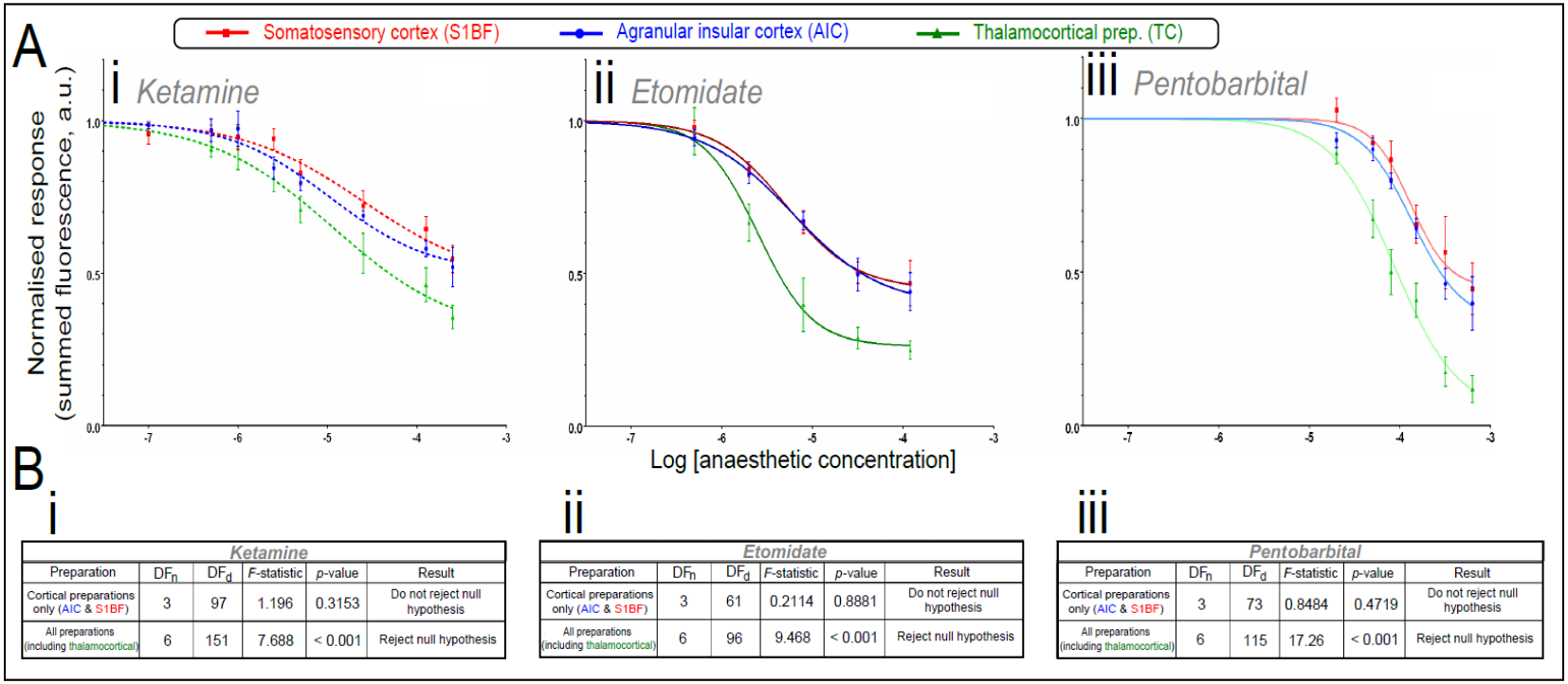

B

i

Ketamine					
Preparation	DF_n	DF_d	*F*-statistic	*p*-value	Result
Cortical preparations only (AIC & S1BF)	3	97	1.196	0.3153	Do not reject null hypothesis
All preparations (including thalamocortical)	6	151	7.688	< 0.001	Reject null hypothesis

ii

Etomidate					
Preparation	DF_n	DF_d	*F*-statistic	*p*-value	Result
Cortical preparations only (AIC & S1BF)	3	61	0.2114	0.8881	Do not reject null hypothesis
All preparations (including thalamocortical)	6	96	9.468	< 0.001	Reject null hypothesis

iii

Pentobarbital					
Preparation	DF_n	DF_d	*F*-statistic	*p*-value	Result
Cortical preparations only (AIC & S1BF)	3	73	0.8484	0.4719	Do not reject null hypothesis
All preparations (including thalamocortical)	6	115	17.26	< 0.001	Reject null hypothesis

Figure 9: Anaesthetics inhibit mesoscopic activity by affecting both cortical and extra-cortical mechanisms. **A**. Drug-specific dose-response curves showing inhibitory effect of increasing anaesthetic doses in in AIC (blue curves), S1BF (red curves) and thalamocortical slices (green curves) for **i**. Ketamine, **ii**. Etomidate and **iii**. Pentobarbital. **B**. Tables showing extra sum-of-squares F-test results, assessing the similarity between the parameters of each dose-response curve fit. For each anaesthetic, the extra sum-of-squares test was run twice: the first compared dose-response relationships in preparations where stimulations were delivered directly to cortical tissue only (AIC & S1BF), while the second comparison also included the dose-response relationships recorded in remote, thalamocortical preparations. For each anaesthetic, the null hypothesis (that the parameters of dose-response curves, i.e. the curve fits, are the same) was never rejected when only direct stimulation experiments were considered, however the null hypothesis was always rejected, for all three anaesthetics, when their dose-response profile in thalamocortical preparations were included, suggesting a significant portion of anaesthetic effects take place outside of the cortex

4.3.3 Effects of anaesthetics on assembly parameters

In addition to providing clear readings of the extent of activation within specific ROIs, measured as the intensity of emitted fluorescence, VSDI data can be analysed further to isolate drug-specific effects on different parameters of evoked assembly dynamics. In **Chapter 3**, two additional parameters in particular were considered: the lateral spread and time course of assembly activity; these can be analysed here to help dissociate further between drug-specific inhibitions of evoked assemblies. Using identical methods as those employed in the previous chapter, the average time course and lateral spread of evoked assemblies were calculated for baseline, near-IC_{50} and maximal anaesthetic doses of each anaesthetic in the three preparations considered so far, and displayed in **Figure 10**, below.

a. Anaesthetic effect on lateral spread of assemblies

The lateral spread of activity was decreased by increasing concentrations of ketamine, etomidate and pentobarbital, **Figure 10A**. Ketamine was found to induce the least decreases, with only AIC preparations showing a significant decrease in lateral spread of evoked assemblies (**Table 7**, comp ID: **4.3.3.a.iv**) while the decreases induced in S1BF (**Table 7**, comparison ID: **4.3.3.a.v**) and thalamocortical slices (comparison ID: **4.3.3.a.vi**) were not found to be significant. Etomidate and pentobarbital on the other hand were both found to restrict assembly lateral spread: etomidate induced significant decreases in AIC (comparison ID: **4.3.3.a.i**), with even greater inhibition seen in thalamocortical slices (comparison ID: **4.3.3.a.iii**), yet despite a pronounced inhibitory trend in S1BF slices, no significant differences were found (comparison ID: **4.3.3.a.ii**). Pentobarbital induced significant decreases in spread at maximal dose (600 μM) in all preparations tested (comparison IDs: AIC – **4.3.3.a.vii**, S1BF – **4.3.3.a.viii**, TC – **4.3.3.a.ix**), yet only induced a significant

decrease at near-IC_{50} dose in thalamocortical slices, contrasting with etomidate's significant near-IC_{50} decreases in AIC and thalamocortical slices.

In summary, anaesthetics were found in all cases to decrease the spatial reach of assemblies, with etomidate inducing the most obvious decreases while ketamine caused the least changes. Furthermore, when considering specific preparations, the greatest decreases were induced in AIC and thalamocortical slices, with S1BF slices being the least sensitive to anaesthetic effect on lateral spread. Although some differences were indeed found, the inhibition profiles exhibited by each anaesthetic were not disparate enough to offer a clear discriminative parameter, especially since all anaesthetics induced changes of the same nature (slow, dose-dependent decreases). Therefore, probing of the impact of anaesthetic on the lateral spread of assemblies did not offer the possibility of clearly distinguishing between anaesthetic agents using this measure alone.

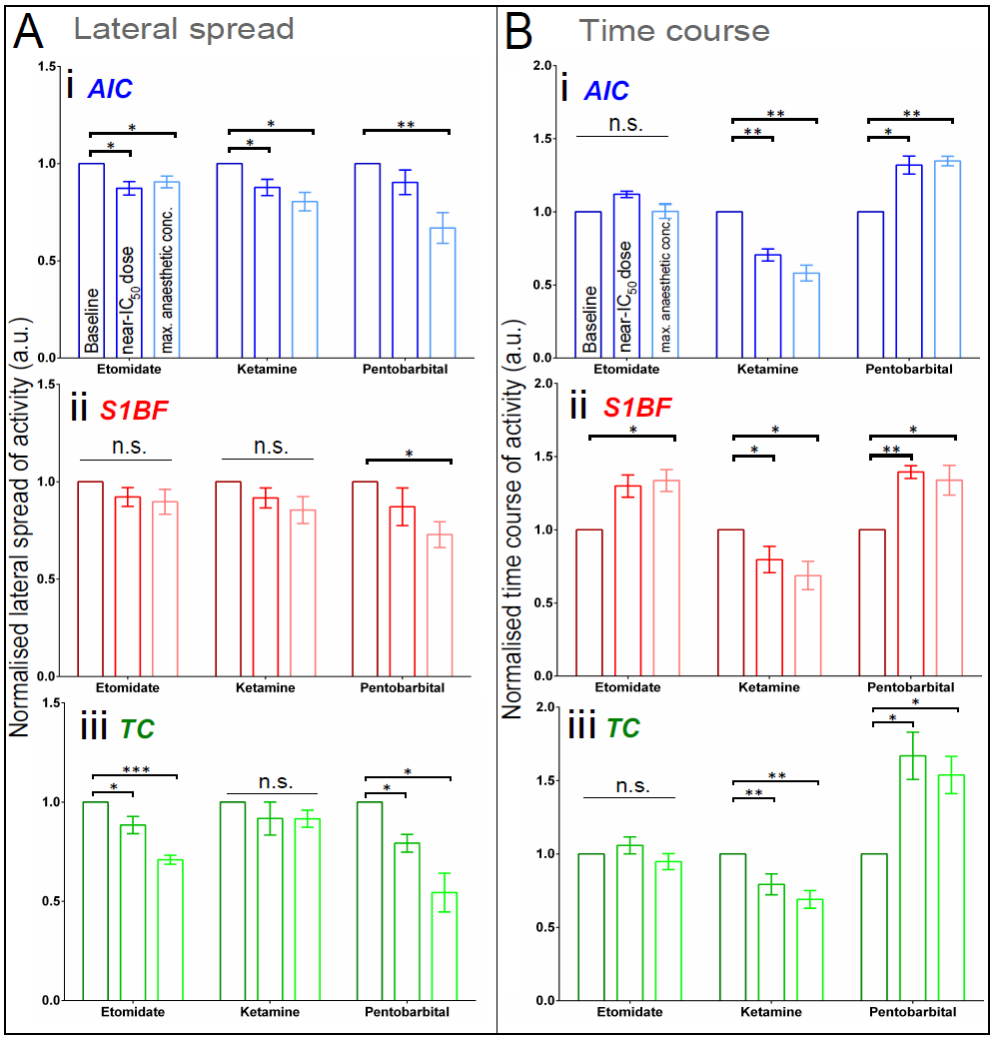

Figure 10: Anaesthetics differentially affect assembly lateral spread and time course of activity. **A**. Effect of increasing anaesthetic concentrations on the lateral spread of evoked assemblies in **i**. AIC-containing slices (blue), **ii**. S1BF-containing slices (red), and **iii**. Thalamocortical slices (green). In each case, only the baseline, near-IC_{50} and maximal doses were taken in account. All anaesthetics induced a decrease in the evoked spread of assemblies. **B**. Effect of increasing anaesthetic concentrations on the time course of evoked activity. Contrasting with the effects induced on lateral spread, anaesthetics induced differential effects on the ability of neuronal networks to terminate activity: etomidate caused only minor changes, ketamine induced a decrease, while pentobarbital induced an increase in time course of activity. See **Table 7** for details of statistical tests and results.

b. Anaesthetic effect on time course of assembly activity

Additionally to the impact of anaesthetics on lateral spread of evoked assemblies, their effect on the time course of activity was also measured in response to their near-IC_{50} and maximal anaesthetic dose perfusions; the results are shown in **Figure 10B**. Contrasting with the effects induced on lateral spread, etomidate was found to have the least impact on the duration of evoked assemblies, with no significant differences found in AIC and thalamocortical slices (**Table 7**, comparison ID: AIC – **4.3.3.b.i**, TC – **4.3.3.b.iii**); etomidate perfusion in S1BF slices however, showed significant lengthening of the time course of activity following perfusion of maximal etomidate dose only (120 μM**,** comparison ID: **4.3.3.b.ii**). Ketamine induced significant dose-dependent decreases in the time course of activity in all tested preparations (comparison ID: AIC – **4.3.3.b.iv**, S1BF – **4.3.3.b.v**, TC – **4.3.3.b.vi**), while pentobarbital induced significant increases in the time course of activity in all tested preparations (comparison ID: AIC – **4.3.3.b.vii**, S1BF – **4.3.3.b.viii**, TC – **4.3.3.b.ix**).

Here, each anaesthetic induced qualitatively different effects: ketamine induced decreases in time course of activity in all preparations, pentobarbital on the other hand induced the opposite effect (increases in time course), while etomidate did not often alter this parameter significantly. These results show that impact of anaesthetics on time course of evoked activity can be used to differentiate between anaesthetic drugs, in addition to suggesting each anaesthetic agent induce inhibitory effects via distinct mesoscopic actions, even when their micro-scale targets are reportedly similar (as is the case between pentobarbital and etomidate).

Statistical test results of anaesthetic effect on intrinsic assembly parameters (lateral spread and time course)							
Comparison ID	**Data set comparison**	**Test parameter(s)**	**Statistical test**	***p* value**	***F*- or *t*-statistics**	**Post-hoc test**	**Significance**
4.3.3.a.i	AIC: Baseline vs near-IC_{50} dose (etomidate)	Lateral spread	Repeated measures, one-way ANOVA	$p = 0.0067$	$F(1.682, 8.409) = 10.29$	$p = 0.0242$	*
	AIC: Baseline vs maximal dose (etomidate)	Lateral spread				$p = 0.0370$	*
4.3.3.a.ii	S1BF: Baseline vs near-IC_{50} dose (etomidate)	Lateral spread	Repeated measures, one-way ANOVA	$p = 0.3238$	$F(1.396, 8.376) = 1.214$	$p = 0.2797$	n.s.
	S1BF: Baseline vs maximal dose (etomidate)	Lateral spread				$p = 0.2572$	n.s.
4.3.3.a.iii	TC: Baseline vs near-IC_{50} dose (etomidate)	Lateral spread	Repeated measures, one-way ANOVA	$p < 0.0001$	$F(1.360, 6.802) = 72.24$	$p = 0.0295$	*
	TC: Baseline vs maximal dose (etomidate)	Lateral spread				$p < 0.001$	***
4.3.3.a.iv	AIC: Baseline vs near-IC_{50} dose (ketamine)	Lateral spread	Repeated measures, one-way ANOVA	$p = 0.0037$	$F(1.519, 7.595) = 14.22$	$p = 0.0159$	*
	AIC: Baseline vs maximal dose (ketamine)	Lateral spread				$p = 0.0150$	*
4.3.3.a.v	S1BF: Baseline vs near-IC_{50} dose (ketamine)	Lateral spread	Repeated measures, one-way ANOVA	$p = 0.1494$	$F(1.285, 6.425) = 2.663$	$p = 0.1494$	n.s.
	S1BF: Baseline vs maximal dose (ketamine)	Lateral spread				$p = 0.1446$	n.s.
4.3.3.a.vi	TC: Baseline vs near-IC_{50} dose (ketamine)	Lateral spread	Repeated measures, one-way ANOVA	$p = 0.3572$	$F(1.199, 5.997) = 1.072$	$p = 0.5289$	n.s.
	TC: Baseline vs maximal dose (ketamine)	Lateral spread				$p = 0.4810$	n.s.
4.3.3.a.vii	AIC: Baseline vs near-IC_{50} dose (pentobarbital)	Lateral spread	Repeated measures, one-way ANOVA	$p = 0.0004$	$F(1.633, 9.799) = 20.77$	$p = 0.1503$	n.s.
	AIC: Baseline vs maximal dose (pentobarbital)	Lateral spread				$p = 0.0028$	**
4.3.3.a.viii	S1BF: Baseline vs near-IC_{50} dose (pentobarbital)	Lateral spread	Repeated measures, one-way ANOVA	$p = 0.0424$	$F(1.785, 8.926) = 4.742$	$p = 0.3456$	n.s.
	S1BF: Baseline vs maximal dose (pentobarbital)	Lateral spread				$p = 0.0240$	*
4.3.3.a.ix	TC: Baseline vs near-IC_{50} dose (pentobarbital)	Lateral spread	Repeated measures, one-way ANOVA	$p = 0.0005$	$F(1.462, 7.311) = 28.72$	$p = 0.0222$	*
	TC: Baseline vs maximal dose (pentobarbital)	Lateral spread				$p = 0.0028$	***
4.3.3.b.i	AIC: Baseline vs near-IC_{50} dose (etomidate)	Time course of activity	Repeated measures, one-way ANOVA	$p = 0.1892$	$F(1.330, 6.650) = 2.167$	$p = 0.1048$	n.s.
	AIC: Baseline vs maximal dose (etomidate)	Time course of activity				$p = 0.9958$	n.s.
4.3.3.b.ii	S1BF: Baseline vs near-IC_{50} dose (etomidate)	Time course of activity	Repeated measures, one-way ANOVA	$p = 0.0563$	$F(1.630, 9.781) = 4.124$	$p = 0.0844$	n.s.
	S1BF: Baseline vs maximal dose (etomidate)	Time course of activity				$p = 0.0298$	*
4.3.3.b.iii	TC: Baseline vs near-IC_{50} dose (etomidate)	Time course of activity	Repeated measures, one-way ANOVA	$p = 0.1307$	$F(1.170, 5.851) = 3.063$	$p = 0.2764$	n.s.
	TC: Baseline vs maximal dose (etomidate)	Time course of activity				$p = 0.2559$	n.s.
4.3.3.b.iv	AIC: Baseline vs near-IC_{50} dose (ketamine)	Time course of activity	Repeated measures, one-way ANOVA	$p = 0.0004$	$F(1.543, 7.716) = 29.28$	$p = 0.0072$	**
	AIC: Baseline vs maximal dose (ketamine)	Time course of activity				$p = 0.0028$	**
4.3.3.b.v	S1BF: Baseline vs near-IC_{50} dose (ketamine)	Time course of activity	Repeated measures, one-way ANOVA	$p = 0.0104$	$F(1.462, 7.308) = 10.16$	$p = 0.0344$	*
	S1BF: Baseline vs maximal dose (ketamine)	Time course of activity				$p = 0.0310$	*
4.3.3.b.vi	TC: Baseline vs near-IC_{50} dose (ketamine)	Time course of activity	Repeated measures, one-way ANOVA	$p = 0.0104$	$F(1.820, 9.102) = 8.136$	$p = 0.0128$	*
	TC: Baseline vs maximal dose (ketamine)	Time course of activity				$p = 0.0428$	*
4.3.3.b.vii	AIC: Baseline vs near-IC_{50} dose (pentobarbital)	Time course of activity	Repeated measures, one-way ANOVA	$p = 0.0187$	$F(1.278, 7.669) = 8.094$	$p = 0.0125$	*
	AIC: Baseline vs maximal dose (pentobarbital)	Time course of activity				$p = 0.0055$	**
4.3.3.b.viii	S1BF: Baseline vs near-IC_{50} dose (pentobarbital)	Time course of activity	Repeated measures, one-way ANOVA	$p = 0.0175$	$F(1.152, 5.578) = 10.40$	$p = 0.0038$	**
	S1BF: Baseline vs maximal dose (pentobarbital)	Time course of activity				$p = 0.0107$	*
4.3.3.b.ix	TC: Baseline vs near-IC_{50} dose (pentobarbital)	Time course of activity	Repeated measures, one-way ANOVA	$p = 0.0119$	$F(1.108, 5.541) = 13.07$	$p = 0.0261$	*
	TC: Baseline vs maximal dose (pentobarbital)	Time course of activity				$p = 0.0140$	*

Table 7: Table of statistical test results for significant effects induced on lateral spread and time course of evoked assemblies. For all ANOVAs performed, Dunnett's multiple comparisons test were performed as post-hoc analysis.

4.3.4 Effect of anaesthetics on LFP and comparison with VSDI

Simultaneously to optical imaging experiments, LFP data were recorded in most experiments, as shown in **Figure 11A**. For clarity purposes, only the results from selected experiments using each anaesthetic are shown, i.e. experiments that included the perfusion of the maximal dose. In those experiments, ketamine was perfused at 5, 125 and 250 μM, etomidate was perfused at 0.5, 8 and 120 μM and pentobarbital at 50, 150 and 600 μM. In all cases, successive perfusions of sharply increasing concentrations, from clinical to supra-clinical ranges, induced significant

dose-dependent inhibitions of evoked activity (**Table 8**, comparison IDs: **4.3.4)**; with the exception of pentobarbital, which produced noticeable yet non-significant (**Table 8**, comparison ID: **4.3.4.iii**,**vi**) increases in LFP deflection magnitude at low doses in local cortical (AIC & S1BF), but not thalamocortical preparations. Ketamine produced the least modulation of LFP amplitude, where even at 250 μM responses were never inhibited by more than 43.0 ± 4.29% from baseline in thalamocortical slices. By comparison, pentobarbital produced the most conspicuous effects showing up to 79 ± 8.20% inhibition from baseline at maximal dose in thalamocortical slices. Etomidate induced an intermediary-level inhibition, with a maximum of 66.41 ± 8.89% decrease in evoked activity in thalamocortical slices. Interestingly, as seen with VSDI data even at maximal doses, evoked activity was never completely inhibited in LFP records. In addition to this, ketamine featured a similar profile of inhibition across all preparations, whereas pentobarbital and etomidate both induced more pronounced effects in thalamocortical slices. This observation is similar to the difference in profile of inhibition seen with VSDI (**Figure 9**): such a level of agreement between VSDI and LFP data confirms that the effects reported here arise from physiological events with direct implications to the process of anaesthesia.

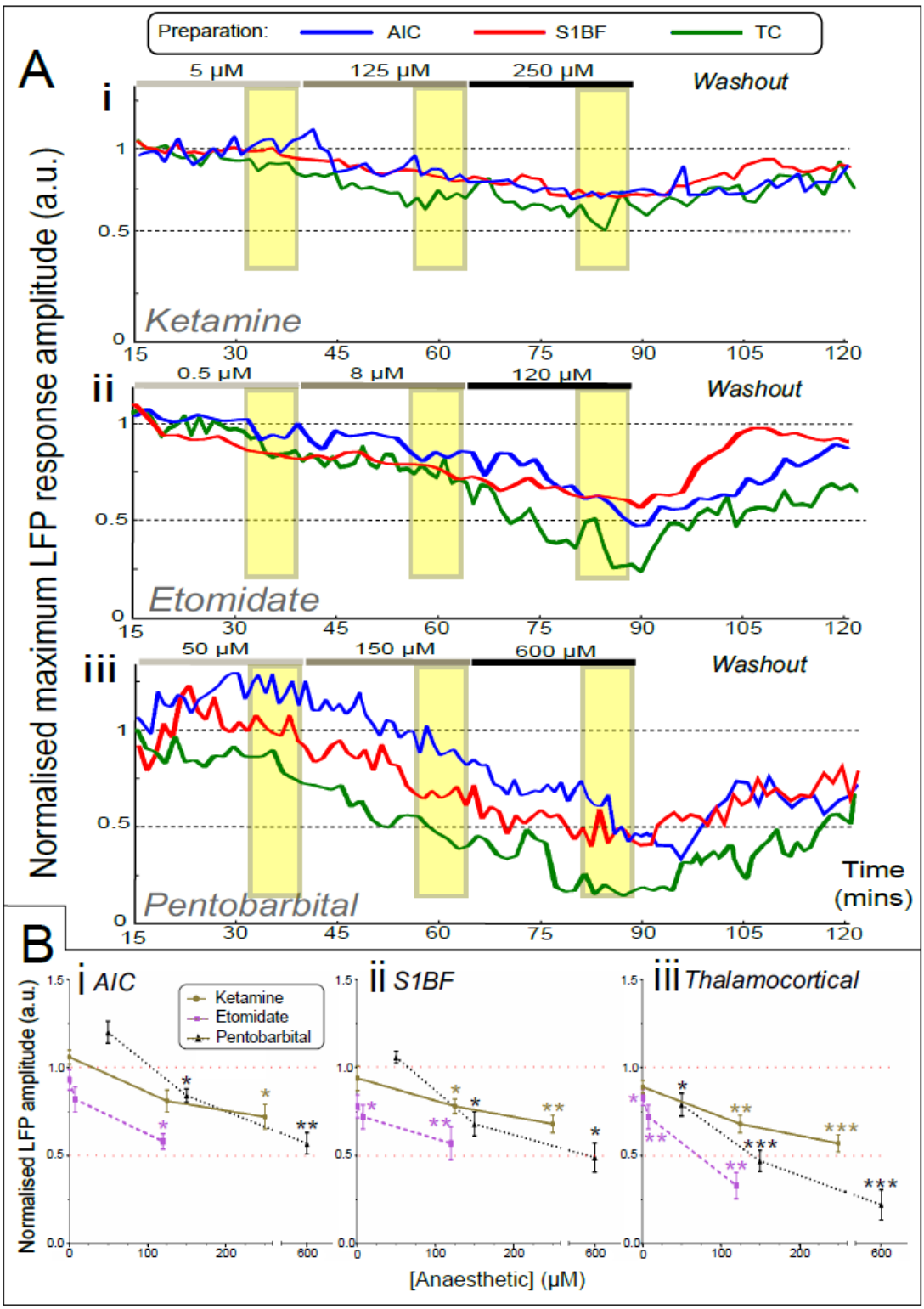

Figure 11: Anaesthetic effects on LFP recordings: here also, a more prominent block of evoked activity is induced by etomidate and pentobarbital. This inhibition is enhanced in thalamocortical slices, except for ketamine, which here too show similar levels of inhibition in all preparations. **AIC** – ketamine: n=5, etomidate: n=4, pentobarbital: n=4; **S1BF** – ketamine: n=4, etomidate: n=4, pentobarbital: n=4; **TC** – ketamine: n=6, etomidate: n=5, pentobarbital: n=6.

Statistical test results of anaesthetic effect measured using LFP slice preparations							
Comparison ID	**Data set comparison**	**Test parameter(s)**	**Statistical test employed**	***p* value**	***F*- or *t*-statistics**	**Post-hoc test (adjusted) *p* value**	**Significance level**
4.3.4.i	AIC: Baseline vs [Drug] 1 (etomidate)	Deflection amplitude	Repeated measures one-way ANOVA	$p = 0.0715$	$F(1.241, 3.722) = 6.110$	$p = 0.6214$	n.s.
	AIC: Baseline vs [Drug] 2 (etomidate)	Deflection amplitude				$p = 0.2734$	n.s.
	AIC: Baseline vs [Drug] 3 (etomidate)	Deflection amplitude				$p = 0.0356$	*
4.3.4.ii	AIC: Baseline vs [Drug] 1 (ketamine)	Deflection amplitude	Repeated measures one-way ANOVA	$p = 0.0130$	$F(1.171, 4.685) = 14.51$	$p = 0.5142$	n.s.
	AIC: Baseline vs [Drug] 2 (ketamine)	Deflection amplitude				$p = 0.0630$	n.s.
	AIC: Baseline vs [Drug] 3 (ketamine)	Deflection amplitude				$p = 0.0065$	**
4.3.4.iii	AIC: Baseline vs [Drug] 1 (pentobarbaital)	Deflection amplitude	Repeated measures one-way ANOVA	$p = 0.0032$	$F(1.204, 3.613) = 46.48$	$p = 0.0927$	n.s.
	AIC: Baseline vs [Drug] 2 (pentobarbaital)	Deflection amplitude				$p = 0.0262$	*
	AIC: Baseline vs [Drug] 3 (pentobarbaital)	Deflection amplitude				$p = 0.0023$	**
4.3.4.iv	S1BF: Baseline vs [Drug] 1 (etomidate)	Deflection amplitude	Repeated measures one-way ANOVA	$p = 0.0037$	$F(1.692, 5.077) = 21.43$	$p = 0.1279$	n.s.
	S1BF: Baseline vs [Drug] 2 (etomidate)	Deflection amplitude				$p = 0.0120$	*
	S1BF: Baseline vs [Drug] 3 (etomidate)	Deflection amplitude				$p = 0.0022$	**
4.3.4.v	S1BF: Baseline vs [Drug] 1 (ketamine)	Deflection amplitude	Repeated measures one-way ANOVA	$p = 0.0077$	$F(1.349, 4.046) = 22.40$	$p = 0.1639$	n.s.
	S1BF: Baseline vs [Drug] 2 (ketamine)	Deflection amplitude				$p = 0.0392$	*
	S1BF: Baseline vs [Drug] 3 (ketamine)	Deflection amplitude				$p = 0.0033$	**
4.3.4.vi	S1BF: Baseline vs [Drug] 1 (pentobarbaital)	Deflection amplitude	Repeated measures one-way ANOVA	$p = 0.0011$	$F(1.386, 4.158) = 59.34$	$p = 0.6739$	n.s.
	S1BF: Baseline vs [Drug] 2 (pentobarbaital)	Deflection amplitude				$p = 0.0300$	*
	S1BF: Baseline vs [Drug] 3 (pentobarbaital)	Deflection amplitude				$p = 0.0122$	*
4.3.4.vii	TC: Baseline vs [Drug] 1 (etomidate)	Deflection amplitude	Repeated measures one-way ANOVA	$p = 0.0023$	$F(1.284, 5.134) = 28.73$	$p = 0.0285$	*
	TC: Baseline vs [Drug] 2 (etomidate)	Deflection amplitude				$p = 0.0072$	**
	TC: Baseline vs [Drug] 3 (etomidate)	Deflection amplitude				$p = 0.0040$	**
4.3.4.viii	TC: Baseline vs [Drug] 1 (ketamine)	Deflection amplitude	Repeated measures one-way ANOVA	$p = 0.0002$	$F(1.543, 7.715) = 36.43$	$p = 0.0653$	n.s.
	TC: Baseline vs [Drug] 2 (ketamine)	Deflection amplitude				$p = 0.0044$	**
	TC: Baseline vs [Drug] 3 (ketamine)	Deflection amplitude				$p < 0.0001$	***
4.3.4.ix	TC: Baseline vs [Drug] 1 (pentobarbaital)	Deflection amplitude	Repeated measures one-way ANOVA	$p = 0.0002$	$F(1.475, 7.376) = 40.70$	$p = 0.0140$	*
	TC: Baseline vs [Drug] 2 (pentobarbaital)	Deflection amplitude				$p = 0.0002$	***
	TC: Baseline vs [Drug] 3 (pentobarbaital)	Deflection amplitude				$p = 0.0003$	***

Table 8: Statistical test result table for LFP data under anaesthetic treatment. For all ANOVAs performed, Dunnett's multiple comparisons test were performed as post-hoc analysis.

4.3.5 Anaesthetic effect in basal forebrain

Having established the effects of anaesthetics in local cortical versus thalamocortical preparations, investigations now focus on the basal forebrain. Here, simple experiments were carried out with perfusions containing near-IC_{50} doses found for each agent in direct stimulation experiments (AIC and S1BF): 2 μM etomidate, 5 μM ketamine and 150 μM pentobarbital. In order to be able to accurately compare them to their cortical equivalent, data were not recorded in basal forebrain until anaesthetics had been perfused for approximately the same amount of time as in cortical experiments, i.e. for ketamine and etomidate, data were recorded in the first epoch, while for pentobarbital experiments, slices were perfused with 50 μM pentobarbital for 25 minutes (no data acquisition), followed by the 150 μM test perfusion (where data were acquired). **Figure 12A** shows the impact of

anaesthetics on the spatio-temporal dynamics of assemblies evoked in basal forebrain: in all cases, anaesthetics induced noticeable decreases in emitted fluorescence of evoked assemblies. **Figure 12B** shows the quantification of the normalised effects of anaesthetics on basal forebrain activity, compared to those obtained in direct stimulation experiments in cortical tissue. Surprisingly, near-IC_{50} doses of anaesthetic were found to induce significant inhibition of evoked assemblies in basal forebrain: 2 μM etomidate caused a 67.15 ± 5.07% decrease in summed fluorescence, 5 μM ketamine produced the least inhibition (32.6 ± 8.09% decrease from baseline), while 150 μM pentobarbital decreased emitted fluorescence the most, 74.0 ± 7.14% compared to baseline level; all of which were found to be significantly different (red stars, **Figure 12B**, see **Table 9**, comparison IDs: **4.3.5i-iii**). Furthermore, not only did anaesthetics induce clear and significant decreases in emitted fluorescence of basal forebrain assemblies, but these decreases were also found to be significantly more extensive than their respective inhibitions, at equal concentrations, in AIC and S1BF experiments (black stars, **Figure 12B**, see **Table 9**, comparison IDs: **4.3.5.iv-vi**). Together, these findings suggest that anaesthetics have a significantly more potent effect on basal forebrain rather than cortical assemblies, and that this effect is even more pronounced for etomidate and pentobarbital compared to those of ketamine.

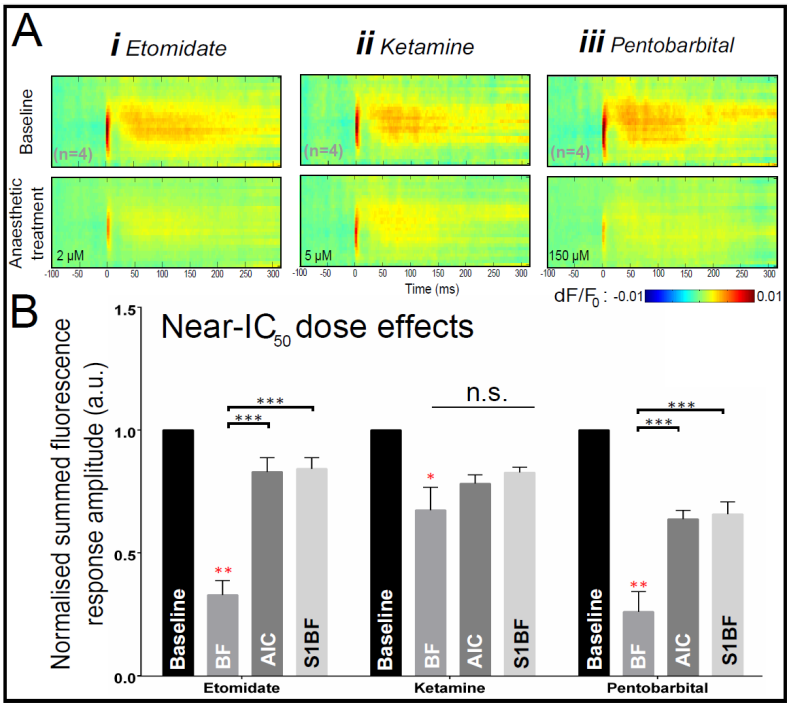

Figure 12: Effect of anaesthetics on basal forebrain activity. **A**. Space-time maps of activity evoked in basal forebrain at baseline (top panels) and at each agent's near-IC_{50} doses in cortical preparations for **i**. Etomidate (2 μM), **ii**. Ketamine (5 μM) and **iii**. Pentobarbital (150 μM). **B**. Quantification and normalisation of summed fluorescence evoked in each preparation showing major decreases: much more extensive than those seen at near-IC_{50} doses in AIC and S1BF.

Statistical test results of anaesthetic potency comparisons between direct stimulation experiments in cortex and basal forebrain							
Comparison ID	**Data set comparison**	**Test parameter(s)**	**Statistical test employed**	***p* value**	***F*- or *t*-statistics**	**Post-hoc test (adjusted) *p* value**	**Significance level**
4.3.5.i	Basal forebrain: baseline vs etomidate	Summed fluorescence	Two-tailed paired t-test	$p = 0.0014$	$t(3) = 11.46$	n/a	**
4.3.5.ii	Basal forebrain: baseline vs ketamine	Summed fluorescence		$p = 0.0398$	$t(3) = 3.488$	n/a	*
4.3.5.iii	Basal forebrain: baseline vs pentobarbital	Summed fluorescence		$p = 0.0029$	$t(3) = 8.974$	n/a	**
4.3.5.iv	Etomidate near-IC50 doses: S1BF vs BF	Summed fluorescence	One-way ANOVA	$p = 0.0001$	$F(2, 13) = 19.12$	$p = 0.0002$	***
	Etomidate near-IC50 doses: S1BF vs AIC	Summed fluorescence				$p = 0.9856$	n.s.
	Etomidate near-IC50 doses: AIC vs BF	Summed fluorescence				$p = 0.0003$	***
4.3.5.v	Ketamine near-IC50 doses: S1BF vs BF	Summed fluorescence	One-way ANOVA	$p = 0.2223$	$F(2, 13) = 0.8676$	$p = 0.4159$	n.s.
	Ketamine near-IC50 doses: S1BF vs AIC	Summed fluorescence				$p = 0.8989$	n.s.
	Ketamine near-IC50 doses: AIC vs BF	Summed fluorescence				$p = 0.6422$	n.s.
4.3.5.vi	Pentobarbital near-IC50 doses: S1BF vs BF	Summed fluorescence	One-way ANOVA	$p < 0.0001$	$F(2, 13) = 22.50$	$p = 0.0001$	***
	Pentobarbital near-IC50 doses: S1BF vs AIC	Summed fluorescence				$p = 0.9713$	n.s.
	Pentobarbital near-IC50 doses: AIC vs BF	Summed fluorescence				$p = 0.0001$	***

Table 9: Statistical test result table for direct stimulation experiments in cortex and basal forebrain data. For all ANOVAs performed, Dunnett's multiple comparisons test were performed as post-hoc analysis.

4.4 Discussion

Not only does this thesis represent the first comprehensive comparison of mesoscopic brain dynamics across several preparations (**Chapter 3**), but also reports a much needed description of anaesthetic action on stimulus-evoked assemblies *in vitro* in real time. In the present chapter, the impact of increasing concentrations of etomidate, pentobarbital and ketamine were probed, and shown to induce dose-dependent effects on mesoscopic neuronal dynamics but in very different and specific ways. In the discussion below, several aspects of the experimental protocol are assessed, in particular the validity of the experimental setup and data acquisition paradigms, followed by a discussion of the results obtained from comparisons of distinct brain slice preparations. In addition to this, the effects seen here at the meso-scale are discussed in light of their previously reported microscopic effects, in an attempt to match known protein targets to mesoscopic impact of anaesthetic perfusions. Furthermore, a discussion of the difficulty which exists in matching results of mesoscopic investigations with clinical measures is undertaken, addressing obstacles such as matching dose with response at multiple levels of brain organisation as well as the advantages of using electrophysiology recordings simultaneously with optical imaging. Finally, the implications of the results presented here to the study of general anaesthesia are discussed.

4.4.1 Validation of experimental protocol

a. Drug perfusion paradigm

In the present experiments, imaging data were acquired for 15 minutes following 10-12 minutes drug perfusion; while for LFP, though data were continuously acquired, only the average deflection amplitudes recorded in the last 5 minutes (10

frames) of each drug epoch (i.e. after 20 minutes of drug perfusion) were acquired for quantification of drug effects, see **Figure 11**. A compromise was therefore found between i) the amount of time necessary for drugs to penetrate the slice, and ii) the shortest possible total-experiment time to guarantee slice health. For the former parameter, where longer perfusion times prior to the start of acquisition of data could be preferred, studies investigating the behaviour of single cells within slice preparations under drug treatment have shown that a 15- to 20-minute perfusion time permitted the induction of full drug effects. These studies in particular focused on drugs targeting membrane channel proteins (L/VGICs), as is the case with anaesthetics, such as when using MK-801 (Homayoun & Moghaddam, 2007), nicotine (Yin and French, 2000). By showing full drug effect in isolated neurons, these studies show 15- to 20-minute perfusion times are adequate for experiment on brain slice preparations.

In the experiments presented here, anaesthetics were allowed to perfuse for only 10-12 minutes, however thanks to a 'soaking' step, a faster transition between concentration steps could be achieved (**Chapter 2**, **Section 2.6.3.d**). With regards to effects of lengthy experiments on slice health, **Figure 4** showed that total-experiment time should be kept to a maximum of 5 recording epochs, after which slice health showed too much variability to allow for the isolation of any meaningful effects. It was therefore important to keep the maximum experiment length to within 2 hours, i.e. 5 recording epochs; this prompted the need for multiple experiments, each testing different anaesthetic concentration ranges, to be carried out per anaesthetic in each preparation except basal forebrain.

b. Combination of multiple anaesthetic concentration ranges

As it is already explained in the introduction (**Section 4.1**), it has been shown in previous research that anaesthetics induce differential effects over incrementally increasing time-scales. The most obvious examples of such time-dependent anaesthetic effects have been reported for ketamine, where within just a few minutes of intravenous inoculation of a hypnotic dose, patients enter a cataleptic physical and dissociated mental state, yet after a few hours many patients can experience a secondary, latent-acting, anti-depressant effect of the drug (Machado-Vieira et al., 2009). Since it could be possible for latent cellular anaesthetic effects to occur in the present experimental preparation, a separate set of experiments were carried out with near-IC_{50} concentrations of each anaesthetic, perfused for 10 and 60 minutes following the start of drug perfusions in AIC, S1BF and thalamocortical preparations: comparison of 'short-' and 'long-perfusion' experiments did show minor levels of variation in proportional decreases of summed fluorescence, yet no significant differences were found between short- and long-perfusion experiments (data not shown). These findings provided credence that the perfusion times prior to acquisition of data were sufficient to record repeatable measures of drug effect, where time was not a factor (**Figure 4**). This was further corroborated with LFP trend graphs, providing a rough reading of the excitability of the tissue in a continuous manner throughout experiments, highlighting the dose-dependent nature of induced anaesthetic effects. Additionally, the fact a plateau was reached when probed using VSDI justified the use of multiple and often overlapping anaesthetic concentration ranges, for compilation of dose-response relationships; such analyses could not have been undertaken otherwise.

4.4.2 Differential effects of anaesthetics in cortical and sub-cortical areas

a. Anaesthetics uniformly inhibit local cortical activity

In the experiments presented here, ketamine, pentobarbital and etomidate were perfused in two different preparations of cortex stimulated directly: the AIC and the S1BF. Local cortical responses, though producing comparable mesoscopic activity patterns, have previously been reported to give rise to qualitatively different assemblies in distinct cortical fields; for example, between visual and auditory cortices (Chakraborty et al., 2007). Additionally, it was shown in **Chapter 3** that comparing assemblies generated within cortical sub-regions featuring altered layer organisation, as is the case between the 6-layered S1BF and 5-layered AIC, showed clear discrepancies; it was therefore expected that anaesthetics would produce altered profiles of assembly inhibition in these same cortical sub-regions. The data obtained here in AIC and S1BF showed the opposite results: regardless of the underlying cortical cytoarchitecture, anaesthetics showed the same potency in both slice preparations, and induced comparable inhibition profiles (**Section 4.3.2.a**). This finding was further confirmed in **Section 4.3.2.c**, where it was shown that for all anaesthetics, the dose-response curve fits for AIC and S1BF were non-significantly different from each other, while this was not the case once the curve fit of thalamocortical data was included in the comparisons (see **Section 4.4.2.b**).

b. Impact on directly- versus remotely-activated assemblies

It was expected in the present experiments that anaesthetics would affect thalamocortical activity more potently than local cortical activity. Not only have anaesthetics been widely reported to affect thalamic activity in particular (Alkire and Miller, 2005; Arhem et al., 2003; Hofle et al., 1997), but they are also able to affect additional crucial processes in thalamocortical preparations. Direct stimulations delivered to cortical tissue, as discussed in **Chapter 3**, depolarise a large amount of neuronal elements in direct proximity of the stimulating electrode, including axons and dendrites. Within milliseconds, the entire network is activated giving rise to a neuronal assembly: in this scenario, anaesthetics can only induce inhibition via cortical mechanisms, including potentiation of IPSCs and depression of EPSCs via their actions on LGICs, as well as tethering passive neuronal membrane properties towards more hyperpolarised states via their actions on VGICs. In thalamocortical slices however, while these cortical mechanisms are still at play, anaesthetics can also affect extra-cortical mechanisms, including the excitability of thalamic networks in VPM as well as the effectiveness of long-range impulse conduction in thalamocortical axons. Not only are thalamocortical neurons in VPM highly sensitive to GABAergic inhibitory input (Angel, 1993; Lees, 1998), but only a few intact axons then communicate this excitation from the thalamus to the cortex. Therefore, even minor inhibitory influences on their axonal conduction efficacy can have a leveraged effect in their resulting cortical activity (Haydon et al., 1984), which requires a significant initial stimulus to gate and then propagate large-scale assemblies. In accordance with this logic, anaesthetic drugs were found to induce a uniform profile of inhibition in cortical stimulation preparations, yet showing significantly more potent inhibitions in thalamocortical slices (**Figure 9**).

Interestingly, this phenomenon was more pronounced for group 1 (etomidate and pentobarbital) rather than for ketamine. This disparity is even more obvious when taking in account the IC_{50} shifts found for each agent in cortical versus thalamocortical preparations (**Figure 13**), possibly implicating a greater proportion of extra-synaptic $GABA_A$ receptors in mediating extra-cortical mechanisms of anaesthetic inhibition (Jia et al., 2005). More work will be required to confirm this relationship, yet these findings provide support to the multi-site hypothesis of anaesthetic action (Dodson and Moss, 1984; Grasshoff et al., 2005).

A

		Measured IC_{50} values (95% C.I.) (μM)		
		Etomidate	Ketamine	Pentobarbital
Preparation	AIC	**5.92** (2.59, 7.83)	**10.60** (5.71, 29.49)	**136.50** (96.23, 178.21)
	S1BF	**4.73** (2.08, 8.81)	**14.52** (9.52, 42.12)	**125.34** (98.81, 204.80)
	TC	**2.42** (1.39, 3.19)	**12.18** (6.17, 32.55)	**85.80** (53.28, 109.2)
Averaging of local cortical IC_{50}s		5.33	12.56	130.92
% change in IC_{50} between local network (AIC & S1BF) and longer-range (TC) connectivity		54.6 (decrease)	3.03 (negligeable change)	34.5 (decrease)

B

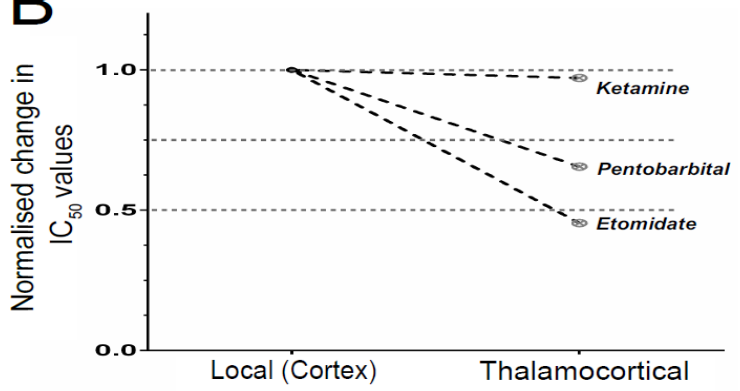

Figure 13: Group 1 anaesthetics significantly affect extra-cortical mechanisms. **A**. IC_{50} values, with 95% confidence intervals (C.I.) in brackets, for etomidate, ketamine and pentobarbital in each preparation (AIC, S1BF and TC). As discussed previously, local cortical preparations gave rise to very similar anaesthetic potencies, while in thalamocortical slices, potencies roughly doubled for pentobarbital and etomidate. For this reason, the IC_{50}s calculated for AIC and S1BF (i.e. '*local cortical IC_{50}s*') were averaged together in order to calculate the proportional increase in potency (i.e. lowering of IC_{50} concentrations in thalamocortical slices). **B**: **i**. Graphical representation of the differences between local cortical and thalamocortical IC_{50}s for each anaesthetic: etomidate and pentobarbital feature

a 54.6 and 34.5% increase in potency, while for ketamine this increase is negligible (3.03% increase).

c. Effect of anaesthetics in basal forebrain

As described previously, the basal forebrain consists of simplified networks under potent GABAergic control. Here, results show a much more prominent effect of anaesthetics in basal forebrain compared to cortex, and this inhibition was more pronounced for etomidate and pentobarbital compared to ketamine (**Figure 12**), confirming GABAergic mechanisms may play a crucial role in affecting this sub-cortical structure. The complexity of cortical networks compared to those of basal forebrain may provide an explanation as to why anaesthetics induce more potent reductions of activity in the latter brain slice preparation. Alternatively, these differences may have been exacerbated as a result of the *in vitro* preparation, which effectively removes any impact arising from the mix of tonic modulation from cholinergic and monoaminergic influence usually present *in vivo*. Monoaminergic modulation of basal forebrain activity has already been reported to be of crucial importance, from all its constituting neurotransmitter species, for regulating the level of basal forebrain activity during specific brain states (Sarter & Bruno, 2002). Furthermore, it has previously been shown that systemic administration of amphetamine, a non-selective catecholaminergic releaser, in rats increases dopamine release in basal forebrain by up to 700% from control levels, which led to enhanced cortical acetylcholine release from basal forebrain, i.e. as a result of an increased activity (Arnold et al., 2001). These reports could provide a possible explanation for the more noticeable effects of anaesthetics in basal forebrain compared to cortex, even though monoamines also play an important role in modulating cortical dynamics. Basal forebrain networks however, seem to be significantly more reliant on monoaminergic innervation than S1BF cortical

networks: while serotonergic afferents have been shown to innervate all layers of cortex extensively (Lidov et al., 1990; Foote, 1987), dopaminergic innervation of the cortex is mostly confined to the frontal cortices (Tassin et al., 1978) and noradrenergic innervation preferentially affects superficial cortical layers (Morrison et al., 1978; Loughlin et al., 1982). This possibility however is contradictory to the fact the AIC is more potently innervated by monoaminergic input, such as with a much increased dopaminergic influence in this frontal brain region, yet despite this difference, anaesthetic effects were very similar in S1BF and AIC. As a result, the differences in reliance on monoaminergic input is unlikely to be the reason for the much increased inhibition seen in basal forebrain, suggesting therefore that this more potent effect most likely arises as a result of the less complex wiring and greater sensitivity to GABAergic control compared to cortex. Furthermore, the differences in anaesthetic potency seen here between cortical and sub-cortical assemblies provides support to the theories that anaesthetics affect specific neuronal networks *in vivo* with some preference (Antkowiak, 2002; Franks, 2008), such as the thalamocortical pathways (Hofle et al., 1997; Alkire et al., 2005), and that they may trigger additive inhibitory effects at multiple levels of brain functioning, from the brainstem to the cortex.

d. Similarities and differences in the actions of ketamine, etomidate and pentobarbital

Each anaesthetic drug employed here induced dose-dependent decreases in neuronal assembly dynamics, particularly in summed fluorescence and lateral spread of activity, as would have been expected for drugs inducing a systemic loss of cerebral function, yet did so at distinct rates: pentobarbital produced the most extensive inhibition at maximal dose, followed by etomidate, while ketamine induced comparatively small effects – this order was conserved across all preparations, confirming the more prominent effect of group 1 anaesthetics on cortical activity. It

was also found that the profile of inhibition of group 1 anaesthetics featured Hill slopes close to or above 1, while that of ketamine remained between 0.6 and 0.75 across all preparations: this difference reflects a more potent effect as well as a more precise effective dose-range for group 1 anaesthetics, implicating actions at $GABA_A$ receptors in producing such effects, and corroborating previous reports (Nelson et al., 2002).

The time course of activity was the most telling parameter however, as each anaesthetic produced clearly discernible results: ketamine caused a shortening of this time course, etomidate did not alter this parameter significantly, except in S1BF, while pentobarbital in all cases retarded the termination of evoked activity. In terms of their effects on specific slice preparations, pentobarbital and etomidate caused a much greater inhibition in thalamocortical compared to local cortical preparations (AIC & S1BF) while ketamine did not show vast differences between its effects in each of the preparations tested (see **Figure 13**): these observations indicate group 1 anaesthetics produce significantly more potent inhibition as a result of extra-cortical mechanisms compared to ketamine.

4.4.3 Interpreting *in vitro* data with respect to target effectors of anaesthesia

The main difficulty which researchers face in investigating anaesthetic mechanisms is the ability to associate specific drug effects to overall behavioural outcomes, in particular when testing mesoscopic effects of anaesthetics *in vitro*. This is because i) there are no accepted end points of anaesthesia in brain slices, i.e. such as loss of righting reflex in rodents or hypnosis in humans, and ii) the precise relationship interlinking mesoscopic effects with specific clinical doses administered to patients remains unclear. Therefore, how could such a link be made between effects seen

here and those that take place at the micro-scale? In response to the former problem, it is assumed that a faithful reproduction of intrinsic, 'resting-state' excitability of cortical networks should be expressed in brain slices that have been harvested with sufficient care. Therefore, this initial level of activity, recorded in the baseline condition of each experimental run, can be used in the detection of any drug-induced deviation from this baseline; providing incremental changes in population dynamic which can to some extent be matched to clinical dose steps. With respect to the latter difficulty, the data acquired here can be considered in light of drug concentrations reported to affect micro-scale targets *in vitro* in the literature (Franks & Lieb, 1984; Friederich & Urban, 1999), see **Section 4.1.3.d – Table 1**, with any apparent agreement between micro-scale effective concentrations and those reported here for significant effects at the meso-scale potentially highlighting key effectors and processes (**Figures 14-16**).

- *Ketamine*

Ketamine, even at high doses, only showed relatively small effects on the dynamics of neuronal assemblies visualised using VSDI: this finding fits with reports that at effective anaesthetic doses, ketamine does not decrease EEG cortical field signals (such as those measured using bispectral index monitors), and may even sometimes increase them (Anderson and Jakobsson, 2004; Schnakers et al., 2005). This may be due to the lack of effects of ketamine on the notoriously inhibitory $GABA_A$ receptor, in addition to stimulating the release of monoamines (Berton and Nestler, 2006; Tso et al., 2004) as well as inducing a physiological enhancement of fast glutamatergic transmission (via AMPA receptors) at low doses *in vivo* (Di Lazzaro et al., 2003). In turn, these findings may explain why ketamine and other similar group 2 anaesthetics induce little hypnosis or immobility (Solt and Forman, 2007), while

their high analgesic properties may arise from their ability to interfere with specific cortical (Anis et al., 1983) and spinal processes (Ebert et al., 1997; Kvarnstrom et al., 2004). With respect to the effective doses of ketamine at putative targets (see **Figure 14**, below), nAChRs and HCN channels have both been reported to be blocked at low micromolar concentrations (see **Table 1**), reducing excitatory inputs with the former, while the latter effect promotes hyperpolarisation. At incrementally higher doses, ketamine also blocks NMDAR and L-type Ca^{2+} channels, since the IC_{50}s of ketamine at these targets are reported between 9 and 20 μM (Hatakeyama et al., 2001; Yamamura et al., 1990), and no direct effects on $GABA_A$Rs. It must be mentioned however, that in the context of intact cortical networks, the cumulative actions of ketamine have been shown to also lead to an increase in the time constants of evoked IPSCs, in the same way barbiturates do (Gage and Robertson, 1985): this finding suggests ketamine may induce some positive modulation of $GABA_A$ receptors via a complex physiological mechanism, much in the same way it increases AMPAR activity (see above), rather than as a result of direct interactions.

The small difference in the magnitude of the inhibition induced in local cortical (red and blue) curves compared to that obtained in thalamocortical slices suggests the relevant targets of ketamine may be uniformly distributed in cortical and extra-cortical tissue, rather than featuring a marked inhibition of extra-cortical elements. Furthermore, though non-significant, ketamine was found to induce a slightly more potent effect in AIC compared to S1BF (especially visible in the 25 μM perfusion): this may be explained at least in part by the greater level of expression of NMDA receptors in rat frontal cortices (645-1047 fmol/mg protein, depending on cortical layer) compared to parietal cortices (519-838 fmol/mg protein, depending on cortical layer) (Monaghan and Cotman, 1985).

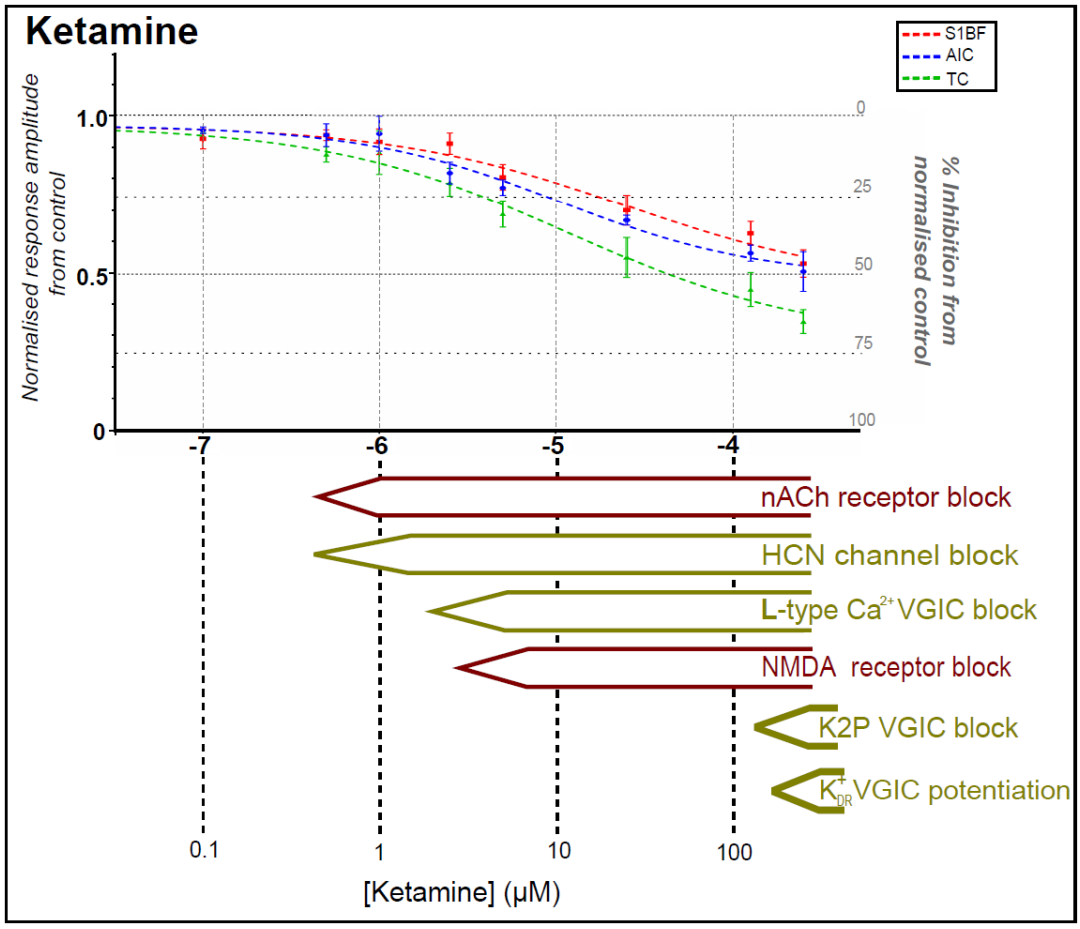

Figure 14: Matching of ketamine-induced mesoscopic effects on assembly generation with reported micro-scale target effective doses. Top graph displays the dose-response relationships acquired in S1BF, AIC and thalamocortical slices using increasing concentrations of ketamine, while the bottom graph matches previously reported effective doses of ketamine at the targets listed here (for references, see **Table 1**); labels represent the approximate concentrations at which ketamine perfusions start to affect the target protein of interest, with increasing concentration leading to greater engagement of the resulting effect (red labels represent LGIC targets while dark yellow labels represent VGIC targets). This figure provides no indication as to the dose-response relationships of ketamine at each target however, ushering caution when considering the associations presented here. Nonetheless, according to these reported effective doses, the inhibition of assembly dynamics as a result of increasing doses of ketamine is primarily mediated by combined actions of (in order of increasing potency) nAChRs, HCN channels, L-type Ca^{2+} VGICs and NMDA receptors. The dose-response curves presented here do not plateau-off, even at high concentrations, and this may be due to the reported impact of ketamine on two further effector targets at high concentrations: K2P VGIC blockade and K^{+}_{DR} VGIC potentiation, which may help to keep neurons hyperpolarised.

- *Etomidate*

Etomidate is widely reported to induce a large part of its effects (including hypnosis, analgesia and amnesia) almost entirely via potentiation of $GABA_A$ receptor currents at sub-micromolar concentrations (Belelli et al., 1997; Krasowski & Harrison, 1999; Rudolph & Antkowiak, 2004). Other relevant targets however have been identified, which have been found to respond to clinically-relevant etomidate concentrations (0.5–40 μM) and include: blockade of sodium-selective VGICs, direct activation of $GABA_A$Rs, nAChR blockade, as well as T-type Ca^{2+}. At supra-clinical concentrations (>40 μM), etomidate has been reported to block 2-pore K^+ VGICs, however the contribution of this effect to clinical anaesthesia remains unclear. Again, it is difficult to attribute targets to observed effects, however **Figure 15** below suggests the most relevant targets of etomidate in inhibiting neuronal assembly generation are its potentiating $GABA_A$R currents with a probable involvement of its blockade of sodium-selective VGICs and nAChRs; there is an added difficulty in attributing specific weights to each effect. Nonetheless, the inhibition induced here on cortical activity has been widely reported to be mediated by a significant lowering of the GABA concentrations required to gate $GABA_A$ receptors in the presence of etomidate (Tomlin et al., 1998; Uchida et al., 1995). One recent study has also implicated TDBzl-etomidate, an analogue of etomidate possessing photo-reactive properties, as a positive modulator of nAChRs (Nirthanan et al., 2008), however this action may be due to the molecular differences between the two drugs, as etomidate itself has been reported to block nAChRs (Zhang et al., 2007).

Contrary to ketamine, the dose-response curves obtained here in AIC and S1BF are nearly entirely superposed, confirming the very similar profiles of inhibition induced in either cortex; this comes in contrast to the much more potent effects of etomidate in inhibiting thalamocortical activity. With regard to this increase in

potency, thalamocortical processing involves the adequate functioning of VPM neuronal networks, long range connections projecting to the S1BF, as well as local cortical networks: this discrepancy may therefore be explained at least in part by the potentiation of high-affinity extra-synaptic receptors located on long-range axonal projections (Bieda and MacIver, 2004), dramatically enhancing tonic 'leak' inhibitory currents. Such an effect, in addition to the blockade of sodium channels, could potentially be of similar potency as that of the enhancement of synaptic $GABA_A$Rs (Yang and Uchida, 1996).

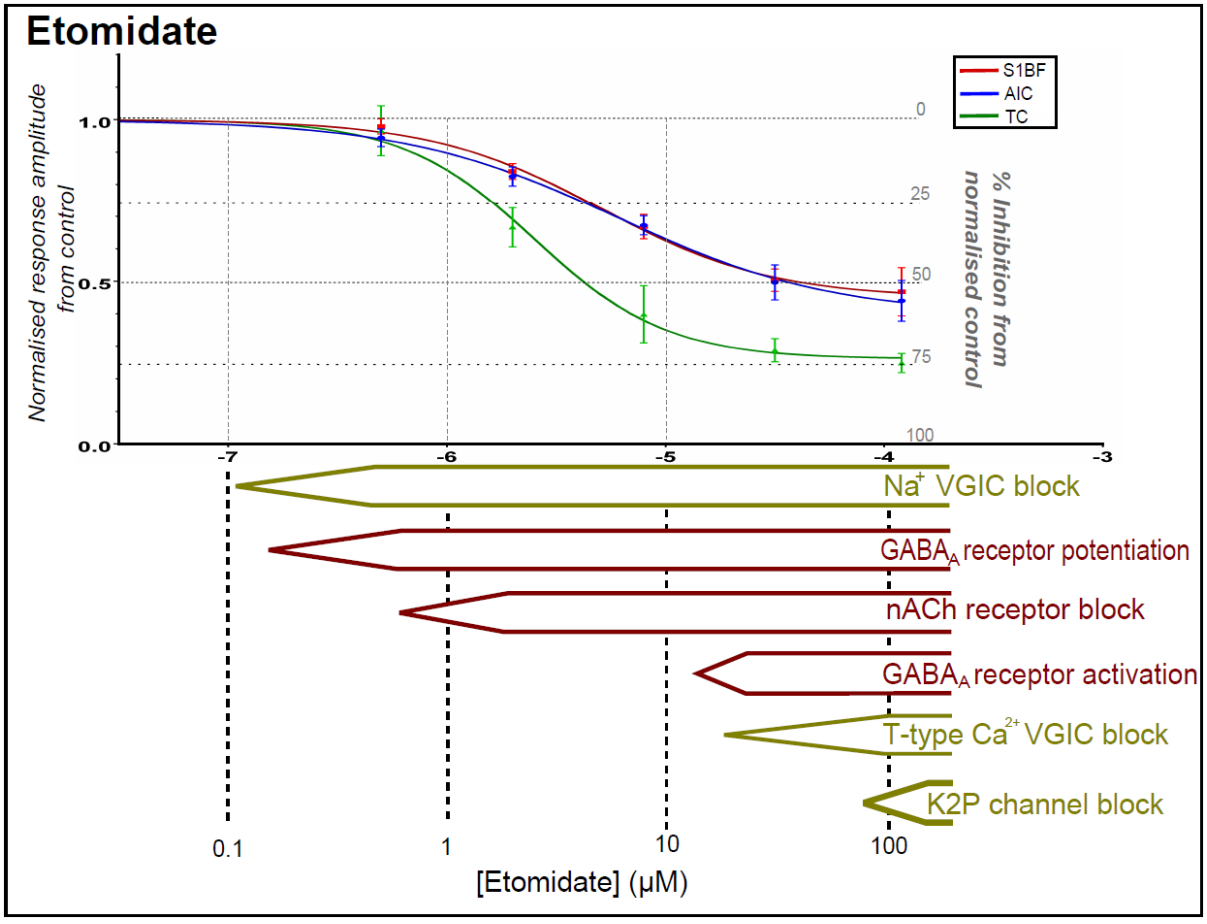

Figure 15: Matching of etomidate-induced mesoscopic effects on assembly generation with reported micro-scale target effective doses. Top graph displays the dose-response relationships acquired in S1BF, AIC and thalamocortical slices using increasing concentrations of etomidate, while the bottom graph matches previously reported effective doses of etomidate at the targets listed here (for references, see **Table 1**); labels represent the approximate concentrations at which etomidate perfusions start to affect the target protein of interest, with increasing concentration leading to greater engagement of the

resulting effect (red labels represent LGIC targets while dark yellow labels represent VGIC targets). This figure provides no indication as to the dose-response relationships of etomidate at each target however, ushering caution when considering the associations presented here. Nonetheless, according to these reported effective doses, inhibition of assembly dynamics as a result of increasing doses of etomidate is primarily mediated by combined actions of (in order of increasing potency) Na^+ VGIC blockade, $GABA_A$ receptor potentiation, nACh receptor, T-type Ca^{2+} and K2P VGIC block. The dose-response curves presented here do plateau-off, especially in thalamocortical preparations, suggesting the most important inhibitory effects are not induced at VGICs, but at LGICs ($GABA_A$ and nACh receptors in particular).

- *Pentobarbital*

Pentobarbital showed the lowest affinities of all tested anaesthetics for its targets, with potentiation of inward rectifying (K^+_{IR}) and leak potassium currents at ≈8 μM (Wan et al., 2003). These actions are suspected of playing a part in the effects seen here in thalamocortical slices, showing noticeable inhibition (≈30% inhibition from normalised controls) when perfused with 20 μM; yet not in cortex (AIC and S1BF) since in those preparations, noticeable inhibition of assemblies is not seen until perfusion with 80 μM (≈20% inhibition). At these higher concentrations however, both a blockade of nAChRs and potentiation of $GABA_A$Rs are now highly included in the drug's effects (Roth et al., 1989) (Dilger et al., 1997), implicating these two receptors as important effectors in pentobarbital-induced cortical inhibition. Again, like ketamine, the dose-response curves seen here do not plateau-off, and this may be due to the successive inclusion of further mechanisms such as direct activation of $GABA_A$Rs (>100 μM; Thompson et al., 1996), followed by the blockade of 5-HT_3Rs (Barann et al., 2000, 1997), T-type Ca^{2+} and Na^+ VGICs (Frenkel et al, 1990; Rehberg et al., 1995; Todorovic & Lingle, 1998; Joksovic et al., 2005). Yet more inhibitory mechanisms are implicated at concentrations >1 mM, which are not

included in the figure below (**Figure 16**) since it is unlikely that pentobarbital is used at such high doses in clinical settings.

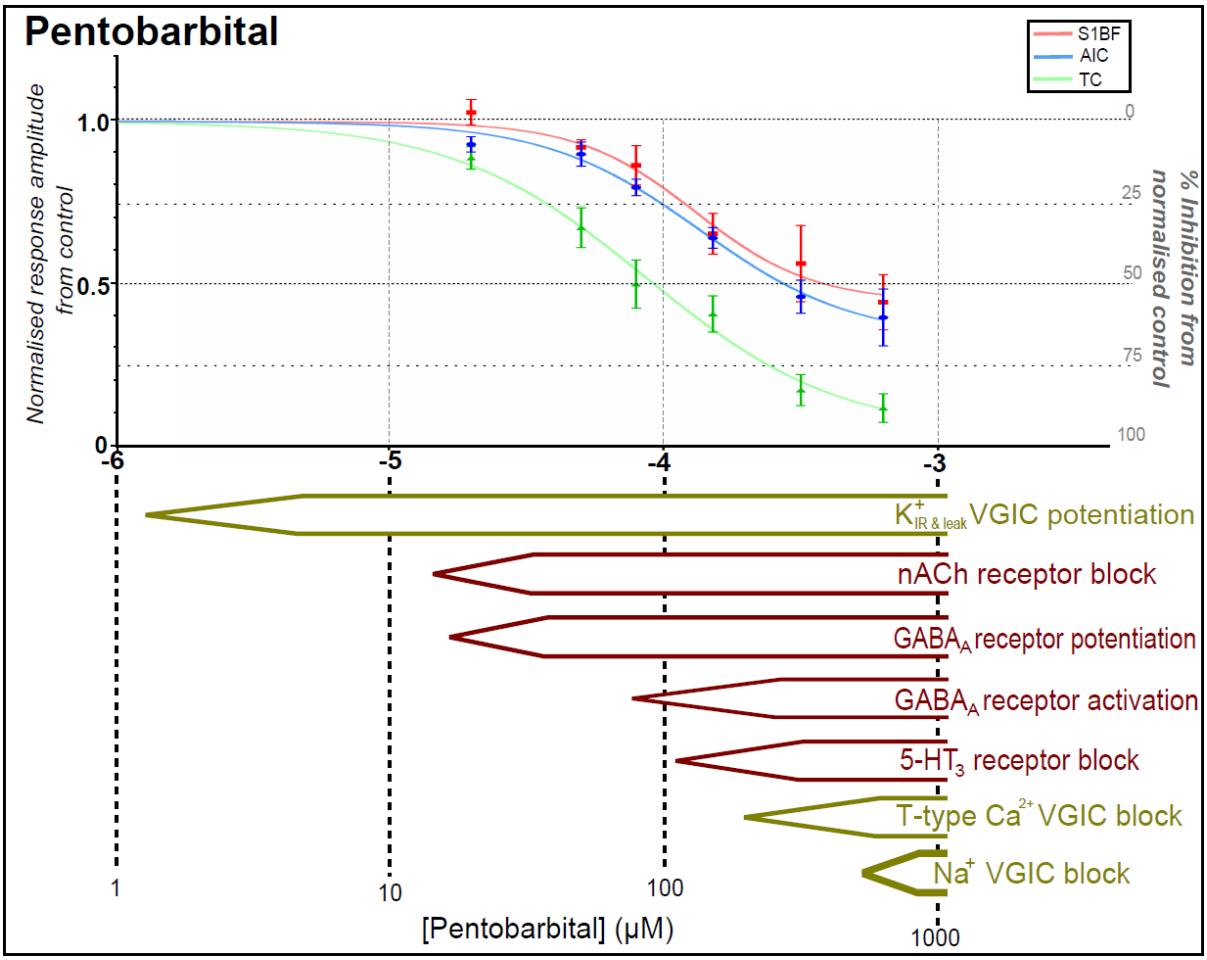

Figure 16: Matching of pentobarbital-induced mesoscopic effects on assembly generation with reported micro-scale target effective doses. Top graph displays the dose-response relationships acquired in S1BF, AIC and thalamocortical slices using increasing concentrations of pentobarbital, while the bottom graph matches previously reported effective doses of pentobarbital at the targets listed here (for references, see **Table 1**); labels represent the approximate concentrations at which pentobarbital perfusions start to affect the target protein of interest, with increasing concentration leading to greater engagement of the resulting effect (red labels represent LGIC targets while dark yellow labels represent VGIC targets). This figure provides no indication as to the dose-response relationships of pentobarbital at each target however, ushering caution when considering the associations presented here. Nonetheless, according to these reported effective doses, the inhibition of assembly dynamics as a result of increasing doses of pentobarbital would appear primarily mediated by combined actions of (in order of increasing potency) potentiation of inward

rectifying (IR) and leak K^+ VGICs, blockade of nAChRs, potentiation and then direct activation of $GABA_A$Rs and blockade of 5-HT_3Rs. The dose-response curves presented here do not plateau-off, even at high concentrations, and this may be due to the reported blockade by pentobarbital of two further effector targets at high concentrations: T-type Ca^{2+} and Na^+ VGICs, which together may induce a significant block of neuronal impulse conduction.

- *Protein targets in the context of mesoscopic neuronal dynamics*

The figures above first provide a visual representation that the original hypothesis, that anaesthetics induce their inhibitory effects via a common and unique mechanism of action, is undeniably false (Solt & Forman, 2007): it can be seen that general anaesthetics impact a range of protein targets, and in all cases possess distinct profiles of inhibitory potentiation, all the while blocking excitatory effectors. One striking finding however, is of the very close correspondence between the IC_{50}s found here for each agent and their reported effective doses at key effector proteins such as $GABA_A$, NMDA and nAChRs, as seen in this section. The interpretation of such effects remains difficult since at the cellular level, these effects all lead to inhibition, however in practice, even at supra-clinical doses, assemblies are never totally silenced. It is difficult to conclusively ascertain the reason for this resilience, but since anaesthetics reduce the excitability of both excitatory and inhibitory neurons, depending on the location and stoichiometry of receptor targets, this could lead to facilitatory overall effects on assembly dynamics. Evidence of anaesthetic-induced facilitation of network activity was presented here as a result of pentobarbital perfusion, which in most preparations produced significant lengthening of the time course of evoked assemblies (**Figure 10B**) as well as non-significant increases in LFP amplitude in cortical preparations (**Figure 11Aiii**); this phenomenon has been reported previously using VSDI in rat brain slices perfused with propofol as well as thiopental (Collins et al., 2007).

The present experiments corroborate that the actions of group 1 anaesthetics (etomidate and pentobarbital) are indeed most potently induced via positive modulation of $GABA_AR$ currents, while for ketamine (group 2-like anaesthetic) inhibition of NMDARs appears crucial. A further observation from the above comparisons however, is of the possible importance of the blockade of nACh receptors, as this effect is reported for *all* anaesthetics tested here (groups 1 & 2) at low micromolar concentrations, correlated with induced inhibitions seen here with VSDI: ketamine, 1-4 μM (Forman et al., 2015); etomidate, 1-15 μM (Hamouda, 2011; Nirthanan, 2008); pentobarbital, ≈25 μM (Roth et al., 1989, Dilger et al., 1997). This common effect on nAChRs will require more work to confirm the exact impact of this blockade in modulating evoked assemblies, however blockade of nAChRs has already been implicated in the induction of amnesia and immobility (Forman et al., 2015; Tassonyi et al., 2002). Anaesthetics also possibly affect the appropriate functioning of calcium VGICs, which all regulate neuronal excitability: T-type Ca^{2+} channels are important for repetitive firing of action potentials in both cardiomyocytes and neurons (Catterall, 2011); P-type channels regulate presynaptic excitability and neurotransmitter release; L-type channels on the other hand are more involved in excitation-contraction coupling of smooth, skeletal and cardiac muscle (Takahashi & Terrar, 1994). Actions of anaesthetics on these target channels, as is the case for example with etomidate-mediated block of P/Q-type calcium channels (Valadao et al., 2013), could therefore lead to notable inhibitory influences via pre-synaptic inhibition and decreased neurotransmitter release.

Of course, the overall anaesthetic effect of each agent actually arises from their cumulative actions at all their respective targets (depending on dose administered), and the difficulty will remain in assigning specific weights to each effect in the context of a measured response. A further challenge will be to predict network-wide effects resulting from anaesthetic modulation of specific micro-scale targets

(Antkowiak, 2002). Comparisons such as those described here provide an initial indication of the salient molecular targets of anaesthetics, probed at the mesoscopic level of brain organisation. This tentative 'bridging' of micro-scale effectors with meso-scale activity could be taken a step further with the direct comparison of clinical concentrations of anaesthetics occurring in the brain during specific anaesthesia stages, however many confounding factors at play when trying to estimate relevant anaesthetic concentrations *in vivo* make this last comparison still too ambiguous and precarious.

4.4.4 Relevance of *in vitro* optical imaging and electrophysiological data in the study of anaesthesia

VSDI is a novel technique offering a unique insight into mesoscopic brain dynamics, however in the context of anaesthesia research *in vitro*, a number of methodological hurdles must first be considered in ensuring relevant experimental protocols are used with respect to *in vivo* process, such as anaesthesia. These include **a)** the estimation of clinically-relevant doses and their resulting concentrations at their target, **b)** knowing what it is, exactly, that optical imaging using voltage-sensitive dyes reveals, i.e. how do anaesthetic effects probed using VSDI compare to those recorded using LFP.

a. Estimating clinically-relevant anaesthetic concentrations

It remains extremely difficult to estimate the exact concentrations which induce appropriate levels of anaesthesia *in vivo*, this is in part because of the manner in

which anaesthetics are inoculated, but also as a result of the chemical nature of anaesthetic drugs and their resulting partitioning in neuronal tissue. The way in which these factors confound the estimation of actual effective concentrations at the target will first be discussed.

- *Anaesthetic doses and concentration at target*

Anaesthetists induce hypnosis, amnesia and immobility at known effective drug doses, usually given in mg/kg, however this information unfortunately provides little indication as to what the resulting drug concentrations are at target effector proteins. This is because upon injection, anaesthetics first disperse in the blood, where significant portions of anaesthetic molecules are immediately removed due to protein binding: ketamine, pentobarbital and etomidate have been reported to bind to protein by up to 26, 56 and 76% of total inoculated dose, respectively (Friederich et al., 1999; Franks & Lieb, 1984). It is therefore free anaesthetic molecules which must then enter the brain by crossing the blood-brain barrier and reach their targets: only a fraction of the administered dose is therefore actually responsible for the perceived behavioural effects. Confounding things further, and among other blood-borne proteins, serum albumin has been reported to enhance drug penetration into fatty tissue (Dreher et al., 2006), increasing the difficulty in estimating final concentrations at the target further. It remains hard to recreate accurate clinical or *in vivo* conditions in slice preparations, however just like for experiments of anaesthetic effect on recombinant receptors expressed in oocytes, these represent model systems (neuronal networks) from which the effects of clinically-relevant anaesthetic dose *ranges* can be investigated.

- *Partitioning of anaesthetics in neuronal tissue*

Upon entry into the brain, fatty anaesthetic molecules have been reported to preferentially imbed in cellular membranes, where they co-localise with their effector membrane proteins. Anaesthetics have low affinities and specificities for the range of protein targets they have been reported to affect, however due to their preferential infiltration of neuronal cell membranes, anaesthetic concentrations can to reach as high as 25 mM at interstitial membrane-to-protein sites (Forman et al., 2015), possibly circumventing the impact of their low affinities. This aggregation of anaesthetic molecules in cell membranes complicates the estimation of actual effective concentrations further, as it suggests that the effective concentrations of free molecules diffusing through the extra-cellular space may not be directly representative of those occurring in fatty micro-domains, where anaesthetic binding sites are found. Indeed, many anaesthetics bind to LGICs and VGICs in concealed binding pockets buried within their trans-membrane compartments; this contrasts with the comparatively well-exposed binding sites of endogenous neurotransmitters such as GABA, dopamine or glutamate. Nonetheless, free anaesthetic concentrations at the target still represent the best estimates currently available, and may even offer the possibility of gaining a better understanding of the actual relevant anaesthetic concentrations within cell membranes, since an equilibrium must exist between free and lipid-bound anaesthetic concentrations. In light of such limitations, the concentration ranges used here for each anaesthetic, and the effects they produced, are nonetheless comparable to those reported for effective modulation of their respective targets, as reported in the literature (**Table 1**); offering a unique insight into anaesthetic action on mesoscopic assembly dynamics.

b. Comparison of VSDI and LFP data

As already discussed in **Chapter 2**, LFP data feature a much smaller receptive field compared to those obtained using VSDI; both as a result of the smaller volume of neuronal tissue from which data are acquired, but also as a result of the greater sensitivity of VSDI in detecting sub-threshold population dynamics. In the experiments presented here, VSDI and LFP data were recorded simultaneously for the vast majority of experiments, however only some of those were selected for presentation here. Some LFP experiments were excluded where electrical noise was too conspicuous within the data, and would drown the evoked response. As a result, experiment numbers were often too low, when taking in account the large variability of results, to conduct robust comparative analyses with VSDI. Nonetheless, the results obtained here with LFP can still be used to confirm that anaesthetics provoked dose-dependent decreases in evoked activity, as can be seen by the gradual lowering of normalised response amplitudes with increasing doses of anaesthetic (**Figure 11A**).

These decreases were more pronounced with etomidate and pentobarbital than with ketamine: a finding which has already been reported previously (Ribeiro et al., 2014), providing some confirmation of the validity of the results presented here. This was also the case when considering VSDI data: decreases seen with VSDI can indeed be matched to those seen with LFP, even in the finding that thalamocortical activity was more potently inhibited than local cortical assemblies. This apparent agreement between VSDI and LFP data highlights the complementarity of both techniques further, as well as substantiating the notion that the effects seen here with VSDI arise from real decreases in neuronal excitability.

With regards to ketamine however, its inhibitory effects were somewhat more visible with VSDI than LFP: electrophysiological recordings show no effect resulting from 5 μM ketamine perfusions (**Figure 11Ai**), whereas VSDI data shows noticeable decreases in all preparations at that concentration (all figures in **Section 4.3.2**). Indeed, the 5 μM perfusion data was chosen as the near-IC_{50} dose for ketamine in all preparations, testament of the more pronounced effects seen with VSDI. In turn, this discrepancy may arise as a result of the wider receptive field of VSDI, or because ketamine affects sub-threshold changes (more comprehensively recorded with VSDI than LFP) preferentially, or a combination of both factors. By comparison, the effects of etomidate and pentobarbital on LFP records were much more pronounced and comparable to the dose-dependent decreases seen with VSDI. Together, these observations confirm that the effects seen here with VSDI reflect true changes in the underlying network excitability as a result of anaesthetic action, as well as highlighting the greater sensitivity of VSDI in revealing clinically-relevant drug effects.

4.4.5 Effect of anaesthetics on mesoscopic cortical computations

The data presented here provides a unique insight into anaesthetic action at the meso-scale, with each anaesthetic affecting the different parameters of assembly dynamics in distinct ways. In turn, modulation of these intrinsic dynamics could lead to disruptions in mesoscopic neuronal signalling. For example in the case of pentobarbital, which reduced overall assembly magnitude yet increased the time course, equating to a much weaker and less well defined response to stimuli, i.e. a significant decrease in the signal-to-noise ratios of evoked activity (White et al., 2012). Furthermore, anaesthetic-induced inhibitions in population activity seen here

with each agent may reflect general decreases in functional processing abilities, as was postulated for the performance of auditory cortices in patients undergoing isoflurane anaesthesia (Madler et al., 1991). Indeed, a lowering of fluorescence intensity in VSDI reflects a less robust depolarisation in dendrites and neuropil compartments in general (Denk et al., 1990; Yuste et al, 1997; Badin et al., 2013), which implicates a less robust signal transmission and integration within populations, and by extension: a reduced overall ability to process incoming information with ongoing activity (Azouz and Gray, 1999; Riggall and Postle, 2012). The possible implications of such decreases in the signal-to-noise ratio of incoming stimuli and processing power of affected brain regions remain hypothetical, however they offer plausible mesoscopic mechanisms in the context of anaesthesia.

It was shown here that in the case of each anaesthetic probed, the profile and magnitude of inhibition of evoked assemblies was nearly identical between S1BF and AIC slice preparations triggered using direct electrical stimulations. This cortical inhibition could, in itself, potentially account for a macroscopic loss of function, i.e. induction of anaesthesia, however in addition to this, anaesthetics are widely reported to also significantly affect extra-cortical mechanisms (Bieda & McIver, 2004). Indeed, this was confirmed here using thalamocortical preparations, where normalised responses were found to be significantly more inhibited when evoked remotely from the thalamus than when elicited in cortex directly. In turn, this more potent decrease of thalamocortical activity could arise as a result of anaesthetic-mediated inhibition of the thalamus, long-range connectivity (Ferrarelli et al., 2010), or possibly a combination of both mechanisms. Furthermore, it has been reported that clinically-relevant concentrations of etomidate and ketamine produce a robust de-coupling of cortical activity, and that this mechanism could account for the loss of function, and therefore LOC, in patients undergoing

anaesthesia (Hentschke et al., 2005; Voss et al., 2012). This decoupling of cortical activity over space could potentially arise from the decreased lateral spread of assemblies seen here at clinically-relevant concentrations of either anaesthetic. This effect potentially leads to a much impaired ability of cortical regions to synchronise their activity, and hence to inadequate stimuli representation and maintenance within cortical computations. In addition to this, anaesthetics have been highly implicated in reducing neuronal excitability in relay nuclei upstream of cortical processing, i.e. inhibition of thalamic (Phillis and Tebecis, 1967; Pirot et al., 1995; Sugiyama et al., 1992) and brainstem nuclei (Bradley and Dray, 1973).

One brain imaging study of cortical and sub-cortical activity in patients undergoing anaesthesia provides complementary findings to those presented here (Velly et al., 2007). In this study, the authors show that upon LOC, patients undergoing sevoflurane or propofol anaesthesia initially featured a much more pronounced decrease in cortical rather than of sub-cortical activity, suggesting inhibition of cortex is central to this induction step, and is consistent with the findings presented here. Following this, a potent inhibition of thalamus was seen in these patients, implicating inhibition of sub-cortical structures, and in particular the thalamus, with successful maintenance of anaesthesia (Brown et al., 2010): indeed, suppression of thalamic activity would ensure very little stimulation from the periphery reaches the cortex (Velly et al., 2007).

In addition to inhibition of thalamocortical activity, potent inhibition of basal forebrain by anaesthetics, as was shown here *in vitro*, may also play a part in maintaining anaesthesia *in vivo*, since such inhibition would result in starving the cortex of its excitatory cholinergic input (Perry et al., 1999). Taken together, the findings presented here are consistent with *in vivo* data acquired in healthy volunteers undergoing anaesthesia: mesoscopic VSDI data obtained in slice preparations, and corroborated with electrophysiological recordings, provide a

precise description of anaesthetic effects in different brain regions, which can be used to bridge micro-scale events with macro-scale behavioural end-points of anaesthesia, thereby offering a mechanistic method for shedding more light on the processes triggered by anaesthetic drugs across levels of organisation.

4.4.6 Conclusions

In the present chapter, the effects of anaesthetics were probed on isolated cortical networks, and these results were used to address multiple comparisons, including of anaesthetic effects between: cortical areas (AIC vs S1BF), locally- and remotely-activated assemblies (S1BF vs TC), and locally-generated assemblies in cortical and basal forebrain preparations (AIC and S1BF vs basal forebrain). Furthermore, the effects of anaesthetics on the specific parameters of assembly dynamics were investigated in an attempt to differentiate between the inhibitions induced by each agent. The conclusions which can be drawn from the research conducted here include:

i) That anaesthetic drugs, regardless of their chemical structure, actions and classification, each induce a uniform profile of inhibition of locally-generated cortical activity, at least between AIC and S1BF, however since these two cortical sub-regions feature strikingly dissimilar mesoscopic layer organisations, this finding could potentially yet cautiously be extended to the cortex in general. This finding comes in contrast to the significantly more potent inhibition induced by each agent on thalamocortical processing when compared to direct stimulations in S1BF: implicating a vast involvement of extra-cortical mechanisms in the behavioural outcome of anaesthesia, which may be mediated by the potent inhibition of sub-cortical regions crucial to the

maintenance of conscious behaviour, such as the thalamus and basal forebrain.

ii) The actions of groups 1 anaesthetic drugs (pentobarbital and etomidate) versus those of ketamine can be readily differentiated by inspection of optical imaging data, and to a greater extent than electrophysiological data. This methodology highlights the importance $GABA_A$ receptors in producing the more potently inhibitory effects of group 1 anaesthetics (etomidate and pentobarbital).

iii) It is proposed that $GABA_A$ and nAChRs represent key targets in the mechanism of action of group 1 anaesthetics (etomidate and pentobarbital); with an additional possibility for the important involvement of Na^+ VGIC block in the case of etomidate. For ketamine however, the main targets highlighted in this exercise were blockade of nACh and NMDARs, as well as of HCN channels. A supplementary finding regards the seemingly crucial importance of nAChR blockade in the process of anaesthesia, as its involvement is common to all three anaesthetics tested here, and all within matching clinically-relevant anaesthetic concentrations.

The present chapter has provided a comprehensive description of the effects of anaesthetics at the meso-scale, all the while attempting to match these mesoscopic effects to reported micro-scale actions of anaesthetics. In doing so, The investigations presented here therefore provide a tentative starting point for attempting to bridge micro-scale actions to macro-scale effects.

Chapter 5: GENERAL DISCUSSION

Optical imaging of VSDs is an engaging technique providing reliable measures of two-dimensional voltage changes emanating from neuronal population activity. In the present thesis, this technique was used in order to simultaneously monitor relatively large areas of neuronal tissue in the goal of investigating the reliance of VSDI signal on underlying network architecture and activity across different brain regions, as well as in investigating the effects of anaesthetics upon these same slice preparations. These investigations provided greater insights into the nature of mesoscopic activity patterns (assemblies), how these assemblies are affected by specific anaesthetic drugs, and in turn helped identify more precisely which micro-scale targets are among the most important in modulating normal population activity.

5.1 Investigating assemblies across brain regions using VSDI and electrophysiology

Here, the combination of VSDI and field potentials were used to characterise and compare the spatio-temporal profiles of evoked assemblies. It was found that, surprisingly, mesoscopic cortical activity was mostly homogeneous, both within and between granular and agranular cortical areas, yet differing greatly from that evoked in sub-cortical regions. This thesis represents the first comprehensive comparison of such a disparate collection of brain areas, including the basal forebrain, a region which remains underexplored using VSDI in light of its importance in controlling

cortical activity (Nunez, 1996), as well its key role in the neuropathology of Alzheimer's disease (Badin et al., 2016; Hefty & Weiner, 1986). Furthermore, the use of the VSDI toolbox (Bourgeois et al., 2014) greatly aided in the analysis, manipulation and rendering of spatio-temporal imaging data; reinforcing the benefits and need for a systematic fashion of presenting VSDI data. This increased level of precision was especially obvious when analysing assembly patterns evoked thalamocortically, with the detection of a biphasic cortical activity profile in the radial orientation of columns: the highest levels of activity were detected in the deep layers, followed by superficial layers while LIV emitted the least fluorescence. This finding is discussed in relation to the impact of slice angle which could affect cortical network morphology, and the possibility of truncation of thalamocortical afferents to superficial layers (**Section 3.4.3**). Not only are the dynamics of neuronal assemblies compared more comprehensively here than previously undertaken, but also contribute further evidence of the practicality of using VSDI for the acquisition of meso-scale parameters of neuronal activity dynamics.

In order to take this research further, it would first be imperative to relate these *in vitro* findings to those produced *in vivo* using VSDI. To date, only few VSDI experiments have focused solely on the actions of anaesthetics on normal cortical processing (Collins et al., 2007; Devonshire et al., 2010; Kratzer et al., 2014, Kratzer et al., 2012), instead focusing on mesoscopic activity during wakefulness *in vivo* (Kuhn et al., 2008; Ferezou et al., 2007). In particular, the recent use of VSDI in VPM *in vivo* (Tang et al., 2015) may mark the beginning of a new era of VSDI, as this is the first report which reports the successful imaging of other structures than the dorsal cortical surface *in vivo*.

5.2 Effect of anaesthetics on cortical and subcortical assemblies

Increasing doses of ketamine, or of etomidate and pentobarbital (group 1 anaesthetics) were all found to induce potent inhibitions of evoked assemblies. Such findings are in agreement with previously published reports of comparable experiments focusing on the micro- and macro-scales using intracellular electrophysiology and imaging techniques such as PET scans (Bonhomme et al., 2001; Hentschke et al., 2005; Hirota et al., 1998). This inhibition was more pronounced for group 1 anaesthetics, both of which also decreased thalamocortical activity significantly more than their effects on direct cortical stimulations compared to ketamine. These findings implicate group 1 anaesthetics as having more prominent actions on extra-cortical mechanisms compared to ketamine, hinting at an important difference in the actions of these drugs which may underpin the dissociative nature of the subjective effects of the latter.

Individually, anaesthetics were found to uniformly inhibit cortical activity, while inducing much greater effects on that evoked in basal forebrain. Comparison of reported micro-scale kinetics of anaesthetics at their protein targets has implicated, in addition to the well-accepted $GABA_A$ and NMDARs, the potential involvement of nAChRs (for group 1 anaesthetics) and HCN channels (for ketamine) as key targets in the effects reported here.

The study of anaesthetic action is a fascinating one, which could benefit greatly from further attention, specifically in gaining better insights into meso-scale processes. GEVIs represent another recent development in the field (Akemann et al., 2010), which could be used in specific neuronal populations to selectively

monitor how anaesthetics selectively affect specific parts of complex neuronal networks (Knopfel, 2012). Such a strategy would allow for the investigation of yet more complex anaesthetic network effects, for example: gauging the occurrence of inhibition of inhibitory cells (Sporns et al., 2004) by anaesthetics, and if processes such as these are involved in the widely-reported anaesthetic-induced increases in cortical activity.

5.3 Final comments

During the course of my DPhil, I have had the privilege of first learning how to use, and then employing some of the most cutting edge research technology, i.e. VSDI, in the investigation of topics of great interest to current Neuroscience, i.e. characterisation of network dynamics and investigation of anaesthetic effect. Furthermore, such endeavour has not only allowed me to complete this doctorate, but also to work on other highly exciting projects, including screening for the bioactivity of drugs with high potential relevance to Alzheimer's disease and affiliated treatments (Badin et al., 2013, Badin et al., 2016), which allowed me to simultaneously apply my expertise to current challenges in fundamental medical research. This imposing project was at times testing and frustrating yet concurrently drove and maintained my love of Research and Neuroscience.

REFERENCES

Abeles, M. (1991). Corticonincs: Neural Circuits of the Cerebral Cortex. Cambridge University Press, New York, New York.

Achermann, P., and A.A. Borbely. (1997). Low-frequency (< 1 Hz) oscillations in the human sleep electroencephalogram. *Neuroscience*. 81:213-222.

Adrian, E.D., and B.H. Matthews. (1934). The interpretation of potential waves in the cortex. *The Journal of physiology*. 81:440-471.

Agmon, A., and B.W. Connors. (1991). Thalamocortical responses of mouse somatosensory (barrel) cortex in vitro. *Neuroscience*. 41:365-379.

Agnati, L.F., D. Guidolin, M. Guescini, S. Genedani, and K. Fuxe. (2010). Understanding wiring and volume transmission. *Brain research reviews*. 64:137-159.

Ahissar, E., R. Sosnik, and S. Haidarliu. (2000). Transformation from temporal to rate coding in a somatosensory thalamocortical pathway. *Nature*. 406:302-306.

Akemann, W., H. Mutoh, A. Perron, J. Rossier, and T. Knopfel. (2010). Imaging brain electric signals with genetically targeted voltage-sensitive fluorescent proteins. *Nature methods*. 7:643-649.

Alegre, M., A. Labarga, I.G. Gurtubay, J. Iriarte, A. Malanda, and J. Artieda. (2002). Beta electroencephalograph changes during passive movements: sensory afferences contribute to beta event-related desynchronization in humans. *Neurosci Lett*. 331:29-32.

Alexander, G.E., M.D. Crutcher, and M.R. DeLong. (1990). Basal ganglia-thalamocortical circuits: parallel substrates for motor, oculomotor, "prefrontal" and "limbic" functions. *Progress in brain research*. 85:119-146.

Alkire, M.T., and J. Miller. (2005). General anesthesia and the neural correlates of consciousness. *Progress in brain research*. 150:229-244.

Alloway, K.D. (2008). Information processing streams in rodent barrel cortex: the differential functions of barrel and septal circuits. *Cereb Cortex*. 18:979-989.

Amaral, D.G., and J. Kurz. (1985). An analysis of the origins of the cholinergic and noncholinergic septal projections to the hippocampal formation of the rat. *J Comp Neurol*. 240:37-59.

Anaclet, C., N.P. Pedersen, L.L. Ferrari, A. Venner, C.E. Bass, E. Arrigoni, and P.M. Fuller. (2015). Basal forebrain control of wakefulness and cortical rhythms. *Nature communications*. 6:8744.

Anderson, J.S., I. Lampl, D.C. Gillespie, and D. Ferster. (2000). The contribution of noise to contrast invariance of orientation tuning in cat visual cortex. *Science (New York, N.Y.* 290:1968-1972.

Anderson, R.E., and J.G. Jakobsson. (2004). Entropy of EEG during anaesthetic induction: a comparative study with propofol or nitrous oxide as sole agent. *Br J Anaesth*. 92:167-170.

Andreasen, N.C., D.S. O'Leary, M. Flaum, P. Nopoulos, G.L. Watkins, L.L. Boles Ponto, and R.D. Hichwa. (1997). Hypofrontality in schizophrenia: distributed dysfunctional circuits in neuroleptic-naive patients. *Lancet*. 349:1730-1734.

Angel, A. (1993). Central neuronal pathways and the process of anaesthesia. *Br J Anaesth*. 71:148-163.

Anis, N.A., S.C. Berry, N.R. Burton, and D. Lodge. (1983). The dissociative anaesthetics, ketamine and phencyclidine, selectively reduce excitation of central mammalian neurones by N-methyl-aspartate. *British journal of pharmacology*. 79:565-575.

Antic, S., L.B. Cohen, Y.W. Lam, M. Wachowiak, D. Zecevic, and M. Zochowski. (1999). Fast multisite optical measurement of membrane potential: three examples. *FASEB journal : official publication of the Federation of American Societies for Experimental Biology*. 13 Suppl 2:S271-276.

Antic, S.D., R.M. Empson, and T. Knopfel. (2016). Voltage imaging to understand connections and functions of neuronal circuits. *Journal of neurophysiology*. 116:135-152.
Antkowiak, B. (2002). In vitro networks: cortical mechanisms of anaesthetic action. *Br J Anaesth*. 89:102-111.
Arhem, P., G. Klement, and J. Nilsson. (2003). Mechanisms of anesthesia: towards integrating network, cellular, and molecular level modeling. *Neuropsychopharmacology : official publication of the American College of Neuropsychopharmacology*. 28 Suppl 1:S40-47.
Arieli, A., A. Sterkin, A. Grinvald, and A. Aertsen. (1996). Dynamics of ongoing activity: explanation of the large variability in evoked cortical responses. *Science (New York, N.Y.* 273:1868-1871.
Armstrong-James, M., K. Fox, and A. Das-Gupta. (1992). Flow of excitation within rat barrel cortex on striking a single vibrissa. *Journal of neurophysiology*. 68:1345-1358.
Armstrong, D.M., C.B. Saper, A.I. Levey, B.H. Wainer, and R.D. Terry. (1983). Distribution of cholinergic neurons in rat brain: demonstrated by the immunocytochemical localization of choline acetyltransferase. *J Comp Neurol*. 216:53-68.
Arnold, H.M., J. Fadel, M. Sarter, and J.P. Bruno. (2001). Amphetamine-stimulated cortical acetylcholine release: role of the basal forebrain. *Brain Res*. 894:74-87.
Augustine, G.J. (2001). How does calcium trigger neurotransmitter release? *Current opinion in neurobiology*. 11:320-326.
Avery, M.C., N. Dutt, and J.L. Krichmar. (2014). Mechanisms underlying the basal forebrain enhancement of top-down and bottom-up attention. *Eur J Neurosci*. 39:852-865.
Azouz, R., and C.M. Gray. (1999). Cellular mechanisms contributing to response variability of cortical neurons in vivo. *J Neurosci*. 19:2209-2223.
Badin, A.S., J. Eraifej, and S. Greenfield. (2013). High-resolution spatio-temporal bioactivity of a novel peptide revealed by optical imaging in rat orbitofrontal cortex in vitro: Possible implications for neurodegenerative diseases. *Neuropharmacology*. 73C:10-18.
Badin, A.S., F.M. Fermani, and S. Greenfield. (2017). The Features and Functions of Neuronal Assemblies: Possible Dependency on Mechanisms beyond Synaptic Transmission. *Front. Neural Circuits*. 10.
Badin, A.S., P. Morrill, I.M. Devonshire, and S.A. Greenfield. (2016). (II) Physiological profiling of an endogenous peptide in the basal forebrain: Age-related bioactivity and blockade with a novel modulator. *Neuropharmacology*. 105:47-60.
Badin, O. (2004). *Ketamine - CIT Project 2004*. [WEB] Accessed: 2 October 2016. http://www.ch.ic.ac.uk/local/projects/badin/index.html
Baker, S.N., N. Philbin, R. Spinks, E.M. Pinches, D.M. Wolpert, D.G. MacManus, Q. Pauluis, and R.N. Lemon. (1999). Multiple single unit recording in the cortex of monkeys using independently moveable microelectrodes. *Journal of neuroscience methods*. 94:5-17.
Bal, T., M. von Krosigk, and D.A. McCormick. (1995). Role of the ferret perigeniculate nucleus in the generation of synchronized oscillations in vitro. *The Journal of physiology*. 483 (Pt 3):665-685.
Bandyopadhyay, S., C. Gonzalez-Islas, and J.J. Hablitz. (2005). Dopamine enhances spatiotemporal spread of activity in rat prefrontal cortex. *Journal of neurophysiology*. 93:864-872.
Bandyopadhyay, S., and J.J. Hablitz. (2007). Dopaminergic modulation of local network activity in rat prefrontal cortex. *Journal of neurophysiology*. 97:4120-4128.
Bane, V., M. Lehane, M. Dikshit, A. O'Riordan, and A. Furey. (2014). Tetrodotoxin: chemistry, toxicity, source, distribution and detection. *Toxins*. 6:693-755.
Baranauskas, G., T. Tkatch, K. Nagata, J.Z. Yeh, and D.J. Surmeier. (2003). Kv3.4 subunits enhance the repolarizing efficiency of Kv3.1 channels in fast-spiking neurons. *Nature neuroscience*. 6:258-266.
Barann, M., J.P. Dilger, H. Bonisch, M. Gothert, A. Dybek, and B.W. Urban. (2000). Inhibition of 5-HT3 receptors by propofol: equilibrium and kinetic measurements. *Neuropharmacology*. 39:1064-1074.
Barann, M., M. Gothert, H. Bonisch, A. Dybek, and B.W. Urban. (1997). 5-HT3 receptors in outside-out patches of N1E-115 neuroblastoma cells: basic properties and effects of pentobarbital. *Neuropharmacology*. 36:655-664.

Barnard, E.A., P. Skolnick, R.W. Olsen, H. Mohler, W. Sieghart, G. Biggio, C. Braestrup, A.N. Bateson, and S.Z. Langer. (1998). International Union of Pharmacology. XV. Subtypes of gamma-aminobutyric acidA receptors: classification on the basis of subunit structure and receptor function. *Pharmacological reviews*. 50:291-313.

Barth, A.L., and J.F. Poulet. (2012). Experimental evidence for sparse firing in the neocortex. *Trends in neurosciences*. 35:345-355.

Bashford, C.L. (1981). The measurement of membrane potential using optical indicators. *Bioscience reports*. 1:183-196.

Beaudet, A., and L. Descarries. (1978). The monoamine innervation of rat cerebral cortex: synaptic and nonsynaptic axon terminals. *Neuroscience*. 3:851-860.

Bechara, A., H. Damasio, and A.R. Damasio. (2000). Emotion, decision making and the orbitofrontal cortex. *Cereb Cortex*. 10:295-307.

Beckstead, R.M. (1979). An autoradiographic examination of corticocortical and subcortical projections of the mediodorsal-projection (prefrontal) cortex in the rat. *J Comp Neurol*. 184:43-62.

Belelli, D., M. Pistis, J.A. Peters, and J.J. Lambert. (1999). General anaesthetic action at transmitter-gated inhibitory amino acid receptors. *Trends in pharmacological sciences*. 20:496-502.

Ben-Ari, Y., E. Cherubini, R. Corradetti, and J.L. Gaiarsa. (1989). Giant synaptic potentials in immature rat CA3 hippocampal neurones. *The Journal of physiology*. 416:303-325.

Berens, P., G.A. Keliris, A.S. Ecker, N.K. Logothetis, and A.S. Tolias. (2008). Comparing the feature selectivity of the gamma-band of the local field potential and the underlying spiking activity in primate visual cortex. *Frontiers in systems neuroscience*. 2:2.

Berger, B., J.P. Tassin, G. Blanc, M.A. Moyne, and A.M. Thierry. (1974). Histochemical confirmation for dopaminergic innervation of the rat cerebral cortex after destruction of the noradrenergic ascending pathways. *Brain Res*. 81:332-337.

Berger, T., A. Borgdorff, S. Crochet, F.B. Neubauer, S. Lefort, B. Fauvet, I. Ferezou, A. Carleton, H.R. Luscher, and C.C. Petersen. (2007). Combined voltage and calcium epifluorescence imaging in vitro and in vivo reveals subthreshold and suprathreshold dynamics of mouse barrel cortex. *Journal of neurophysiology*. 97:3751-3762.

Bernasconi, C., A. von Stein, C. Chiang, and P. Konig. (2000). Bi-directional interactions between visual areas in the awake behaving cat. *Neuroreport*. 11:689-692.

Berridge, M.J. (1998). Neuronal calcium signaling. *Neuron*. 21:13-26.

Berridge, M.J., P. Lipp, and M.D. Bootman. (2000). The versatility and universality of calcium signalling. *Nature reviews. Molecular cell biology*. 1:11-21.

Berton, O., and E.J. Nestler. (2006). New approaches to antidepressant drug discovery: beyond monoamines. *Nature reviews. Neuroscience*. 7:137-151.

Beul, S.F., and C.C. Hilgetag. (2014). Towards a "canonical" agranular cortical microcircuit. *Frontiers in neuroanatomy*. 8:165.

Bianchi, M.T., E.J. Botzolakis, A.H. Lagrange, and R.L. Macdonald. (2009). Benzodiazepine modulation of GABA(A) receptor opening frequency depends on activation context: a patch clamp and simulation study. *Epilepsy research*. 85:212-220.

Bieda, M.C., and M.B. MacIver. (2004). Major role for tonic GABAA conductances in anesthetic suppression of intrinsic neuronal excitability. *Journal of neurophysiology*. 92:1658-1667.

Biel, M. (2009). Cyclic nucleotide-regulated cation channels. *J Biol Chem*. 284:9017-9021.

Blumenfeld, H. (2005). Cellular and network mechanisms of spike-wave seizures. *Epilepsia*. 46 Suppl 9:21-33.

Bolz, J., and C.D. Gilbert. (1986). Generation of end-inhibition in the visual cortex via interlaminar connections. *Nature*. 320:362-365.

Bonhomme, V., P. Fiset, P. Meuret, S. Backman, G. Plourde, T. Paus, M.C. Bushnell, and A.C. Evans. (2001). Propofol anesthesia and cerebral blood flow changes elicited by vibrotactile stimulation: a positron emission tomography study. *Journal of neurophysiology*. 85:1299-1308.

Bootman, M.D., M.J. Berridge, and H.L. Roderick. (2002). Calcium signalling: more messengers, more channels, more complexity. *Current biology : CB*. 12:R563-565.

Borst, J.G., F. Helmchen, and B. Sakmann. (1995). Pre- and postsynaptic whole-cell recordings in the medial nucleus of the trapezoid body of the rat. *The Journal of physiology*. 489 (Pt 3):825-840.
Bosboom, J.L., D. Stoffers, C.J. Stam, B.W. van Dijk, J. Verbunt, H.W. Berendse, and E. Wolters. (2006). Resting state oscillatory brain dynamics in Parkinson's disease: an MEG study. *Clin Neurophysiol*. 117:2521-2531.
Bostock, H., T.A. Sears, and R.M. Sherratt. (1983). The spatial distribution of excitability and membrane current in normal and demyelinated mammalian nerve fibres. *The Journal of physiology*. 341:41-58.
Bourgeois, E.B., B.N. Johnson, A.J. McCoy, L. Trippa, A.S. Cohen, and E.D. Marsh. (2014). A toolbox for spatiotemporal analysis of voltage-sensitive dye imaging data in brain slices. *PLoS One*. 9:e108686.
Bradley, P.B., and A. Dray. (1973). Modification of the responses of brain stem neurones to transmitter substances by anaesthetic agents. *British journal of pharmacology*. 48:212-224.
Brashear, H.R., L. Zaborszky, and L. Heimer. (1986). Distribution of GABAergic and cholinergic neurons in the rat diagonal band. *Neuroscience*. 17:439-451.
Brecht, M. (2007). Barrel cortex and whisker-mediated behaviors. *Current opinion in neurobiology*. 17:408-416.
Brecht, M., A. Roth, and B. Sakmann. (2003). Dynamic receptive fields of reconstructed pyramidal cells in layers 3 and 2 of rat somatosensory barrel cortex. *The Journal of physiology*. 553:243-265.
Bressler, S.L., and J.A. Kelso. (2001). Cortical coordination dynamics and cognition. *Trends in cognitive sciences*. 5:26-36.
Brown, E.N., R. Lydic, and N.D. Schiff. (2010). General anesthesia, sleep, and coma. *N Engl J Med*. 363:2638-2650.
Brown, R.M., A.M. Crane, and P.S. Goldman. (1979). Regional distribution of monoamines in the cerebral cortex and subcortical structures of the rhesus monkey: concentrations and in vivo synthesis rates. *Brain Res*. 168:133-150.
Brown, S.P., and S. Hestrin. (2009). Cell-type identity: a key to unlocking the function of neocortical circuits. *Current opinion in neurobiology*. 19:415-421.
Brown, W.J. (1993). Short communication: The maintenance of a scale of illuminance with quartz halogen tungsten filament lamps. *Metrologia*. 30.
Brumberg, J.C., D.J. Pinto, and D.J. Simons. (1999). Cortical columnar processing in the rat whisker-to-barrel system. *Journal of neurophysiology*. 82:1808-1817.
Bruno, R.M., and B. Sakmann. (2006). Cortex is driven by weak but synchronously active thalamocortical synapses. *Science (New York, N.Y.*. 312:1622-1627.
Brunori, M., B. Vallone, F. Cutruzzola, C. Travaglini-Allocatelli, J. Berendzen, K. Chu, R.M. Sweet, and I. Schlichting. (2000). The role of cavities in protein dynamics: crystal structure of a photolytic intermediate of a mutant myoglobin. *Proc Natl Acad Sci U S A*. 97:2058-2063.
Bryan, A., C.J.D. Pomfrett, J. Davidson, B.J. Pollard, T. Quraishi, P. Wright, R. Robinson, S.T. Ahsan, and H. McCann. (2011). Functional electrical impedance tomography by evoked response: a new device for the study of human brain function during anaesthesia. *Brit J Anaesth*. 106:428p-429p.
Bullock, T.H., and G.A. Horridge. (1965). Structure and Function in the Nervous Systems of Invertebrates. WH Freeman, San Francisco.
Burkey, A.R., E. Carstens, and L. Jasmin. (1999). Dopamine reuptake inhibition in the rostral agranular insular cortex produces antinociception. *J Neurosci*. 19:4169-4179.
Burns, S.P., D. Xing, and R.M. Shapley. (2010). Comparisons of the dynamics of local field potential and multiunit activity signals in macaque visual cortex. *J Neurosci*. 30:13739-13749.
Buzsaki, G., C.A. Anastassiou, and C. Koch. (2012). The origin of extracellular fields and currents--EEG, ECoG, LFP and spikes. *Nature reviews. Neuroscience*. 13:407-420.
Buzsaki, G., and A. Draguhn. (2004). Neuronal oscillations in cortical networks. *Science (New York, N.Y.* 304:1926-1929.
Campagna, J.A., K.W. Miller, and S.A. Forman. (2003). Mechanisms of actions of inhaled anesthetics. *N Engl J Med*. 348:2110-2124.

Carrillo-Reid, L., J.E. Miller, J.P. Hamm, J. Jackson, and R. Yuste. (2015). Endogenous sequential cortical activity evoked by visual stimuli. *J Neurosci*. 35:8813-8828.
Carter, S. (1951). Use of Anticonvulsant Drugs. *GP*. 4:41-46.
Catterall, W.A. (2011). Voltage-gated calcium channels. *Cold Spring Harbor perspectives in biology*. 3:a003947.
Cauller, L.J., and B.W. Connors. (1994). Synaptic physiology of horizontal afferents to layer I in slices of rat SI neocortex. *J Neurosci*. 14:751-762.
Cechetto, D.F., and S.J. Chen. (1990). Subcortical sites mediating sympathetic responses from insular cortex in rats. *Am J Physiol*. 258:R245-255.
Chagnac-Amitai, Y., and B.W. Connors. (1989). Horizontal spread of synchronized activity in neocortex and its control by GABA-mediated inhibition. *Journal of neurophysiology*. 61:747-758.
Chakraborty, S., A. Sandberg, and S.A. Greenfield. (2007). Differential dynamics of transient neuronal assemblies in visual compared to auditory cortex. *Exp Brain Res*. 182:491-498.
Chan-Palay, V., W. Lang, U. Haesler, C. Kohler, and G. Yasargil. (1986). Distribution of altered hippocampal neurons and axons immunoreactive with antisera against neuropeptide Y in Alzheimer's-type dementia. *J Comp Neurol*. 248:376-394.
Chawla, D., E.D. Lumer, and K.J. Friston. (1999). The relationship between synchronization among neuronal populations and their mean activity levels. *Neural Comput*. 11:1389-1411.
Chemla, S., and F. Chavane. (2010). Voltage-sensitive dye imaging: Technique review and models. *Journal of physiology, Paris*. 104:40-50.
Chemla, S., and W.K. Witharana. (2016). Spatiotemporal after-effects of transcranial direct current stimulation on sensory-evoked activity in rat S1: A pilot VSDI study. *J Curr. Neurobiol.* 7:30-35.
Chen, X., S. Shu, and D.A. Bayliss. (2009). HCN1 channel subunits are a molecular substrate for hypnotic actions of ketamine. *J Neurosci*. 29:600-609.
Chen, Y., C.R. Palmer, and E. Seidemann. (2012). The relationship between voltage-sensitive dye imaging signals and spiking activity of neural populations in primate V1. *Journal of neurophysiology*. 107:3281-3295.
Chmielowska, J., G.E. Carvell, and D.J. Simons. (1989). Spatial organization of thalamocortical and corticothalamic projection systems in the rat SmI barrel cortex. *J Comp Neurol*. 285:325-338.
Chung, S.K., P.H. Reinhart, B.L. Martin, D. Brautigan, and I.B. Levitan. (1991). Protein kinase activity closely associated with a reconstituted calcium-activated potassium channel. *Science (New York, N.Y.* 253:560-562.
Clark, D.L., and B.S. Rosner. (1973). Neurophysiologic effects of general anesthetics. I. The electroencephalogram and sensory evoked responses in man. *Anesthesiology*. 38:564-582.
Cobb, M. (2002). Timeline: exorcizing the animal spirits: Jan Swammerdam on nerve function. *Nature reviews. Neuroscience*. 3:395-400.
Coburn, B. (1989). Neural modeling in electrical stimulation. *Critical reviews in biomedical engineering*. 17:133-178.
Cohen, L.B., and S. Lesher. (1986). Optical monitoring of membrane potential: methods of multisite optical measurement. *Society of General Physiologists series*. 40:71-99.
Cohen, L.B., and B.M. Salzberg. (1978). Optical measurement of membrane potential. *Reviews of physiology, biochemistry and pharmacology*. 83:35-88.
Collins, T.F., E.O. Mann, M.R. Hill, E.J. Dommett, and S.A. Greenfield. (2007a). Dynamics of neuronal assemblies are modulated by anaesthetics but not analgesics. *Eur J Anaesthesiol*. 24:609-614.
Collins, T.F.T., E.O. Mann, M.R.H. Hill, E.J. Dommett, and S.A. Greenfield. (2007b). Dynamics of neuronal assemblies are modulated by anaesthetics but not analgesics. *Eur J Anaesth*. 24:609-614.
Colquhoun, D., and L.G. Sivilotti. (2004). Function and structure in glycine receptors and some of their relatives. *Trends in neurosciences*. 27:337-344.
Connors, B.W., M.J. Gutnick, and D.A. Prince. (1982). Electrophysiological properties of neocortical neurons in vitro. *Journal of neurophysiology*. 48:1302-1320.

Constantinople, C.M., and R.M. Bruno. (2013). Deep cortical layers are activated directly by thalamus. *Science (New York, N.Y.* 340:1591-1594.
Contreras, D., and R. Llinas. (2001). Voltage-sensitive dye imaging of neocortical spatiotemporal dynamics to afferent activation frequency. *J Neurosci*. 21:9403-9413.
Coyle, J.T., D.L. Price, and M.R. DeLong. (1983). Alzheimer's disease: a disorder of cortical cholinergic innervation. *Science (New York, N.Y.* 219:1184-1190.
Cruikshank, S.J., H. Urabe, A.V. Nurmikko, and B.W. Connors. (2010). Pathway-specific feedforward circuits between thalamus and neocortex revealed by selective optical stimulation of axons. *Neuron*. 65:230-245.
Crunelli, V., and S.W. Hughes. (2010). The slow (<1 Hz) rhythm of non-REM sleep: a dialogue between three cardinal oscillators. *Nature neuroscience*. 13:9-17.
Cull-Candy, S., S. Brickley, and M. Farrant. (2001). NMDA receptor subunits: diversity, development and disease. *Current opinion in neurobiology*. 11:327-335.
Cullinan, W.E., and L. Zaborszky. (1991). Organization of ascending hypothalamic projections to the rostral forebrain with special reference to the innervation of cholinergic projection neurons. *J Comp Neurol*. 306:631-667.
de Deyne, C., M. Struys, J. Decruyenaere, J. Creupelandt, and F. Colardyn. (1998). Use of continuous bispectral EEG monitoring to assess depth of sedation in ICU patients. *Intensive care medicine*. 24:1294.
Defelipe, J. (2011). The evolution of the brain, the human nature of cortical circuits, and intellectual creativity. *Frontiers in neuroanatomy*. 5:29.
DeFelipe, J., L. Alonso-Nanclares, and J.I. Arellano. (2002). Microstructure of the neocortex: comparative aspects. *J Neurocytol*. 31:299-316.
DeFelipe, J., I. Ballesteros-Yanez, M.C. Inda, and A. Munoz. (2006). Double-bouquet cells in the monkey and human cerebral cortex with special reference to areas 17 and 18. *Progress in brain research*. 154:15-32.
Dehaene, S., and J.-P. Changeux. (2003). Neural mechanisms for access to consciousness. *Journal of cognitive neuroscience*. 12:432-443.
Denk, W., J.H. Strickler, and W.W. Webb. (1990). Two-photon laser scanning fluorescence microscopy. *Science (New York, N.Y.* 248:73-76.
Derdikman, D., R. Hildesheim, E. Ahissar, A. Arieli, and A. Grinvald. (2003). Imaging spatiotemporal dynamics of surround inhibition in the barrels somatosensory cortex. *J Neurosci*. 23:3100-3105.
Descarries, L., and N. Mechawar. (2000). Ultrastructural evidence for diffuse transmission by monoamine and acetylcholine neurons of the central nervous system. *Progress in brain research*. 125:27-47.
Descarries, L., K.C. Watkins, and Y. Lapierre. (1977). Noradrenergic axon terminals in the cerebral cortex of rat. III. Topometric ultrastructural analysis. *Brain Res*. 133:197-222.
Deschenes, M., P. Veinante, and Z.W. Zhang. (1998). The organization of corticothalamic projections: reciprocity versus parity. *Brain research. Brain research reviews*. 28:286-308.
Devonshire, I.M., E.J. Dommett, T.H. Grandy, A.C. Halliday, and S.A. Greenfield. (2010a). Environmental enrichment differentially modifies specific components of sensory-evoked activity in rat barrel cortex as revealed by simultaneous electrophysiological recordings and optical imaging in vivo. *Neuroscience*. 170:662-669.
Devonshire, I.M., T.H. Grandy, E.J. Dommett, and S.A. Greenfield. (2010b). Effects of urethane anaesthesia on sensory processing in the rat barrel cortex revealed by combined optical imaging and electrophysiology. *Eur J Neurosci*. 32:786-797.
Devonshire, I.M., J.E. Mayhew, and P.G. Overton. (2007). Cocaine preferentially enhances sensory processing in the upper layers of the primary sensory cortex. *Neuroscience*. 146:841-851.
Di Lazzaro, V., A. Oliviero, P. Profice, M.A. Pennisi, F. Pilato, G. Zito, M. Dileone, R. Nicoletti, P. Pasqualetti, and P.A. Tonali. (2003). Ketamine increases human motor cortex excitability to transcranial magnetic stimulation. *The Journal of physiology*. 547:485-496.
Di, S., C. Baumgartner, and D.S. Barth. (1990). Laminar analysis of extracellular field potentials in rat vibrissa/barrel cortex. *Journal of neurophysiology*. 63:832-840.

Diamond, M.E., M. Armstrong-James, and F.F. Ebner. (1992). Somatic sensory responses in the rostral sector of the posterior group (POm) and in the ventral posterior medial nucleus (VPM) of the rat thalamus. *J Comp Neurol*. 318:462-476.

Dilger, J.P., R. Boguslavsky, M. Barann, T. Katz, and A.M. Vidal. (1997). Mechanisms of barbiturate inhibition of acetylcholine receptor channels. *The Journal of general physiology*. 109:401-414.

Dingledine, R. (2013). Brain slices. Springer Science & Business Media.

Dinstein, I., K. Pierce, L. Eyler, S. Solso, R. Malach, M. Behrmann, and E. Courchesne. (2011). Disrupted neural synchronization in toddlers with autism. *Neuron*. 70:1218-1225.

Divac, I. (1975). Magnocellular nuclei of the basal forebrain project to neocortex, brain stem, and olfactory bulb. Review of some functional correlates. *Brain Res*. 93:385-398.

Dodson, B.A., and J. Moss. (1984). Molecular mechanisms of action of general anesthetics. *Molecular and cellular biochemistry*. 64:97-103.

Donchin, E., and D.B. Smith. (1970). The contingent negative variation and the late positive wave of the average evoked potential. *Electroencephalography and clinical neurophysiology*. 29:201-203.

Douglas, R.J., C. Koch, M. Mahowald, K.A. Martin, and H.H. Suarez. (1995). Recurrent excitation in neocortical circuits. *Science (New York, N.Y.* 269:981-985.

Douglas, R.J., and K.A. Martin. (1991). A functional microcircuit for cat visual cortex. *The Journal of physiology*. 440:735-769.

Douglas, R.J., and K.A. Martin. (2004). Neuronal circuits of the neocortex. *Annual review of neuroscience*. 27:419-451.

Dreher, M.R., W. Liu, C.R. Michelich, M.W. Dewhirst, F. Yuan, and A. Chilkoti. (2006). Tumor vascular permeability, accumulation, and penetration of macromolecular drug carriers. *Journal of the National Cancer Institute*. 98:335-344.

Druga, R. (2009). Neocortical inhibitory system. *Folia biologica*. 55:201-217.

Ebert, B., S. Mikkelsen, C. Thorkildsen, and F.M. Borgbjerg. (1997). Norketamine, the main metabolite of ketamine, is a non-competitive NMDA receptor antagonist in the rat cortex and spinal cord. *European journal of pharmacology*. 333:99-104.

Ebner, T.J., and G. Chen. (1995). Use of voltage-sensitive dyes and optical recordings in the central nervous system. *Progress in neurobiology*. 46:463-506.

Egger, V., T. Nevian, and R.M. Bruno. (2008). Subcolumnar dendritic and axonal organization of spiny stellate and star pyramid neurons within a barrel in rat somatosensory cortex. *Cereb Cortex*. 18:876-889.

Eghbali, M., J.P. Curmi, B. Birnir, and P.W. Gage. (1997). Hippocampal GABA(A) channel conductance increased by diazepam. *Nature*. 388:71-75.

Elliott, R., R.J. Dolan, and C.D. Frith. (2000). Dissociable functions in the medial and lateral orbitofrontal cortex: evidence from human neuroimaging studies. *Cereb Cortex*. 10:308-317.

Emson, P.C., G. Paxinos, G. Le Gal La Salle, Y. Ben-Ari, and A. Silver. (1978). Choline acetyltransferase and acetylcholinesterase containing projectionsfrom the basal forebrain to the amygdaloid complex of the rat. *Brain. Res.* 165:271-285.

Engel, A.K., and W. Singer. (2001). Temporal binding and the neural correlates of sensory awareness. *Trends in cognitive sciences*. 5:16-25.

Enyedi, P., and G. Czirjak. (2010). Molecular background of leak K+ currents: two-pore domain potassium channels. *Physiological reviews*. 90:559-605.

Favorov, O.V., and M.E. Diamond. (1990). Demonstration of discrete place-defined columns--segregates--in the cat SI. *J Comp Neurol*. 298:97-112.

Fehervari, T.D., Y. Okazaki, H. Sawai, and T. Yagi. (2015). In Vivo Voltage-Sensitive Dye Study of Lateral Spreading of Cortical Activity in Mouse Primary Visual Cortex Induced by a Current Impulse. *PLoS One*. 10:e0133853.

Feldmeyer, D. (2012). Excitatory neuronal connectivity in the barrel cortex. *Frontiers in neuroanatomy*. 6:24.

Feldmeyer, D., J. Lubke, and B. Sakmann. (2006). Efficacy and connectivity of intracolumnar pairs of layer 2/3 pyramidal cells in the barrel cortex of juvenile rats. *The Journal of physiology*. 575:583-602.

Fengler, B.T. (2008). Should etomidate be used for rapid-sequence intubation induction in critically ill septic patients? *The American journal of emergency medicine*. 26:229-232.
Ferezou, I., S. Bolea, and C.C. Petersen. (2006). Visualizing the cortical representation of whisker touch: voltage-sensitive dye imaging in freely moving mice. *Neuron*. 50:617-629.
Ferrarelli, F., M. Massimini, S. Sarasso, A. Casali, B.A. Riedner, G. Angelini, G. Tononi, and R.A. Pearce. (2010). Breakdown in cortical effective connectivity during midazolam-induced loss of consciousness. *Proc Natl Acad Sci U S A*. 107:2681-2686.
Filion, M., and L. Tremblay. (1991). Abnormal spontaneous activity of globus pallidus neurons in monkeys with MPTP-induced parkinsonism. *Brain Res*. 547:142-151.
Fitzpatrick, D. (1996). The functional organization of local circuits in visual cortex: insights from the study of tree shrew striate cortex. *Cereb Cortex*. 6:329-341.
Flood, P., and M.D. Krasowski. (2000). Intravenous anesthetics differentially modulate ligand-gated ion channels. *Anesthesiology*. 92:1418-1425.
Fluhler, E., V.G. Burnham, and L.M. Loew. (1985). Spectra, membrane binding, and potentiometric responses of new charge shift probes. *Biochemistry*. 24:5749-5755.
Foote, S.L., and J.H. Morrison. (1987). Extrathalamic modulation of cortical function. *Annual review of neuroscience*. 10:67-95.
Forman, S.A., D.C. Chiara, and K.W. Miller. (2015). Anesthetics target interfacial transmembrane sites in nicotinic acetylcholine receptors. *Neuropharmacology*. 96:169-177.
Forman, S.A., and K.W. Miller. (2011). Anesthetic sites and allosteric mechanisms of action on Cys-loop ligand-gated ion channels. *Canadian journal of anaesthesia = Journal canadien d'anesthesie*. 58:191-205.
Fox, M.D., A.Z. Snyder, J.L. Vincent, M. Corbetta, D.C. Van Essen, and M.E. Raichle. (2005). The human brain is intrinsically organized into dynamic, anticorrelated functional networks. *Proc Natl Acad Sci U S A*. 102:9673-9678.
Franks, N.P. (2008). General anaesthesia: from molecular targets to neuronal pathways of sleep and arousal. *Nature reviews. Neuroscience*. 9:370-386.
Franks, N.P., and W.R. Lieb. (1984). Do general anaesthetics act by competitive binding to specific receptors? *Nature*. 310:599-601.
Freeman, W.J. (2000). Neurodynamics: An Exploration in Mesoscopic Brain Dynamics. Springer-Verlag, London, Great Britain. 399 pp.
Frenkel, C., D.S. Duch, and B.W. Urban. (1990). Molecular actions of pentobarbital isomers on sodium channels from human brain cortex. *Anesthesiology*. 72:640-649.
Freund, T.F., and I. Katona. (2007). Perisomatic inhibition. *Neuron*. 56:33-42.
Freund, T.F., and V. Meskenaite. (1992). gamma-Aminobutyric acid-containing basal forebrain neurons innervate inhibitory interneurons in the neocortex. *Proc Natl Acad Sci U S A*. 89:738-742.
Friederich, P., and B.W. Urban. (1999). Interaction of intravenous anesthetics with human neuronal potassium currents in relation to clinical concentrations. *Anesthesiology*. 91:1853-1860.
Frostig, R.D., C.H. Chen-Bee, B.A. Johnson, and N.S. Jacobs. (2017). Imaging Cajal's neuronal avalanche: how wide-field optical imaging of the point-spread advanced the understanding of neocortical structure-function relationship. *Neurophotonics*. 4:031217.
Fukuda, M., Y. Hata, M. Ohshima, and T. Tsumoto. (1998). Role of NMDA receptors in the propagation of excitation in rat visual cortex as studied by optical imaging. *Neuroscience research*. 31:9-21.
Furukawa, H., S.K. Singh, R. Mancusso, and E. Gouaux. (2005). Subunit arrangement and function in NMDA receptors. *Nature*. 438:185-192.
Furuta, T., T. Kaneko, and M. Deschenes. (2009). Septal neurons in barrel cortex derive their receptive field input from the lemniscal pathway. *J Neurosci*. 29:4089-4095.
Fuxe, K., A.B. Dahlstrom, G. Jonsson, D. Marcellino, M. Guescini, M. Dam, P. Manger, and L. Agnati. (2010). The discovery of central monoamine neurons gave volume transmission to the wired brain. *Progress in neurobiology*. 90:82-100.

Gabbott, P.L., and S.J. Bacon. (1996). Local circuit neurons in the medial prefrontal cortex (areas 24a,b,c, 25 and 32) in the monkey: I. Cell morphology and morphometrics. *J Comp Neurol*. 364:567-608.

Gabbott, P.L., T.A. Warner, P.R. Jays, P. Salway, and S.J. Busby. (2005). Prefrontal cortex in the rat: projections to subcortical autonomic, motor, and limbic centers. *J Comp Neurol*. 492:145-177.

Gage, P.W., and B. Robertson. (1985). Prolongation of inhibitory postsynaptic currents by pentobarbitone, halothane and ketamine in CA1 pyramidal cells in rat hippocampus. *British journal of pharmacology*. 85:675-681.

Galarreta, M., and S. Hestrin. (2001). Spike transmission and synchrony detection in networks of GABAergic interneurons. *Science (New York, N.Y.* 292:2295-2299.

Gandolfi, D., J. Mapelli, and E. D'Angelo. (2015). Long-Term Spatiotemporal Reconfiguration of Neuronal Activity Revealed by Voltage-Sensitive Dye Imaging in the Cerebellar Granular Layer. *Neural plasticity*. 2015:284986.

Ganguly, R., and D. Guha. (2008). Alteration of brain monoamines & EEG wave pattern in rat model of Alzheimer's disease & protection by Moringa oleifera. *The Indian journal of medical research*. 128:744-751.

Garcia, P.S., S.E. Kolesky, and A. Jenkins. (2010). General anesthetic actions on GABA(A) receptors. *Current neuropharmacology*. 8:2-9.

Garthwaite, J., E. Southam, and M. Anderton. (1989). A kainate receptor linked to nitric oxide synthesis from arginine. *J Neurochem*. 53:1952-1954.

Gaykema, R.P., and L. Zaborszky. (1996). Direct catecholaminergic-cholinergic interactions in the basal forebrain. II. Substantia nigra-ventral tegmental area projections to cholinergic neurons. *J Comp Neurol*. 374:555-577.

Gelperin, A., L.D. Rhines, J. Flores, and D.W. Tank. (1993). Coherent network oscillations by olfactory interneurons: modulation by endogenous amines. *Journal of neurophysiology*. 69:1930-1939.

Gelperin, A., and D.W. Tank. (1990). Odour-modulated collective network oscillations of olfactory interneurons in a terrestrial mollusc. *Nature*. 345:437-440.

Gerard, R.W. (1931). Nerve Conduction in Relation to Nerve Structure. *In* The Quarterly Review of Biology. Vol. 6. University of Chicago Press, Department of Physiology, University of Chicago. 59-83.

Gerfen, C.R., and R.M. Clavier. (1979). Neural inputs to the prefrontal agranular insular cortex in the rat: horseradish peroxidase study. *Brain research bulletin*. 4:347-353.

Gerstner, W., and W. Kistler. (2002). Spiking Neuron Models. Cambridge University Press, Cambridge.

Gharachorloo, N., and S. Gupta. (1989). A characterisation of ten rasterisation techniques. *Computer Graphics*. 23:355-368.

Gibbs, J.W., 3rd, Y.F. Zhang, M.D. Shumate, and D.A. Coulter. (2000). Regionally selective blockade of GABAergic inhibition by zinc in the thalamocortical system: functional significance. *Journal of neurophysiology*. 83:1510-1521.

Gilbert, C.D. (1992). Horizontal integration and cortical dynamics. *Neuron*. 9:1-13.

Gilbert, C.D., and T.N. Wiesel. (1989). Columnar specificity of intrinsic horizontal and corticocortical connections in cat visual cortex. *J Neurosci*. 9:2432-2442.

Gobel, W., and F. Helmchen. (2007). In vivo calcium imaging of neural network function. *Physiology*. 22:358-365.

Golomb, D., and Y. Amitai. (1997). Propagating neuronal discharges in neocortical slices: computational and experimental study. *Journal of neurophysiology*. 78:1199-1211.

Gomez, R.S., C. Guatimosim, and M.V. Gomez. (2003). Mechanism of Action of Volatile Anesthetics: Role of Protein Kinase C. *Cellular and Molecular Neurobiology*. 23:877-885.

Goodin, D.S. (1990). Clinical utility of long latency 'cognitive' event-related potentials (P3): the pros. *Electroencephalography and clinical neurophysiology*. 76:2-5; discussion 1.

Gottlieb, J.P., and A. Keller. (1997). Intrinsic circuitry and physiological properties of pyramidal neurons in rat barrel cortex. *Exp Brain Res*. 115:47-60.

Grandy, T.H., S.A. Greenfield, and I.M. Devonshire. (2012). An evaluation of in vivo voltage-sensitive dyes: pharmacological side effects and signal-to-noise ratios after effective removal of brain-pulsation artifacts. *Journal of neurophysiology*. 108:2931-2945.

Grasshoff, C., U. Rudolph, and B. Antkowiak. (2005). Molecular and systemic mechanisms of general anaesthesia: the 'multi-site and multiple mechanisms' concept. *Current opinion in anaesthesiology*. 18:386-391.

Gray, C.M. (1994). Synchronous oscillations in neuronal systems: mechanisms and functions. *Journal of computational neuroscience*. 1:11-38.

Gray, C.M., and D.A. McCormick. (1996). Chattering cells: superficial pyramidal neurons contributing to the generation of synchronous oscillations in the visual cortex. *Science (New York, N.Y.* 274:109-113.

Gray, C.M., and W. Singer. (1989). Stimulus-specific neuronal oscillations in orientation columns of cat visual cortex. *Proc Natl Acad Sci U S A*. 86:1698-1702.

Greenberg, D.S., A.R. Houweling, and J.N. Kerr. (2008). Population imaging of ongoing neuronal activity in the visual cortex of awake rats. *Nature neuroscience*. 11:749-751.

Greenfield, S.A., and T.F. Collins. (2005). A neuroscientific approach to consciousness. *Progress in brain research*. 150:11-23.

Greicius, M. (2008). Resting-state functional connectivity in neuropsychiatric disorders. *Current opinion in neurology*. 21:424-430.

Grinvald, A., L.B. Cohen, S. Lesher, and M.B. Boyle. (1981). Simultaneous optical monitoring of activity of many neurons in invertebrate ganglia using a 124-element photodiode array. *Journal of neurophysiology*. 45:829-840.

Grinvald, A., R.D. Frostig, E. Lieke, and R. Hildesheim. (1988). Optical imaging of neuronal activity. *Physiological reviews*. 68:1285-1366.

Grinvald, A., and R. Hildesheim. (2004). VSDI: a new era in functional imaging of cortical dynamics. *Nature reviews. Neuroscience*. 5:874-885.

Grinvald, A., A. Manker, and M. Segal. (1982). Visualization of the spread of electrical activity in rat hippocampal slices by voltage-sensitive optical probes. *The Journal of physiology*. 333:269-291.

Grinvald, A., B.M. Salzberg, and L.B. Cohen. (1977). Simultaneous recording from several neurones in an invertebrate central nervous system. *Nature*. 268:140-142.

Gritti, I., L. Mainville, M. Mancia, and B.E. Jones. (1997). GABAergic and other noncholinergic basal forebrain neurons, together with cholinergic neurons, project to the mesocortex and isocortex in the rat. *J Comp Neurol*. 383:163-177.

Gruter, T., V. Wiescholleck, V. Dubovyk, V. Aliane, and D. Manahan-Vaughan. (2015). Altered neuronal excitability underlies impaired hippocampal function in an animal model of psychosis. *Frontiers in behavioral neuroscience*. 9:117.

Gupta, A., Y. Wang, and H. Markram. (2000). Organizing principles for a diversity of GABAergic interneurons and synapses in the neocortex. *Science (New York, N.Y.* 287:273-278.

Gustafsson, F. (1996). Determining the initial states in forward-backward filtering. *IEEE Trans Sig Proc*. 44:988-992.

Haberly, L.B., and J.L. Price. (1978). Association and commissural fiber systems of the olfactory cortex of the rat. II. Systems originating in the olfactory peduncle. *J Comp Neurol*. 181:781-807.

Haidarliu, S., and E. Ahissar. (2001). Size gradients of barreloids in the rat thalamus. *J Comp Neurol*. 429:372-387.

Hallanger, A.E., A.I. Levey, H.J. Lee, D.B. Rye, and B.H. Wainer. (1987). The origins of cholinergic and other subcortical afferents to the thalamus in the rat. *J Comp Neurol*. 262:105-124.

Hamouda, A.K., D.S. Stewart, S.S. Husain, and J.B. Cohen. (2011). Multiple transmembrane binding sites for p-trifluoromethyldiazirinyl-etomidate, a photoreactive Torpedo nicotinic acetylcholine receptor allosteric inhibitor. *J Biol Chem*. 286:20466-20477.

Hampel, H., A. Mitchell, K. Blennow, R.A. Frank, S. Brettschneider, L. Weller, and H.J. Moller. (2004). Core biological marker candidates of Alzheimer's disease - perspectives for diagnosis, prediction of outcome and reflection of biological activity. *Journal of neural transmission*. 111:247-272.

Han, F., N. Caporale, and Y. Dan. (2008). Reverberation of recent visual experience in spontaneous cortical waves. *Neuron*. 60:321-327.

Hanchar, H.J., P.D. Dodson, R.W. Olsen, T.S. Otis, and M. Wallner. (2005). Alcohol-induced motor impairment caused by increased extrasynaptic GABA(A) receptor activity. *Nature neuroscience*. 8:339-345.

Harrison, N.L., and M.A. Simmonds. (1985). Quantitative studies on some antagonists of N-methyl D-aspartate in slices of rat cerebral cortex. *British journal of pharmacology*. 84:381-391.

Hatakeyama, N., M. Yamazaki, N. Shibuya, S. Yamamura, and Y. Momose. (2001). Effects of ketamine on voltage-dependent calcium currents and membrane potentials in single bullfrog atrial cells. *Journal of anesthesia*. 15:149-153.

Haydon, D.A., J.R. Elliott, and B.M. Hendry. (1984). Effects of anesthetics on the squid giant axon. *Current Topics in Membranes and Transport*. 22:445-482.

Hazra, A., F. Gu, A. Aulakh, C. Berridge, J.L. Eriksen, and J. Ziburkus. (2013). Inhibitory neuron and hippocampal circuit dysfunction in an aged mouse model of Alzheimer's disease. *PLoS One*. 8:e64318.

He, Y., Z.J. Chen, and A.C. Evans. (2007). Small-world anatomical networks in the human brain revealed by cortical thickness from MRI. *Cereb Cortex*. 17:2407-2419.

Hebb, D.O. (1949). The organization of behavior : a neuropsychological theory. Wiley, New York. xix, 335 p. pp.

Hefti, F., and W.J. Weiner. (1986). Nerve growth factor and Alzheimer's disease. *Annals of neurology*. 20:275-281.

Heinke, W., and C. Schwarzbauer. (2002). In vivo imaging of anaesthetic action in humans: approaches with positron emission tomography (PET) and functional magnetic resonance imaging (fMRI). *Br J Anaesth*. 89:112-122.

Hemmings, H.C., Jr., and A.I. Adamo. (1994). Effects of halothane and propofol on purified brain protein kinase C activation. *Anesthesiology*. 81:147-155.

Henny, P., and B.E. Jones. (2008). Projections from basal forebrain to prefrontal cortex comprise cholinergic, GABAergic and glutamatergic inputs to pyramidal cells or interneurons. *Eur J Neurosci*. 27:654-670.

Hentschke, H., C. Schwarz, and B. Antkowiak. (2005). Neocortex is the major target of sedative concentrations of volatile anaesthetics: strong depression of firing rates and increase of GABAA receptor-mediated inhibition. *Eur J Neurosci*. 21:93-102.

Henze, D.A., and G. Buzsaki. (2001). Action potential threshold of hippocampal pyramidal cells in vivo is increased by recent spiking activity. *Neuroscience*. 105:121-130.

Hering, H., and M. Sheng. (2001). Dendritic spines: structure, dynamics and regulation. *Nature reviews. Neuroscience*. 2:880-888.

Herkenham, M. (1980). Laminar organization of thalamic projections to the rat neocortex. *Science (New York, N.Y.* 207:532-535.

Heurteaux, C., N. Guy, C. Laigle, N. Blondeau, F. Duprat, M. Mazzuca, L. Lang-Lazdunski, C. Widmann, M. Zanzouri, G. Romey, and M. Lazdunski. (2004). TREK-1, a K+ channel involved in neuroprotection and general anesthesia. *The EMBO journal*. 23:2684-2695.

Hill-Venning, C., D. Belelli, J.A. Peters, and J.J. Lambert. (1997). Subunit-dependent interaction of the general anaesthetic etomidate with the gamma-aminobutyric acid type A receptor. *British journal of pharmacology*. 120:749-756.

Hill, A.V. (1910). The possible effects of the aggregation of the molecules of haemoglobin on its dissociation curves. *J Physiol (London)*

40:iv-vii.

Hill, M.R., and S.A. Greenfield. (2014). Characterization of early cortical population response to thalamocortical input in vitro. *Frontiers in neuroscience*. 7:273.

Hille, B. (2001). Ion channels and excitable membranes. Sinauer Associates, Inc., Sunderland, Massachusetts, USA. 795 pp.

Hirota, K., S.H. Roth, J. Fujimura, A. Masuda, and Y. Ito. (1998). GABAergic mechanisms in the action of general anesthetics. *Toxicology letters*. 100-101:203-207.

Hoeflinger, B.F., C.A. Bennett-Clarke, N.L. Chiaia, H.P. Killackey, and R.W. Rhoades. (1995). Patterning of local intracortical projections within the vibrissae representation of rat primary somatosensory cortex. *J Comp Neurol*. 354:551-563.

Hoffman, D.A., J.C. Magee, C.M. Colbert, and D. Johnston. (1997). K+ channel regulation of signal propagation in dendrites of hippocampal pyramidal neurons. *Nature*. 387:869-875.
Hofle, N., T. Paus, D. Reutens, P. Fiset, J. Gotman, A.C. Evans, and B.E. Jones. (1997). Regional cerebral blood flow changes as a function of delta and spindle activity during slow wave sleep in humans. *J Neurosci*. 17:4800-4808.
Holt, G.R., and C. Koch. (1999). Electrical interactions via the extracellular potential near cell bodies. *Journal of computational neuroscience*. 6:169-184.
Homayoun, H., and B. Moghaddam. (2007). NMDA receptor hypofunction produces opposite effects on prefrontal cortex interneurons and pyramidal neurons. *J Neurosci*. 27:11496-11500.
Hoogland, P.V., E. Welker, and H. Van der Loos. (1987). Organization of the projections from barrel cortex to thalamus in mice studied with Phaseolus vulgaris-leucoagglutinin and HRP. *Exp Brain Res*. 68:73-87.
Hopfield, J.J. (1982). Neural networks and physical systems with emergent collective computational abilities. *Proc Natl Acad Sci U S A*. 79:2554-2558.
Hopfinger, J.B., M.H. Buonocore, and G.R. Mangun. (2000). The neural mechanisms of top-down attentional control. *Nature neuroscience*. 3:284-291.
Hopfinger, J.B., and J.S. Maxwell. (2005). Appearing and disappearing stimuli trigger a reflexive modulation of visual cortical activity. *Brain research. Cognitive brain research*. 25:48-56.
Horton, J.C., and D.L. Adams. (2005). The cortical column: a structure without a function. *Philosophical transactions of the Royal Society of London. Series B, Biological sciences*. 360:837-862.
Hsieh, C.Y., S.J. Cruikshank, and R. Metherate. (2000). Differential modulation of auditory thalamocortical and intracortical synaptic transmission by cholinergic agonist. *Brain Res*. 880:51-64.
Hubel, D.H., and T.N. Wiesel. (1962). Receptive fields, binocular interaction and functional architecture in the cat's visual cortex. *The Journal of physiology*. 160:106-154.
Hubel, D.H., and T.N. Wiesel. (1968). Receptive fields and functional architecture of monkey striate cortex. *The Journal of physiology*. 195:215-243.
Imry, Y. (1997). Introduction to mesoscopic physics. Oxford University Press, New York, NY.
Ingber, L. (1992). Generic mesoscopic neural networks based on statistical mechanics of neocortical interactions. *Physical review. A*. 45:2183-2186.
Ingrid. (2012). *Benzodiazepins: GABA-BENZODIAZEPINE RECEPTOR COMPLEX*. [WEB] Accessed: 12th July 2016. http://technology-in-medicine.com/benzodiazepines-gaba-benzodiazepine-receptor-complex1-buy-cheap-cipro.html
Irifune, M., T. Shimizu, M. Nomoto, and T. Fukuda. (1992). Ketamine-induced anesthesia involves the N-methyl-D-aspartate receptor-channel complex in mice. *Brain Res*. 596:1-9.
Isaacson, J.S., and M. Scanziani. (2011). How inhibition shapes cortical activity. *Neuron*. 72:231-243.
Ito, M. (1985). Processing of vibrissa sensory information within the rat neocortex. *Journal of neurophysiology*. 54:479-490.
Izhikevich, E.M. (2002). Resonance and selective communication via bursts in neurons having subthreshold oscillations. *Bio Systems*. 67:95-102.
Jasmin, L., A.R. Burkey, A. Granato, and P.T. Ohara. (2004). Rostral agranular insular cortex and pain areas of the central nervous system: a tract-tracing study in the rat. *J Comp Neurol*. 468:425-440.
Jellema, T., C.H. Brunia, and W.J. Wadman. (2004). Sequential activation of microcircuits underlying somatosensory-evoked potentials in rat neocortex. *Neuroscience*. 129:283-295.
Jeong, J. (2004). EEG dynamics in patients with Alzheimer's disease. *Clin Neurophysiol*. 115:1490-1505.
Jia, F., L. Pignataro, C.M. Schofield, M. Yue, N.L. Harrison, and P.A. Goldstein. (2005). An extrasynaptic GABAA receptor mediates tonic inhibition in thalamic VB neurons. *Journal of neurophysiology*. 94:4491-4501.
Jin, S., and L.R. Collins. (2007). Dynamics of dissolved polymer chains in isotropic turbulence. *New J Phys*. 9.

Jin, W., R.J. Zhang, and J.Y. Wu. (2002). Voltage-sensitive dye imaging of population neuronal activity in cortical tissue. *Journal of neuroscience methods*. 115:13-27.
Johnson, B.A., and R.D. Frostig. (2016). Long, intrinsic horizontal axons radiating through and beyond rat barrel cortex have spatial distributions similar to horizontal spreads of activity evoked by whisker stimulation. *Brain structure & function*. 221:3617-3639.
Johnston, D., and S.M.-S. Wu. (1995). Foundations of Cellular Neurophysiology. MIT Press, Cambridge, MA.
Johnston, M.V., M. McKinney, and J.T. Coyle. (1979). Evidence for a cholinergic projection to neocortex from neurons in basal forebrain. *Proc Natl Acad Sci U S A*. 76:5392-5396.
Joksovic, P.M., B.C. Brimelow, J. Murbartian, E. Perez-Reyes, and S.M. Todorovic. (2005). Contrasting anesthetic sensitivities of T-type Ca2+ channels of reticular thalamic neurons and recombinant Ca(v)3.3 channels. *British journal of pharmacology*. 144:59-70.
Jones, B.E. (2005). From waking to sleeping: neuronal and chemical substrates. *Trends in pharmacological sciences*. 26:578-586.
Jones, B.E., and A.C. Cuello. (1989). Afferents to the basal forebrain cholinergic cell area from pontomesencephalic--catecholamine, serotonin, and acetylcholine--neurons. *Neuroscience*. 31:37-61.
Jones, E.G. (1975). Varieties and distribution of non-pyramidal cells in the somatic sensory cortex of the squirrel monkey. *J Comp Neurol*. 160:205-267.
Jones, E.G. (2002). Thalamic circuitry and thalamocortical synchrony. *Philosophical transactions of the Royal Society of London. Series B, Biological sciences*. 357:1659-1673.
Jones, E.G., and T.P. Powell. (1970). An electron microscopic study of the laminar pattern and mode of termination of afferent fibre pathways in the somatic sensory cortex of the cat. *Philosophical transactions of the Royal Society of London. Series B, Biological sciences*. 257:45-62.
Jones, M.S., and D.S. Barth. (2002). Effects of bicuculline methiodide on fast (>200 Hz) electrical oscillations in rat somatosensory cortex. *Journal of neurophysiology*. 88:1016-1025.
Karakas, S., O.U. Erzengin, and E. Basar. (2000). The genesis of human event-related responses explained through the theory of oscillatory neural assemblies. *Neurosci Lett*. 285:45-48.
Katzel, D., B.V. Zemelman, C. Buetfering, M. Wolfel, and G. Miesenbock. (2011). The columnar and laminar organization of inhibitory connections to neocortical excitatory cells. *Nature neuroscience*. 14:100-107.
Katzner, S., I. Nauhaus, A. Benucci, V. Bonin, D.L. Ringach, and M. Carandini. (2009). Local origin of field potentials in visual cortex. *Neuron*. 61:35-41.
Kawaguchi, Y., and Y. Kubota. (1997). GABAergic cell subtypes and their synaptic connections in rat frontal cortex. *Cereb Cortex*. 7:476-486.
Kelly, R.M., and P.L. Strick. (2003). Cerebellar loops with motor cortex and prefrontal cortex of a nonhuman primate. *J Neurosci*. 23:8432-8444.
Kerr, J.N., C.P. de Kock, D.S. Greenberg, R.M. Bruno, B. Sakmann, and F. Helmchen. (2007). Spatial organization of neuronal population responses in layer 2/3 of rat barrel cortex. *J Neurosci*. 27:13316-13328.
Khawaled, R., A. Bruening-Wright, J.P. Adelman, and J. Maylie. (1999). Bicuculline block of small-conductance calcium-activated potassium channels. *Pflugers Archiv : European journal of physiology*. 438:314-321.
Killackey, H.P. (1973). Anatomical evidence for cortical subdivisions based on vertically discrete thalamic projections from the ventral posterior nucleus to cortical barrels in the rat. *Brain Res*. 51:326-331.
Killackey, H.P., and S.M. Sherman. (2003). Corticothalamic projections from the rat primary somatosensory cortex. *J Neurosci*. 23:7381-7384.
Kim, U., and F.F. Ebner. (1999). Barrels and septa: separate circuits in rat barrels field cortex. *J Comp Neurol*. 408:489-505.
Kisley, M.A., and G.L. Gerstein. (1999). Trial-to-trial variability and state-dependent modulation of auditory-evoked responses in cortex. *J Neurosci*. 19:10451-10460.
Kleckner, N.W., and R. Dingledine. (1988). Requirement for glycine in activation of NMDA-receptors expressed in Xenopus oocytes. *Science (New York, N.Y.* 241:835-837.

Knopfel, T. (2012). Genetically encoded optical indicators for the analysis of neuronal circuits. *Nature reviews. Neuroscience*. 13:687-700.
Knopfel, T., J. Diez-Garcia, and W. Akemann. (2006). Optical probing of neuronal circuit dynamics: genetically encoded versus classical fluorescent sensors. *Trends in neurosciences*. 29:160-166.
Koch, C. (1999). Biophysics of Computation: Information Procesing in Single Neurons. Oxford University Press, New York, New York.
Koch, C., and S. Greenfield. (2007). How does consciousness happen? *Sci Am*. 297:76-83.
Konnerth, A., A.L. Obaid, and B.M. Salzberg. (1987). Optical recording of electrical activity from parallel fibres and other cell types in skate cerebellar slices in vitro. *The Journal of physiology*. 393:681-702.
Kopp Lugli, A., C.S. Yost, and C.H. Kindler. (2009). Anaesthetic mechanisms: update on the challenge of unravelling the mystery of anaesthesia. *Eur J Anaesthesiol*. 26:807-820.
Kowalski, N., D.A. Depireux, and S.A. Shamma. (1996a). Analysis of dynamic spectra in ferret primary auditory cortex. I. Characteristics of single-unit responses to moving ripple spectra. *Journal of neurophysiology*. 76:3503-3523.
Kowalski, N., D.A. Depireux, and S.A. Shamma. (1996b). Analysis of dynamic spectra in ferret primary auditory cortex. II. Prediction of unit responses to arbitrary dynamic spectra. *Journal of neurophysiology*. 76:3524-3534.
Krasowski, M.D., and N.L. Harrison. (1999). General anaesthetic actions on ligand-gated ion channels. *Cellular and molecular life sciences : CMLS*. 55:1278-1303.
Kratzer, S., C. Mattusch, R. Haseneder, M. Eder, E. Kochs, and G. Rammes. (2012). Xenon Dose-Dependently Reduces Neuronal Activity Propagation in the Thalamocortical Network: a Voltage-Sensitive Dye Imaging study. *Anaesthesiology*.
Kratzer, S., C. Mattusch, R. Haseneder, M. Eder, E. Kochs, and G. Rammes. (2014). Propofol Modulates Spatial Cortical Signal Propagation in Acute Thalamocortical Brain Slices. *Anaesthesiology*.
Kreiman, G., C.P. Hung, A. Kraskov, R.Q. Quiroga, T. Poggio, and J.J. DiCarlo. (2006). Object selectivity of local field potentials and spikes in the macaque inferior temporal cortex. *Neuron*. 49:433-445.
Krettek, J.E., and J.L. Price. (1977a). The cortical projections of the mediodorsal nucleus and adjacent thalamic nuclei in the rat. *J Comp Neurol*. 171:157-191.
Krettek, J.E., and J.L. Price. (1977b). Projections from the amygdaloid complex to the cerebral cortex and thalamus in the rat and cat. *J Comp Neurol*. 172:687-722.
Kringelbach, M.L., and E.T. Rolls. (2004). The functional neuroanatomy of the human orbitofrontal cortex: evidence from neuroimaging and neuropsychology. *Progress in neurobiology*. 72:341-372.
Kuhn, B., W. Denk, and R.M. Bruno. (2008). In vivo two-photon voltage-sensitive dye imaging reveals top-down control of cortical layers 1 and 2 during wakefulness. *Proc Natl Acad Sci U S A*. 105:7588-7593.
Kvarnstrom, A., R. Karlsten, H. Quiding, and T. Gordh. (2004). The analgesic effect of intravenous ketamine and lidocaine on pain after spinal cord injury. *Acta anaesthesiologica Scandinavica*. 48:498-506.
Kwan, K.Y., N. Sestan, and E.S. Anton. (2012). Transcriptional co-regulation of neuronal migration and laminar identity in the neocortex. *Development*. 139:1535-1546.
Land, P.W., and K. Kandler. (2002). Somatotopic organization of rat thalamocortical slices. *Journal of neuroscience methods*. 119:15-21.
Landisman, C.E., and B.W. Connors. (2007). VPM and PoM nuclei of the rat somatosensory thalamus: intrinsic neuronal properties and corticothalamic feedback. *Cereb Cortex*. 17:2853-2865.
Lavallee, P., and M. Deschenes. (2004). Dendroarchitecture and lateral inhibition in thalamic barreloids. *J Neurosci*. 24:6098-6105.
Lees, G. (1998). Molecular mechanisms of anaesthesia: light at the end of the channel? *Br J Anaesth*. 81:491-493.
Lefort, S., C. Tomm, J.-C.F. Sarria, and C.C. Petersen. (2008). The excitatory neuronal network of the C2 barrel column in mouse primary somatosensory cortex. *Neuron*. 61:301-316.

Lehmann, J., J.I. Nagy, S. Atmadia, and H.C. Fibiger. (1980). The nucleus basalis magnocellularis: the origin of a cholinergic projection to the neocortex of the rat. *Neuroscience*. 5:1161-1174.
Letinic, K., R. Zoncu, and P. Rakic. (2002). Origin of GABAergic neurons in the human neocortex. *Nature*. 417:645-649.
Levey, A.I., A.E. Hallanger, and B.H. Wainer. (1987). Cholinergic nucleus basalis neurons may influence the cortex via the thalamus. *Neurosci Lett*. 74:7-13.
Lewis, D.A., M.J. Campbell, S.L. Foote, M. Goldstein, and J.H. Morrison. (1987). The distribution of tyrosine hydroxylase-immunoreactive fibers in primate neocortex is widespread but regionally specific. *J Neurosci*. 7:279-290.
Lewis, P.R., and C.C. Shute. (1967). The cholinergic limbic system: projections to hippocampal formation, medial cortex, nuclei of the ascending cholinergic reticular system, and the subfornical organ and supra-optic crest. *Brain : a journal of neurology*. 90:521-540.
Li, Y., S. Tong, D. Liu, Y. Gai, X. Wang, J. Wang, Y. Qiu, and Y. Zhu. (2008). Abnormal EEG complexity in patients with schizophrenia and depression. *Clin Neurophysiol*. 119:1232-1241.
Lidov, H.G., R. Grzanna, and M.E. Molliver. (1980). The serotonin innervation of the cerebral cortex in the rat--an immunohistochemical analysis. *Neuroscience*. 5:207-227.
Lin, L., C.J. LeBlanc, T.W. Deacon, and O. Isacson. (1998). Chronic cognitive deficits and amyloid precursor protein elevation after selective immunotoxin lesions of the basal forebrain cholinergic system. *Neuroreport*. 9:547-552.
Lin, L., R. Osan, and J.Z. Tsien. (2006). Organizing principles of real-time memory encoding: neural clique assemblies and universal neural codes. *Trends in Neuroscience*. 29:48-57.
Linden, H., K.H. Pettersen, and G.T. Einevoll. (2010). Intrinsic dendritic filtering gives low-pass power spectra of local field potentials. *Journal of computational neuroscience*. 29:423-444.
Linden, H., T. Tetzlaff, T.C. Potjans, K.H. Pettersen, S. Grun, M. Diesmann, and G.T. Einevoll. (2011). Modeling the spatial reach of the LFP. *Neuron*. 72:859-872.
Lippert, M.T., K. Takagaki, W. Xu, X. Huang, and J.Y. Wu. (2007). Methods for voltage-sensitive dye imaging of rat cortical activity with high signal-to-noise ratio. *Journal of neurophysiology*. 98:502-512.
Liu, G., and R.W. Tsien. (1995). Properties of synaptic transmission at single hippocampal synaptic boutons. *Nature*. 375:404-408.
Liu, X., S. Basavaraj, R. Krishnan, and J. Yan. (2011). Contributions of the thalamocortical system towards sound-specific auditory plasticity. *Neuroscience and biobehavioral reviews*. 35:2155-2161.
Llinas, R., and U. Ribary. (1993). Coherent 40-Hz oscillation characterizes dream state in humans. *Proc Natl Acad Sci U S A*. 90:2078-2081.
Loew, L. (1996). Potentiometric dyes: Imaging electrical activity of cell membranes. *Pure Appl Chem*. 68.
Logothetis, N.K. (2008). What we can do and what we cannot do with fMRI. *Nature*. 453:869-878.
Lopes da Silva, F. (1991a). Neural mechanisms underlying brain waves: from neural membranes to networks. *Electroencephalography and clinical Neurology*. 79:81-93.
Lopes da Silva, F. (1991b). Neural mechanisms underlying brain waves: from neural membranes to networks*. *Electroencephalograph and clinical Neurophysiology*. 79:81-93.
Lopez-Munoz, F., R. Ucha-Udabe, and C. Alamo. (2005). The history of barbiturates a century after their clinical introduction. *Neuropsychiatric disease and treatment*. 1:329-343.
Lorente de No, R. (1922). La corteza cerebral de raton. *Trabajos del Laboratorio de Investigaciones Biologicas de la Universidad de Madrid*. 20:41-78.
Lorente de No, R. (1947). Action potential of the motoneurons of the hypoglosus nucleus. *J. Cell. Physiol.* 29:207-287.
Lorente de No, R. (1992). The cerebral cortex of the mouse (a first contribution--the "acoustic" cortex). *Somatosensory & motor research*. 9:3-36.
Loughlin, S.E., S.L. Foote, and J.H. Fallon. (1982). Locus coeruleus projections to cortex: topography, morphology and collateralization. *Brain research bulletin*. 9:287-294.

Lu, S.-M., and R.C. Lin. (1993). Thalamic Afferents of the Rat Barrel Cortex: A Light-and Electron-Microscopic Study Using Phaseolus vulgaris Leucoagglutinin as an Anterograde Tracer. *Somato. & Motor Res.* 10:1-16.

Ma, P.M. (1991). The barrelettes--architectonic vibrissal representations in the brainstem trigeminal complex of the mouse. I. Normal structural organization. *J Comp Neurol*. 309:161-199.

MacDonald, J.F., Z. Miljkovic, and P. Pennefather. (1987). Use-dependent block of excitatory amino acid currents in cultured neurons by ketamine. *Journal of neurophysiology*. 58:251-266.

Machado-Vieira, R., G. Salvadore, N. Diazgranados, and C.A. Zarate, Jr. (2009). Ketamine and the next generation of antidepressants with a rapid onset of action. *Pharmacology & therapeutics*. 123:143-150.

Madler, C., I. Keller, D. Schwender, and E. Poppel. (1991). Sensory Information Processing During General Anaesthesia: Effect of Isoflurane on Auditory Evoked Neuronal Oscillations. *Br J Anaesth*. 66:81-87.

Magee, J.C., and D. Johnston. (1997). A synaptically controlled, associative signal for Hebbian plasticity in hippocampal neurons. *Science (New York, N.Y.* 275:209-213.

Magistretti, P.J., L. Pellerin, D.L. Rothman, and R.G. Shulman. (1999). Energy on demand. *Science (New York, N.Y.* 283:496-497.

Maldonado, P.E., and G.L. Gerstein. (1996). Neuronal assembly dynamics in the rat auditory cortex during reorganization induced by intracortical microstimulation. *Exp Brain Res*. 112:431-441.

Mann, E.O., and O. Paulsen. (2005). Mechanisms underlying gamma ('40 Hz') network oscillations in the hippocampus--a mini-review. *Progress in biophysics and molecular biology*. 87:67-76.

Mann, E.O., J.M. Suckling, N. Hajos, S.A. Greenfield, and O. Paulsen. (2005a). Perisomatic feedback inhibition underlies cholinergically induced fast network oscillations in the rat hippocampus in vitro. *Neuron*. 45:105-117.

Mann, E.O., T. Tominaga, M. Ichikawa, and S.A. Greenfield. (2005b). Cholinergic modulation of the spatiotemporal pattern of hippocampal activity in vitro. *Neuropharmacology*. 48:118-133.

Manns, I.D., B. Sakmann, and M. Brecht. (2004). Sub- and suprathreshold receptive field properties of pyramidal neurones in layers 5A and 5B of rat somatosensory barrel cortex. *The Journal of physiology*. 556:601-622.

Markram, H., M. Toledo-Rodriguez, Y. Wang, A. Gupta, G. Silberberg, and C. Wu. (2004). Interneurons of the neocortical inhibitory system. *Nature reviews. Neuroscience*. 5:793-807.

Marshall, L., H. Helgadottir, M. Molle, and J. Born. (2006). Boosting slow oscillations during sleep potentiates memory. *Nature*. 444:610-613.

Martin, D., and D. Lodge. (1985). Ketamine acts as a non-competitive N-methyl-D-aspartate antagonist on frog spinal cord in vitro. *Neuropharmacology*. 24:999-1003.

Maxim, V., L. Sendur, J. Fadili, J. Suckling, R. Gould, R. Howard, and E. Bullmore. (2005). Fractional Gaussian noise, functional MRI and Alzheimer's disease. *NeuroImage*. 25:141-158.

May, A. (2011). Experience-dependent structural plasticity in the adult human brain. *Trends in cognitive sciences*. 15:475-482.

McCasland, J.S., and L.S. Hibbard. (1997). GABAergic neurons in barrel cortex show strong, whisker-dependent metabolic activation during normal behavior. *J Neurosci*. 17:5509-5527.

McGuire, B.A., J.P. Hornung, C.D. Gilbert, and T.N. Wiesel. (1984). Patterns of synaptic input to layer 4 of cat striate cortex. *J Neurosci*. 4:3021-3033.

Melander, T., T. Hokfelt, A. Rokaeus, A.C. Cuello, W.H. Oertel, A. Verhofstad, and M. Goldstein. (1986). Coexistence of galanin-like immunoreactivity with catecholamines, 5-hydroxytryptamine, GABA and neuropeptides in the rat CNS. *J Neurosci*. 6:3640-3654.

Mennerick, S., M. Chisari, H.J. Shu, A. Taylor, M. Vasek, L.N. Eisenman, and C.F. Zorumski. (2010). Diverse voltage-sensitive dyes modulate GABAA receptor function. *J Neurosci*. 30:2871-2879.

Mesulam, M.M. (1990). Large-scale neurocognitive networks and distributed processing for attention, language, and memory. *Annals of neurology*. 28:597-613.

Mesulam, M.M., E.J. Mufson, A.I. Levey, and B.H. Wainer. (1983a). Cholinergic innervation of cortex by the basal forebrain: cytochemistry and cortical connections of the septal area, diagonal band nuclei, nucleus basalis (substantia innominata), and hypothalamus in the rhesus monkey. *J Comp Neurol*. 214:170-197.

Mesulam, M.M., E.J. Mufson, B.H. Wainer, and A.I. Levey. (1983b). Central cholinergic pathways in the rat: an overview based on an alternative nomenclature (Ch1-Ch6). *Neuroscience*. 10:1185-1201.

Metherate, R., and J.H. Ashe. (1995). Synaptic interactions involving acetylcholine, glutamate, and GABA in rat auditory cortex. *Exp Brain Res*. 107:59-72.

Metherate, R., and S.J. Cruikshank. (1999). Thalamocortical inputs trigger a propagating envelope of gamma-band activity in auditory cortex in vitro. *Exp Brain Res*. 126:160-174.

Meyer, H.S., D. Schwarz, V.C. Wimmer, A.C. Schmitt, J.N. Kerr, B. Sakmann, and M. Helmstaedter. (2011). Inhibitory interneurons in a cortical column form hot zones of inhibition in layers 2 and 5A. *Proc Natl Acad Sci U S A*. 108:16807-16812.

Meyer, H.S., V.C. Wimmer, M. Hemberger, R.M. Bruno, C.P. de Kock, A. Frick, B. Sakmann, and M. Helmstaedter. (2010a). Cell type-specific thalamic innervation in a column of rat vibrissal cortex. *Cereb Cortex*. 20:2287-2303.

Meyer, H.S., V.C. Wimmer, M. Oberlaender, C.P. de Kock, B. Sakmann, and M. Helmstaedter. (2010b). Number and laminar distribution of neurons in a thalamocortical projection column of rat vibrissal cortex. *Cereb Cortex*. 20:2277-2286.

Miller, J.E., I. Ayzenshtat, L. Carrillo-Reid, and R. Yuste. (2014). Visual stimuli recruit intrinsically generated cortical ensembles. *Proc Natl Acad Sci U S A*. 111:E4053-4061.

Mirollo, R.E., and S.H. Strogatz. (1990). Synchronization of Pulse-Coupled Biological Oscillators. *SIAM J App. Math.* 50:1645-1662.

Mitzdorf, U. (1985). Current source-density method and application in cat cerebral cortex: investigation of evoked potentials and EEG phenomena. *Physiological reviews*. 65:37-100.

Moaddel, R., G. Abdrakhmanova, J. Kozak, K. Jozwiak, L. Toll, L. Jimenez, A. Rosenberg, T. Tran, Y. Xiao, C.A. Zarate, and I.W. Wainer. (2013). Sub-anesthetic concentrations of (R,S)-ketamine metabolites inhibit acetylcholine-evoked currents in alpha7 nicotinic acetylcholine receptors. *European journal of pharmacology*. 698:228-234.

Moczydlowski, E.G. (2013). The molecular mystique of tetrodotoxin. *Toxicon : official journal of the International Society on Toxinology*. 63:165-183.

Moiseeva, N.I., and Z.A. Aleksanian. (1986). Slow-wave oscillations of the multi-unit activity average frequency in the human brain during drowsiness and sleep. *Electroencephalography and clinical neurophysiology*. 63:431-437.

Molleman, A. (2003). Patch Clamping: An Introductory Guide to Patch Clamping Electrophysiology. John Wiley & Sons, Chichester, England.

Monaghan, D.T., and C.W. Cotman. (1985). Distribution of N-methyl-D-aspartate-sensitive L-[3H]glutamate-binding sites in rat brain. *J Neurosci*. 5:2909-2919.

Monconduit, L., A. Lopez-Avila, J.L. Molat, M. Chalus, and L. Villanueva. (2006). Corticofugal output from the primary somatosensory cortex selectively modulates innocuous and noxious inputs in the rat spinothalamic system. *J Neurosci*. 26:8441-8450.

Morrison, J.H., R. Grzanna, M.E. Molliver, and J.T. Coyle. (1978). The distribution and orientation of noradrenergic fibers in neocortex of the rat: an immunofluorescence study. *J Comp Neurol*. 181:17-39.

Moss, G.W., W.R. Lieb, and N.P. Franks. (1991). Anesthetic inhibition of firefly luciferase, a protein model for general anesthesia, does not exhibit pressure reversal. *Biophys J*. 60:1309-1314.

Mountcastle, V.B. (1997). The columnar organization of the neocortex. *Brain : a journal of neurology*. 120 (Pt 4):701-722.

Movshon, J.A., I.D. Thompson, and D.J. Tolhurst. (1978). Spatial summation in the receptive fields of simple cells in the cat's striate cortex. *The Journal of physiology*. 283:53-77.

Muller, L., and A. Destexhe. (2012). Propagating waves in thalamus, cortex and the thalamocortical system: Experiments and models. *Journal of physiology, Paris*. 106:222-238.

Murakami, S., and Y. Okada. (2006). Contributions of principal neocortical neurons to magnetoencephalography and electroencephalography signals. *The Journal of physiology*. 575:925-936.

Murthy, V.N., and E.E. Fetz. (1996). Oscillatory activity in sensorimotor cortex of awake monkeys: synchronization of local field potentials and relation to behavior. *Journal of neurophysiology*. 76:3949-3967.

Nelson, L.E., T.Z. Guo, J. Lu, C.B. Saper, N.P. Franks, and M. Maze. (2002). The sedative component of anesthesia is mediated by GABA(A) receptors in an endogenous sleep pathway. *Nature neuroscience*. 5:979-984.

Nicolelis, M.A., L.A. Baccala, R.C. Lin, and J.K. Chapin. (1995). Sensorimotor encoding by synchronous neural ensemble activity at multiple levels of the somatosensory system. *Science (New York, N.Y.* 268:1353-1358.

Nicolelis, M.A., E.E. Fanselow, and A.A. Ghazanfar. (1997). Hebb's dream: the resurgence of cell assemblies. *Neuron*. 19:219-221.

Nirthanan, S., G. Garcia, 3rd, D.C. Chiara, S.S. Husain, and J.B. Cohen. (2008). Identification of binding sites in the nicotinic acetylcholine receptor for TDBzl-etomidate, a photoreactive positive allosteric effector. *J Biol Chem*. 283:22051-22062.

Nita, D.A., M. Steriade, and F. Amzica. (2003). Hyperpolarisation rectification in cat lateral geniculate neurons modulated by intact corticothalamic projections. *The Journal of physiology*. 552:325-332.

Nordhausen, C.T., E.M. Maynard, and R.A. Normann. (1996). Single unit recording capabilities of a 100 microelectrode array. *Brain Res*. 726:129-140.

Nowak, L.G., and J. Bullier. (1997). Axons, but not cell bodies, are activated by electrical stimulation in cortical grey matter I. Evidence from chronaxie measurements. *Exp Brain Res*. 118:477-488.

Nunez, A. (1996). Unit activity of rat basal forebrain neurons: relationship to cortical activity. *Neuroscience*. 72:757-766.

Nunez, P.L. (2006). Electric fields of the brain: The neurophysiscs of EEG. Oxford University Press, Oxford.

O'Connell, A.D., M.J. Morton, and M. Hunter. (2002). Two-pore domain K+ channels-molecular sensors. *Biochim Biophys Acta*. 1566:152-161.

O'Connor, D.H., S.P. Peron, D. Huber, and K. Svoboda. (2010). Neural activity in barrel cortex underlying vibrissa-based object localization in mice. *Neuron*. 67:1048-1061.

O'Kusky, J., and M. Colonnier. (1982). A laminar analysis of the number of neurons, glia, and synapses in the adult cortex (area 17) of adult macaque monkeys. *J Comp Neurol*. 210:278-290.

Ohki, K., S. Chung, Y.H. Ch'ng, P. Kara, and R.C. Reid. (2005). Functional imaging with cellular resolution reveals precise micro-architecture in visual cortex. *Nature*. 433:597-603.

Olsen, R.W., and W. Sieghart. (2009). GABA A receptors: subtypes provide diversity of function and pharmacology. *Neuropharmacology*. 56:141-148.

Oppenheim, A.V., and R.W. Schafer. (1975). Digital Signal Processing. Prentice Hall, Engelwood Cliffs, NJ.

Orser, B.A. (2007). Lifting the fog around anesthesia. *Sci Am*. 296:54-61.

Pais-Vieira, M., M.A. Lebedev, M.C. Wiest, and M.A. Nicolelis. (2013). Simultaneous top-down modulation of the primary somatosensory cortex and thalamic nuclei during active tactile discrimination. *J Neurosci*. 33:4076-4093.

Palkovits, M., E. Mezey, R.L. Eskay, and M.J. Brownstein. (1986). Innervation of the nucleus of the solitary tract and the dorsal vagal nucleus by thyrotropin-releasing hormone-containing raphe neurons. *Brain Res*. 373:246-251.

Palmer, L.A., A.C. Rosenquist, and R.J. Tusa. (1978). The retinotopic organization of lateral suprasylvian visual areas in the cat. *J Comp Neurol*. 177:237-256.

Pandit, J.J., T.M. Cook, W.R. Jonker, and E. O'Sullivan. (2013). A national survey of anaesthetists (NAP5 Baseline) to estimate an annual incidence of accidental awareness during general anaesthesia in the UK. *Br J Anaesth*. 110:501-509.

Paoletti, P., and J. Neyton. (2007). NMDA receptor subunits: function and pharmacology. *Current opinion in pharmacology*. 7:39-47.

Papo, D., J.M. Buldu, S. Boccaletti, and E.T. Bullmore. (2014). Complex network theory and the brain. *Philosophical transactions of the Royal Society of London. Series B, Biological sciences*. 369.

Parikh, V., R. Kozak, V. Martinez, and M. Sarter. (2007). Prefrontal acetylcholine release controls cue detection on multiple timescales. *Neuron*. 56:141-154.

Parsons, T.D., D. Kleinfeld, F. Raccuia-Behling, and B.M. Salzberg. (1989). Optical recording of the electrical activity of synaptically interacting Aplysia neurons in culture using potentiometric probes. *Biophys J*. 56:213-221.

Paxinos, G., and C. Watson. (1998). The Rat Brain. Elsevier, San Diego, USA.

Pellegrino, R.G., P.S. Spencer, and J.M. Ritchie. (1984). Sodium channels in the axolemma of unmyelinated axons: a new estimate. *Brain Res*. 305:357-360.

Penttonen, M., and G. Buzsaki. (2003). Natural logarithmic relationship between brain oscillators. *Thalamus & Related Systems*. 2:145-152.

Penttonen, M., N. Nurminen, R. Miettinen, J. Sirvio, D.A. Henze, J. Csicsvari, and G. Buzsaki. (1999). Ultra-slow oscillation (0.025 Hz) triggers hippocampal afterdischarges in Wistar rats. *Neuroscience*. 94:735-743.

Perry, E., M. Walker, J. Grace, and R. Perry. (1999). Acetylcholine in mind: a neurotransmitter correlate of consciousness? *Trends in neurosciences*. 22:273-280.

Peterka, D.S., H. Takahashi, and R. Yuste. (2011). Imaging voltage in neurons. *Neuron*. 69:9-21.

Peters, A. (1979). Thalamic input to the cerebral cortex. *Trends in neurosciences*. 2:183-185.

Peters, A., and C. Sethares. (1997). The organization of double bouquet cells in monkey striate cortex. *J Neurocytol*. 26:779-797.

Petersen, C.C., T.T. Hahn, M. Mehta, A. Grinvald, and B. Sakmann. (2003). Interaction of sensory responses with spontaneous depolarization in layer 2/3 barrel cortex. *Proc Natl Acad Sci U S A*. 100:13638-13643.

Petersen, C.C., and B. Sakmann. (2001). Functionally independent columns of rat somatosensory barrel cortex revealed with voltage-sensitive dye imaging. *J Neurosci*. 21:8435-8446.

Petersen, C.C.H. (2007). The functional organization of the barrel cortex. *Neuron*. 56:339-355.

Pfurtscheller, G., A. Stancak, Jr., and C. Neuper. (1996). Event-related synchronization (ERS) in the alpha band--an electrophysiological correlate of cortical idling: a review. *International journal of psychophysiology : official journal of the International Organization of Psychophysiology*. 24:39-46.

Phillis, J.W., and A.K. Tebecis. (1967). The effects of pentobarbitone sodium on acetylcholine excitation and noradrenaline inhibition of thalamic neurons. *Life sciences*. 6:1621-1625.

Pickens, C.L., M.P. Saddoris, B. Setlow, M. Gallagher, P.C. Holland, and G. Schoenbaum. (2003). Different roles for orbitofrontal cortex and basolateral amygdala in a reinforcer devaluation task. *J Neurosci*. 23:11078-11084.

Pinto, L., M.J. Goard, D. Estandian, M. Xu, A.C. Kwan, S.H. Lee, T.C. Harrison, G. Feng, and Y. Dan. (2013). Fast modulation of visual perception by basal forebrain cholinergic neurons. *Nature neuroscience*. 16:1857-1863.

Pirot, S., J. Glowinski, and A.M. Thierry. (1995). Excitatory responses evoked in prefrontal cortex by mediodorsal thalamic nucleus stimulation: influence of anaesthesia. *European journal of pharmacology*. 285:45-54.

Pisciotta, M., G. Morgavi, and H. Jahnsen. (2010). Characterization of the in vitro propagation of epileptiform electrophysiological activity in organotypic hippocampal slice cultures coupled to 3D microelectrode arrays. *Brain Res*. 1358:46-53.

Poirazi, P., T. Brannon, and B.W. Mel. (2003). Pyramidal neuron as two-layer neural network. *Neuron*. 37:989-999.

Porter, J.T., B. Cauli, K. Tsuzuki, B. Lambolez, J. Rossier, and E. Audinat. (1999). Selective excitation of subtypes of neocortical interneurons by nicotinic receptors. *J Neurosci*. 19:5228-5235.

Poulet, J.F., and C.C. Petersen. (2008). Internal brain state regulates membrane potential synchrony in barrel cortex of behaving mice. *Nature*. 454:881-885.

Povysheva, N.V., G. Gonzalez-Burgos, A.V. Zaitsev, S. Kroner, G. Barrionuevo, D.A. Lewis, and L.S. Krimer. (2006). Properties of excitatory synaptic responses in fast-spiking interneurons and pyramidal cells from monkey and rat prefrontal cortex. *Cereb Cortex*. 16:541-552.

Práwdicz-Neminski, W.W. (1925). Zur Kenntnis der elektrischen und der Innervationsvorgänge in den funktionellen Elementen und Geweben des tierischen Organismus. Elektrocerebrogramm der Säugetiere. *Pflügers Archiv European Journal of Physiology*. 209:362-382.
Prechtl, J.C., L.B. Cohen, B. Pesaran, P.P. Mitra, and D. Kleinfeld. (1997). Visual stimuli induce waves of electrical activity in turtle cortex. *Proc Natl Acad Sci U S A*. 94:7621-7626.
Preuss, S., and W. Stein. (2013). Comparison of two voltage-sensitive dyes and their suitability for long-term imaging of neuronal activity. *PLoS One*. 8:e75678.
Priebe, N.J., F. Mechler, M. Carandini, and D. Ferster. (2004). The contribution of spike threshold to the dichotomy of cortical simple and complex cells. *Nature neuroscience*. 7:1113-1122.
Prinz, H. (2010). Hill coefficients, dose-response curves and allosteric mechanisms. *Journal of chemical biology*. 3:37-44.
Putzke, C., P.J. Hanley, G. Schlichthorl, R. Preisig-Muller, S. Rinne, M. Anetseder, R. Eckenhoff, C. Berkowitz, T. Vassiliou, H. Wulf, and L. Eberhart. (2007). Differential effects of volatile and intravenous anesthetics on the activity of human TASK-1. *American journal of physiology. Cell physiology*. 293:C1319-1326.
Rakic, P. (2009). Evolution of the neocortex: a perspective from developmental biology. *Nature reviews. Neuroscience*. 10:724-735.
Rall, W. (1962). Electrophysiology of a dendritic neuron model. *Biophys J*. 2:145-167.
Razali, N., and Y.H. Wah. (2011). Power comparisons of shapiro-wilk, kolmogorov-smirnov, lilliefors and anderson-darling tests. *J Stat Mod & Anal*. 2:21-33.
Rehberg, B., E. Bennett, Y.H. Xiao, S.R. Levinson, and D.S. Duch. (1995). Voltage- and frequency-dependent pentobarbital suppression of brain and muscle sodium channels expressed in a mammalian cell line. *Mol Pharmacol*. 48:89-97.
Reibel, Y., M. HJung, M. Bouhifd, B. Cunin, and C. Draman. (2003). CCD or CMOS camera noise characterisation. *Eur. Phys. J. AP*. 21:75-80.
Reichova, I., and S.M. Sherman. (2004). Somatosensory corticothalamic projections: distinguishing drivers from modulators. *Journal of neurophysiology*. 92:2185-2197.
Research, D.S.S. (2016). *Statistical Power Calculator: Average, Two-Sample Toolkit*. [WEB] Accessed: 11th of October 2016. https://www.dssresearch.com/KnowledgeCenter/toolkitcalculators/statisticalpowercalculators.aspx
Ribeiro, P.O., A.R. Tome, H.B. Silva, R.A. Cunha, and L.M. Antunes. (2014). Clinically relevant concentrations of ketamine mainly affect long-term potentiation rather than basal excitatory synaptic transmission and do not change paired-pulse facilitation in mouse hippocampal slices. *Brain Res*. 1560:10-17.
Richter, L., C. de Graaf, W. Sieghart, Z. Varagic, M. Morzinger, I.J. de Esch, G.F. Ecker, and M. Ernst. (2012). Diazepam-bound GABAA receptor models identify new benzodiazepine binding-site ligands. *Nature chemical biology*. 8:455-464.
Riedel, G., B. Platt, and J. Micheau. (2003). Glutamate receptor function in learning and memory. *Behavioural brain research*. 140:1-47.
Riedner, B.A., V.V. Vyazovskiy, R. Huber, M. Massimini, S. Esser, M. Murphy, and G. Tononi. (2007). Sleep homeostasis and cortical synchronization: III. A high-density EEG study of sleep slow waves in humans. *Sleep*. 30:1643-1657.
Riggall, A.C., and B.R. Postle. (2012). The relationship between working memory storage and elevated activity as measured with functional magnetic resonance imaging. *J Neurosci*. 32:12990-12998.
Ringach, D.L. (2009). Spontaneous and driven cortical activity: implications for computation. *Current opinion in neurobiology*. 19:439-444.
Rinkus, G.J. (2010). A cortical sparse distributed coding model linking mini- and macrocolumn-scale functionality. *Frontiers in neuroanatomy*. 4:17.
Ritchie, J.M., and R.B. Rogart. (1977). Density of sodium channels in mammalian myelinated nerve fibers and nature of the axonal membrane under the myelin sheath. *Proc Natl Acad Sci U S A*. 74:211-215.

Ritchie, J.M., R.B. Rogart, and G.R. Strichartz. (1976). A new method for labelling saxitoxin and its binding to non-myelinated fibres of the rabbit vagus, lobster walking leg, and garfish olfactory nerves. *The Journal of physiology*. 261:477-494.

Robbins, T.W., and A.F. Arnsten. (2009). The neuropsychopharmacology of fronto-executive function: monoaminergic modulation. *Annual review of neuroscience*. 32:267-287.

Rockland, K.S., and D.N. Pandya. (1979). Laminar origins and terminations of cortical connections of the occipital lobe in the rhesus monkey. *Brain Res*. 179:3-20.

Rodriguez, G., D. Arnaldi, and A. Picco. (2011). Brain functional network in Alzheimer's disease: diagnostic markers for diagnosis and monitoring. *International journal of Alzheimer's disease*. 2011:481903.

Roland, P.E., A. Hanazawa, C. Undeman, D. Eriksson, T. Tompa, H. Nakamura, S. Valentiniene, and B. Ahmed. (2006). Cortical feedback depolarization waves: a mechanism of top-down influence on early visual areas. *Proc Natl Acad Sci U S A*. 103:12586-12591.

Rolls, E.T. (2000). The orbitofrontal cortex and reward. *Cereb Cortex*. 10:284-294.

Rorig, B., and B. Sutor. (1996). Serotonin regulates gap junction coupling in the developing rat somatosensory cortex. *Eur J Neurosci*. 8:1685-1695.

Rosnow, R.L., and R. Rosenthal. (1991). If you're looking at the cell means, you're not looking at only the interaction (unless all main effects are zero).
. *Psychological bulletin*. 110:574-576.

Rosow, C., and P.J. Manberg. (2001). Bispectral index monitoring. *Anesthesiology clinics of North America*. 19:947-966, xi.

Ross, W.N., B.M. Salzberg, L.B. Cohen, A. Grinvald, H.V. Davila, A.S. Waggoner, and C.H. Wang. (1977). Changes in absorption, fluorescence, dichroism, and Birefringence in stained giant axons: : optical measurement of membrane potential. *The Journal of membrane biology*. 33:141-183.

Roth, S.H., S.A. Forman, L.M. Braswell, and K.W. Miller. (1989). Actions of pentobarbital enantiomers on nicotinic cholinergic receptors. *Mol Pharmacol*. 36:874-880.

Rubino, D., K.A. Robbins, and N.G. Hatsopoulos. (2006). Propagating waves mediate information transfer in the motor cortex. *Nature neuroscience*. 9:1549-1557.

Rudebeck, P.H., M.E. Walton, B.H. Millette, E. Shirley, M.F. Rushworth, and D.M. Bannerman. (2007). Distinct contributions of frontal areas to emotion and social behaviour in the rat. *Eur J Neurosci*. 26:2315-2326.

Rudolph, U., and B. Antkowiak. (2004). Molecular and neuronal substrates for general anaesthetics. *Nature reviews. Neuroscience*. 5:709-720.

Rusch, D., H. Zhong, and S.A. Forman. (2004). Gating allosterism at a single class of etomidate sites on alpha1beta2gamma2L GABA A receptors accounts for both direct activation and agonist modulation. *J Biol Chem*. 279:20982-20992.

Rye, D.B., B.H. Wainer, M.M. Mesulam, E.J. Mufson, and C.B. Saper. (1984). Cortical projections arising from the basal forebrain: a study of cholinergic and noncholinergic components employing combined retrograde tracing and immunohistochemical localization of choline acetyltransferase. *Neuroscience*. 13:627-643.

Sabatini, B.L., and W.G. Regehr. (1999). Timing of synaptic transmission. *Annual review of physiology*. 61:521-542.

Salaun, C., G.W. Gould, and L.H. Chamberlain. (2005). Lipid raft association of SNARE proteins regulates exocytosis in PC12 cells. *J Biol Chem*. 280:19449-19453.

Salzberg, B.M. (1989). Optical recording of voltage changes in nerve terminals and in fine neuronal processes. *Annual review of physiology*. 51:507-526.

Salzberg, B.M., H.V. Davila, and L.B. Cohen. (1973). Optical recording of impulses in individual neurones of an invertebrate central nervous system. *Nature*. 246:508-509.

Salzberg, B.M., A. Grinvald, L.B. Cohen, H.V. Davila, and W.N. Ross. (1977). Optical recording of neuronal activity in an invertebrate central nervous system: simultaneous monitoring of several neurons. *Journal of neurophysiology*. 40:1281-1291.

Sarter, M., and J.P. Bruno. (2002). The neglected constituent of the basal forebrain corticopetal projection system: GABAergic projections. *Eur J Neurosci*. 15:1867-1873.

Sarter, M., B. Givens, and J.P. Bruno. (2001). The cognitive neuroscience of sustained attention: where top-down meets bottom-up. *Brain research. Brain research reviews*. 35:146-160.
Sato, T.K., I. Nauhaus, and M. Carandini. (2012). Traveling waves in visual cortex. *Neuron*. 75:218-229.
Scanziani, M., and M. Hausser. (2009). Electrophysiology in the age of light. *Nature*. 461:930-939.
Schevon, C.A., R.R. Goodman, G. McKhann, Jr., and R.G. Emerson. (2010). Propagation of epileptiform activity on a submillimeter scale. *Journal of clinical neurophysiology : official publication of the American Electroencephalographic Society*. 27:406-411.
Schmitzer-Torbert, N., J. Jackson, D. Henze, K. Harris, and A.D. Redish. (2005). Quantitative measures of cluster quality for use in extracellular recordings. *Neuroscience*. 131:1-11.
Schnakers, C., S. Majerus, and S. Laureys. (2005). Bispectral analysis of electroencephalogram signals during recovery from coma: preliminary findings. *Neuropsychological rehabilitation*. 15:381-388.
Schnoebel, R., M. Wolff, S.C. Peters, M.E. Brau, A. Scholz, G. Hempelmann, H. Olschewski, and A. Olschewski. (2005). Ketamine impairs excitability in superficial dorsal horn neurones by blocking sodium and voltage-gated potassium currents. *British journal of pharmacology*. 146:826-833.
Schoenbaum, G., and M. Roesch. (2005). Orbitofrontal cortex, associative learning, and expectancies. *Neuron*. 47:633-636.
Schoenbaum, G., M.R. Roesch, and T.A. Stalnaker. (2006a). Orbitofrontal cortex, decision-making and drug addiction. *Trends in neurosciences*. 29:116-124.
Schoenbaum, G., B. Setlow, and S.J. Ramus. (2003). A systems approach to orbitofrontal cortex function: recordings in rat orbitofrontal cortex reveal interactions with different learning systems. *Behavioural brain research*. 146:19-29.
Schoenbaum, G., B. Setlow, M.P. Saddoris, and M. Gallagher. (2006b). Encoding changes in orbitofrontal cortex in reversal-impaired aged rats. *Journal of neurophysiology*. 95:1509-1517.
Schubert, D., R. Kotter, and J.F. Staiger. (2007). Mapping functional connectivity in barrel-related columns reveals layer- and cell type-specific microcircuits. *Brain structure & function*. 212:107-119.
Schubert, D., J.F. Staiger, N. Cho, R. Kotter, K. Zilles, and H.J. Luhmann. (2001). Layer-specific intracolumnar and transcolumnar functional connectivity of layer V pyramidal cells in rat barrel cortex. *J Neurosci*. 21:3580-3592.
Segal, M., and S. Landis. (1974). Afferents to the hippocampus of the rat studied with the method of retrograde transport of horseradish peroxidase. *Brain Res*. 78:1-15.
Semba, K., P.B. Reiner, E.G. McGeer, and H.C. Fibiger. (1988). Brainstem afferents to the magnocellular basal forebrain studied by axonal transport, immunohistochemistry, and electrophysiology in the rat. *J Comp Neurol*. 267:433-453.
Sergent, C., S. Baillet, and S. Dehaene. (2005). Timing of the brain events underlying access to consciousness during the attentional blink. *Nature neuroscience*. 8:1391-1400.
Sharon, D., D. Jancke, F. Chavane, S. Na'aman, and A. Grinvald. (2007). Cortical response field dynamics in cat visual cortex. *Cereb Cortex*. 17:2866-2877.
Shirvalkar, P.R. (2009). Hippocampal neural assemblies and conscious remembering. *Journal of neurophysiology*. 101:2197-2200.
Shoham, D., D.E. Glaser, A. Arieli, T. Kenet, C. Wijnbergen, Y. Toledo, R. Hildesheim, and A. Grinvald. (1999). Imaging cortical dynamics at high spatial and temporal resolution with novel blue voltage-sensitive dyes. *Neuron*. 24:791-802.
Siegel, M.S., and E.Y. Isacoff. (1997). A genetically encoded optical probe of membrane voltage. *Neuron*. 19:735-741.
Sikes, R.W., Z. Gottesfeld, and J.F. DeFrance. (1983). Origin of cingulate cortex cholinergic innervation in the rat. *Brain research bulletin*. 10:429-432.
Silva, L.R., Y. Amitai, and B.W. Connors. (1991). Intrinsic oscillations of neocortex generated by layer 5 pyramidal neurons. *Science (New York, N.Y.* 251:432-435.

Singer, W., A.K. Engel, A.K. Kreiter, M.H. Munk, S. Neuenschwander, and P.R. Roelfsema. (1997). Neuronal assemblies: necessity, signature and detectability. *Trends in cognitive sciences*. 1:252-261.
Sloviter, R.S., and J.L. Brisman. (1995). Lateral inhibition and granule cell synchrony in the rat hippocampal dentate gyrus. *J Neurosci*. 15:811-820.
Softky, W. (1994). Sub-millisecond coincidence detection in active dendritic trees. *Neuroscience*. 58:13-41.
Solt, K., and S.A. Forman. (2007). Correlating the clinical actions and molecular mechanisms of general anesthetics. *Current opinion in anaesthesiology*. 20:300-306.
Sommers, D., and N. Kopell. (1993). Rapid synchronization through fast threshold modulation. *Biol. Cybern.* 68:393-407.
Somogyi, P., G. Tamas, R. Lujan, and E.H. Buhl. (1998). Salient features of synaptic organisation in the cerebral cortex. *Brain research. Brain research reviews*. 26:113-135.
Song, I., and R.L. Huganir. (2002). Regulation of AMPA receptors during synaptic plasticity. *Trends in neurosciences*. 25:578-588.
Sorra, K.E., and K.M. Harris. (2000). Overview on the structure, composition, function, development, and plasticity of hippocampal dendritic spines. *Hippocampus*. 10:501-511.
Sotty, F., M. Danik, F. Manseau, F. Laplante, R. Quirion, and S. Williams. (2003). Distinct electrophysiological properties of glutamatergic, cholinergic and GABAergic rat septohippocampal neurons: novel implications for hippocampal rhythmicity. *The Journal of physiology*. 551:927-943.
Speckmann, E.-J., H. Caspers, and C.E. Elger. 1984. Neuronal Mechanisms Underlying the Generation of Field Potentials. *In* Self-Regulation of the Brain and Behavior. T. Elbert, B. Rockstroh, W. Lutzenberger, and N. Birbaumer, editors. Springer Berlin Heidelberg, Berlin, Heidelberg. 9-25.
Spencer, K.M., M.A. Niznikiewicz, M.E. Shenton, and R.W. McCarley. (2008). Sensory-evoked gamma oscillations in chronic schizophrenia. *Biological psychiatry*. 63:744-747.
Sporns, O., D.R. Chialvo, M. Kaiser, and C.C. Hilgetag. (2004). Organization, development and function of complex brain networks. *Trends in cognitive sciences*. 8:418-425.
Spors, H., and A. Grinvald. (2002). Spatio-temporal dynamics of odor representations in the mammalian olfactory bulb. *Neuron*. 34:301-315.
Spruston, N. (2008). Pyramidal neurons: dendritic structure and synaptic integration. *Nature reviews. Neuroscience*. 9:206-221.
Staiger, J.F., I. Flagmeyer, D. Schubert, K. Zilles, R. Kotter, and H.J. Luhmann. (2004). Functional diversity of layer IV spiny neurons in rat somatosensory cortex: quantitative morphology of electrophysiologically characterized and biocytin labeled cells. *Cereb Cortex*. 14:690-701.
Stam, C.J., B.F. Jones, G. Nolte, M. Breakspear, and P. Scheltens. (2007). Small-world networks and functional connectivity in Alzheimer's disease. *Cereb Cortex*. 17:92-99.
Stangroom, J. (2016). *Effect Size Calculator for T-test*. [WEB] Accessed: 12th of October 2016. http://www.socscistatistics.com/effectsize/Default3.aspx
Steinmetz, P.N., A. Manwani, C. Koch, M. London, and I. Segev. (2000). Subthreshold voltage noise due to channel fluctuations in active neuronal membranes. *Journal of computational neuroscience*. 9:133-148.
Stephenson, F.A. (2006). Structure and trafficking of NMDA and GABAA receptors. *Biochemical Society transactions*. 34:877-881.
Steriade, M. (1999). Coherent oscillations and short-term plasticity in corticothalamic networks. *Trends in neurosciences*. 22:337-345.
Steriade, M. (2006). Grouping of brain rhythms in corticothalamic systems. *Neuroscience*. 137:1087-1106.
Steriade, M., and M. Deschenes. 1988. Intrathalamic and brainstem-thalamic networks invovled in resting and alert states. *In* Cellular thalamic mechanisms. Elsevier, Amsterdam. 51-76.
Steriade, M., M. Deschenes, L. Domich, and C. Mulle. (1985). Abolition of spindle oscillations in thalamic neurons disconnected from nucleus reticularis thalami. *Journal of neurophysiology*. 54:1473-1497.

Steriade, M., I. Timofeev, and F. Grenier. (2001). Natural waking and sleep states: a view from inside neocortical neurons. *Journal of neurophysiology*. 85:1969-1985.
Stett, A., W. Barth, S. Weiss, H. Haemmerle, and E. Zrenner. (2000). Electrical multisite stimulation of the isolated chicken retina. *Vision research*. 40:1785-1795.
Stosiek, C., O. Garaschuk, K. Holthoff, and A. Konnerth. (2003). In vivo two-photon calcium imaging of neuronal networks. *Proc Natl Acad Sci U S A*. 100:7319-7324.
Stroganova, T.A., G. Nygren, M.M. Tsetlin, I.N. Posikera, C. Gillberg, M. Elam, and E.V. Orekhova. (2007). Abnormal EEG lateralization in boys with autism. *Clin Neurophysiol*. 118:1842-1854.
Sturtevant, J.M. (1977). Heat capacity and entropy changes in processes involving proteins. *Proc Natl Acad Sci U S A*. 74:2236-2240.
Sugiyama, K., T. Muteki, and K. Shimoji. (1992). Halothane-induced hyperpolarization and depression of postsynaptic potentials of guinea pig thalamic neurons in vitro. *Brain Res*. 576:97-103.
Takahashi, H., and D.A. Terrar. (1994). Effects of etomidate on whole-cell and single L-type calcium channel currents in guineapig isolated ventricular myocytes. *Br J Anaesth*. 73:812-819.
Takahashi, K., M. Saleh, R.D. Penn, and N.G. Hatsopoulos. (2011). Propagating waves in human motor cortex. *Frontiers in human neuroscience*. 5:40.
Takahashi, N., T. Sasaki, A. Usami, N. Matsuki, and Y. Ikegaya. (2007). Watching neuronal circuit dynamics through functional multineuron calcium imaging (fMCI). *Neuroscience research*. 58:219-225.
Tallon-Baudry, C., and O. Bertrand. (1999). Oscillatory gamma activity in humans and its role in object representation. *Trends in cognitive sciences*. 3:151-162.
Tang, Q., V. Tsytsarev, A. Frank, Y. Wu, C.W. Chen, R.S. Erzurumlu, and Y. Chen. (2016). In Vivo Mesoscopic Voltage-Sensitive Dye Imaging of Brain Activation. *Scientific reports*. 6:25269.
Tang, Q., V. Tsytsarev, C.P. Liang, F. Akkentli, R.S. Erzurumlu, and Y. Chen. (2015). In Vivo Voltage-Sensitive Dye Imaging of Subcortical Brain Function. *Scientific reports*. 5:17325.
Tanifuji, M., T. Sugiyama, and K. Murase. (1994). Horizontal propagation of excitation in rat visual cortical slices revealed by optical imaging. *Science (New York, N.Y.* 266:1057-1059.
Tasaki, I., and A. Warashina. (1976). Dye-membrane interaction and its changes during nerve excitation. *Photochemistry and photobiology*. 24:191-207.
Tasaki, I., A. Watanabe, R. Sandlin, and L. Carnay. (1968). Changes in fluorescence, turbidity, and birefringence associated with nerve excitation. *Proc Natl Acad Sci U S A*. 61:883-888.
Tassin, J.P., J. Bockaert, G. Blanc, L. Stinus, A.M. Thierry, S. Lavielle, J. Premont, and J. Glowinski. (1978). Topographical distribution of dopaminergic innervation and dopaminergic receptors of the anterior cerebral cortex of the rat. *Brain Res*. 154:241-251.
Tassonyi, E., E. Charpantier, D. Muller, L. Dumont, and D. Bertrand. (2002). The role of nicotinic acetylcholine receptors in the mechanisms of anesthesia. *Brain research bulletin*. 57:133-150.
Tehovnik, E.J. (1996). Electrical stimulation of neural tissue to evoke behavioral responses. *Journal of neuroscience methods*. 65:1-17.
Tehovnik, E.J., K. Lee, and P.H. Schiller. (1994). Stimulation-evoked saccades from the dorsomedial frontal cortex of the rhesus monkey following lesions of the frontal eye fields and superior colliculus. *Exp Brain Res*. 98:179-190.
Tehovnik, E.J., and W.M. Slocum. (2004). Behavioural state affects saccades elicited electrically from neocortex. *Neuroscience and biobehavioral reviews*. 28:13-25.
Tehovnik, E.J., A.S. Tolias, F. Sultan, W.M. Slocum, and N.K. Logothetis. (2006). Direct and indirect activation of cortical neurons by electrical microstimulation. *Journal of neurophysiology*. 96:512-521.
Theyel, B.B., C.C. Lee, and S.M. Sherman. (2010). Specific and nonspecific thalamocortical connectivity in the auditory and somatosensory thalamocortical slices. *Neuroreport*. 21:861-864.
Thompson, A.J., H.A. Lester, and S.C. Lummis. (2010). The structural basis of function in Cys-loop receptors. *Quarterly reviews of biophysics*. 43:449-499.
Thompson, S.A., P.J. Whiting, and K.A. Wafford. (1996). Barbiturate interactions at the human GABAA receptor: dependence on receptor subunit combination. *British journal of pharmacology*. 117:521-527.

Thornton, C. (1991). Evoked potentials in anaesthesia. *Eur J Anaesthesiol*. 8:89-107.
Todorovic, S.M., and C.J. Lingle. (1998). Pharmacological properties of T-type Ca2+ current in adult rat sensory neurons: effects of anticonvulsant and anesthetic agents. *Journal of neurophysiology*. 79:240-252.
Tominaga, T., Y. Tominaga, H. Yamada, G. Matsumoto, and M. Ichikawa. (2000). Quantification of optical signals with electrophysiological signals in neural activities of Di-4-ANEPPS stained rat hippocampal slices. *Journal of neuroscience methods*. 102:11-23.
Tomlin, S.L., A. Jenkins, W.R. Lieb, and N.P. Franks. (1998). Stereoselective effects of etomidate optical isomers on gamma-aminobutyric acid type A receptors and animals. *Anesthesiology*. 88:708-717.
Trageser, J.C., and A. Keller. (2004). Reducing the uncertainty: gating of peripheral inputs by zona incerta. *J Neurosci*. 24:8911-8915.
Traynelis, S.F., M. Hartley, and S.F. Heinemann. (1995). Control of proton sensitivity of the NMDA receptor by RNA splicing and polyamines. *Science (New York, N.Y.* 268:873-876.
Tregellas, J.R., D.B. Davalos, D.C. Rojas, M.C. Waldo, L. Gibson, K. Wylie, Y.P. Du, and R. Freedman. (2007). Increased hemodynamic response in the hippocampus, thalamus and prefrontal cortex during abnormal sensory gating in schizophrenia. *Schizophrenia research*. 92:262-272.
Tremblay, L., and W. Schultz. (2000). Reward-related neuronal activity during go-nogo task performance in primate orbitofrontal cortex. *Journal of neurophysiology*. 83:1864-1876.
Tsau, Y., L. Guan, and J.Y. Wu. (1999). Epileptiform activity can be initiated in various neocortical layers: an optical imaging study. *Journal of neurophysiology*. 82:1965-1973.
Tso, M.M., K.L. Blatchford, L.F. Callado, D.P. McLaughlin, and J.A. Stamford. (2004). Stereoselective effects of ketamine on dopamine, serotonin and noradrenaline release and uptake in rat brain slices. *Neurochem Int*. 44:1-7.
Tsytsarev, V., C. Bernardelli, and K. Maslov. (2012). Living Brain Optical Imaging: Technology, Methods and Applications. *J. Neuroscience and Neuroengineering*. 1:180-192.
Tsytsarev, V., L.D. Liao, K.V. Kong, Y.H. Liu, R.S. Erzurumlu, M. Olivo, and N.V. Thakor. (2014). Recent progress in voltage-sensitive dye imaging for neuroscience. *Journal of nanoscience and nanotechnology*. 14:4733-4744.
Tusa, R.J., L.A. Palmer, and A.C. Rosenquist. (1978). The retinotopic organization of area 17 (striate cortex) in the cat. *J Comp Neurol*. 177:213-235.
Tusa, R.J., A.C. Rosenquist, and L.A. Palmer. (1979). Retinotopic organization of areas 18 and 19 in the cat. *J Comp Neurol*. 185:657-678.
Tuteja, N. (2009). Signaling through G protein coupled receptors. *Plant signaling & behavior*. 4:942-947.
Uchida, I., G. Kamatchi, D. Burt, and J. Yang. (1995). Etomidate potentiation of GABAA receptor gated current depends on the subunit composition. *Neurosci Lett*. 185:203-206.
Urbain, N., and M. Deschenes. (2007). A new thalamic pathway of vibrissal information modulated by the motor cortex. *J Neurosci*. 27:12407-12412.
Urban, B.W. 2008. The Site of Anesthetic Action. *In* Modern Anesthetics. Vol. 182. Springer Heidelberg, Berlin.
Uusi-Oukari, M., L.S. Kontturi, S.A. Kallinen, and V. Salonen. (2010). AMPA receptors serum-dependently mediate GABAA receptor alpha1 and alpha6 subunit down-regulation in cultured mouse cerebellar granule cells. *Neurochem Int*. 56:720-726.
Valadao, P.A., L.A. Naves, R.S. Gomez, and C. Guatimosim. (2013). Etomidate evokes synaptic vesicle exocytosis without increasing miniature endplate potentials frequency at the mice neuromuscular junction. *Neurochem Int*. 63:576-582.
Van Essen, D.C. (2005). Corticocortical and thalamocortical information flow in the primate visual system. *Progress in brain research*. 149:173-185.
van Haeften, T., L. Baks-te-Bulte, P.H. Goede, F.G. Wouterlood, and M.P. Witter. (2003). Morphological and numerical analysis of synaptic interactions between neurons in deep and superficial layers of the entorhinal cortex of the rat. *Hippocampus*. 13:943-952.

van Kerkoerle, T., M.W. Self, B. Dagnino, M.A. Gariel-Mathis, J. Poort, C. van der Togt, and P.R. Roelfsema. (2014). Alpha and gamma oscillations characterize feedback and feedforward processing in monkey visual cortex. *Proc Natl Acad Sci U S A*. 111:14332-14341.

Vanderwolf, C.H., A. Raithby, M. Snider, C. Cristi, and C. Tanner. (1993). Effects of some cholinergic agonists on neocortical slow wave activity in rats with basal forebrain lesions. *Brain research bulletin*. 31:515-521.

Varga, C., A. Sik, P. Lavallee, and M. Deschenes. (2002). Dendroarchitecture of relay cells in thalamic barreloids: a substrate for cross-whisker modulation. *J Neurosci*. 22:6186-6194.

Veinante, P., and M. Deschenes. (1999). Single- and multi-whisker channels in the ascending projections from the principal trigeminal nucleus in the rat. *J Neurosci*. 19:5085-5095.

Veinante, P., M.F. Jacquin, and M. Deschenes. (2000). Thalamic projections from the whisker-sensitive regions of the spinal trigeminal complex in the rat. *J Comp Neurol*. 420:233-243.

Velly, L.J., M.F. Rey, N.J. Bruder, F.A. Gouvitsos, T. Witjas, J.M. Regis, J.C. Peragut, and F.M. Gouin. (2007). Differential dynamic of action on cortical and subcortical structures of anesthetic agents during induction of anesthesia. *Anesthesiology*. 107:202-212.

Vogel, E.K., S.J. Luck, and K.L. Shapiro. (1998). Electrophysiological evidence for a postperceptual locus of suppression during the attentional blink. *Journal of experimental psychology. Human perception and performance*. 24:1656-1674.

Voss, L.J., C.H. Baas, L. Hansson, D.A. Steyn-Ross, M. Steyn-Ross, and J.W. Sleigh. (2012). Investigation into the effect of the general anaesthetics etomidate and ketamine on long-range coupling of population activity in the mouse neocortical slice. *European journal of pharmacology*. 689:111-117.

Voytko, M.L. (1996). Cognitive functions of the basal forebrain cholinergic system in monkeys: memory or attention? *Behavioural brain research*. 75:13-25.

Vyazovskiy, V.V., B.A. Riedner, C. Cirelli, and G. Tononi. (2007). Sleep homeostasis and cortical synchronization: II. A local field potential study of sleep slow waves in the rat. *Sleep*. 30:1631-1642.

Waggoner, A.S., and A. Grinvald. (1977). Mechanisms of rapid optical changes of potential sensitive dyes. *Ann N Y Acad Sci*. 303:217-241.

Wagner, L.E., 2nd, K.J. Gingrich, J.C. Kulli, and J. Yang. (2001). Ketamine blockade of voltage-gated sodium channels: evidence for a shared receptor site with local anesthetics. *Anesthesiology*. 95:1406-1413.

Wahl-Schott, C., and M. Biel. (2008). HCN channels: Structure, cellular regulation and physiological function. *Cellular and Molecular Life Sciences*. 66:470-494.

Wan, X., D.A. Mathers, and E. Puil. (2003). Pentobarbital modulates intrinsic and GABA-receptor conductances in thalamocortical inhibition. *Neuroscience*. 121:947-958.

Wang, S., Z. Yao, J. Wang, Y. Ai, D. Li, Y. Zhang, J. Mao, H. Gu, Y. Ruan, and J. Mao. (2006). Evidence for a distinct group of nestin-immunoreactive neurons within the basal forebrain of adult rats. *Neuroscience*. 142:1209-1219.

Waterhouse, B.D., H.C. Moises, and D.J. Woodward. (1980). Noradrenergic modulation of somatosensory cortical neuronal responses to iontophoretically applied putative neurotransmitters. *Experimental neurology*. 69:30-49.

Watt, A.J., H. Cuntz, M. Mori, Z. Nusser, P.J. Sjostrom, and M. Hausser. (2009). Traveling waves in developing cerebellar cortex mediated by asymmetrical Purkinje cell connectivity. *Nature neuroscience*. 12:463-473.

Watts, D.J., and S.H. Strogatz. (1998). Collective dynamics of 'small-world' networks. *Nature*. 393:440-442.

Wei, W., N. Zhang, Z. Peng, C.R. Houser, and I. Mody. (2003). Perisynaptic localization of delta subunit-containing GABA(A) receptors and their activation by GABA spillover in the mouse dentate gyrus. *J Neurosci*. 23:10650-10661.

Weinberger, D.R., and K.F. Berman. (1988). Speculation on the meaning of cerebral metabolic hypofrontality in schizophrenia. *Schizophrenia bulletin*. 14:157-168.

Weiss, D.S., and J.J. Hablitz. (1984). Interaction of penicillin and pentobarbital with inhibitory synaptic mechanisms in neocortex. *Cell Mol Neurobiol*. 4:301-317.

Welker, E., P.V. Hoogland, and H. Van der Loos. (1988). Organization of feedback and feedforward projections of the barrel cortex: a PHA-L study in the mouse. *Exp Brain Res*. 73:411-435.
Werner, G. (2007). Brain dynamics across levels of organization. *Journal of physiology, Paris*. 101:273-279.
West, A.E., W.G. Chen, M.B. Dalva, R.E. Dolmetsch, J.M. Kornhauser, A.J. Shaywitz, M.A. Takasu, X. Tao, and M.E. Greenberg. (2001). Calcium regulation of neuronal gene expression. *Proc Natl Acad Sci U S A*. 98:11024-11031.
Wester, J.C., and D. Contreras. (2012). Columnar interactions determine horizontal propagation of recurrent network activity in neocortex. *J Neurosci*. 32:5454-5471.
White, B., L.F. Abbott, and J. Fiser. (2012). Suppression of cortical neural variability is stimulus- and state-dependent. *Journal of neurophysiology*. 108:2383-2392.
White, E.L. (1978). Identified neurons in mouse Sml cortex which are postsynaptic to thalamocortical axon terminals: a combined Golgi-electron microscopic and degeneration study. *J Comp Neurol*. 181:627-661.
White, E.L. (1979). Thalamocortical synaptic relations: a review with emphasis on the projections of specific thalamic nuclei to the primary sensory areas of the neocortex. *Brain Res*. 180:275-311.
Whitehouse, P.J., D.L. Price, R.G. Struble, A.W. Clark, J.T. Coyle, and M.R. Delon. (1982). Alzheimer's disease and senile dementia: loss of neurons in the basal forebrain. *Science (New York, N.Y.* 215:1237-1239.
Whittington, M.A., and R.D. Traub. (2003). Interneuron diversity series: inhibitory interneurons and network oscillations in vitro. *Trends in neurosciences*. 26:676-682.
Wilent, W.B., and D. Contreras. (2004). Synaptic responses to whisker deflections in rat barrel cortex as a function of cortical layer and stimulus intensity. *J Neurosci*. 24:3985-3998.
Williams, M.N., D.S. Zahm, and M.F. Jacquin. (1994). Differential foci and synaptic organization of the principal and spinal trigeminal projections to the thalamus in the rat. *Eur J Neurosci*. 6:429-453.
Wilson, F.A., S.P. O'Scalaidhe, and P.S. Goldman-Rakic. (1994). Functional synergism between putative gamma-aminobutyrate-containing neurons and pyramidal neurons in prefrontal cortex. *Proc Natl Acad Sci U S A*. 91:4009-4013.
Wimmer, V.C., R.M. Bruno, C.P. de Kock, T. Kuner, and B. Sakmann. (2010). Dimensions of a projection column and architecture of VPM and POm axons in rat vibrissal cortex. *Cereb Cortex*. 20:2265-2276.
Winters, W.D., T. Ferrar-Allado, C. Guzman-Flores, and M. Alcaraz. (1972). The cataleptic state induced by ketamine: a review of the neuropharmacology of anesthesia. *Neuropharmacology*. 11:303-315.
Wong, E.H., J.A. Kemp, T. Priestley, A.R. Knight, G.N. Woodruff, and L.L. Iversen. (1986). The anticonvulsant MK-801 is a potent N-methyl-D-aspartate antagonist. *Proc Natl Acad Sci U S A*. 83:7104-7108.
Wong, Y.T., M.M. Fabiszak, Y. Novikov, N.D. Daw, and B. Pesaran. (2016). Coherent neuronal ensembles are rapidly recruited when making a look-reach decision. *Nature neuroscience*. 19:327-334.
Woolsey, T.A. 1988. Barrels, Vibrissae, and Topographic Representations. *In* Sensory Systems: II. Birkhäuser Boston. 7-9.
Woolsey, T.A., and H. Van der Loos. (1970). The structural organization of layer IV in the somatosensory region (SI) of mouse cerebral cortex. The description of a cortical field composed of discrete cytoarchitectonic units. *Brain Res*. 17:205-242.
Woolum, J.C., and F. Strumwasser. (1978). Membrane-potential-sensitive dyes for optical monitoring of activity in Aplysia neurons. *Journal of neurobiology*. 9:185-193.
Wu, J.Y., L. Guan, L. Bai, and Q. Yang. (2001). Spatiotemporal properties of an evoked population activity in rat sensory cortical slices. *Journal of neurophysiology*. 86:2461-2474.
Wu, J.Y., L. Guan, and Y. Tsau. (1999). Propagating activation during oscillations and evoked responses in neocortical slices. *J Neurosci*. 19:5005-5015.
Wu, J.Y., H. Xiaoying, and Z. Chuan. (2008). Propagating waves of activity in the neocortex: what they are, what they do. *Neuroscientist*. 14:487-502.

Wyllie, D.J., M.R. Livesey, and G.E. Hardingham. (2013). Influence of GluN2 subunit identity on NMDA receptor function. *Neuropharmacology*. 74:4-17.
Xing, D., C.I. Yeh, and R.M. Shapley. (2009). Spatial spread of the local field potential and its laminar variation in visual cortex. *J Neurosci*. 29:11540-11549.
Xu, W., X. Huang, K. Takagaki, and J.Y. Wu. (2007). Compression and reflection of visually evoked cortical waves. *Neuron*. 55:119-129.
Yamamura, T., and O. Kemmotsu. (1990). [Synaptic mechanisms of excitatory amino acids and NMDA receptor mediated brain excitability]. *Masui. The Japanese journal of anesthesiology*. 39:1448-1459.
Yang, J., and I. Uchida. (1996). Mechanisms of etomidate potentiation of GABAA receptor-gated currents in cultured postnatal hippocampal neurons. *Neuroscience*. 73:69-78.
Yin, R., and E.D. French. (2000). A comparison of the effects of nicotine on dopamine and non-dopamine neurons in the rat ventral tegmental area: an in vitro electrophysiological study. *Brain research bulletin*. 51:507-514.
Yue, C., and Y. Yaari. (2004). KCNQ/M channels control spike afterdepolarization and burst generation in hippocampal neurons. *J Neurosci*. 24:4614-4624.
Yuste, R. (2011). Dendritic spines and distributed circuits. *Neuron*. 71:772-781.
Yuste, R., A. Peinado, and L.C. Katz. (1992). Neuronal domains in developing neocortex. *Science (New York, N.Y.* 257:665-669.
Yuste, R., D.W. Tank, and D. Kleinfeld. (1997). Functional study of the rat cortical microcircuitry with voltage-sensitive dye imaging of neocortical slices. *Cereb Cortex*. 7:546-558.
Zaborszky, L. (2002). The modular organization of brain systems. Basal forebrain: the last frontier. *Progress in brain research*. 136:359-372.
Zaborszky, L., and W.E. Cullinan. (1989). Hypothalamic axons terminate on forebrain cholinergic neurons: an ultrastructural double-labeling study using PHA-L tracing and ChAT immunocytochemistry. *Brain Res*. 479:177-184.
Zaborszky, L., and W.E. Cullinan. (1996). Direct catecholaminergic-cholinergic interactions in the basal forebrain. I. Dopamine-beta-hydroxylase- and tyrosine hydroxylase input to cholinergic neurons. *J Comp Neurol*. 374:535-554.
Zaborszky, L., W.E. Cullinan, and A. Braun. (1991). Afferents to basal forebrain cholinergic projection neurons: an update. *Advances in experimental medicine and biology*. 295:43-100.
Zaborszky, L., W.E. Cullinan, and V.N. Luine. (1993). Catecholaminergic-cholinergic interaction in the basal forebrain. *Progress in brain research*. 98:31-49.
Zaborszky, L., and A. Duque. (2000). Local synaptic connections of basal forebrain neurons. *Behavioural brain research*. 115:143-158.
Zaborszky, L., L. Heimer, F. Eckenstein, and C. Leranth. (1986). GABAergic input to cholinergic forebrain neurons: an ultrastructural study using retrograde tracing of HRP and double immunolabeling. *J Comp Neurol*. 250:282-295.
Zaborszky, L., C. Leranth, and L. Heimer. (1984). Ultrastructural evidence of amygdalofugal axons terminating on cholinergic cells of the rostral forebrain. *Neurosci Lett*. 52:219-225.
Zaugg, M., E. Lucchinetti, D.R. Spahn, T. Pasch, C. Garcia, and M.C. Schaub. (2002). Differential effects of anesthetics on mitochondrial K(ATP) channel activity and cardiomyocyte protection. *Anesthesiology*. 97:15-23.
Zecevic, D., M. Djurisic, L.B. Cohen, S. Antic, M. Wachowiak, C.X. Falk, and M.R. Zochowski. (2003). Imaging nervous system activity with voltage-sensitive dyes. *Current protocols in neuroscience / editorial board, Jacqueline N. Crawley ... [et al.]*. Chapter 6:Unit 6 17.
Zhang, D., Z.H. Pan, M. Awobuluyi, and S.A. Lipton. (2001). Structure and function of GABA(C) receptors: a comparison of native versus recombinant receptors. *Trends in pharmacological sciences*. 22:121-132.
Zhang, F., V. Gradinaru, A.R. Adamantidis, R. Durand, R.D. Airan, L. de Lecea, and K. Deisseroth. (2010). Optogenetic interrogation of neural circuits: technology for probing mammalian brain structures. *Nature protocols*. 5:439-456.

Zhang, Y., J.C. He, X.K. Liu, Y. Zhang, Y. Wang, and T. Yu. (2014). Assessment of the effect of etomidate on voltage-gated sodium channels and action potentials in rat primary sensory cortex pyramidal neurons. *European journal of pharmacology*. 736:55-62.

Zhang, Y., M.J. Laster, E.I. Eger, 2nd, M. Sharma, and J.M. Sonner. (2007). Blockade of acetylcholine receptors does not change the dose of etomidate required to produce immobility in rats. *Anesthesia and analgesia*. 104:850-852.

Zhang, Z., and S.M. Oppenheimer. (1997). Characterization, distribution and lateralization of baroreceptor-related neurons in the rat insular cortex. *Brain Res*. 760:243-250.

Zhang, Z.W., and M. Deschenes. (1997). Intracortical axonal projections of lamina VI cells of the primary somatosensory cortex in the rat: a single-cell labeling study. *J Neurosci*. 17:6365-6379.

Zimmerman, S.A., M.V. Jones, and N.L. Harrison. (1994). Potentiation of gamma-aminobutyric acidA receptor Cl- current correlates with in vivo anesthetic potency. *The Journal of pharmacology and experimental therapeutics*. 270:987-991.

Zochowski, M., M. Wachowiak, C.X. Falk, L.B. Cohen, Y.W. Lam, S. Antic, and D. Zecevic. (2000). Imaging membrane potential with voltage-sensitive dyes. *The Biological bulletin*. 198:1-21.

Zoli, M., A. Jansson, E. Sykova, L.F. Agnati, and K. Fuxe. (1999). Volume transmission in the CNS and its relevance for neuropsychopharmacology. *Trends in pharmacological sciences*. 20:142-150.